Light-Induced Emergent Quantum Phenomena in Ultracold Atomic Gases

Dissertation
zur Erlangung des akademischen Grades
Doctor of Philosophy

eingereicht an der
Fakultät für Mathematik, Informatik und Physik
der Leopold-Franzens-Universität Innsbruck

von
Stefan Ostermann, M.Sc.

Betreuung der Dissertation:
Univ.-Prof. Dr. Helmut Ritsch,
Institut für Theoretische Physik,
Universität Innsbruck

Innsbruck, Oktober 2018

Zusammenfassung

Die Entwicklung neuer Technologien, welche die Manipulation atomarer Gase mit Hilfe von Laserlicht ermöglichen, bereitete den Weg für eine neue interdisziplinäre Ära der Physik. Diese neuen Techniken verbesserten die Kühlung von Atomwolken signifikant, was zu der experimentellen Realisierung von Bose-Einstein-Kondensation führte. Plaziert man diese ultrakalten Quantengase in optischen Gittern, ergibt sich ein System, welches viele Eigenschaften komplexer Festkörpersysteme abdeckt. Somit sind diese Systeme eine ideale Plattform für die Quantensimulation von Festkörpern. In diesen "traditionellen" Quantensimulationssystemen generieren die Lichtfelder allerdings ein extern vorgegebenes Potenzial für die Atome.

Das ändert sich, wenn die Atomwolke mit den Moden eines optischen Resonators wechselwirkt. Die Wechselwirkung zwischen der atomaren Bewegung und den Resonatormoden führt zu einem dynamischen optischen Potenzial, welches zusätzlich lang- oder unendlich reichweitige Wechselwirkungen zwischen den Atomen induziert. Die resultierenden kollektiven Instabilitäten ermöglichen die Simulation neuer, faszinierender Quantenphasen. Das diesbezüglich prominenteste Beispiel ist die Selbstorganisation von Atomen in einem Stehwellenresonator, wobei die superradiante Phase des Quanten-Dicke-Hamiltonians realisiert wird. Der Phasenübergang von homogener zu periodischer Dichte, welcher bei einer kritschen Lichtintensität auftritt, bricht die diskrete Symmetrie des entsprechenden Hamiltonians. Inspiriert durch Effekte aus der Festkörperphysik lag der Forschungsschwerpunkt der letzten Jahre auf neuen Systemen, in welchen jeweils Phasenübergänge mit kontinuierlicher Symmetriebrechung auftreten.

Die vorliegende Arbeit ist eine Zusammenfassung meiner Beiträge zu diesem Forschungsfeld. In einem ersten Ansatz studieren wir lichtinduzierte Instabilitäten von kalten, thermischen Gasen und Bose-Einstein-Kondensaten in verschiedenen Modenkonfigurationen eines Ringresonators. Die fundamentalen Moden dieser Resonatorgeometrie sind ebene Wellen mit einer kontinuierlichen Translationssymmetrie. Die spontane Brechung dieser kontinuierlichen Symmetrie bei einer kritischen Laserintensiät resultiert in neuen emergenten Quantenphasen. Zunächst analysieren wir die verschiedenen Phasen eines kalten thermischen Gases in einem Ringresonator, welcher durch die Spiegel mit zwei nichtinterferierenden, gegenläufigen Lichtfeldern gepumpt wird. Abhänging vom Verhältnis zwischen den Intensitäten der zwei Pumpfelder realisiert dieses System zwei unterschiedliche Phasen – einerseits einen kollektiven Atomlaser und andererseits einen verallgemeinerten, selbstorganisierten Zustand. Weiters demonstrieren wir, dass der selbstgeordnete Zustand eines Bose-Einstein-Kondensats in einem transversal gepumpten Ringresonator eine suprasolide Phase realisiert. In einem weiteren Schritt werden durch die Erweiterung dieser Systeme auf Spinor-Bose-Einstein-Kondensate auch Spin Freiheitsgrade inkludiert. In diesem Fall können Spinsysteme mit langreichweitigen

Wechselwirkungen, welche in topologisch nicht trivialen Spinzuständen resultieren, simuliert werden.

Ein alternativer Ansatz, in welchem ein Bose-Einstein-Kondensat mit zwei nicht interferierenden, gegenläufigen Strahlen im freien Raum wechselwirkt, führt zu noch komplexeren Phänomenen. Während optische Resonatoren immer einen diskreten Satz an Moden auswählen, setzen sich Lichtfelder im freien Raum aus einem ganzen Modenkontinuum zusammen. Für hinreichend große Lichtintensitäten zeigt dieses System daher eine periodische Dichteverteilung mit kristallinen Eigenschaften, wie zum Beispiel langreichweitiger Phonon-Dynamik. Der so erhaltene Zustand ermöglicht somit die Simulation eines synthetischen Kristalls, welcher durch Licht übertragene, langreichweitige Wechselwirkungen aufweist, in einer kontrollierten Umgebung.

Abstract

The development of new techniques to manipulate atomic gases with laser light introduced a new era of interdisciplinary physics. These new tools improved the cooling of atom clouds significantly, resulting in the experimental realization of Bose-Einstein condensation. Placing these ultracold quantum gases in optical lattices generates an ideal platform for quantum simulation, since these systems capture many properties of complex condensed matter systems. In these "traditional" quantum simulation setups, however, the laser fields create an externally prescribed potential for the condensate.

This changes if the atom cloud is manipulated via the modes of an optical resonator. In this case the direct back-action of the atomic motion onto the resonator modes results in a dynamic optical potential, which mediates long or infinite range interactions between the atoms. The resulting collective instabilities allow the simulation of new intriguing quantum phases. The most prominent example is the self-organization of atoms in a standing wave resonator, which realizes the superradiant phase of the quantum Dicke Hamiltonian. This system undergoes a phase transition from a homogeneous to a periodic state beyond a critical light intensity breaking the discrete symmetry of the corresponding Hamiltonian. Inspired by condensed matter systems the focus of recent research has been the study of new setups where the phase transition breaks a continuous symmetry.

The present work summarizes my contribution to these efforts. In a first approach, we study light-induced instabilities of both, cold thermal atoms and Bose-Einstein condensates, in different mode configurations of a ring resonator. The plane wave modes of this resonator geometry possess a continuous translational symmetry. We show that this symmetry is spontaneously broken beyond a critical pump strength, resulting in new types of emergent quantum phases. Initially, we analyze the different phases of a cold thermal gas in a ring resonator, which is pumped through the cavity mirrors with two non-interfering counterpropagating light fields. Depending on the relative ratio between the two beam intensities, this system realizes two different phases, the so-called collective atomic recoil laser (CARL) and a generalized self-ordered phase. We then demonstrate that the self-ordered state of a Bose-Einstein condensate inside a transversally pumped ring resonator realizes the peculiar phase of a supersolid. In a further step, a generalization of this system to include spin degrees of freedom by using a spinor Bose-Einstein condensate yields new intriguing phenomena. In this case spin-systems with long-range interactions leading to topologically non-trivial spin states can be simulated by tuning easily accessible cavity parameters.

An alternative approach, where a Bose-Einstein condensate acts back on two non-interfering counterpropagating beams in free space, reveals even more complex physics. Whereas optical resonators always select a discrete set of modes, light fields in free space consist of a whole continuum of modes. As a result, for sufficiently large light intensities this system exhibits a phase transition from homogeneous to periodic order with crystalline properties such as long-range phonon dynamics. Hence, the resulting state allows the simulation of a synthetic crystal with light mediated long-range interactions in a well-controllable environment.

Danksagung

Zu allererst gilt Univ.-Prof. Dr. Helmut Ritsch ein Dank für die professionelle Betreuung meiner Dissertation. Seine vielen Ideen und seine physikalische Intuition lenkten diese Arbeit in die richtigen Bahnen. Die vorgelebte, unermüdliche Faszination für wissenschaftliche Themen, welche weit über sein Fachgebiet hinaus reichen, war mir stets eine willkommene Quelle der Motivation. Auch die von ihm zur Verfügung gestellten technischen Spielzeuge und Knobeleien waren immer wieder eine erfrischende Abwechslung im beruflichen Alltag. An dieser Stelle seinen auch die regelmäßigen Gruppenaktivitäten in der Tiroler Bergwelt erwähnt, welche zu einer sehr angenehmen und entspannten Arbeitsatmosphäre in der Arbeitsgruppe Ritsch beitrugen.

Des weiteren möchte ich mich auch bei meinen direkten Kollaborationspartnern Tobias Grießer, Francesco Piazza und Farokh Mivehvar bedanken. Ihre Erfahrung, ihr wissenschaftlicher Sachverstand und ihre Geduld in unzähligen Diskussionen waren ein essenzieller Bestandteil für die Entstehung dieser Arbeit. Allen ehemaligen und aktuellen Mitarbeitern der Ritsch-Gruppe, Elvia Colella, Claudiu Genes, Raphael Holzinger, Daniela Holzmann, Christoph Hotter, Arthur Jungkind, Sebastian Krämer, Thomas Maier, Wolfgang Niedenzu, Laurin Ostermann, David Plankensteiner, Katrin Sandner, Raimar Sandner, Matthias Sonnleitner, Valentin Torggler, Prasanna Venkatesh, Dominik Winterauer, Hashem Zoubi sowie unserem Langzeitgast Karol Gietka sei für die freundschaftliche und unterstützende Zusammenarbeit in den letzten Jahren gedankt. Christiane Ebongue, Daniela Holzmann und Hon-Wai Lau danke ich für die produktive Arbeit an den gemeinsamen Publikationen.

Auch dem Sekretariat des Instituts für Theoretische Physik, Nicole Jorda, Birgit Laimer, Elke Stenico und Elke Wölflmaier gilt ein großes Dankeschön für die stets unkomplizierte und schnelle Abwicklung bürokratischer Angelegenheiten. Hans Embacher danke ich für die professionelle Wartung unsere Computersysteme.

Bedanken möchte ich mich neben dem akademischen Umfeld auch bei all meinen Freunden außerhalb der Welt der Physik, welche zweifelsohne einen wichtigen Beitrag zur Fertigstellung dieser Arbeit leisteten. Bei verschiedensten Freizeitaktivitäten halfen sie mir immer wieder meinen Kopf frei zu bekommen und gewährleisteten den zeitweise notwendigen Abstand von der wissenschaftlichen Arbeit. Bei jedem einzelnen, welcher Teil des einen oder anderen Abenteuers war, sei es beim Schifahren, Mountainbiken, Bergsteigen, Volleyball oder auf Reisen, möchte ich mich an dieser Stelle bedanken.

Ein großer Dank gilt auch dem erweiterten Kreis meiner Familie für den stetigen Rückhalt. Insbesondere meinen Eltern Elisabeth und Rudi danke ich von ganzem Herzen für die vielseitige Unterstützung über die letzten Jahre und dafür, dass sie mich stets ermutigten den eingeschlagenen Weg fortzusetzen. Meiner Schwester Verena und meinem Bruder Raphael danke ich für die vielen lustigen Stunden.

Die letzten Jahre, welche ich der Arbeit an dieser Dissertation widmete, wären nur halb so schön gewesen, hätte ich sie nicht mit der liebenswertesten und besten Frau an meiner Seite verbracht. Mein aufrichtiger Dank an Carmen für die uneingeschränkte Unterstützung in allen Belangen!

Die Liste wichtiger Personen ließe sich beliebig erweitern. All jenen, welche direkt oder indirekt zum Entstehen dieser Dissertation beigetragen haben, jedoch an dieser Stelle nicht explizit erwähnt werden, sei an dieser Stelle ein herzliches Dankeschön ausgesprochen.

Contents

1 Introduction

The early twentieth century brought up one of the most remarkable revolutions in modern science leading to a completely new understanding of nature on the atomic scale. The related theory based on these new insights is commonly known as quantum theory and has proven to be a successful tool to describe and explain many properties of the microscopic world. The starting point for the development of quantum theory is Max Planck's work on black-body radiation in 1900 where he assumed that a body at a certain temperature can only emit and absorb radiation energy in discrete portions. Consequently, he could derive the emission spectrum for black-body radiation [1.1, 1.2]. In his work explaining the photoelectric effect [1.3] in 1905, Albert Einstein elaborated a physical interpretation for this initially peculiar assumption of quantized energies. He introduced the notion of particles of light – now often referred to as *photons* – carrying a well-defined amount of energy and momentum. Einstein's finding of the quantized character of light lies at the heart of quantum theory and it resulted in a whole series of new interpretations and developments in the following decades. In particular, the insight of Louis de Broglie in 1923 that not only light can have the characteristics of a particle but also microscopic particles can have wave-like properties [1.4] lead to the notion of quantum matter which has fundamentally different properties compared to classical matter. Following this insight Erwin Schrödinger showed in 1926 that the dynamics of a quantum system can be described by a wave equation [1.5] and a year later Paul Dirac introduced the first formalism to describe the interaction between quantized light and quantized matter [1.6]. This led to the first rigorous quantum theory of radiation developed by Encrico Fermi in 1932 [1.7] which established the basis of modern quantum electrodynamics (QED) as it was formulated by Richard Feynman in 1950 [1.8].

1.1 Manipulating Cold Atoms with Laser Light

Einstein's hypothesis revealed that light can impose forces on neutral atoms. This is a direct result of the imposed recoil kick on the atom due to the emission and absorption of light, i. e. of a photon. This hypothesis was experimentally proven by Otto Robert Frisch in 1933 when he showed that a beam of neutral sodium atoms can be deflected by a near resonant emission lamp [1.9]. After this first experimental evidence it took until 1960 for the first realization of a laser by Theodore H. Maiman [1.10] based on a theoretical work by Charles Hard Townes and Arthur Leonard Schawlow [1.11]. This motivated an in depth study of light matter interactions. The particular properties of laser light (monochromatic, spatially coherent, high intensity, etc.) and the good controllability of the laser parameters made it the ideal light source for the purpose of studying and analyzing radiation force effects on neutral atoms. This revealed that the radiation force acting on an atom in a coherent light field (e. g. a laser field) consists of two fundamentally different parts, the radiation pressure force and the dipole force [1.12].

The radiation pressure force is related to the absorption of a photon followed by spontaneous emission to free space. In contrast to the incoming light beam, the spontaneous emission process has no directional preference and hence the recoil kicks in different spatial directions average out. This results in a net momentum transfer parallel to the incoming laser beam. Therefore, the radiation pressure force always pushes the particle away from the light source. The strength of the radiation pressure depends on the spontaneous emission rate of the atom which can be tuned by changing the laser frequency. The dissipative nature of this force plays an important role in the most prominent cooling schemes for atom clouds, especially for the Doppler cooling method [1.13, 1.14]. In this case, the atoms are illuminated by two counterpropagating beams with frequencies close to the atomic transition frequency resulting in a velocity dependent friction force. The ability to cool single atoms, ions or molecules and even atomic gases to very low temperatures increased the controllability of these systems significantly. Modifications of the fundamental Doppler cooling scheme to reach even lower temperatures [1.15] together with some additional evaporative cooling methods resulted in the first experimental realization of Bose-Einstein condensation in 1995 [1.16, 1.17]. In this peculiar phase of quantum matter all particles of an ultracold atomic cloud behave like a single matter wave which is a direct result of a macroscopic population of the lowest energy state. Bose-Einstein condensates have proven to be a valuable tool for many experimental implementations studying some of the most puzzling features of quantum mechanics.

In contrast to the radiation pressure force, which is mainly used to manipulate the momentum degrees of freedom of the particles, the dipole force can be used to manipulate the particles' positions. This implies that cold atomic gases and Bose-Einstein condensates can be efficiently trapped in an optical potential [1.18], which in the simplest possible way is generated by two counterpropagating interfering laser beams. The coherent scattering of photons from one beam to the other results in a conservative potential for the atoms. A particularly important application of these light generated potentials are optical tweezers developed by Arthur Ashkin in the 1980s who received the Nobel Prize in physics in 2018 for his research in this direction [1.19]. The dipole force can be either attractive or repulsive depending on the difference between the laser frequency and the internal atomic transition frequency. If the frequency of the incoming laser beams is smaller than the atomic transition frequency (red detuning) the particles are dragged to the intensity maxima, whereas in the case where the laser frequency is bigger than the atomic frequency (blue detuning) the particles are pushed to the intensity minima. The spatial dependence of the resulting optical potential is given by the light intensity gradient. For example in the setup of two running waves with opposite direction the resulting periodic intensity pattern leads to a periodic optical lattice for the atoms. Optical lattices together with the cooling methods described above became an important tool in different fields of physics ranging from quantum computing [1.20, 1.21] to precise time measurements with optical lattice clocks [1.22]. The controlled manipulation of single atoms or atomic clouds by light became a major research direction in the past decades, which is commonly known as quantum optics.

1.2 Quantum Simulation with Atoms in Optical Lattices

The idea of quantum simulation was first proposed by R. Feynman in 1982 [1.23]. The basic principle is to simulate complex quantum mechanical systems by experimentally implementing systems with similar properties which are easier to control and analyze. Cold (bosonic or fermionic) atomic gases trapped in optical lattices have proven to be a valuable setup to simulate otherwise inaccessible condensed matter and solid state systems. The most prominent example is a dilute atomic gas trapped in an optical lattice, which under some conditions can be readily described by a Bose-Hubbard model [1.24]. The Bose-Hubbard model originates from solid-state physics and it describes the physics of spinless bosons on a lattice [1.25]. The model predicts a quantum phase transition between a superfluid state and a Mott-insulator state [1.26] which was first experimentally realized with a Bose-Einstein condensate in an optical lattice in 2002 [1.27]. Since then many other systems were analyzed by the means of quantum simulation based on ultracold quantum gases in optical lattices [1.28] and there is a lot of ongoing research in this field until today [1.29–1.32].

However, most quantum simulation setups based on optical lattices cannot account for long-range interaction between particles, which plays an important role in many condensed matter systems. In most systems the lattice is assumed to be deep such that the tight-binding approximation leading to Bose-Hubbard type of Hamiltonians holds. This results in local contact interaction between the particles but the long range interaction via the light field is suppressed. Due to the high photon numbers the optical potential plays the role of a classical static potential for the atoms. In a well known approach, long-range interactions between the atoms trapped in the optical lattice can be included by using Rydberg states of atoms [1.33] or condensates of magnetic atoms [1.34]. Nevertheless, the optical lattice acts as an externally fixed and prescribed potential and the back-action of the atom dynamics on the potential may be neglected. This changes if the atoms are coupled to the modes of an optical resonator or any other system which increases the interaction between the atoms and the light fields significantly.

1.3 Generalized Quantum Simulation

The great success of quantum simulation in classical static optical lattices led to the search for new types of setups where the back action of the atom dynamics on the light fields is no longer negligible. The most prominent setup which fulfills this criterion are cold atoms coupled to the mode of an optical resonator. In an optical resonator the photons are reflected back and forth many times between two parallel mirrors before they leak out through one of the mirrors [1.35]. This results in long photon storage times in such a device which implied the commonly used notion optical cavity. The related research direction is known as cavity quantum electrodynamics (cavity QED).

The strong interaction between the atoms and single cavity photons which is a direct result of the long photon storage time results in a significant back action of the atomic motion on the cavity field. This leads to complex coupled non-linear dynamics resulting in a broad variety of effects [1.36]. In particular, the generalization of the Bose-Hubbard model for atomic gases in conventional optical lattices to resonator generated optical lattices [1.37] revealed that the resonator generated long-range interactions lead to remarkable modifications of the phase diagram [1.38–1.40].

The light induced interaction between atoms leads to non-trivial collective effects and the most prominent effect in the context of quantum simulation is the self-organization of atoms in an optical cavity. Theoretically predicted in 2002 [1.41] and first experimentally realized with cold thermal atoms in 2003 [1.42], self-organization arises if a cold gas of atoms is placed inside a standing wave resonator and is illuminated from the side. For small laser intensities the atomic density distribution stays homogeneous and no light is scattered into the cavity mode. If the laser intensity, however, exceeds a certain threshold a light-induced collective instability occurs and the particles start to scatter in phase and the cavity mode gets populated resulting in a periodic dipole potential for the atoms. Thus, the particles are trapped in their self-generated optical potential leading to a periodic density pattern. The mechanism governing the generation of the optical potential and the nature of the phase transition from homogeneous to periodic order is fundamentally different to the case of optical lattices where the potential is prescribed externally and the particles are trapped in this prescribed geometry. Hence, the setup of a transversally pumped standing wave resonator allows the simulation of different types of phase transitions compared to traditional quantum simulation setups with optical lattices. The realization of self-organization with a Bose-Einstein condensate at ETH Zurich revealed, that the phase transition from homogeneous to periodic order realizes the Dicke quantum phase transition [1.43], which was already predicted in 1953 [1.44]. This paved the way for new systems allowing quantum simulation of different types of problems by the means of this highly non-linear quantum optical setups. In the past decade many new setups which aim for the generalization of this fundamental self-organization setup by including additional degrees of freedom to the system were proposed and realized. In this case the cavity geometries are modified or the atoms are coupled to other non-linear optical devices such as optical nano-fibres or photonic crystal fibres. This then leads to richer dynamics and the ability to trigger even more complex types of phase transitions [1.45–1.50].

1.4 Outline of the Thesis

The articles contained in the present thesis contribute to the search for novel geometries allowing to simulate more complex effects and phase transitions in ultracold quantum gases by the means of light induced collective instabilities. The fundamental principle in all works presented in the following is the analysis of new systems with continuous symmetries and photon mediated long-range interactions. The spontaneous breaking of continuous symmetries is a fundamental mechanism in different fields of physics ranging from condensed matter theory to elementary particle physics. Thus, light induced continuous symmetry breaking opens up the opportunity to simulate such mechanisms in a well-controllable environment. The main part of this thesis is made up by four published articles and one preprint. They contain analytical and numerical studies on the physics of modified cavity geometries as well as a generalization of the concept of self-ordering to free space. This thesis is organized as follows:

In chapter 2 an elementary introduction to the basic concepts and models, which are contained in the publications of this thesis, is provided. Starting from the description of classical electromagnetic fields, the basic properties of optical resonators are introduced and different relevant resonator geometries are discussed. After a short description of the quantization of the resonator light fields the interaction between light and matter is discussed for classical and quantized light fields. The last two sections in this chapter are devoted to the various types of studied atomic media. First, an overview over relevant quantities for thermal gases is given, and a method to study the dynamics of a classical thermal gas coupled to laser light fields based on the Vlasov equation is introduced. Second, the effect of Bose-Einstein condensation is discussed briefly. In addition, an overview of different methods to analyze the properties of Bose-Einstein condensates is presented.

In chapter 3 two most prominent examples of light induced instabilities of atom clouds coupled to resonator modes are discussed. These two instabilities form the basis for many discussions and interpretations of the results gained for generalized systems in the following works. First the instability leading to Collective Atomic Recoil Lasing (CARL) in the classical Vlasov picture is examined. Second, in section 3.2, the effect of self-organization of a BEC in a standing wave resonator is described and analyzed in a fully quantum mechanical description.

The following chapters contain the publications making up the main part of the thesis. In the publication contained in chapter 4 [1.51] we study a generalized ring cavity setup where a classical thermal gas is coupled to two counterpropagating, non-interfering cavity modes. This system with an a priori continuous translational symmetry can be related to a generalized CARL instability as well as to the case of a transversally pumped ring-cavity depending on the imbalance between the two pump intensities.

In chapter 5 a similar type of geometry for a BEC in free space is proposed [1.52]. We show that under certain conditions a collective instability can be induced even without an optical resonator. This results in spontaneous crystallization of the light fields together with the atoms. As a consequence the system breaks its continuous translational symmetry. The publication presented in chapter 6 [1.53] contains an in depth analysis of this transition, particularly taking into account important quantities for experimental implementations of the studied setup. At this point it should be mentioned that a first experimental evidence of the proposed phase transition has been published recently [1.54].

In the publication contained in chapter 7 [1.55] we show that the continuous symmetry breaking of a Bose-Einstein condensate in a transversally pumped ring-cavity realizes the peculiar phase of a supersolid. This unique phase of quantum matter which is characterized by a gapless Goldstone mode shows features of both a solid and a superfluid.

In chapter 8 the ring cavity setup studied on a classical level in chapter 4 is extended to account for the simulation of non-trivial spin dynamics [1.56]. This can be achieved by coupling a spinor condensate to the non-interfering pumped modes of the cavity. We show that a topological phase transition from a topologically trivial state to a topologially non-trivial spin state characterized by a global topological invariant can be simulated efficiently in the presented setup.

The concluding remarks on this thesis are presented in chapter 9. After this an additional publication on light forces near optical fibres [1.57] with major contributions of the author of the present thesis, which does not lie exactly in the research field covered of the other publications contained in the thesis is presented.

2 Theoretical Background

In this chapter we give an overview of the physical systems and theoretical frameworks which are used in the publications contained in this thesis. As it was already mentioned in the previous chapter the essential concept of cavity quantum electrodynamics is the manipulation of atomic positions and momenta with light fields. The light fields can be either classical or quantum. Therefore, we first discuss the physics of classical electromagnetic fields in dielectric media. Based on this we describe the properties of different optical resonator geometries which play a crucial role in the setups studied in the following publications. We then focus on the different radiation forces, which can be imposed on atoms, and introduce the concept of the AC-Stark shift providing an optical potential for the atoms in classical light fields. The generalization to the interaction of atoms with quantized light fields leads to the Jaynes-Cummings model which is understood to be the most simple model to describe the interaction between quantum matter and quantized light fields. The last two sections introduce two important methods to describe the atomic ensembles studied throughout this thesis. First, we give an overview of the basic properties of a classical thermal gas coupled to laser light fields where the dynamics can be readily described by a Vlasov equation. The last chapter gives an introduction on Bose-Einstein condensation and we introduce some important methods to describe and understand important properties of a condensate.

2.1 Electromagnetic Fields in Dielectric Media

The dynamics of electromagnetic fields is described by Maxwell's equations

$$\nabla \cdot \mathbf{D} = \rho, \tag{2.1a}$$
$$\nabla \cdot \mathbf{B} = 0, \tag{2.1b}$$
$$\nabla \times \mathbf{E} + \partial_t \mathbf{B} = 0, \tag{2.1c}$$
$$\nabla \times \mathbf{H} - \partial_t \mathbf{D} = \mathbf{j}, \tag{2.1d}$$

with the electric and magnetic fields $\mathbf{E}$ and $\mathbf{B}$. The charge density is denoted as ρ and the current density as $\mathbf{j}$. The properties of the dispersive material are included via the electric displacement $\mathbf{D} = \varepsilon \mathbf{E} = \varepsilon_0 \mathbf{E} + \mathbf{P}$ where ε (ε_0) is the permittivity (in free space) and $\mathbf{P}$ is the polarization density of the material. The magnetic field in a medium with permeability μ is defined via $\mathbf{H} = \mathbf{B}/\mu = \mathbf{B}/\mu_0 + \mathbf{M}$. Here, μ_0 is the permittivity of the vaccum and $\mathbf{M}$ is the magnetization density. For the sake of simplicity let us first focus on non-dispersive and isotropic media which implies that the permittivity is a space and frequency independent quantity. In the following we will always assume no charge densities or currents inside the medium, i. e. $\rho = 0$ and $\mathbf{j} = 0$. The latter assumption results in no magnetization of the medium ($\mathbf{M} = 0$) resulting in $\mathbf{H} = \mu_0 \mathbf{B}$.

Calculating the curl of Eq. (2.1c), i. e. $\nabla \times \nabla \times \mathbf{E} + \partial_t (\nabla \times \mathbf{B}) = 0$ by using the other three equations results in the inhomogeneous wave equation for electric fields inside a dielectric medium

$$\Delta \mathbf{E}(\mathbf{x}, t) - \frac{1}{c^2} \partial_t^2 \mathbf{E}(\mathbf{x}, t) = \mu_0 \partial_t^2 \mathbf{P}(\mathbf{x}, t), \tag{2.2}$$

where the speed of light in vacuum is defined as $c := 1/\sqrt{\varepsilon_0 \mu_0}$.

Assuming monochromatic waves $\mathbf{E}(\mathbf{x}, t) = \mathrm{Re}\big[\boldsymbol{\mathcal{E}}(\mathbf{x}) e^{i\omega t}\big]$ results in the inhomogeneous Helmholtz equation

$$\Delta \boldsymbol{\mathcal{E}}(\mathbf{x}) + \frac{\omega^2}{c^2} \boldsymbol{\mathcal{E}}(\mathbf{x}) = -\mu_0 \omega^2 \boldsymbol{\mathcal{P}}(\mathbf{x}), \tag{2.3}$$

describing the spatial shape of the field amplitudes. In the present work we will only deal with linear media which means that the polarization density depends linearly on the electric field via the relation $\mathcal{P}(\mathbf{x}) = \varepsilon_0 \chi \mathcal{E}(\mathbf{x})$ where χ denotes the electric susceptibility of the medium. The susceptibility is zero in vacuum and it takes non-zero values for any dielectric medium. For linear media the Helmholtz equation can, therefore, be simplified to

$$\Delta \boldsymbol{\mathcal{E}}(\mathbf{x}) + k^2 \left(1 + \chi\right) \boldsymbol{\mathcal{E}}(\mathbf{x}) = 0, \tag{2.4}$$

where we introduced the wavenumber $k := \omega/c = 2\pi/\lambda$. The coefficient in the second term of Eq. (2.4) can be understood as the modified wavenumber due to the presence of the medium $\tilde{k} = k\sqrt{1+\chi} = kn$ with the refractive index n.

The discussion up to now was based on a non-dispersive and isotropic medium. In the case of dispersive and anisotropic media the Maxwell equations (2.1) are still applicable. Therefore, the easiest generalization of the model described above to dispersive and anisotropic media may be performed by making the susceptiblility space and frequency dependent $\chi \to \chi(\omega, x)$ in Eq. (2.4). The resulting Helmholtz equation will play an important role in the model presented in the chapters 5 and 6.

2.2 Optical Resonators

Due to their specific properties optical resonators have become an important tool in quantum optics. They have a broad range of applications ranging from spectral analysis of light, as optical filters and as resonators for many different types of lasers. Due to the strong improvement of optical resonators in the past decades they now can be used to store single photons for sufficiently long times [2.1] (several microseconds in the optical regime and hundreds of milliseconds in the microwave regime). Therefore, the interaction between a photon which is reflected back and forth many times inside the resonator and an atom or ion placed inside the resonator can be enhanced significantly. The fact that optical resonators can be used as containers for photons resulted in the term optical cavity which will be used as a synonym for optical resonator throughout this thesis.

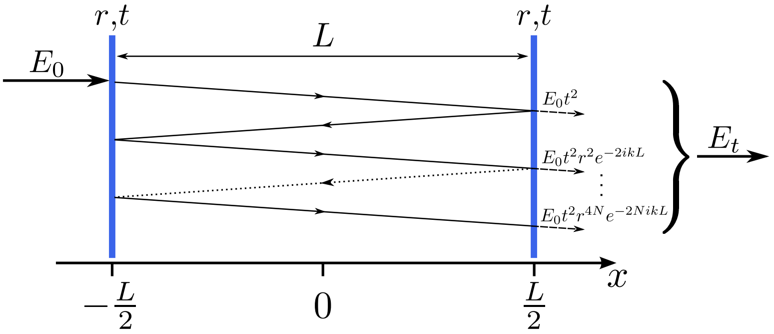

Figure 2.1: Schematic drawing of a Fabry-Pérot resonator. The light field is reflected back and forth between the resonator mirrors and it leaks out after N runs. The mirrors are separated by a length L and have a reflectivity r and a transmittance t.

Since the models in the following publications use classical and quantized electromagnetic fields, we will discuss both cases. In addition, we will first discuss the simplest resonator geometry which is the Fabry-Pérot resonator (often also referred to as standing wave cavity). Hereby we introduce some important quantities characterizing the most important features of a resonator. In the following section we then introduce the ring resonator geometry which plays an important role in some of the systems studied in this thesis.

2.2.1 Standing Wave Resonators

An ideal standing wave or Fabry-Pérot resonator consists of two transmitting, plane, parallel mirrors at a distance L with a reflection coefficient r and a transmission coefficient t as it is shown in Fig. 2.1. In the following we will always assume non-absorbing mirrors which results in real valued reflection- and transmission coefficients.

Classical Electromagnetic Field

First we focus on classical light fields which later will be generalized to quantized fields. We will restrict the discussion to one dimension along the resonator axis (x-direction). The fundamental modes of an empty ($\chi = 0$) standing wave resonator are solutions of the one-dimensional Helmholtz equation

$$(\partial_x^2 + k^2)\mathbf{f}(x) = 0, \tag{2.5}$$

which fulfill the boundary condition that the electric field has to vanish at the mirror positions. This condition is fulfilled for eigenmodes of the form

$$\mathbf{f}_{n,\sigma}(x) = \mathbf{e}_\sigma \cos(k_n x) \quad \text{with} \quad k_n = \frac{n\pi}{L} \quad \text{for} \quad n \in \mathbb{N} \quad \text{and} \quad \sigma \in \{1, 2\}. \tag{2.6}$$

The two polarization vectors $\mathbf{e}_{1,2}$ are orthogonal to each other and the wavevector $\mathbf{k}_n = k_n \mathbf{e}_x$ defines the propagation direction of the field. Real polarization vectors correspond to linear field polarizations whereas complex vectors describe circular or elliptical polarizations [2.2]. Any arbitrary field inside the resonator can be written as the superposition of the fundamental resonator modes with amplitudes $c_{n,\sigma}$

$$\boldsymbol{\mathcal{E}}(x) = \sum_{n,\sigma} \mathbf{f}_{n,\sigma}(x) = \sum_{n,\sigma} \mathbf{e}_\sigma c_{n,\sigma} \cos(k_n x). \tag{2.7}$$

The eigenfrequencies associated with the fundamental modes (2.6) are defined as $\omega_n = ck_n$.

Let us now briefly summarize the most important quantities characterizing a standing wave resonator. The distance between two resonator eigenfrequencies $\omega_n = ck_n$ defines the free spectral range of the resonator

$$\omega_{\text{FSR}} = \omega_{n+1} - \omega_n = \frac{\pi}{L} c. \tag{2.8}$$

One of the fundamental properties of an optical resonator is the filtering of all frequencies which do not coincide with these eigenfrequencies. The quality of this filtering mechanism is mainly governed by the reflectivity r of the resonator mirrors. As it can be seen from the schematic drawing in Fig. 2.1 the transmitted light field passing the resonator can be written as

$$E_t = E_0 t^2 \left(1 + r^2 e^{-2ikL} + r^4 e^{-4ikL} + \dots\right) = E_0 t^2 \frac{1}{1 - r^2 e^{-2ikL}}. \tag{2.9}$$

The transmitted light intensity which is related to the light field via the relation $I = (c\varepsilon_0/2)|E|^2$ normalized to the incoming intensity is then given as

$$\frac{I_t}{I_0} = \frac{(1-r^2)^2}{(1-r^2)^2 + 4r^2 \sin^2(kL)} = \frac{1}{1 + F \sin^2(\omega L/c)}, \tag{2.10}$$

where we defined $F := \left(\frac{2r}{1-r^2}\right)^2$ and used the energy conservation condition $t^2 = 1 - r^2$ [2.3]. An exemplary plot of the cavity transmission spectrum (2.10) is shown in Fig. 2.2. It reaches its maximum at the mode eigenfrequencies ω_n. However, for finite values of F some frequencies around ω_n have a non-zero transmittance. This leads to an important quantity related to the quality of an optical resonator, the so-called linewidth. It is defined as the full-width-half-maximum (FWHM) of the transmittance (2.10) and it measures how narrow the peaks of the transmittance are around ω_n (see Fig. 2.2). It is easy to see that Eq. (2.10) reaches a value of 1/2 if the condition

$$kL = \arcsin\left(\frac{1}{\sqrt{F}}\right) \approx \frac{1}{\sqrt{F}}, \tag{2.11}$$

is fulfilled. The last approximation holds if $F \gg 1$ which is typically the case for optical resonators. Therefore, the frequency at which the transmittance is half is given as $\omega_{1/2} = c/(L\sqrt{F}) = \omega_{\text{FSR}}/(\pi\sqrt{F})$ resulting in the cavity linewidth

$$\Delta\omega = \frac{2\omega_{\text{FSR}}}{\pi\sqrt{F}}. \tag{2.12}$$

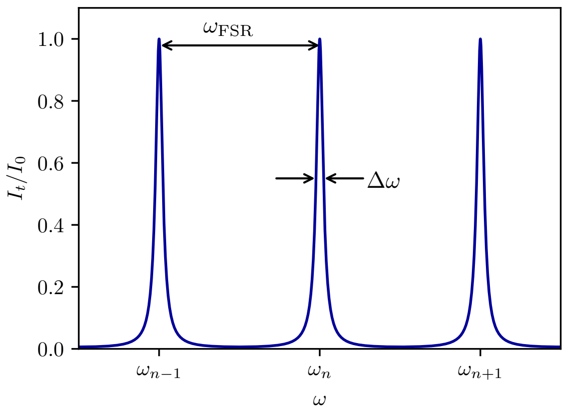

Figure 2.2: Frequency dependence of the transmitted light intensity through a Fabry-Pérot resonator (2.10) with highly reflecting mirrors ($r = 0.99$). The maximal intensity is transmitted at the resonance frequencies ω_n which are separated by the free spectral range ω_{FSR}. The linewidth $\Delta\omega$ is defined as the FWHM of the intensity peaks.

Based on this quantity one can define the Q-factor of the cavity which is defined as the ratio between the resonance frequency and the cavity linewidth; $Q := \omega_0/\Delta\omega$. Another important measure for the quality of an optical cavity is the finesse defined as

$$\mathcal{F} = \frac{\omega_{\mathrm{FSR}}}{\Delta\omega} = \frac{\pi\sqrt{F}}{2} = \frac{\pi|r|}{1-r^2}, \tag{2.13}$$

which solely depends on the reflectivity of the mirrors. The last important quantity which has to be mentioned at this stage is the cavity decay rate defined as

$$\kappa = \frac{\Delta\omega}{2} = \frac{\omega_{\mathrm{FSR}}}{2\mathcal{F}}. \tag{2.14}$$

It describes the rate at which light leaks out of the resonator and it decreases with decreasing (increasing) linewith (finesse). A small decay rate leads to long light storage times. The decay rate is significantly small in high-Q cavities with narrow linewidth resulting in storage times much longer than the optical period of the light field.

As a final remark it should be mentioned that in experiments the resonators are not built up by two planar mirrors as in the Fabry-Pérot case, but by two mirrors with curved surfaces leading to a 3 dimensional Gaussian beam shape. Nevertheless, the quantities defined above are still a good approximation if one assumes one dimensional motion along the center of the cavity axis as it will be the case in the following works. A generalization of the discussion above to three dimensions and for curved cavity mirrors can be found in corresponding literature, e. g. [2.3, 2.4].

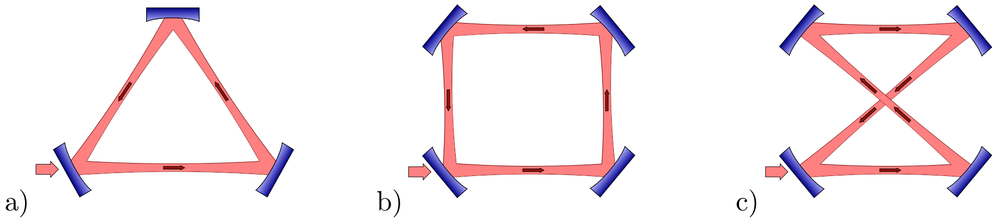

Figure 2.3: Different ring cavity schemes. a) Ring resonator consisting of three mirrors. This is the minimal amount of mirrors needed to generate running wave modes. b) Four mirror geometry and c) Bow-tie geometry.

Quantization of the Electromagnetic Field

Up to now we were solely discussing classical light fields. At this point we would like to give a very short introduction, how these fields can be quantized. The basic idea behind the quantization of the electromagnetic field is that every field mode behaves as a quantized harmonic oscillator. Therefore we introduce the bosonic creation (annihilation) operator $\hat{a}^\dagger_{n,\sigma}$ ($\hat{a}_{n,\sigma}$) which creates (destroys) a photon in the n-th resonator mode with polarization σ. These operators fulfill the bosonic commutation relation $\left[\hat{a}_{n,\sigma}, \hat{a}^\dagger_{n',\sigma'}\right] = \delta_{n,n'}\delta_{\sigma,\sigma'}$. Based on this one finds that the light field inside an optical resonator given in Eq. (2.7) can be quantized by performing the replacement $c_{n,\sigma} \rightarrow \sqrt{\hbar\omega_c/(2\varepsilon_0 L)}\hat{a}_{n,\sigma}$ and, in addition, making the resulting field operator hermitian [2.5]. This results in the quantized electromagnetic field of a standing wave resonator (in one dimension)

$$\hat{\boldsymbol{\mathcal{E}}}(x) = i\sqrt{\frac{\hbar\omega_c}{2\varepsilon_0 L}} \sum_{n,\sigma} \cos(k_n x) \left(\mathbf{e}_\sigma \hat{a}_{n,\sigma} - \mathbf{e}^*_\sigma \hat{a}^\dagger_{n,\sigma}\right), \tag{2.15}$$

with the cavity resonance frequency $\omega_c = \omega_1 = ck_1$.

2.2.2 Ring Resonators

The standing wave resonator geometry discussed in the previous section plays an important role in many different fields of quantum optics. However, the resonator geometry which will be the focus in several publications contained in this thesis is the so-called ring resonator, often also referred to as running-wave resonator. In such a resonator geometry the fundamental modes consist of running waves travelling along a closed path in one direction without reversing their propagation direction. In Fig. 2.3 the most prominent ring resonator geometries are depicted. The ring cavity again supports only a discrete set of single frequencies due to its large free spectral range. The fundamental modes of a ring cavity, however, consist of plane waves propagating in opposite directions

$$\mathbf{f}^\pm_{n,\sigma}(x) = \mathbf{e}^\pm_\sigma e^{\pm i k_n x} \quad \text{with} \quad k_n = \frac{n\pi}{L} \quad \text{and} \quad \sigma \in \{1, 2\}, \tag{2.16}$$

where L is the total propagation path length in the resonator. Again any field inside a ring resonator can be written as a superposition of the fundamental modes

$$\boldsymbol{\mathcal{E}}(x) = \sum_{n,\sigma} \left(\mathbf{e}_\sigma^+ c_{n\sigma}^+ e^{ik_n x} + \mathbf{e}_\sigma^- c_{n\sigma}^- e^{-ik_n x} \right). \tag{2.17}$$

To clarify to the difference between a ring resonator and a standing wave resonator let us consider a special case. We define the complex mode amplitude as $c_{n,\sigma}^\pm = |c_{n,\sigma}^\pm| \exp(\pm i\phi)$ and assume $|c_{n\sigma}^+| = |c_{n\sigma}^-| \equiv |c_{n,\sigma}|$ together with $\mathbf{e}_\sigma^+ = \mathbf{e}_\sigma^-$. In this case the field given in Eq. (2.17) reduces to $\boldsymbol{\mathcal{E}}(x) = \sum_{n,\sigma} \mathbf{e}_\sigma |c_{n,\sigma}| \cos(k_n x + \phi)$. This resulting mode decomposition strongly reminds us of the electric field of a standing wave resonator as it was introduced in the previous section. However, the major difference between a ring resonator and a Fabry-Pérot resonator is that the latter requires a vanishing electric field at the mirror surfaces. Thus in the case of a spatially modulated light field the phase ϕ can take arbitrary values in a ring cavity geometry. In the case of a standing wave resonator the phase ϕ could only take discrete values which fulfill the boundary condition of a vanishing field at the mirror surface. This also implies that any spatial translation of the field inside of a ring cavity is allowed which is directly related to the continuous translational symmetry of the ring cavity geometry playing an important role in the works in the chapters 4, 7 and 8.

The electric field of a ring resonator (2.17) can be quantized following the same procedure as discussed in the previous section resulting in

$$\hat{\boldsymbol{\mathcal{E}}}(x) = i\sqrt{\frac{\hbar\omega_c}{2\varepsilon_0 L}} \sum_{n,\sigma} \left(\mathbf{e}_\sigma^+ \hat{a}_{n\sigma}^+ e^{ik_n x} + \mathbf{e}_\sigma^- \hat{a}_{n\sigma}^- e^{-ik_n x} - \text{h.c.} \right). \tag{2.18}$$

2.3 Light-Matter Interaction

The manipulation of atoms with laser light fields is the fundamental concept in quantum optics. This opens up the possibility to trap particles in potentials generated by laser light. Here the fundamental principles about the interaction of atoms with laser light are recast in a compressed form.

The interaction between neutral atoms and light is dominated by two fundamentally different processes which lead to different forces on the atom. In the following discussion the atoms are always assumed as two level atoms with a ground state $|g\rangle$ and an excited state $|e\rangle$. The two states are separated by an energy $\hbar\omega_{eg}$ where ω_{eg} is the atomic transition or resonance frequency. Let us shortly give a phenomenological description of the processes in the photon picture leading to the radiation forces before we turn to a more quantitative analysis. The first process which can occur if a two level atom is coupled to a light field is the absorption of a photon followed by its spontaneous emission in all spatial directions. The recoil kicks due to these spontaneous emission processes average to zero whereas the momentum of the incoming photons always points along the laser beam, see Fig. 2.4a). The induced net force due to this dissipative process is called radiation pressure and it always points in the direction of the incoming

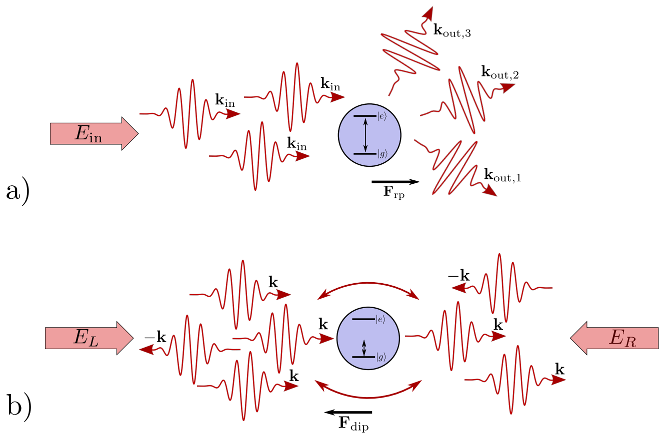

Figure 2.4: a) Schematic picture describing the physics behind the dissipative radiation pressure force $\mathbf{F}_{\text{rp}}$ for a single atom. The incident photons are absorbed and spontaneously emitted into arbitrary directions in space resulting in a net force pointing in the direction of the incident laser beam. b) Schematic picture for to the dispersive dipole force $\mathbf{F}_{\text{dip}}$. The force is a result of redistribution of photons between the two counterpropagating incoming laser beams. For red detuning $\omega_L - \omega_{eg} < 0$ the force points to the maxima of the intensity, i. e. to positions with high photon densities.

laser beam. For a plane wave it simplifies to $\mathbf{F}_{\text{rp}} = \Gamma_{\text{sp}}\hbar\mathbf{k}$ where Γ_{sp} is the spontaneous decay rate and $\mathbf{k}$ is the wave vector of the incoming laser beam defining the propagation direction. Due to its dissipative nature the radiation pressure force plays an important role in many laser cooling mechanisms. However, this force only contributes if the laser frequency is close to the atomic resonance frequency. If the frequency of the laser photons $\hbar\omega_L$ is sufficiently off-resonant with the atomic transition frequency ω_{eg} the population of the excited state will remain small and the radiation pressure force may be neglected due to the negligible spontaneous decay rate in this case. But there is a second process which gets more relevant in this far off-resonant parameter regime. The simplest phenomenological description is found by considering an atom between two counterpropagating interfering light beams. In this case a photon is absorbed and again emitted via stimulated emission [see Fig. 2.4b)]. This energy conserving scattering process between the two fields with opposite propagation directions results in the conservative dipole force resulting in a potential for the atoms. The spatial shape of the potential depends on the phase gradient of the total electromagnetic field. Throughout this thesis we assume to be in the so-called red-detuned regime, i. e. the photon frequency is smaller than the atomic transition frequency $\omega_L - \omega_{eg} < 0$. In this case the dipole force attracts the atoms to the field maxima. Let us now turn to a more quantitative analysis of the effects leading to this light generated potential of the atoms.

2.3.1 Interaction with a Classical Field

Consider a classical standing wave laser light field $\mathbf{E}(\mathbf{x},t) = \mathbf{e}\mathcal{E}_L(\mathbf{x})\left(e^{-i\omega_L t - i\phi(\mathbf{x})} + c.c\right)$ interacting with a two level atom with groundstate $|g\rangle$ and excited state $|e\rangle$ separated by an energy $\hbar\omega_{eg}$. The Hamiltonian in the dipole approximation reads (we set $\omega_g = 0$ without loss of generality)

$$\hat{H} = \hat{H}_{\text{at}} + \hat{H}_{\text{int}} = \frac{\hat{\mathbf{p}}^2}{2m} + \hbar\omega_{eg}\left|e\right\rangle\left\langle e\right| - \hat{\mathbf{d}}\cdot\mathbf{E}(\hat{\mathbf{x}},t), \tag{2.19}$$

where $\hat{\mathbf{p}} = i\hbar\nabla$ is the momentum operator, m is the atomic mass and $\hat{\mathbf{d}}$ is the dipole operator. An atom has no permanent dipole which could interact with the light field, i. e. $\left\langle g\right|\hat{\mathbf{d}}\left|g\right\rangle = \left\langle e\right|\hat{\mathbf{d}}\left|e\right\rangle = 0$, but the laser field itself can induce an atomic dipole by changing the internal state of the atom. Therefore, the dipole operator can be written as $\hat{\mathbf{d}} = \mathbf{d}\hat{\sigma}_+ + \mathbf{d}^*\hat{\sigma}_-$ with the reduced dipole $\mathbf{d} = \left\langle e\right|\hat{\mathbf{d}}\left|g\right\rangle$ and the transition operators $\hat{\sigma}_+ = \left|e\right\rangle\left\langle g\right|$ and $\hat{\sigma}_- = \left|g\right\rangle\left\langle e\right|$. In this case the interaction Hamiltonian $\hat{H}_{\text{int}} = -\hat{\mathbf{d}}\cdot\mathbf{E}(\hat{\mathbf{x}},t)$ reduces to

$$\hat{H}_{\text{int}} = -\frac{\hbar\Omega(\hat{\mathbf{x}})}{2}\left[e^{-i(\omega_L t + \phi(\hat{\mathbf{x}}))}\sigma_+ + e^{-i(\omega_L t + \phi(\hat{\mathbf{x}}))}\sigma_-\right] + \text{h.c.} \tag{2.20}$$

where we introduced the Rabi frequency $\Omega(\hat{\mathbf{x}}) = \mathcal{E}_L(\hat{\mathbf{x}})\left\langle e\right|\mathbf{d}\cdot\mathbf{e}\left|g\right\rangle$. Changing into a frame rotating at the laser frequency via an unitary transformation $\hat{U} = e^{i\omega_L t|e\rangle\langle e|}$ and performing the so-called rotating-wave approximation [2.6], i. e. neglecting fast rotating terms $\propto 2\omega_L t$ results in the modified interaction Hamiltonian

$$\hat{H}_{\text{int}}^{\text{RWA}} = -\hbar\delta\left|e\right\rangle\left\langle e\right| - \frac{\hbar\Omega(\hat{\mathbf{x}})}{2}e^{-i\phi(\hat{\mathbf{x}})}\sigma_+ - \frac{\hbar\Omega^\dagger(\hat{\mathbf{x}})}{2}e^{i\phi(\hat{\mathbf{x}})}\sigma_-, \tag{2.21}$$

where $\delta = \omega_L - \omega_{eg}$ denotes the detuning of the light field from the atomic resonance frequency. The eigenenergies of this Hamiltonian are

$$E_\pm = -\frac{\hbar\delta}{2} \pm \frac{\hbar}{2}\sqrt{\delta^2 + |\Omega(\mathbf{x})|^2}. \tag{2.22}$$

For sufficiently large detuning $\delta \gg \omega_{eg}$ the population of the excited state and, as a result, the saturation $s \approx |\Omega(\mathbf{x})|^2/(2\delta^2)$ will be small. Thus, the eigenvalues simplify to

$$E_\pm \approx -\frac{\hbar\delta}{2} \pm \frac{\hbar\delta}{2}\left(1 + \frac{|\Omega(\mathbf{x})|^2}{2\delta^2}\right). \tag{2.23}$$

The second term in the braket corresponds to a shift of the eigenenergies due to the interaction with the light fields and is called AC-Stark shift. The shifted ground state can be interpreted as the relevant potential for the motion of atoms [2.7]. Therefore, the light induced dipole potential due to the conservative interaction between light and matter is given as

$$V(\mathbf{x}) = \frac{\hbar|\Omega(\mathbf{x})|^2}{4\delta}. \tag{2.24}$$

A spatially inhomogeneous field like the standing wave we assumed in the above treatment can, therefore, lead to a space dependent ground-state potential in which the atom can be trapped. The localization of the potential minima depends on the sign of the detuning δ. If the laser frequency ω_L is smaller than the transition frequency ω_{eg} which corresponds to red detuning with respect to the transition frequency ($\delta < 0$) the potential minima coincide with the maxima of the light intensity. As a result the particles are trapped in the maxima of the intensity distribution and are called high-field seekers. In the case of positive (or blue) detuning $\delta > 0$ the potential minima lie at the regions with low intensity. Particles in this regime are called low-field seekers. For most practical purposes the light fields are chosen to be red detuned with respect to the atomic transition frequency.

2.3.2 Interaction with a Quantum Field

The description of the interaction between a single atom fixed at a certain position x and a quantized standing wave light field follows the same principle method as for a classical field. The electric field in the interaction Hamiltonian has to be replaced by its corresponding field operator which has been introduced in section 2.2. For the sake of simplicity we restrict our discussion to one dimension. This leads to an interaction Hamiltonian of the form

$$\hat{H}_{\text{int}} = -\hat{\mathbf{d}} \cdot \hat{\mathbf{E}}(x) = i\sqrt{\frac{\hbar\omega_L}{2\varepsilon_0 L}} \cos(kx) \left(\mathbf{d}\hat{\sigma}_+ + \mathbf{d}^*\hat{\sigma}_-\right) \left(\mathbf{e}\hat{a} - \mathbf{e}^*\hat{a}^\dagger\right). \tag{2.25}$$

The Hamiltonian of the uncoupled system is given as

$$\hat{H}_0 = \hbar\omega_L \hat{a}^\dagger \hat{a} + \hbar\omega_{eg} \left|e\right\rangle \left\langle e\right|. \tag{2.26}$$

The interaction Hamiltonian (2.25) can be transformed to the interaction picture via

$$\hat{H}^I_{\text{int}}(t) = e^{i\hat{H}_0 t/\hbar} \hat{H}_{\text{int}} e^{-i\hat{H}_0 t/\hbar} \tag{2.27}$$

resulting in the following relations for the single terms in Eq. (2.25)

$$(\hat{\sigma}_+\hat{a})_I = \hat{\sigma}_+\hat{a}e^{-i(\omega_L-\omega_{eg})t}, \tag{2.28}$$

$$(\hat{\sigma}_-\hat{a})_I = \hat{\sigma}_-\hat{a}e^{-i(\omega_L+\omega_{eg})t}, \tag{2.29}$$

$$(\hat{\sigma}_+\hat{a}^\dagger)_I = \hat{\sigma}_+\hat{a}^\dagger e^{i(\omega_L+\omega_{eg})t}, \tag{2.30}$$

$$(\hat{\sigma}_-\hat{a}^\dagger)_I = \hat{\sigma}_-\hat{a}^\dagger e^{-i(-\omega_L+\omega_{eg})t}. \tag{2.31}$$

Again the rotating wave approximation amounts to neglecting fast rotating terms with frequencies $\propto \omega_L + \omega_{eg}$ leading to the interaction Hamiltonian in the rotating wave approximation in the interaction picture

$$\hat{H}^I_{\text{int}} = i\sqrt{\frac{\hbar\omega_L}{2\varepsilon_0 L}} \cos(kx) \left(\hat{\sigma}_+\hat{a}\mathbf{d}\cdot\mathbf{e}e^{-i(\omega_L-\omega_{eg})t} - \hat{\sigma}_-\hat{a}^\dagger\mathbf{d}^*\cdot\mathbf{e}^*e^{-i(-\omega_L+\omega_{eg})t}\right). \tag{2.32}$$

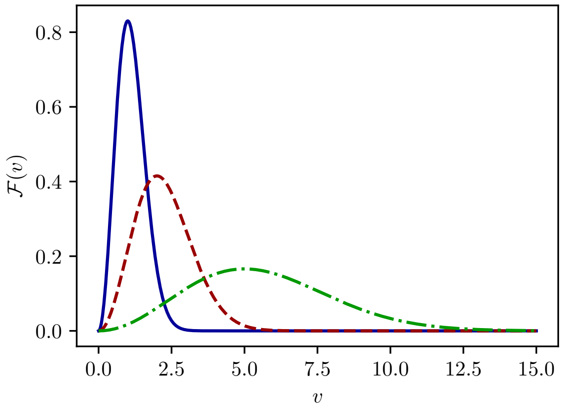

Figure 2.5: Maxwell-Boltzmann distribution (2.35) for different thermal velocities, $v_T = 1.0$ (solid blue), $v_T = 2.0$ (dashed red) and $v_T = 5.0$ (dash-dotted green)

Transforming this Hamiltonian back into the Schrödinger picture and adding the Hamiltonians of the uncoupled systems (2.26) leads to the famous Jaynes-Cummings Hamiltonian [2.8]

$$\hat{H} = \hbar\omega_L \hat{a}^\dagger \hat{a} + \hbar\omega_{eg}\hat{\sigma}_+\hat{\sigma}_- + \hbar g(x)\left(\hat{\sigma}_+\hat{a} + \hat{\sigma}_-\hat{a}^\dagger\right), \tag{2.33}$$

with the coupling $g(x) := i\sqrt{\frac{\omega_0}{2\hbar\varepsilon_0 L}}\cos(kx)\,\langle e|\,\hat{\mathbf{d}}\cdot\mathbf{e}\,|g\rangle$ where $\hat{\mathbf{d}}\cdot\mathbf{e}$ is made purely imaginary by specific phase choice for $|g\rangle$ and $|e\rangle$.

The Jaynes-Cummings model is the simplest possible model to describe the interaction between quantum matter with quantized light fields. It can be solved analytically and contains the main physics which is relevant in many experimental setups. Similar Hamiltonians for generalized geometries also including particle motion will be used in the works contained in the chapters 7 and 8.

2.4 Vlasov Model for Thermal Gas Dynamics

In the previous section we showed that the interaction of a single two-level atom with laser light fields yields a potential which allows to trap the atom. The present thesis, however, focuses on the dynamics of whole clouds of atoms in different laser light geometries. In this case treating the ensemble of atoms in a full quantum manner restricts the number of atoms which can be simulated significantly. However, there are several different methods to describe and characterize the dynamics of such systems efficiently. If one is particularly interested in the spatial and momentum distributions of the particles moving in a specific laser light geometry the atoms can be treated as classical point particles, i. e. a gas of particles in thermal equilibrium at a certain temperature T. In this case the probability distribution to find a particle at velocity $\mathbf{v}$ for a given temperature T is Gaussian

$$F_{3D}(\mathbf{v}) = \frac{1}{(\sqrt{\pi} v_T)^3} e^{-\left(\frac{\mathbf{v}}{v_T}\right)^2}, \tag{2.34}$$

where we introduced the thermal velocity $\frac{m v_T^2}{2} = k_B T$ associated with a certain temperature T (k_B is the Boltzmann constant). The probability density related to the distribution (2.34) can be found by calculating the integral over the probability distribution in spherical coordinates, i. e. $\int_{\mathbb{R}^3} d\mathbf{v} F_{\mathrm{3D}}(\mathbf{v}) = 4\pi \int_0^\infty dv v^2 F_{3D}(v)$ with $v = |\mathbf{v}| = \sqrt{v_x^2 + v_y^2 + v_z^2}$. This leads to the Maxwell-Boltzmann probability density

$$\mathcal{F}(v) = \frac{4}{\sqrt{\pi} v_T^3} v^2 e^{-\left(\frac{v}{v_T}\right)^2} \tag{2.35}$$

which is shown in Fig. 2.5 for different values of v_T. Note that for a one-dimensional system the velocity distribution (2.34) reduces to $F_{1D}(v) = \frac{1}{\sqrt{\pi} v_{\mathrm{T}}} \exp[-(v/v_T)^2]$.

The Vlasov equation, which will be introduced in the following, originates from plasma physics. However, it can also be used to describe the dynamics of classical particles interacting via laser light fields. The Vlasov equation describes the dynamics of the phase-space distribution function $f(\mathbf{x}, \mathbf{v}, t)$ of a cloud of particles experiencing a certain force $\mathbf{F} = -\nabla\phi(\mathbf{x})$. Using Liouville's theorem, stating that (for a Hamiltonian system) the phase-space distribution function does not change in time, i. e. $\frac{df(\mathbf{x},\mathbf{v},t)}{dt} = 0$ one finds the Vlasov equation for particles moving in a given potential $\phi(\mathbf{x})$

$$\frac{df(\mathbf{x}, \mathbf{v}, t)}{dt} = \frac{\partial f}{\partial t} + \frac{\partial f}{\partial \mathbf{x}} \frac{\partial \mathbf{x}}{\partial t} + \frac{\partial f}{\partial \mathbf{v}} \frac{\partial \mathbf{v}}{\partial t} \tag{2.36}$$

$$= \frac{\partial f}{\partial t} + \mathbf{v} \frac{\partial f}{\partial \mathbf{x}} - \nabla\phi(\mathbf{x}) \frac{\partial f}{\partial \mathbf{v}} = 0. \tag{2.37}$$

In the case of plasma theory the potential $\phi(\mathbf{x})$ corresponds to the Coulomb interactions between the charged plasma particles. In the present case, however, the potential will be the light generated potential given in Eq. (2.24). In this case the dynamics of the gas can, for sufficiently short times, be reliably approximated by a Vlasov equation [2.9, 2.10]. Therefore, the Vlasov equation (2.37) is a versatile tool to study the dynamics of a gas coupled to laser light fields in the classical limit. In chapter 3 we will give a minimal example how the Vlasov equation can be used to describe the instability leading to collective atomic recoil lasing. Furthermore, the approach will be used to analyze the system studied in the publication in chapter 4.

2.5 Bose-Einstein Condensates

The first experimental realization of a Bose-Einstein condensate (BEC) in 1995 [2.11, 2.12] was the starting point of a new area of interdisciplinary physics. BECs became the major ingredient in many setups for quantum simulation of condensed matter systems. In particular Bose-Einstein condensates (BECs) interacting with laser light – as they are studied in the present thesis – became a prominent research direction. The effect of Bose-Einstein condensation was predicted by Satyendra Nath Bose and Albert Einstein in 1924 as a result of the derivation of Planck's quantum radiation law from a purely quantum mechanical system [2.13, 2.14]. Heuristically, a BEC is a state of matter where all atoms in the Bose gas condense in the lowest accessible quantum state if the gas is cooled down below a certain critical temperature. In other words, all Bosons occupy the same motional ground state and form one giant matter wave. In the following we give a short summary of important features of a Bose-Einstein condensate and present some basic methods and tools which will play an important role in some of the following chapters. For a detailed discussion of the broad field of Bose-Einstein condensation we refer to relevant literature [2.15, 2.16].

2.5.1 Critical Temperature

The Hamiltonian for N non-interacting particles in an external potential $V(\mathbf{x})$ reads

$$\hat{H} = \sum_{i=1}^{N} \left[\frac{\hat{\mathbf{p}}_i^2}{2m} + V(\hat{\mathbf{x}}_i) \right], \tag{2.38}$$

with the position operators $\hat{\mathbf{x}}_i$ and the mometum operators $\hat{\mathbf{p}}_i = -i\hbar\nabla_i$. The corresponding many-body Hamiltonian in second-quantization is given as

$$\hat{H} = \int d\mathbf{x} \left[\hat{\psi}^\dagger(\mathbf{x}) \left(\frac{-\hbar^2}{2m}\nabla^2 + V(\mathbf{x}) \right) \hat{\psi}(\mathbf{x}) \right], \tag{2.39}$$

where the particle creation and annihilation operators fulfill the bosonic commutation relation $\left[\hat{\psi}(\mathbf{x}), \hat{\psi}^\dagger(\mathbf{x}')\right] = \delta(\mathbf{x} - \mathbf{x}')$. This Hamiltonian can be transformed into momentum space via $\hat{\psi}(\mathbf{x}) = 1/\sqrt{\mathcal{V}} \sum_{\mathbf{p}} \hat{a}_{\mathbf{p}} \exp(i\mathbf{p}\cdot\mathbf{x}/\hbar)$ where we assumed a box with a volume $\mathcal{V}$ leading to discrete momenta. For the moment we will neglect the external potential $V(\mathbf{x}) = 0$. The resulting Hamiltonian in second quantization in momentum space for an ideal non-interacting Bose gas reads

$$\hat{H} = \sum_{\mathbf{p}} \frac{\mathbf{p}^2}{2m} \hat{b}_{\mathbf{p}}^\dagger \hat{b}_{\mathbf{p}}, \tag{2.40}$$

where the creation (annihilation) operators create (destroy) a particle in the state with momentum $\mathbf{p}$ and fulfill the bosonic commutation relation $\left[\hat{b}_{\mathbf{p}}, \hat{b}_{\mathbf{p}'}^\dagger\right] = \delta_{\mathbf{p},\mathbf{p}'}$. For a given temperature T the momentum states are occupied following a Bose-Einstein statistics, meaning that the average occupation number of the energy state with momentum $\mathbf{p}$ is given by

$$n_{\mathbf{p}} = \frac{1}{e^{\frac{E_{\mathbf{p}} - \mu}{k_B T}} - 1}, \tag{2.41}$$

with the energy $E_{\mathbf{p}} = \mathbf{p}^2/(2m)$ and the chemical potential μ which fixes the total particle number

$$N = \sum_{\mathbf{p}} n_{\mathbf{p}} = \sum_{\mathbf{p}} \frac{1}{e^{\frac{E_{\mathbf{p}}-\mu}{k_B T}} - 1}. \tag{2.42}$$

Note that the chemical potential has to fulfill the constraint $\mu < E_0$, otherwise Eq. (2.41) would result in negative occupation numbers. If the chemical potential approaches E_0 the occupation number of the $p = 0$ state becomes increasingly large which results in the formation of a BEC. Hence, the critical temperature for Bose-Einstein condensation is defined as the temperature at which a macroscopic number of particles starts occupying the lowest energy level at $p = 0$ for $\mu = E_0$.

From this condition the critical density for Bose-Einstein condensation can be calculated via

$$n_C = \frac{N_C}{\mathcal{V}} = \int \frac{d\mathbf{p}}{(2\pi\hbar)^3} \frac{1}{e^{\frac{E_{\mathbf{p}}}{k_B T}} - 1}. \tag{2.43}$$

Here we performed the replacement $\sum_{\mathbf{p}} \to \mathcal{V} \int d^3\mathbf{p}/(2\pi\hbar)^3$ which is valid in the case of a large volume $\mathcal{V}$ where the momentum becomes a continuous variable. Eq. (2.43) is the critical density where all particles are occupying excited single particle states but not the $p = 0$ state in the case of $\mu = E_0$ (we can choose $\mu = E_0 = 0$ without loss of generality). As soon as this critical density is exceeded particles start to occupy the lowest energy state and the condensate fraction starts to grow. The integral in Eq. (2.43) can be calculated as

$$n_C = \frac{4\pi}{(2\pi\hbar)^3} \int_0^\infty dp \frac{p^2}{e^{\frac{p^2}{2mk_B T}} - 1} = \frac{(2mk_B T)^{\frac{3}{2}}}{2\pi^2\hbar^3} \zeta\left(\frac{3}{2}\right) \frac{\sqrt{\pi}}{4} \tag{2.44}$$

with the Riemann ζ-function; $\zeta\,(3/2) \approx 2.6124$. From this critical density one can find the critical temperature for Bose-Einstein condensation for an ideal gas of Bosons for a given particle density n as

$$T_C = \frac{2\pi\hbar^2}{mk_B} \left(\frac{1}{\zeta\left(\frac{3}{2}\right)} n \right)^{\frac{2}{3}} \approx 3.31 \frac{\hbar^2}{mk_B} n^{\frac{2}{3}}. \tag{2.45}$$

For temperatures below this critical temperatures particles start forming a condensate, i. e. a macroscopic fraction of the particles occupying the lowest motional quantum state. The total number of particles is, therefore given as the sum of condensed particles and the atoms are still in a thermal state $N = N_{\mathrm{BEC}}(T) + N_{\mathrm{th}}$. From this one can calculate the fraction of condensed particles as

$$N_{\mathrm{BEC}}(T) = N \left[1 - \left(\frac{T}{T_C} \right)^{\frac{3}{2}} \right]. \tag{2.46}$$

For the limiting case of $T = 0$ all particles are condensed.

2.5.2 Gross-Pitaevskii Equation

It turns out that particle-particle interactions which were neglected in the treatment above play an important role to describe some of the fundamental properties of a BEC. Interactions can be added to the theory by adding an interaction potential of the form $V_{\text{int}} = V_0 \sum_{i \neq j} \delta(\mathbf{x}_i - \mathbf{x}_j)$.

The Hamiltonian for N interacting quantum particles then reads

$$\hat{H} = \sum_{i=1}^{N} \left[\frac{\hat{\mathbf{p}}_i^2}{2m} + V(\hat{\mathbf{x}}_i) \right] + V_0 \sum_{i \neq j} \delta(\hat{\mathbf{x}}_i - \hat{\mathbf{x}}_j). \tag{2.47}$$

Assuming only low energy collisions to be relevant the interaction between particles is dominated by s-wave collisions and the interaction Hamiltonian reduces to $H_{\text{int}} = g\delta(\mathbf{x} - \mathbf{x}')$ with $g = (4\pi\hbar^2 a)/(2m)$ where a is the s-wave scattering length. The many-body Hamiltonian in second-quantization reads

$$\hat{H} = \int d\mathbf{x} \left[\hat{\psi}^\dagger(\mathbf{x}) \left(\frac{-\hbar^2}{2m} \nabla^2 + V(\mathbf{x}) \right) \hat{\psi}(\mathbf{x}) + \frac{g}{2} \hat{\psi}^\dagger(\mathbf{x}) \hat{\psi}^\dagger(\mathbf{x}) \hat{\psi}(\mathbf{x}) \hat{\psi}(\mathbf{x}) \right]. \tag{2.48}$$

The particle creation and annihilation operators again fulfill the bosonic commutation relation $\left[\hat{\psi}(\mathbf{x}), \hat{\psi}^\dagger(\mathbf{x}')\right] = \delta(\mathbf{x} - \mathbf{x}')$. To find the explicit time dependence of these operators one has to solve the Heisenberg equation of motion

$$i\hbar\partial_t \hat{\psi}(\mathbf{x}, t) = \left[\hat{\psi}(\mathbf{x}, t), \hat{H}\right] = \left(\frac{-\hbar^2}{2m} \nabla^2 + V(\mathbf{x}) + g\hat{\psi}^\dagger(\mathbf{x}, t)\hat{\psi}(\mathbf{x}, t) \right) \hat{\psi}(\mathbf{x}, t). \tag{2.49}$$

The simplest version of (2.49) is obtained in the mean field limit where the field operators are replaced by their corresponding expectation values $\hat{\psi}(\mathbf{x}) \to \langle \hat{\psi}(\mathbf{x}) \rangle \equiv \psi(\mathbf{x}, t)$. This leads to the time-dependent Gross-Pitaevskii equation

$$i\hbar \frac{\partial}{\partial t} \psi(\mathbf{x}, t) = \left[-\frac{\hbar^2}{2m} \nabla^2 + V(\mathbf{x}) + g|\psi(\mathbf{x}, \mathbf{t})|^2 \right] \psi(\mathbf{x}, \mathbf{t}). \tag{2.50}$$

The related stationary Gross-Piteaevski equation can now be found by inserting the ansatz $\psi(\mathbf{x}, t) = \psi(\mathbf{x}) e^{-i\mu t/\hbar}$ into Eq. (2.50) which leads to

$$\left[-\frac{\hbar^2}{2m} \nabla^2 + V(\mathbf{x}) + g|\psi(\mathbf{x})|^2 \right] \psi(\mathbf{x}) = \mu\psi(\mathbf{x}). \tag{2.51}$$

This equation describes the spatial distribution of a BEC in an external potential $V(\mathbf{x})$ including particle interactions.

Another way to derive the stationary GP equation is performing the Hartree-Fock ansatz for the wave function

$$\Psi(\mathbf{x}_1, \ldots, \mathbf{x}_N) = \prod_{i=1}^{N} \phi(\mathbf{x}_i), \tag{2.52}$$

where the single particle wavefunctions $\phi(\mathbf{x})$ are normalized as $\int |\phi(\mathbf{x})|^2 = 1$. By introducing the mean-field wavefunction $\psi(\mathbf{x}) = \sqrt{N}\phi(\mathbf{x})$ one can write the mean field energy functional of the Hamiltonian (2.47) as

$$E = \int d\mathbf{x} \left[\psi^*(\mathbf{x}) \left(-\frac{\hbar^2}{2m}\nabla^2 + V(\mathbf{x}) \right) \psi(\mathbf{x}) + \frac{g}{2}|\psi(\mathbf{x})|^4 \right]. \tag{2.53}$$

Minimizing this energy functional under the additional condition that the particle number is conserved, i. e. minimizing $E - \mu N$ with the chemical potential μ leads to the stationary Gross-Pitaevskii equation given in Eq. (2.51)

The description of a BEC in the mean-field limit via the GP equation works extremely well for many practical purposes. Possible scenarios where the mean-field treatment breaks down might be systems with strong interactions, low-dimensional systems or the dynamics close to critical points. The Gross-Pitaevskii equation plays an important role in the models presented in the chapters 5 and 6.

2.5.3 Elementary Excitations

Some important features of a BEC are revealed by performing Bogoliubov theory to calculate the elementary excitation spectra of the condensate [2.15]. The heart of this theory is the linearization of the Gross-Pitaevskii equation which in a more complex form will appear on several stages in this thesis. This method gives a lot of insights of the physics of the condensate such as dynamical instabilities, stability of stationary states and many more. Therefore, we would like to explain the derivation for the simplest case of a homogeneous condensate in free space and discuss some important features of a BEC.

To calculate the elementary excitations above a stationary mean field solution $\psi_0(\mathbf{x})$ perturbations around this solution are include by expanding the wave function as $\psi(\mathbf{x}, t) = \psi_0(\mathbf{x}) + \delta\psi(\mathbf{x}, t)e^{-i\mu t/\hbar}$. Linearizing the GP-equation (2.50) with respect to $\delta\psi$ results in

$$i\hbar\partial_t\delta\psi(\mathbf{x}) = \left(-\frac{\hbar^2}{2m}\nabla^2 + V(\mathbf{x}) - \mu \right) \delta\psi(\mathbf{x}) \tag{2.54}$$

$$+ g \left[|\psi_0|^2(\mathbf{x})|^2\delta\psi(\mathbf{x}) + \psi_0(\mathbf{x}) \left(\psi_0(\mathbf{x})\delta\psi^*(\mathbf{x}) + \psi_0^*(\mathbf{x})\delta\psi(\mathbf{x}) \right) \right]. \tag{2.55}$$

Performing a Bogoliubov transformation

$$\delta\psi(\mathbf{x}, t) = u(\mathbf{x})e^{-i\omega t} + v^*(\mathbf{x})e^{i\omega t} \tag{2.56}$$

results in a pair of coupled equations for $u(\mathbf{x})$ and $v(\mathbf{x})$

$$\hbar\omega u(\mathbf{x}) = \left(-\frac{\hbar^2}{2m}\nabla^2 + V(\mathbf{x}) - \mu \right) u(\mathbf{x}) + 2g|\psi_0|^2u(\mathbf{x}) + g\psi_0\psi_0 v(\mathbf{x}) \tag{2.57}$$

$$\hbar\omega v(\mathbf{x}) = -\left(-\frac{\hbar^2}{2m}\nabla^2 + V(\mathbf{x}) - \mu \right)^* v(\mathbf{x}) - 2g|\psi_0|^2v(\mathbf{x}) - g\psi_0^*\psi_0^* u(\mathbf{x}). \tag{2.58}$$

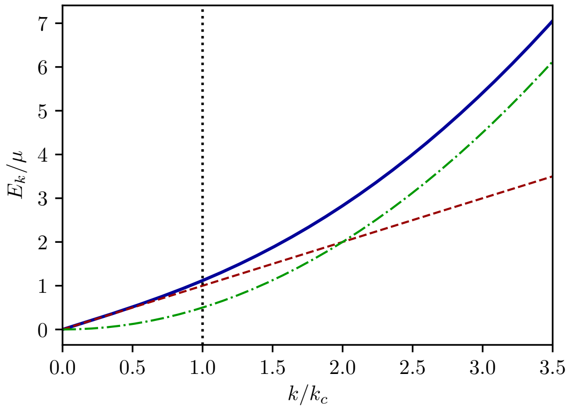

Figure 2.6: Comparison between the Bogoliubov spectrum of a BEC (solid blue line) (2.60) and the linear linear phonon spectrum (dashed red) and the quadratic dispersion relation of a non-interacting BEC (dash dotted green). The vertical black dotted line marks the critical wavenumber for superfluidity.

If we now assume a homogeneous BEC in real space, i. e. $\psi_0 = \sqrt{N}$ and $V(\mathbf{x}) = 0$, we find via Eq. (2.51) that the chemical potential in this case is given as $\mu = gN$. In the case of a homogeneous system u and v are plane waves $u(\mathbf{x}) = \tilde{u}e^{i\mathbf{kx}}$, $v(\mathbf{x}) = \tilde{v}e^{i\mathbf{kx}}$. In this case the set of equations (2.57) and (2.57) takes the matrix form

$$\hbar\omega \begin{pmatrix} \tilde{u} \\ \tilde{v} \end{pmatrix} = \begin{pmatrix} \frac{\hbar^2 k^2}{2m} + gN & gN \\ -gN & \frac{-\hbar^2 k^2}{2m} - gN \end{pmatrix} \begin{pmatrix} \tilde{u} \\ \tilde{v} \end{pmatrix}. \tag{2.59}$$

Diagonalizing the 2x2 matrix in Eq. (2.59) leads to the famous Bogoliubov dispersion relation for a BEC

$$E_k = \sqrt{\frac{\hbar^2 k^2}{2m}\left(\frac{\hbar^2 k^2}{2m} + 2gN\right)} = \hbar k\sqrt{\frac{\hbar^2 k^2}{2m} + \frac{gN}{m}}. \tag{2.60}$$

One realizes that for sufficiently small values of k the dispersion is linear $E_k \approx \hbar k\sqrt{gN/m}$ (see Fig. 2.6). In this case the elementary excitations are sound waves with a sound-velocity $c_S = \sqrt{gN/m}$. This linear behaviour for small values of k is in contrast to the case of a non-interacting BEC where the dispersion relation is quadratic $\propto k^2$. This implies that the propagating sound-wave (often also referred to as phonon-mode) is due to the collective motion of the BEC atoms.

Based on the model of an interacting BEC discussed above one can also describe the effect of superfluidity of a condensate. The Landau critical velocity for a flowing liquid to experience superfluidity is given as

$$v_c = \min_k \left(\frac{E_k}{\hbar k}\right). \tag{2.61}$$

If the velocity exceeds this critical value the flowing condensate will experience friction. In a non-interacting condensate with a quadratic dispersion relation $\propto k^2$ the critical velocity is zero, implying that in this case the BEC cannot be superfluid. In the case of an interacting BEC, however, the critical velocity for the Bogoliubov dispersion relation Eq. (2.60) is the sound velocity $v_c = c_S = \sqrt{gN/m} \neq 0$. Hence, for sufficiently small velocities the BEC is superfluid. The corresponding critical wavenumber in the dispersion is found as $k_c = \sqrt{mgN}/\hbar$ (vertical dotted line in Fig. 2.6).

The method of linearizing the system's equations of motion will appear on several stages in the publications in this thesis. It is a versatile tool to analyze and understand the fundamental physics of a system and to calculate critical points at which the system gets dynamically unstable.

3 Light-Induced Instabilities of Atom Clouds

After this short introduction of the basic theoretical models and tools, which will be relevant for the rest of the thesis, the following chapter introduces two well-established geometries which were subject to detailed theoretical as well as experimental studies in the past decades. The fundamental results obtained with these types of setups motivate the extension of theses systems to account for more general scenarios and symmetries. The underlying principle in all of these systems are induced instabilities of atom clouds by coupling them to light fields. In the following two fundamental instabilities in different resonator geometries will be introduced. We will start with the historically first related instability, which was established in this context the so-called collective recoil laser. This run-away process is a good example how tiny modulations in an initially homogeneous cloud can be exponentially amplified if the atoms interact with light fields via the processes described in section 2.3. In the second chapter we will introduce the concept of self-organization in a standing wave cavity, which paved the way to study induced instabilities in more complex geometries as it is done in this thesis. In particular, we will discuss the discrete symmetry breaking occurring in this setup. This then motivates the search for more general setups which break a continuous symmetry as they are studied in the papers contained in this thesis. In the following discussion we will only point out the fundamental physical mechanisms, which are important to understand the basic properties of the systems. A much more detailed discussion of the related physics can be found in [3.1].

3.1 Collective Atomic Recoil Lasing (CARL)

The concept of a novel tunable laser geometry called Collective Atomic Recoil Laser (CARL) was postulated in 1994 [3.2, 3.3] in close analogy to the free-electron laser [3.4]. Collective atomic recoil lasing occurs if a cold or ultracold atomic gas is put into a strong light field propagating in one direction. In this case a collective instability (the so-called CARL instability) leads to transient bunching of the atoms and as a result to coherent backscattering of radiation. The most straightforward way to understand and realize the CARL instability is the case of a cold atomic gas coupled to the modes of an unidirectionally pumped ring-cavity; see Fig. 3.1. The atoms are assumed to be two level atoms dispersively interacting with the cavity fields. One fundamental cavity mode (α_+) is pumped through the cavity mirrors with a pump strength η whereas the second counterpropagating mode (α_-) is solely populated by the field which is reflected from the atomic ensemble. The frequencies of the cavity modes are chosen

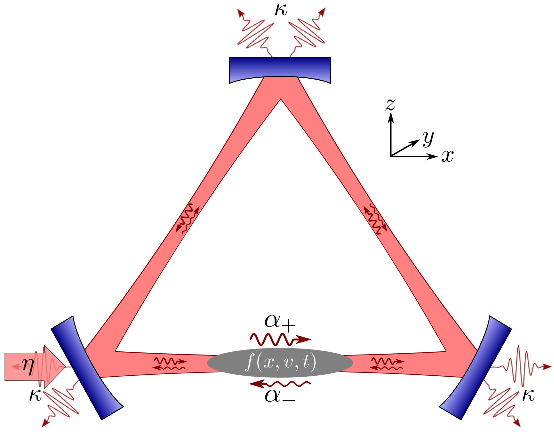

Figure 3.1: Typical setup leading to Collective Atomic Recoil Lasing (CARL). An initially homogeneous cloud of atoms is put into one branch of a ring-cavity which is pumped from one side with a pump strength η. The mode α_+ is populated via the pump fields whereas α_- is solely populated by fields which are reflected from the atomic density. The cavity decay rate is denotes as κ

far off resonant with respect to the internal atomic transition leading to a dispersive potential for the atoms due to the AC-Stark shift (see section 2.3). In contrast to some other light induced instabilities, which may occur in Bose-Einstein condensates, in particular, superradiant Rayleigh scattering [3.5] where the coherence of the quantum gas plays an important role, the CARL instability is much less sensitive to the thermal motion of the atoms. Therefore, it can also be realized with thermal atoms [3.6] since the coherence in the case of CARL is stored in the light field of the cavity [3.7].

This implies that the Vlasov equation approach which was discussed in section 2.4 applies to describe the dynamics of the CARL system [3.8]. We restrict our discussion to one dimension along x. In this case the dynamics of the phase-space density $f(x, v, t)$ is governed by the one-dimensional Vlasov equation (2.37)

$$\frac{\partial f}{\partial t} + v\frac{\partial f}{\partial x} - \frac{d}{dx}\phi(x)\frac{\partial f}{\partial v} = 0. \tag{3.1}$$

The total electric field inside the ring cavity is given as $\mathbf{E}(x) = \mathbf{e}(\alpha_+(t)e^{ikx} + \alpha_-(t)e^{-ikx})$ and the explicit time dependence of the mode amplitudes which is a direct result of the back-action of the atom-cloud density $\rho(x, t) = \int dv f(x, v, t)$ to the mode amplitudes is governed by the two coupled differential equations

$$\dot{\alpha}_+(t) = \left[i(\Delta_c - NU_0) - \kappa\right]\alpha_+ - iU_0\Theta\alpha_- + \eta, \tag{3.2}$$

$$\dot{\alpha}_-(t) = \left[i(\Delta_c - NU_0) - \kappa\right]\alpha_- - iU_0\Theta^*\alpha_+, \tag{3.3}$$

with the cavity detuning $\Delta_c := \omega_p - \omega_c$ defined as the difference between the pump field frequency ω_p and the cavity resonance frequency ω_c. U_0 denotes the optical potential

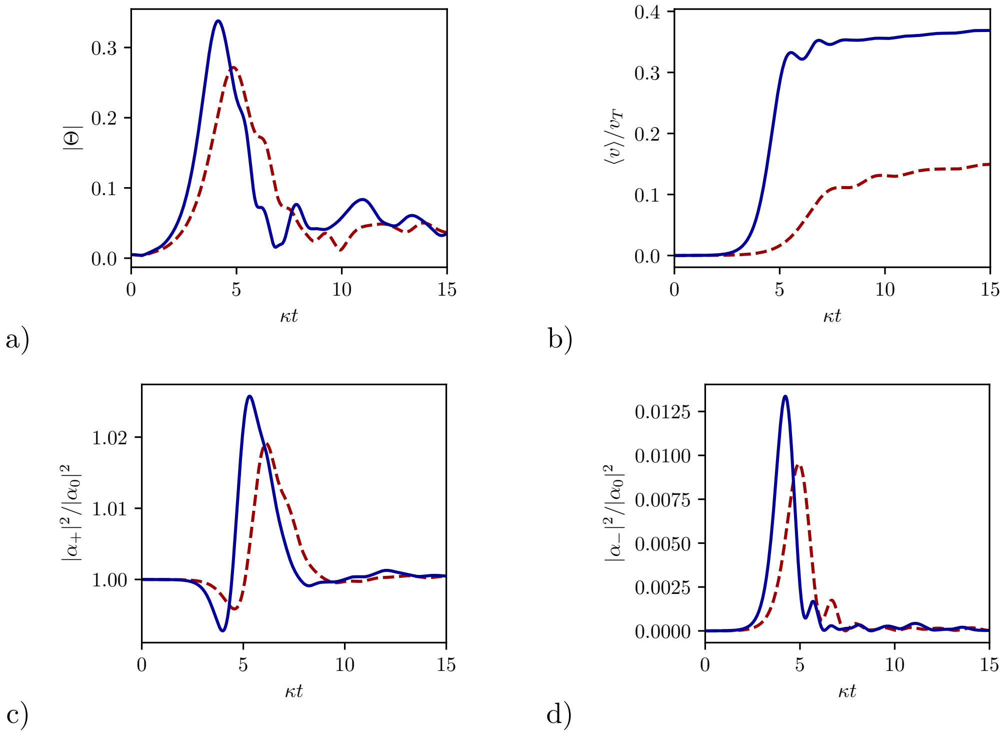

Figure 3.2: Time evolution of a) the absolute value of the bunching parameter, b) the mean-velocity, c) the pumped mode intensity and d) the unpumped mode intensity for a CARL geometry. The solid blue curves (dashed red curves) correspond to $\eta = 2.0\eta_c$ ($\eta = 1.8\eta_c$). The other parameters are $N = 10^5$, $kv_T = 1.5\kappa$, $\Delta_C - NU_0 = -\kappa$ and $U_0 = 1/N$.

depth per photon in the cavity as well as the cavity mode frequency shift per particle. The particle number is denoted as N and κ is the cavity decay rate. The bunching parameter $\Theta := \int dx \rho(x,t) e^{-2ikx}$ couples the two differential equations. It measures the magnitude of density modulations in the atom cloud. As long as the atomic density is homogeneous the bunching parameter is equal to zero resulting in $\alpha_-(t) = 0$ since only the α_+ mode is pumped with a pump strength η. Due to the light induced long-range interactions a collective instability (CARL instability) can be triggered for sufficiently large light intensities. In this case small density fluctuations in the nearly homogeneous atomic gas are exponentially amplified leading to bunching of the atoms, resulting in coherent backscattering of photons into the α_- mode. This results in the build up of a self-consistent optical lattice due to the interference between the two counterpropagating modes. This potential can be calculated via (2.24) and reads

$$\phi(x) = \hbar U_0 \left(|\alpha_+|^2 + |\alpha_-|^2 + \alpha_+^* \alpha_- e^{2ikx} + \alpha_+ \alpha_-^* e^{2ikx} \right) . \tag{3.4}$$

It is the non-trivial interplay between the light mode dynamics (3.3) and the atomic

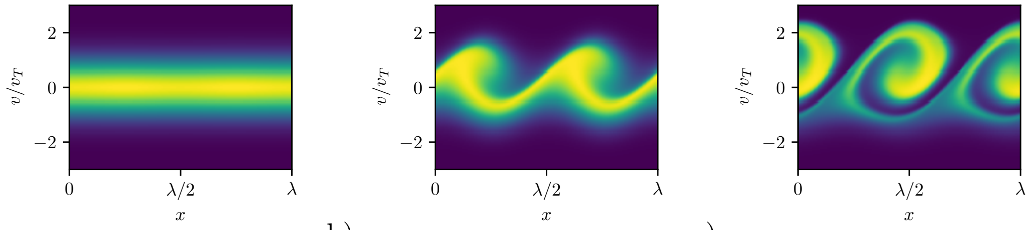

a) b) c)

Figure 3.3: Typical time evolution of the phase space density for a CARL instability far beyond threshold, $\eta = 2.0\eta_c$. a) Spatially homogeneous density at $t = 0\kappa^{-1}$, b) the CARL instability leads to atomic bunching ($t = 10\kappa^{-1}$) which results in a run away process c) $t = 15\kappa^{-1}$.

dynamics (3.1) which leads to this complex behaviour characteristic for collective atomic recoil lasing. Analyzing this set of differential equations with focus on collective dynamic instabilities [3.8] reveals the threshold formula for the critical pump strength

$$\eta_c^2 = \sqrt{\pi}\frac{2(k_B T)^{3/2}}{\hbar}\frac{\kappa(\kappa^2+\delta_c^2)}{NU_0^2}. \tag{3.5}$$

For pump intensities beyond this threshold the initially homogeneous atomic distribution gets unstable. The atomic bunching is exponentially growing which in turn results in a gain in the light intensities of the cavity modes as it can be seen in Figs. 3.2a), 3.2c) and 3.2d). In particular, the unpumped mode α_- is getting populated due to the collective scattering of light resulting in a coherent light pulse. Fig. 3.2b) shows the time evolution of the center of mass velocity $\langle v\rangle = \int dv v \int dx f(x,v,t)$. Its increasing behaviour for all times shows that the CARL instability is a run-away process. The bunched atoms are accelerated along the propagation direction of the pump beam. As a result CARL constitutes a real dynamical instability of the system and it never reaches a steady-state. In Fig. 3.3 a typical time evolution of the phase-space density $f(x,v,t)$ is shown. As an initial condition we choose a spatially homogeneous thermal gas with a thermal distribution $F_{1D}(v) = 1/(\sqrt{\pi}v_T)\exp[-(v/v_T)^2]$; [see Fig. 3.3a)]. The instability leads to atom bunching in a self-consistent optical lattice with $\lambda/2$-periodicity [see Eq. (3.4)] which is moving in the direction of the cavity pump beam. The atoms start to bunch at the potential minima (which correspond to the field intensity maxima if we assume red detuning with respect to the atomic transition frequencies, i. e. $U_0 < 0$) and are accelerated in the propagation direction of the pump mode (x-direction).

The reason for this run away process is the continuous symmetry of the chosen setup. The boundary conditions for the fields in a ring-cavity allow any arbitrary phase for the light fields (see section 2.2.2). Therefore, any spatial translation of the atomic cloud $x \to x + \Delta x$ can be compensated by a phase change of the cavity modes $\alpha_\pm \to \alpha_\pm e^{\pm i\Delta x/2}$. The atomic bunching of atoms for light intensities beyond threshold breaks this continuous symmetry. Hence, the CARL setup is an example how the continuous symmetry of a system can be broken via light induced instabilities. Finally it should be remarked that even though we restricted the treatment to a classical thermal gas in classical light fields, the CARL instability was also observed with quantum gases [3.7] which results in similar effects as the ones described above.

3.2 Self-organization in a Standing Wave Cavity

Another important geometry when talking about light induced instabilities of atom clouds is the self-organization of atoms in a transversally pumped standing wave cavity. In this case a cloud of atoms is placed inside a standing wave resonator and illuminated from the side with a standing wave laser field as it is schematically depicted in Fig. 3.4a). The atoms are assumed to be two-level atoms coupling to a single cavity mode with a resonance frequency ω_c far off resonant from the internal atomic transition. The pump mode frequency is ω_p and the pump strength is denoted as η and the cavity mode is subject to decay at a rate κ. In general, the atoms can be a classical thermal gas [3.9, 3.10] or a quantum gas [3.11] and the dynamics of the atomic density as well as the nature of the phase transition is qualitatively the same. However, the realization of self-organization with a BEC, which led to the first realization of the Dicke-phase transition [3.12], has generated widespread interest from different field of physics. Thus, we will focus on the case of self-ordering of a BEC coupled to a quantized cavity mode in the following.

The many-body Hamiltonian in second quantization of the composite system

$$\hat{H} = \hat{H}_A + \hat{H}_C + \hat{H}_{AC}, \tag{3.6}$$

is made up of the single Hamiltonians [3.1]

$$\hat{H}_A = \int d^3\mathbf{x}\hat{\psi}^\dagger(\mathbf{x}) \left(\frac{\mathbf{p}^2}{2m} + V_{\text{ext}}(\mathbf{x}) + \frac{g}{2}\hat{\psi}^\dagger(\mathbf{x})\hat{\psi}(\mathbf{x})\right) \hat{\psi(\mathbf{x})}, \tag{3.7a}$$

$$\hat{H}_C = -\hbar\Delta_c\hat{a}^\dagger\hat{a}, \tag{3.7b}$$

$$\hat{H}_{AC} = \int d^3\mathbf{x}\hat{\psi}^\dagger(\mathbf{x}) \left(\hbar U_0 \cos^2(kx)\hat{a}^\dagger\hat{a} + \hbar\eta\cos(kx)\cos(kz)(\hat{a}^\dagger + \hat{a})\right) \hat{\psi}(\mathbf{x}), \tag{3.7c}$$

where the first line corresponds to the bare atomic Hamiltonian including particle-particle interactions with an interaction strength g and the second line amounts for the single cavity mode where $\Delta_c = \omega_p - \omega_c$ is the detuning of the pump field frequency ω_p with respect to the cavity resonance frequency ω_c. The creation (annihilation) operator $\hat{a}^\dagger$ ($\hat{a}$) creates (destroys) a photon in the cavity mode. The first term in the third line $\propto \cos^2(kx)$ describes the cavity generated periodic potential along the cavity axis with a potential depth U_0. In the following we will always assume high-field seeking particles, i. e. red-detuning of the pump field with respect to the internal atomic frequency ($U_0 < 0$). The second term $\propto \cos(kx)\cos(kz)$ describes the scattering process between the pump mode in z-direction and the cavity mode in x-direction. In the following discussion we will omit the external potential $V_{\text{ext}}(\mathbf{x})$ in Eq. (3.7a) which usually is present due to the confinement of the BEC via some external trap but it is

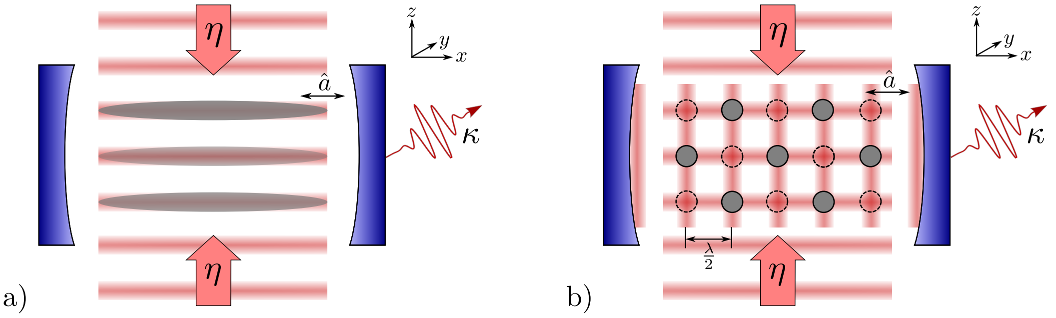

Figure 3.4: Schematic picture for self-organization in a transversally pumped single mode standing wave cavity. a) Below threshold $\eta < \eta_c$ the BEC density is homogeneous along the cavity axis (x-direction) and the cavity mode is empty. b) For $\eta > \eta_c$ the system's Z_2 symmetry is broken and the BEC self-organizes in one of the two possible configurations (solid grey circles or dashed empty circles)

not important for the discussion of the fundamental physics leading to self-organization.

The dynamics of the coupled atom cavity system is governed by the Heisenberg equations of motion $i\hbar\partial_t\hat{\psi} = [\hat{\psi}, \hat{H}]$ and $i\hbar\partial_t\hat{a} = [\hat{a}, \hat{H}] - i\hbar\kappa\hat{a}$ where in the latter equation cavity losses at a rate κ were included phenomenologically. Performing a linear stability analysis of the mean field steady state solutions in close analogy to the method presented in section 2.5.3 shows that the system undergoes a phase transition from homogeneous to periodic order if the cavity pump strength exceeds a critical value [3.11]

$$\eta_c^2 = \frac{[(\Delta_c - NU_0)^2 + \kappa^2](\omega_{\text{rec}} + 2Ng)}{-2N(\Delta_c - NU_0)}, \tag{3.8}$$

where N is the particle number of the BEC and $\omega_{\text{rec}} := \hbar k^2/(2m)$ is the recoil frequency.

Let us discuss the symmetries of the single Hamiltonians in (3.7). $\hat{H}_A$ and $\hat{H}_C$ are invariant under any spatial translation $x \to x + \Delta x$ thus they have a continuous translational symmetry (for $V_{\text{ext}}(\mathbf{x}) = 0$). In addition, $\hat{H}_C$ has a continuous $U(1)$ symmetry since it is invariant under any phase rotation $\hat{a} \to \hat{a}e^{i\phi}$. The coupling Hamlitonian $\hat{H}_{AC}$, however, has only a discrete symmetry. Performing the spatial translation $x \to x + \lambda/2$ results in a minus sign in the second term in Eq. (3.7c), i. e. $\cos(kx)\cos(kz)(\hat{a}^\dagger + \hat{a}) \to -\cos(kx)\cos(kz)(\hat{a}^\dagger + \hat{a})$. However, the minus sign can be compensated by a phase rotation $\Delta\phi = \pi$ of the cavity mode $\hat{a}$. Therefore, the total Hamiltonian $\hat{H}$ is invariant under the symmetry transformations $x \to x + \lambda/2$ and $\hat{a} \to \hat{a}e^{i\pi}$. The first term $\propto \cos^2(kx)$ in Eq. (3.7c) is $\lambda/2$-periodic along the cavity axis whereas the second term $\propto \cos(kx)\cos(kz)$ is only λ-periodic. Hence, the Hamiltonian (3.6) has a global λ periodicity. As a result the self-organized steady state solutions above threshold (3.8) will be λ periodic. There are two possible ways to realize a λ-periodic density grating in the $\lambda/2$-periodic cavity generated potential as it is schematically shown in Fig. 3.4b). The groundstate for the perfect quantum system examined here will always be a superposition of the two possible patterns. In experiments, however, small fluctuations of external parameters will always result in a spontaneous choice between the two possible phases. Hence, the particles spontaneously choose even- or odd sights of the resulting potential. Thus, at the phase transition from a homogeneous BEC in x-direction [see Fig. 3.4a)] to a λ-periodic density grating the system randomly chooses between the two possible configurations [see Fig. 3.4b)]. This amounts to a breaking of the so-called discrete Z_2 symmetry of the Hamiltonian.

The first realization of self-organization with a BEC has sparkled widespread interest from different fields in physics, since the system allows the simulation of a phase transition breaking a discrete symmetry in a well-controllable environment. In particular, in the case of self-ordering of a BEC the Hamiltonian (3.6) can be mapped to the Dicke-Model [3.13] often also referred to as Tavis-Cummings model [3.14]. The system of a transversally driven BEC in a cavity is equivalent to this model if the electronic atomic states are replaced by a pair of motional atomic states [3.12, 3.15]. Therefore, the realization of self-organization in a standing wave cavity was the first experimental realization of the Dicke phase transition. In this case the system undergoes a transition from a normal to a superradiant phase. The latter is characterized by a macroscopic occupation of the cavity mode $\hat{a}$.

The two examples given in this chapter show that light induced instabilities of atom clouds coupled to different dynamic laser light geometries are a valuable tool to simulate phase transitions known from other fields of physics. This opens up a rather different approach to quantum simulation where the non-trivial interplay between the dynamic field amplitudes and their back action on the atomic dynamics leads to symmetry breaking and complex dynamics in the initially homogeneous system. This resulted in a strong research direction to generalize the setup discussed above to account for more complex and general situations. In particular, the generalization to continuous symmetries [3.16–3.18] and inducing tunable interactions between different lattice sites [3.19, 3.20] in the symmetry broken state is still focus of ongoing research. The publications presented in the following chapters are important steps in this research direction.

4 Publication

EUROPHYSICS LETTERS **109**, 43001 (2015)

Atomic Self-Ordering in a Ring-Cavity with Counterpropagating Pump Fields[†]

S. Ostermann[1], T. Grießer[1] and H.Ritsch[1]

[1]*Institut für Theoretische Physik, Universität Innsbruck,*
Technikerstraße 25, A-6020 Innsbruck, Austria

The collective dynamics of mobile scatterers and light in optical resonators generates complex behaviour. For strong transverse illumination a phase transition from homogeneous to crystalline particle order appears. In contrast, cold particles inside a single-side pumped ring cavity exhibit an instability towards bunching and collective acceleration called collective atomic recoil lasing (CARL). We demonstrate that by driving two orthogonally polarized counter propagating modes of a ring resonator one realises both cases within one system. As a function of the two pump intensities the corresponding phase diagram exhibits regions in which either a generalized form of self-ordering towards a travelling density wave with constant centre-of-mass velocity or a CARL instability is formed. Time dependent control of the cavity driving then allows to accelerate or slow down and trap a sufficiently dense beam of linearly polarizable particles.

doi: 10.1209/0295-5075/109/43001

[†] The author of the present thesis performed all the calculations and numerical simulations in this publication, except the calculation leading to the relationship between the phase-velocity, the order parameter and the realtive pump asymmetry, which was obtained by T. Grießer. For all other aspects of this work T. Grießer acted as a discussion partner.

4.1 Introduction

Ultracold particles in an optical resonator interact non-locally via collective scattering of photons in and out of the cavity modes. Under suitable conditions this induces collective instabilities [4.1] or even crystallisation of the particles [4.2–4.4]. One of the earliest examples of such an instability, developed in close analogy to free electron lasers [4.5], was studied in the so called collective atomic recoil lasing (CARL) [4.1, 4.6, 4.7]. This type of instability can be realised in a single side pumped ring cavity and it reveals a transient bunching concurrent with coherent collective backscattering of pump light for an ensemble of fast particles counterpropagating the pump field of the cavity. In an alternative geometry, considering cold particles with transverse pump in a standing wave cavity, a phase transition from homogeneous to crystalline order was predicted [4.8] and experimentally verified [4.9, 4.10]. Later this was identified and as well confirmed as a quantum phase transition also occurring at zero temperature [4.3, 4.11].

In this paper we show that in a generalized geometry using two counter propagating pump fields of orthogonal polarization, a very similar type of phase transition appears, where the system breaks its translational symmetry and transforms into periodic order. The geometry is related to the configuration studied in [4.12], where no cavity was present. It is important to note that the pump fields injected from two sides into the ring cavity do not interfere and hence do not form a prescribed optical lattice, as they have orthogonal polarization. A lattice only appears through interference of pump and backscattered light. The two fields of orthogonal polarization interact only indirectly by scattering from the same atomic density distribution [4.12].

This work is organized as follows: After a short presentation of the model, we study general properties of the system and exhibit its relation to known models. In particular using a Vlasov-type approach we study the stability boundary of the homogeneous distribution. To understand the system's behaviour in more detail, we perform specific numerical simulations in part two. We reveal that selfordered solutions with a constant centre of mass velocity can be realised. In addition we show that the system allows for slowing down a fast atomic or molecular beam. In the last part we derive expressions which enable to state whether our configuration settles in a selfordered phase or a CARL instability depending on the pump parameters.

4.2 Model

Let us consider a large ensemble of N polarizable particles within a ring cavity supporting pairs of orthogonally polarized counterpropagating modes. For simplicity, we assume them to be confined along the cavity axis and linearly polarizable with a real scalar polarizability, i.e. atoms with a ground state with zero total angular momentum $F = 0$. For optically polarized atoms with tensor polarizabilities, the equations below would have to be adapted accordingly. In addition, for sufficiently large detuning from any optical resonance we can largely neglect mode mixing due to spontaneous Raman transitions to other Zeeman levels and thus we simply end up with an effective polarizability for

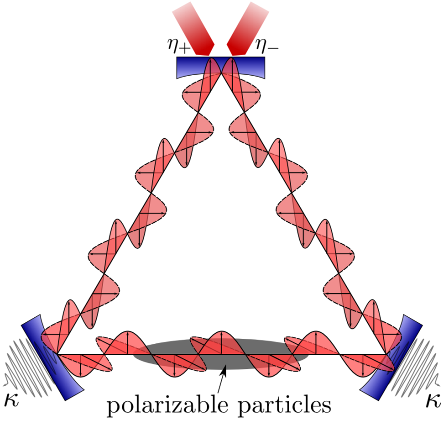

Figure 4.1: Schematic picture of the considered setup.

each field mode.

Note that this description explicitly excludes optical pumping and polarization gradient cooling as in optical molasses. When enhanced by cavity feedback this tends to localize the particles in space as shown in some earlier work [4.13]. While this is certainly an interesting generalization of our model, such ordering is a single-particle effect an thus fundamentally different from the collective selfordering dynamics into a lattice structure studied in our present work below.

In a semiclassical point particle description the time evolution of the mode amplitudes a_n of the intra cavity field $\mathbf{E}(\mathbf{x}) := \sum_n a_n \mathbf{f}_n(\mathbf{x})$ is governed by the equations [4.14]

$$\dot{a}_n(t) = (i\Delta_c - \kappa)a_n(t) - \mathrm{i}U_0 \sum_{j=1}^{N} \mathbf{E}(\mathbf{x}_j)\cdot\mathbf{f}_n^*(\mathbf{x}_j) + \eta_n \tag{4.1}$$

where 2κ is the cavity linewidth and $\Delta_c := \omega_p - \omega_c$ denotes the detuning between the pump field (ω_p) and the cavity modes (ω_c) and U_0 determines the interaction strength. Physically, U_0 represents the optical potential depth per photon in the cavity as well as the cavity mode frequency shift per particle. In general, U_0 can be complex but we will restrict our treatment to real U_0, meaning that we only consider dispersive atom-light interactions.

We approximate the mode functions $\mathbf{f}_n$ in the interaction zone as plane waves, so that their polarization is constant. In the following we will only consider four different modes, hence we will change notation from $\{a_1, a_2, a_3, a_4\} \to \{\alpha_+, \alpha_-, \beta_+, \beta_-\}$ and $\{\mathbf{f}_1, \mathbf{f}_2, \mathbf{f}_3, \mathbf{f}_4\} \to \{\mathbf{f}_\alpha^+, \mathbf{f}_\alpha^-, \mathbf{f}_\beta^+, \mathbf{f}_\beta^-\}$, where

$$\mathbf{f}_{\alpha,\beta}^{\pm}(\mathbf{x}) = \exp(\pm \mathrm{i}\mathbf{k}\cdot\mathbf{x})\,\mathbf{e}_{\alpha,\beta} \tag{4.2}$$

and the polarization vectors fulfil the orthogonality relation $\mathbf{e}_\alpha \cdot \mathbf{e}_\beta = \delta_{\alpha,\beta}$. Two counterpropagating, orthogonally polarized modes $\mathbf{f}_\alpha^+$ and $\mathbf{f}_\beta^-$ are pumped with amplitudes $\eta_1 \equiv \eta_+$ and $\eta_4 \equiv \eta_-$, while the other two modes $\mathbf{f}_\alpha^-$ and $\mathbf{f}_\beta^+$ are only populated by scattered photons. This configuration represents only a slight change as compared to standard ring cavity cooling scheme [4.15–4.17], but constitutes a very different situation physically. As the two counterpropagating pump fields do not interfere, no prescribed optical lattice is formed and the system is inherently translation invariant. Note that imperfect mirrors in principle could lead to scattering between the two polarizations. Fortunately in a three mirror ring cavity the two orthogonal polarization modes are sufficiently frequency shifted due to the polarization dependent mirror reflection, so that no resonant scattering between the modes will occur.

The force on a particle within the cavity field is given by the gradient of the optical dipole potential $\phi(x) = \hbar U_0|\mathbf{E}(\mathbf{x})|^2$ associated with the local field intensity, hence $m\ddot{\mathbf{x}}_j = -\nabla\phi(\mathbf{x}_j)$ with particle mass m. We restrict our treatment to the one dimensional motion along the cavity axis, so that $\mathbf{x}_j$ is replaced by x_j. Under these assumptions eqs. (4.1) and (4.2) lead to:

$$\dot{\alpha}_+ = (\mathrm{i}\delta - \kappa)\alpha_+ - \mathrm{i}NU_0\,\theta\,\alpha_- + \eta_+ \tag{4.3a}$$
$$\dot{\alpha}_- = (\mathrm{i}\delta - \kappa)\alpha_- - \mathrm{i}NU_0\,\theta^*\,\alpha_+ \tag{4.3b}$$
$$\dot{\beta}_+ = (\mathrm{i}\delta - \kappa)\beta_+ - \mathrm{i}NU_0\,\theta\,\beta_- \tag{4.3c}$$
$$\dot{\beta}_- = (\mathrm{i}\delta - \kappa)\beta_- - \mathrm{i}NU_0\,\theta^*\,\beta_+ + \eta_-, \tag{4.3d}$$

where $\theta = 1/N\sum_n e^{-2\mathrm{i}kx_j}$ defines the orderparameter and $\delta := \Delta_c - NU_0$ is the effective cavity detuning. These eqs. (4.3) describe two independent CARL geometries with different propagation directions (cf. Fig. 4.1) which interact via the atomic density inhomogeneities. It should be mentioned that the detuning δ and the cavity decay rate κ are in general different for the two counterpropagating modes. However, this does not influence the basic physics discussed in this work and would add unnecessary complexity. Therefore we assume equal detuning and decay rate for all modes in the following.

The light induced optical potential explicitly reads:

$$\phi = \hbar U_0(\alpha_+\alpha_-^*\mathrm{e}^{2\mathrm{i}kx} + \alpha_+^*\alpha_-\mathrm{e}^{-2\mathrm{i}kx} + \beta_+\beta_-^*\mathrm{e}^{2\mathrm{i}kx} + \beta_+^*\beta_-\mathrm{e}^{-2\mathrm{i}kx}). \tag{4.4}$$

For very large particle numbers the numerical simulation of equations of motion can be achieved only at large computational cost. However, in the limit $N \to \infty$ the dynamics of the gas can, for sufficiently short times be reliably approximated by a Vlasov equation (in 1D) [4.18, 4.19]

$$\frac{\partial f}{\partial t} + v\frac{\partial f}{\partial x} - \frac{1}{m}\frac{\partial \phi}{\partial x}\frac{\partial f}{\partial v} = 0 \tag{4.5}$$

for the corresponding one-body phase space distribution function $f(x, v, t)$. Such a treatment misses, however, correlations in the density and field fluctuations which lead to cooling and heating on longer time scales [4.20]. Assuming periodic boundary conditions allows to restrict our treatment to the truncated phase space with $x \in (0, \lambda)$.

4.3 Stability Analysis

Let us now investigate the coupled dynamics of the field modes and particles as described by eqs. (4.3)–(4.5). For a spatially homogeneous distribution the system is fully translation invariant and thus $\theta = 0$. For this reason the state defined by, $\alpha_-^0 = \beta_+^0 = 0$ as well as

$$f(x,v,t) = \lambda^{-1} F(v), \quad \alpha_+^0 = \frac{\eta_+}{\kappa - i\delta}, \quad \beta_-^0 = \frac{\eta_-}{\kappa - i\delta}. \tag{4.6}$$

constitutes a stationary solution of the system (4.3)–(4.5), regardless of the velocity distribution $F(v)$. Note that in the following we only consider thermal (i. e. Maxwell-Boltzmann) velocity distributions

$$F(v) = \frac{1}{\sqrt{\pi} v_\mathrm{T}} e^{-\left(\frac{v}{v_T}\right)^2}. \tag{4.7}$$

Here we introduced the thermal velocity v_T which is connected to the temperature via $m v_\mathrm{T}^2/2 = k_\mathrm{B} T$.

In this stationary state only forward scattering occurs without photon redistribution between the modes and thus there are no forces on the particles. Only deviations from perfect spatial homogeneity can lead to backscattering and the build-up of an optical lattice. To find out under which conditions such deviations are amplified and a subsequent phase transition to an ordered phase can occur, we perform a linear stability analysis following Landau [4.21]. As a result we find that the steady state (4.6) is unstable if and only if the dispersion relation $D(s)$ has at least one zero with a positive real part, where

$$D(s) := \delta^2 + (s+\kappa)^2 + \left[(s+\kappa)A - \mathrm{i}\delta S\right] I(s). \tag{4.8}$$

In (4.8) we defined the total pump parameter S and the pump asymmetry A according to

$$S := |\eta_+|^2 + |\eta_-|^2, \quad A := |\eta_+|^2 - |\eta_-|^2. \tag{4.9}$$

Furthermore,

$$I(s) := \frac{N U_0^2 v_R}{\kappa^2 + \delta^2} \int_{-\infty}^{\infty} \frac{F'(v)}{s + 2\mathrm{i}kv} \,\mathrm{d}v \tag{4.10}$$

with the recoil velocity $v_\mathrm{R} = 2\hbar k/m$. One finds that for every given pump asymmetry there exists a critical total pump parameter S_c such that the homogeneous state is unstable for $S > S_c$ and stable otherwise.

For equal pump intensities, i. e. $A = 0$, we recognize that (4.8) is almost exactly the same dispersion relation as one obtains for a transversally pumped ring-cavity. The only difference is that the wavenumber is multiplied by a factor 2 and the transversal pump-intensity is replaced by the sum of the two pump intensities S [4.18]. Obviously there exists a close analogy between the present setup with equal pump strengths and a transversally pumped ring-cavity. As in the latter case there appear stable selforganized solutions beyond an instability threshold [4.18], which is given by

$$S_c^{A=0} := \frac{k_B T}{N U_0^2} \frac{(\kappa^2 + \delta^2)^2}{\hbar|\delta|}. \tag{4.11}$$

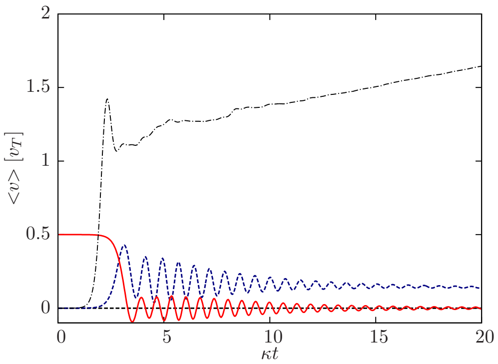

Figure 4.2: Evolution of the centre of mass velocity for the same parameters as in Fig. 4.3. Sufficiently small $A/S = 0.3$ (dashed blue) leads to a selforganized solution with a constant centre of mass velocity whereas for large $A/S = 0.8$ (dash dotted black) the CARL phase is realised which results in an indefinitely increasing centre of mass velocity. The solid red curve shows the evolution of the mean velocity for a initial distribution with initially $<v>\neq 0$ and $A = 0$.

The other extreme case, $A = \pm S$, corresponds to a pure CARL instability [4.18] in which case no selforganization can take place as shown in sec.4 of [4.18].

While the dependence of the critical pump parameter on the pump asymmetry can not be found in closed form, solving $D(0 + \mathrm{i}\omega) = 0$ for $A(\omega)$ and $S(\omega)$ yields the stability boundary using $\omega \in \mathbb{R}$ as parameter, cf. Fig. 4.5. The central question in the following is whether and under which conditions there occurs selforganization for nonzero pump asymmetries.

4.4 Numerical Simulation

To gain deeper insight into the systems behaviour we have numerically solved the Maxwell-Vlasov equations (4.3)–(4.5) for an initial condition close to homogeneous in space and a negative effective detuning δ. These simulations confirm our predictions for the $A = 0$ case. Furthermore they reveal that for sufficiently small A and above threshold the system does evolve into a selfordered state, albeit one in which the gas possesses a non vanishing centre of mass velocity v_{ph} constant in time. In the process of forming such a travelling wave the continuous translation symmetry is broken. As a matter of fact, the gas moves in the direction of the stronger pump beam. However, we find that, for a given S, as soon as A exceeds a certain value, there still occurs a CARL instability resulting in a runaway centre of mass velocity. For an illustration of these processe see figs. 4.2 - 4.4. Movies of typical phase space evolutions are available in the online supplemental material (*asym03.mp4* and *asym08.mp4*).

While we have started from a particle ensemble at rest up to now and found a moving

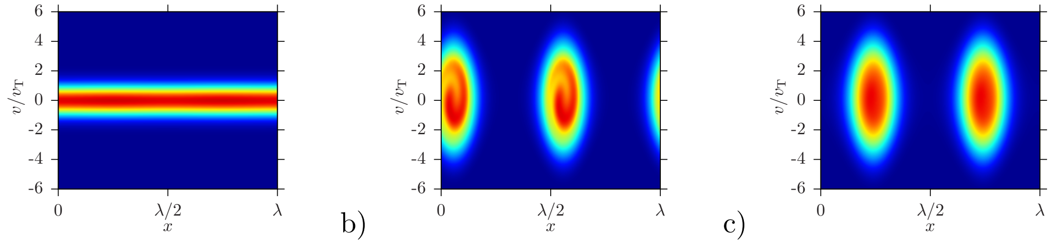
a) b) c)

Figure 4.3: Snapshots from the time evolution of the phase space density for a relative pump asymmetry $A/S = 0.3$ (the full movie of the time evolution can be found on-line, *396.5kB*, *asym03.mp4*). The parameters are chosen to be: $kv_\mathrm{T} = 1.5\kappa$, $N = 2\cdot 10^5$, the effective cavity detuning is set to $\delta = -\kappa$ and $U_0 = -1/N$. a) Spatially homogeneous distribution at $t = 0\kappa^{-1}$. b) During the ordering process at $t = 15\kappa^{-1}$. c) Selfordered state at $t = 32\kappa^{-1}$. If one compares figs. b) and c) one finds that the spatially periodic distribution is shifted in space. This implies that the system exhibits a certain constant (see Fig. 4.2) center of mass velocity.

gas in a steady state, one can turn the idea around and use this setup to efficiently slowing down a cold atomic or molecular beam by collective scattering, improving a similar approach which has already been presented in [4.16] (see the red curve in Fig. 4.2).

4.5 BGK Waves

As we have seen above, in the case of instability and depending on the pump asymmetry, the gas either enters the CARL regime, in which the centre of mass is accelerated indefinitely, or it settles in a selfordered, travelling-wave state with a constant phase velocity (i. e. centre of mass velocity). Let us therefore investigate this latter type of solution more closely. From equation (4.5) one deduces that any nonlinear wave with phase velocity v_ph must be of the BGK (Bernstein-Greene-Kruskal) form [4.22]

$$f(x,v,t) = G\left(\frac{m(v-v_\mathrm{ph})^2}{2} + \phi(x,t)\right), \tag{4.12}$$

where $G(.)$ is an arbitrary function. Furthermore, $\phi(x,t)$ may depend on (x,t) only through $x - v_\mathrm{ph}t$, which implies that $\alpha_- e^{-2ikv_\mathrm{ph}t}, \beta_+ e^{2ikv_\mathrm{ph}t}$ as well as α_+, β_- all be independent of time. To actually find the phase velocity from the equations of motion we require $G(.)$, which is obtained as the solution of an initial value problem and thus in general out of reach. Nevertheless it is possible to deduce a relationship between the phase velocity, the order parameter and the relative pump asymmetry in the form ($\Theta := N|\theta|$)

$$\frac{A}{S} = \frac{-4\delta(\kappa^2+\delta^2-U_0^2\Theta^2)kv_\mathrm{ph}}{4(\kappa^2+\delta^2)k^2v_\mathrm{ph}^2 + (\kappa^2+\delta^2-U_0^2\Theta^2)^2 + (2\kappa U_0\Theta)^2} \tag{4.13}$$

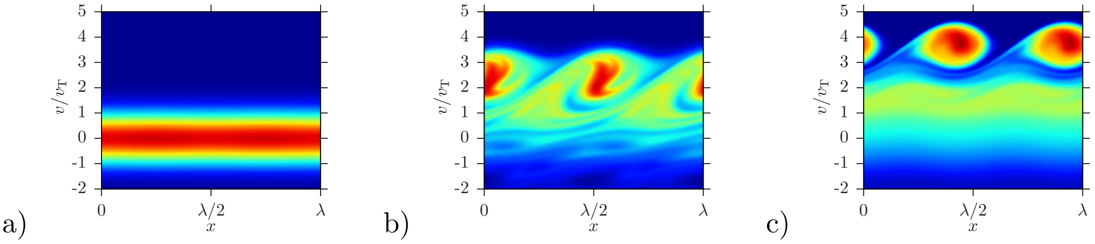

Figure 4.4: Snapshots from the time evolution of the phase space density for a relative pump asymmetry $A/S = 0.8$ (the full movie of the time evolution can be found on-line *412.6kB, asym08.mp4*). The rest of the parameters are chosen to be equal to the ones chosen in Fig. 4.3. a) Spatially homogeneous distribution at $t = 0\kappa^{-1}$. b) CARL instability at $t = 10\kappa^{-1}$ and c) CARL instability at $t = 20\kappa^{-1}$.

fulfilled by any nonlinear wave solution. From (4.13) we find that for $\delta < 0$ the wave travels in the direction of the stronger pump beam, as long as $N|U_0| \le \sqrt{\kappa^2 + \delta^2}$. As soon as the inequality is violated, waves with sufficiently large order parameters propagate in the opposite direction. As such waves have never been observed numerically we have reason to expect them to be dynamically unstable. Hence we stipulate that the order parameter satisfies the bound $N|U_0||\theta| \le \sqrt{\kappa^2 + \delta^2}$. Furthermore, eqn. (4.13) allows to conclude that if

$$\frac{|A|}{S} > \frac{|\delta|}{\sqrt{\kappa^2 + \delta^2}} \tag{4.14}$$

there exists *no* BGK-wave solution at all. This implies that if the homogeneous solution is unstable and the asymmetry exceeds the bound (4.14), the gas will *necessarily* enter the CARL regime.

Eqn. (4.13) can also be viewed as determining the necessary relative pump asymmetry A/S, which is needed to generate a wave with a prescribed phase velocity v_{ph} and order $|\theta|$. Notice, however, that the necessary total pump strength S can not be inferred. In particular, in order to stop a beam (i. e. to achieve $v_{\mathrm{ph}} = 0$) the pump asymmetry has to be equal to zero.

The foregoing statements exhaust the characterization of the BGK solutions in absence of knowing $G(.)$. Without going into details we state that for gas with temperature $kv_T \gg \kappa$, one finds that a BGK-wave will develop as soon as $S > S_{\mathrm{BGK}}$, where

$$S_{\mathrm{BGK}} := S_c^{A=0}\left[1 + \left(\frac{\hbar A}{2k_B T}\frac{NU_0^2}{\sqrt{\kappa^2 + \delta^2}}\right)^2\right]. \tag{4.15}$$

The results of the stability analysis and the discussion above are summarized in Fig. 4.5. Obviously there seems to be a sharp transition from the BGK phase to the CARL phase. This fact has also been proven to be right in numerical tests.

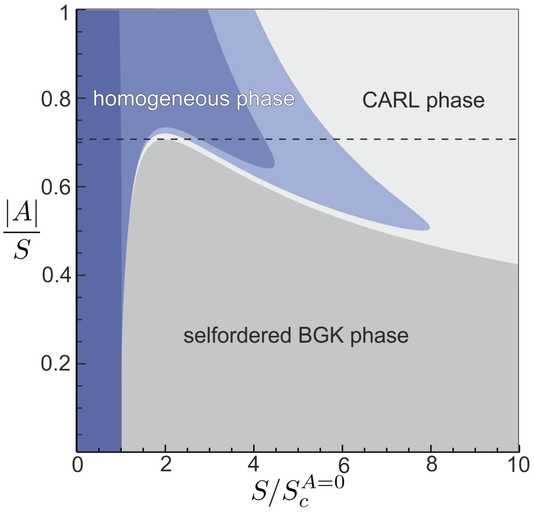

Figure 4.5: Phase diagramm. The blue regions correspond to a stable homogeneous gas for different temperatures. From dark to light blue we have chosen $kv_T = 1.5,\ 50,\ 100\,\kappa$. The dark grey region, bounded by (4.15), marks the parameter regime where a warm gas transitions to a BGK state (4.12). The dashed black line corresponds to the bound (4.14).

4.6 Conclusions and Outlook

We demonstrated that utilizing orthogonally polarized counter propagating modes the physics of light induced selfordering is observable, similarly to the case of a transversely pumped ring resonator. In the case of no pump asymmetry the two setups are fully equivalent [4.18]. However, the system considered in this work is more versatile, because, in principle, by the choice of the pump asymmetry, ordered particle distributions with any prescribed centre of mass velocity can be generated. Therefore the control of the pump intensity allows for controlling the motion of gas particles inside the ring cavity. As a consequence, a particle beam can be effectively slowed down and trapped. Note that a different loss rate for the two polarization modes, as it often appears in practice, can be easily compensated by a correspondingly enlarged pump.

Analogous physics should be present at zero temperature allowing to control and study degenerate quantum gases. For example a similar behaviour of a superfluid gas inside a transversally pumped cavity has been experimentally observed recently [4.23]. Interesting effects can also be expected in the case of particles in optical lattices. Here collective scattering from orthogonally polarized modes can be used to gain insight into the particle quantum statistics at minimal perturbation or to induce tailored long-range interactions.

Acknowledgemets

We thank C. Zimmermann for helpful discussions on experimental implementability of the system and acknowledge support by the Austrian Science Fund FWF through projects SFB FoQuS P13 and I1697-N27.

5 Publication

Physical Review X **6**, 021026 (2016)

Spontaneous Crystallization of Light and Ultracold Atoms†

S. Ostermann[1], F. Piazza[1] and H.Ritsch[1]

[1]*Institut für Theoretische Physik, Universität Innsbruck,*
Technikerstraße 21, A-6020 Innsbruck, Austria

Coherent scattering of light from ultracold atoms involves an exchange of energy and momentum introducing a wealth of nonlinear dynamical phenomena. As a prominent example particles can spontaneously form stationary periodic configurations which simultaneously maximize the light scattering and minimize the atomic potential energy in the emerging optical lattice. Such self-ordering effects resulting in periodic lattices via bimodal symmetry breaking have been experimentally observed with cold gases and Bose-Einstein condensates (BECs) inside an optical resonator. Here, we study a new regime of periodic pattern formation for an atomic BEC in free space, driven by far off-resonant counterpropagating and noninterfering lasers of orthogonal polarization. In contrast to previous works, no spatial light modes are preselected by any boundary conditions and the transition from homogeneous to periodic order amounts to a crystallization of both light and ultracold atoms breaking a continuous translational symmetry. In the crystallized state the BEC acquires a phase similar to a supersolid with an emergent intrinsic length scale whereas the light-field forms an optical lattice allowing phononic excitations via collective backscattering, which are gapped due to the infinte-range interactions. The system we study constitutes a novel configuration allowing the simulation of synthetic solid-state systems with ultracold atoms including long-range phonon dynamics.

doi: 10.1103/PhysRevX.6.021026

---

† The author of the present thesis performed all the calculations and numerical simulations in this publication. For all other aspects of this work F. Piazza contributed in an intensive advisory role.

5.1 Introduction

For a gas of pointlike particles off resonantly illuminated by coherent light, the individual dipoles oscillate in phase, each emitting radiation in a characteristic pattern. When several particles contribute to the scattering, the corresponding amplitudes interfere, which leads to a strongly angle-dependent scattering distribution [5.1, 5.1–5.3]. In addition, if the motional degree of freedom is relevant on the considered time scales, any high field seeking particle will be drawn towards the corresponding local light field maxima, where in turn light scattering is enhanced. This directional energy and momentum transfer between the gas and the field leads to an instability resulting in density fluctuations and potentially also in the formation of an ordered pattern. While for a room temperature gas this typically occurs only at very high pump powers [5.4–5.6], it can become important for very strong scatterers as larger nano- or microparticles [5.7–5.13]. The stringent threshold conditions can be relaxed by laser cooling the gas to temperatures well below the mK-range as well as by recycling the scattered light in optical resonators. In this case much weaker forces and thus lower light power is needed to a create substantial back-action effect of the scattered light onto the particles. This back-action was predicted to lead to roton-like instabilities and spatial bunching even at moderate pump powers, as observed in several configurations [5.14–5.25].

A relevant question is thus whether these instabilities can in some cases lead to the formation of a stable crystalline phase in the steady state of such driven, dissipative systems. The first and simplest instance of such crystals is the self-ordered phase of transversally driven atoms in optical resonators [5.26–5.29], with the corresponding transition observable also as a quantum phase transition at zero temperature [5.30, 5.31]. It has been shown recently that a similar phase is also realizable in longitudinally pumped ring-cavities [5.32].

While this self-ordered phase shows some aspects shared by standard crystals like a roton-like mode [5.33], other characteristic features like the breaking of a continuous translational symmetry and a crystal spacing which is not externally fixed are both missing, since the resonator mirrors select a single electromagnetic mode. In order to include such features one necessarily needs to couple the particles to several electromagnetic modes, ideally a continuum. This is the case in one-dimensional tapered optical nanofibers [5.34, 5.35] or confocal cavities [5.36], where transversally driven atoms are predicted to spontaneously break the continuous symmetry into a crystal phase. The existence of a continuum of electromagnetic modes opens up the possibility for photons to crystallize, as it was studied with light propagating under electromagnetically induced transparency conditions through a nonlinear medium [5.37, 5.38].

In this work, we propose and characterise a novel crystalline phase of light and ultracold atoms. We consider a mirror symmetric and translation invariant setup as it is depicted in Fig. 5.1. It involves an elongated Bose-Einstein condensate (BEC) longitudinally illuminated by two counter propagating Gaussian beams far detuned from any atomic resonance. The beams have either orthogonal polarization or a sufficiently large frequency difference to suppress any interference effects. Above a finite driving intensity both atoms and light break a continuous translational symmetry leading

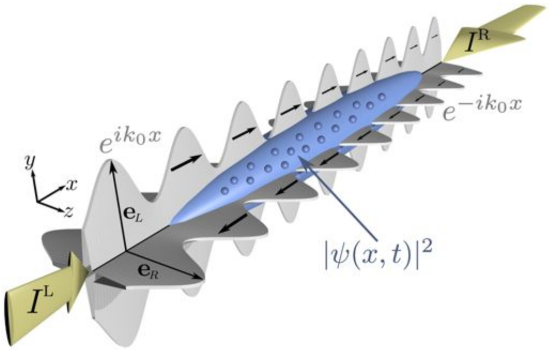

Figure 5.1: Schematic representation of the considered setup. An elongated BEC interacting with two counterpropagating, noninterfering laser beams of orthogonal polarization. The two beams are far detuned from any atomic resonance in order to avoid mixing between the two polarizations. Both polarizations are assumed to be equivalent with respect to the considered atomic transition, the latter thus involving a spherically (or at least cylindrically) symmetric ground-state. Alternatively to the use of two different polarizations, sufficiently different frequencies of the two counterpropagating lasers can be chosen.

to pattern formation with an intrinsically defined lattice spacing determined by the polarizability and density of the gas. The resulting state corresponds to a supersolid BEC trapped in an emerging optical lattice, the latter showing collective phononic excitations. The appearance of an emergent length scale in combination with lattice phonons – i.e. the appearance of a crystal of light – is a crucial difference to configurations where the drive is transverse to the direction in which the system organises [5.34–5.36].

A useful property of the chosen geometry is that ample information about the coupled system dynamics can be retrieved from the reflected light fields in a completely noninvasive manner. The present study opens a new direction in (ultra)cold atom-lattice physics, naturally including long-range phonon-type interactions and real-time nondestructive monitoring.

5.2 Model

We consider a trapped atomic BEC interacting with the electromagnetic (EM) field driven by two far off-resonant, counterpropagating, orthogonally polarized laser beams, as depicted in Fig. 5.1. In the dispersive regime considered below, the EM field provides an optical potential for the BEC [see Eq. (5.1)], while the BEC significantly modifies the refractive index [see Eq. (5.3)], thus both field and matter are dynamical quantities.

The BEC is treated within the Gross-Pitaevskii (GP) mean-field approximation [5.39], whereby the condensate wave function satisfies the equation

$$i\hbar\frac{\partial}{\partial t}\psi(x,t) = \left[\frac{-\hbar^2}{2m}\frac{\partial^2}{\partial x^2} + V(x)\right]\psi(x,t) + \frac{g_c N}{A}|\psi(x,t)|^2\psi(x,t), \tag{5.1}$$

where m denotes the particle's mass, g_c is the effective s-wave atom-atom interaction strength, and N is the atom number . For computational simplicity we assume the BEC to be confined by an extra transverse trapping potential $V_{\text{trap}}(x,y,z)$ such that the dynamics along the y and z axis is negligible. Therefore, the BEC wave function ψ is assumed to be in the ground state of the transverse trap with characteristic size $d_y = d_z = \sqrt{A}$, where A denotes the BEC cross section. Such a quasi one-dimensional treatment is eligible if the BEC's chemical potential μ is much smaller than the characteristic transverse trap frequency: $\mu \ll \hbar\omega_{y,z}$. The wavefunction satisfies the normalization condition: $\int dx|\psi(x,t)|^2 = 1$.

The total optical potential for the BEC has two contributions:

$$V(x) = V_{\text{trap}}(x) + V_{\text{opt}}(x), \tag{5.2}$$

representing the *static* trapping potential V_{trap} and the longitudinal (along x) optical potential V_{opt} determined by the *dynamical* part of the injected and scattered EM field [see Eq. (5.5)]. The latter consists of two far off-resonant fields with orthogonal polarizations driven from the left (L) and right (R) side of the BEC as depicted in Fig. 5.1. The two polarization components of the field satisfy the Helmholtz Eq. (5.3).

The atoms inside the BEC are described as linearly polarizable particles with a scalar polarizability α where the imaginary part is negligibly small, i. e. spontaneous emission of the atoms is neglected. This corresponds to the assumption that the driving laser frequency ω_l is sufficiently far detuned form any atomic resonance to prevent substantial internal excitation. This avoids spontaneous emission and thus mixing of the two counterpropagating EM components via Raman scattering as it is used for near resonant polarization gradient cooling may be neglected.

While for spin-polarized atoms the polarizability is field direction dependent in general, we assume the same polarizability for both polarizations orthogonal to the laser axis being the quantization axis. This corresponds to transitions from a spherically (or at least cylindrically) symmetric atomic ground-state. The impinging laser fields from left and right are approximated by plane waves so that we can write the EM field components as $\mathbf{E}_{\text{L,R}}(x,t) = \left(E_{\text{L,R}}(x)e^{i\omega_l t} + \text{c.c.}\right)\mathbf{e}_{L,R}$ with the orthogonality condition $\mathbf{e}_L \cdot \mathbf{e}_R = 0$. As the light transit time through the sample is negligible compared to all other time scales, the propagation delay of the EM field is adiabatically eliminated and the two field envelops (L for the field from left and R for the field from right) satisfy the Helmholtz equations

$$\frac{\partial^2}{\partial x^2}E_{\text{L,R}}(x) + k_0^2(1+\chi(x))E_{\text{L,R}}(x) = 0 \tag{5.3}$$

with the wavenumber k_0 of the incoming beams and the susceptibility $\chi(x)$ of the BEC. This susceptibility depends on the condensate's density and is given by

$$\chi(x) = \frac{\alpha N}{\epsilon_0 A}|\psi(x)|^2, \tag{5.4}$$

where $\psi(x,t)$ is the solution of Eq. (5.1). The directionality of the field propagation in the Helmholtz equations [Eq (5.3)] is defined by the boundary conditions, according to which the L-component has a finite imposed amplitude on the left end of the system and the R-component has such on the right end (see also Appendix 5.10).

As soon as one knows the spatial distribution of the electric fields, one can calculate the optical potential for the atoms via

$$V_{\text{opt}}(x) = -\frac{\alpha}{A}\left(|E_{\text{L}}(x)|^2 + |E_{\text{R}}(x)|^2\right). \tag{5.5}$$

Inserting the optical potential Eq. (5.5) into Eq. (5.1) leaves us with the set of three coupled differential equations: the GP Eq. (5.1) and the two Helmholtz equations [Eq (5.3)], describing the nonlinear dynamics of our system. The degree of nonlinearity resulting from the atom-light coupling is quantified by the dimensionless constant ζ defined as

$$\zeta := \frac{\alpha N}{\varepsilon_0 \lambda_0 A} = \frac{\alpha}{\epsilon_0} n \frac{L}{\lambda_0}\ , \tag{5.6}$$

where $n = N/AL$ is the three-dimensional density of the homogeneous BEC with L its characteristic extension along x. Due to the adiabatic approximation involved in the Helmholtz equation, the EM fields depend only parametrically on time through the dynamical refractive index set by the BEC density.

Due to the orthogonality of the two chosen polarizations there is no interference between the two counterpropagating components of the EM fields. Therefore, the optical potential (5.5) only depends on the absolute value squared of the fields. This important feature guarantees the translation invariance of the setup along the x direction nevertheless maintaining a mirror symmetric setup. Indeed, since we are driving with plane-wave lasers, as long as the BEC density is homogeneous, the EM fields $E_{\text{L,R}}(x)$ in Eq. (5.3) are also plane waves, leading to a translation invariant optical potential (5.5). This invariance with respect to continuous translations is spontaneously broken above a finite driving intensity, as discussed in section 5.3. In the resulting crystalline phase, the lattice constant is intrinsically established as it is discussed in section 5.4. This is due to the fact that no specific modes are selected and the fields can counterpropagate independently.

5.3 Dynamical Instability towards Crystallisation

As already mentioned above, due to the orthogonality of the polarizations of the two injected counter-propagating laser fields the particles do not feel any longitudinal optical forces. Naively, one could thus expect the BEC to remain unperturbed independently of the pump intensity. In this section we show that this is actually not the case, as above a particular threshold driving strength small density fluctuations lead to backscattering of light which in turn amplifies these fluctuations. This leads to an instability towards crystallization in the longitudinal direction. The latter can be described by considering the collective excitation spectrum of the system for a spatially homogeneous density distribution of the BEC $\psi_0(x,t) = 1/\sqrt{L}$ with the corresponding propagating field

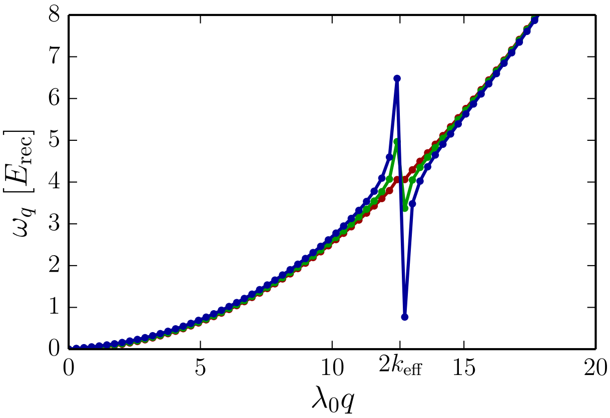

Figure 5.2: Excitation spectrum (5.8) in the homogeneous phase for different field intensities $I^{L,R} = 2.0$ (red), $I^{L,R} = 20.0$ (green) and $I^{L,R} = 60.0$ (blue) ($\zeta = 0.1$, $L = 100\lambda_0$, $g_c N/A\lambda_0 = E_{\mathrm{rec}}$).

solution of Eq. (5.3). These are plane waves of the form $E^{(0)}_{\mathrm{L,R}} = C \exp(\pm i k_{\mathrm{eff}} x)$, with the modified wavenumber

$$k_{\mathrm{eff}} = \frac{2\pi}{\lambda_0}\sqrt{1 + \zeta\lambda_0|\psi_0|^2} = \frac{2\pi}{\lambda_0}\sqrt{1 + \frac{\alpha}{\epsilon_0}n}, \tag{5.7}$$

where C is a real number fixed by the driving strength.

The spectrum is obtained by linearizing the coupled equations [Eqs. (5.1) and(5.3)] with the ansatz $\psi = (\psi_0 + \delta\psi)e^{-i\mu t}$ and $E_{\mathrm{L,R}} = E^{(0)}_{L,R} + \delta E_{L,R}$. Here $\delta\psi$ and δE are small deviations from the stationary solutions ψ_0 or $E^{(0)}_{L,R}$ and μ is the BEC chemical potential (see Appendix 5.9 for details). This yields

$$\hbar^2\omega_q^2 = \frac{\hbar^2 q^2}{2m}\left[\frac{\hbar^2 q^2}{2m} + 2gn\frac{64\pi^2 A\zeta^2}{cNL}\frac{1}{q^2 - 4k_{\mathrm{eff}}^2}I^{L,R}\right]. \tag{5.8}$$

Here $I^{L,R}$ denotes the intensity (in W/m^2) of the incoming light which we have chosen to be equal from left and right.

The above analytical expression Eq. (5.8) is very useful to understand some essential features of the atom-light interaction in the present setup and in particular the nature of the crystallisation transition. Apart from the last term, we recognize the known form of the Bogoliubov spectrum of interacting BECs [5.39], with the linear-in-q behavior corresponding to phononic excitations at low q. The last term on the other hand is the only one resulting from the atom-light interactions. The first thing to note is that its denominator vanishes at $q = \pm 2k_{\mathrm{eff}}$, which tells immediately that the modified wavenumber (5.7) sets the favoured momentum for the appearance of the instability. However, the vanishing of the denominator is compensated by the diverging BEC length L, at every finite atom number N (note that $\zeta \sim N$). The limit $L \to \infty$ of Eq. (5.8)

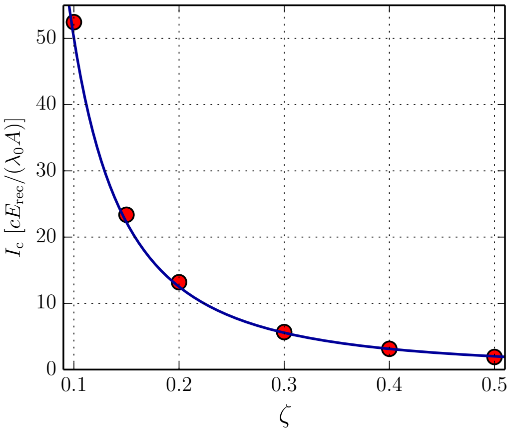

Figure 5.3: ζ dependence of the critical intensity. The solid blue line depicts the analytical result defined by Eq. (5.9) whereas the red dots depict numerical threshold estimations for large system sizes ($L = 120\lambda_0$) ($\zeta = 0.1$, $g_c N/A\lambda_0 = E_{\mathrm{rec}}$).

actually *has* to be taken, since the stationary plane-wave solution $E^{(0)}_{\mathrm{L,R}} \sim \exp(\pm i k_{\mathrm{eff}})$ about which we linearized only makes sense for a homogeneous *and* infinite atomic medium, so that the edges may be neglected. This indeed allows us to neglect the reflection of the incident wave by the change in refractive index at the BEC edges. Such finite-size effects, included in the numerical solutions described in section 5.4, become irrelevant for large systems, as we demonstrate below.

One way to obtain the proper result for Eq. (5.8) in the limit $L \to \infty$ is to consider that for any finite L the allowed momenta q take only quantized values as multiples of $2\pi/L$. Before taking the limit $L \to \infty$ it is instructive to compute the spectrum (5.8) for fixed finite L, as it is shown in Fig. 5.2 for different values of $I^{L,R}$. One recognizes a gap opening at $q = 2k_{\mathrm{eff}}$ for any finite $I^{L,R}$, i.e. any finite driving strength. The spectrum develops a minimum at the finite momentum $q = 2k_{\mathrm{eff}} + (2\pi)/L$, which corresponds to a roton minimum in the language commonly adopted for standard crystal formation [5.40]. It constitutes a generalization to continuous-symmetry breaking of the roton-like instability observed with a BEC in an optical cavity [5.33]. In a similar manner as in standard crystals, the crystallisation threshold can be calculated by finding the drive intensity at which the roton energy approaches zero. This leads to the threshold-condition $\omega_{2k_{\mathrm{eff}}+(2\pi)/L} = 0$. We are now in the position to take the limit $L \to \infty$. In doing this we note that we have to keep the atom number N constant in order to get a finite critical drive strength. Otherwise, if we perform the standard thermodynamic limit $N/L = \mathrm{const.}$, the energy of the system diverges and the crystallisation threshold vanishes. This divergence is an artefact of our model in which the light-mediated atom-atom interaction is of infinite range since the EM field is adiabatically adapting to the BEC configuration. The inclusion of the dynamics of the EM field (retardation

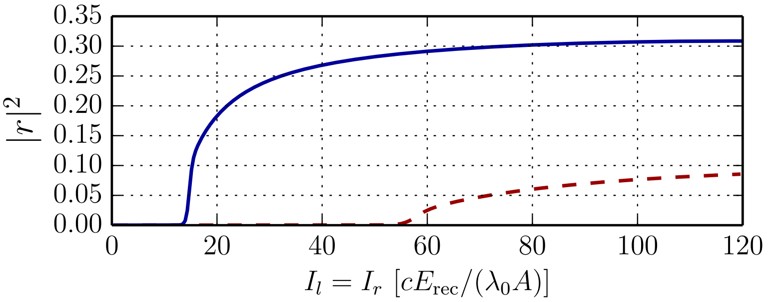

Figure 5.4: Dependence of the reflection coefficient of the BEC on the incoming field amplitudes for different atom-field couplings $\zeta = 0.1$ (dashed red) and $\zeta = 0.2$ (solid blue). The remaining parameters are the same as in Fig. 5.2.

effects) would introduce a finite range and thus eliminate the divergence in the energy. Still, the resulting range is expected to be larger than the typical BEC size L so than our calculation should be valid for any realistic system size. Taking the $L \to \infty$ limit we thus get the critical driving intensity

$$I_c^{\rm L,R} = \frac{cE_{rec}N}{\lambda_0 A}\frac{1}{\zeta^2} = cE_{rec}\frac{\varepsilon_0^2}{\alpha^2}\frac{1}{n}\frac{\lambda_0}{L}, \tag{5.9}$$

where we introduced the recoil energy $E_{\rm rec} := \hbar\omega_{rec} = \hbar^2 k_0^2/(2m)$. Note that in the $L \to \infty$ limit with constant N the BEC becomes more and more dilute, which renders the direct atom-atom coupling $\sim g_c$ eventually irrelevant. In Fig. 5.3 the analytical expression (5.9) is compared with numerically estimated thresholds for large system sizes (see section 5.4). We find full agreement between the linear instability threshold and the numerical threshold found by studying the imaginary time evolution of eqns. (5.1) and (5.3). This numerical approach to finite-sized systems is described next.

5.4 Crystal of Light and Atoms

After showing that the homogeneous system is unstable above a certain driving intensity, we are going to show that a stable crystalline phase is reached and study its properties by numerically solving the coupled GP [Eq. (5.1)] and Helmholtz [Eq. (5.3)] equations. We perform an imaginary time evolution of the system Eqs. (5.1)–(5.3), i. e. replace $t \to i\tau$, which yields the ground state of the system for long enough evolution times. For a detailed description of the numerical methods, see Appendix 5.10.

To determine the crystal transition point as a function of driving intensity we compute the total reflectivity of the BEC with respect to the intensity of either one of the incident beams, which we again take to be equal. For large enough system sizes, a clear threshold behavior is visible at a critical driving intensity, whereby the reflectivity grows from essentially zero with almost infinite slope, cf. Fig. 5.4. The hereby found critical intensity is in perfect agreement with the analytical result(see Fig. 5.3). As mentioned

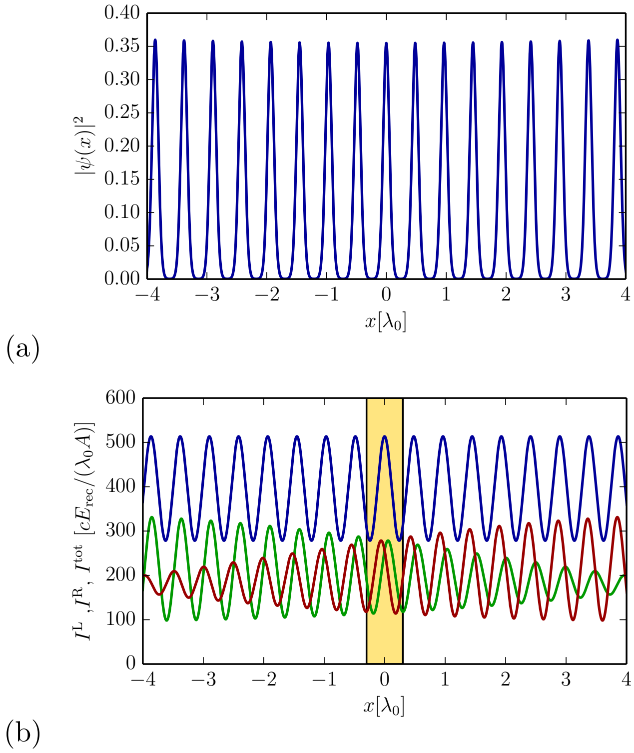

Figure 5.5: (a) Crystal ground state for $\zeta = 0.1$, $I_l = I_r = 200$ and (b) corresponding intensity distribution for the field from left (green) and right (red). The solid blue line depicts the sum of both intensities. A zoom into the yellow shaded region can be found in Fig. 5.8. The remaining parameters are $g_c N/A\lambda_0 = E_{\mathrm{rec}}$ and $L = 10\lambda_0$.

already in the previous section, finite-size effects manifest due to the presence of the edges of the BEC. In the calculations described in this section and in section 5.6, there is no further trapping potential along x and the BEC is confined within a box of size L, so that the BEC has sharp edges for the light impinging at $x = 0$ and $x = L$ (see Appendix 5.10 for more details). In section 5.7 we add an harmonic trap along x and show that the qualitative behavior is the same as described here. The BEC edges create a quick increase of the refractive index which induces a small amount of reflection of the incoming beam. As apparent from Fig. 5.4 this reflection is irrelevant for large system sizes compared to the reflection present in the crystalline phase.

The large light reflection above threshold is due to the appearance of a large spatial modulation of the BEC, forming the density grating shown in Fig. 5.5(a). This corresponds to a continuous symmetry breaking at the threshold leading to a crystalline phase which for the phase-coherent BEC implies supersolid order. Each peak in the density grating reflects the incoming light, resulting in a damped modulation of the intensity of each polarization component across the condensate, as shown in Fig. 5.5(b). While the modulation of each component's intensity $I^{\mathrm{L,R}}$ is damped across the system, the modulation of the total intensity $I^{\mathrm{tot}} = I^{\mathrm{L}} + I^{\mathrm{R}}$ is not damped, resulting in a periodic optical-lattice potential for the BEC which matches its density grating.

An important feature of the optical lattice emerging in the crystalline phase is the intrinsic character of the lattice spacing, which is not fixed externally but rather set by the BEC density and atom polarizability. This is a clear difference with respect to the self-ordering in optical resonators where the spacing is externally fixed by the cavity mirrors [5.26]; and also to the case of self-ordering of transversally driven atoms coupled to the continuum of modes of optical fibers, where the spacing is fixed by the driving frequency and fiber dispersion [5.34, 5.35]. As anticipated in section 5.3, the appearance of the roton-like instability at the characteristic momentum $2k_{\mathrm{eff}}$ leads to the following prediction for the emergent lattice spacing:

$$d = \frac{\pi}{k_{\mathrm{eff}}} = \frac{\lambda_0}{2\sqrt{1+\frac{\zeta\lambda_0}{L}}} = \frac{\lambda_0}{2\sqrt{1+\frac{\alpha}{\epsilon_0}n}}. \tag{5.10}$$

The emergent spacing is always smaller than the one in vacuum $\lambda_0/2$. This feature can be qualitatively reproduced also within a toy-model where the medium is approximated by a set of beam splitters [5.41]. This typically small but nonetheless crucial effect is also present when using counterpropagating beams with equal polarization and is essential for atom trapping in optical lattices [5.42]. Would the atoms indeed be trapped with the vacuum spacing $\lambda_0/2$, the EM field would be perfectly reflected and no standing wave could actually be formed and thus no trapping be possible. It is only through the slight renormalization $d < \lambda_0/2$ that perfect reflection is avoided. What our scheme with orthogonally polarized counterpropagating beams allows is to make the small renormalization of d coincide with the appearance of a large density modulation out of a homogeneous phase, i. e. a crystallisation.

The existence of an intrinsic lattice spacing in the crystalline phase implies as well the presence of phononic excitations of the the lattice, as discussed in the next section.

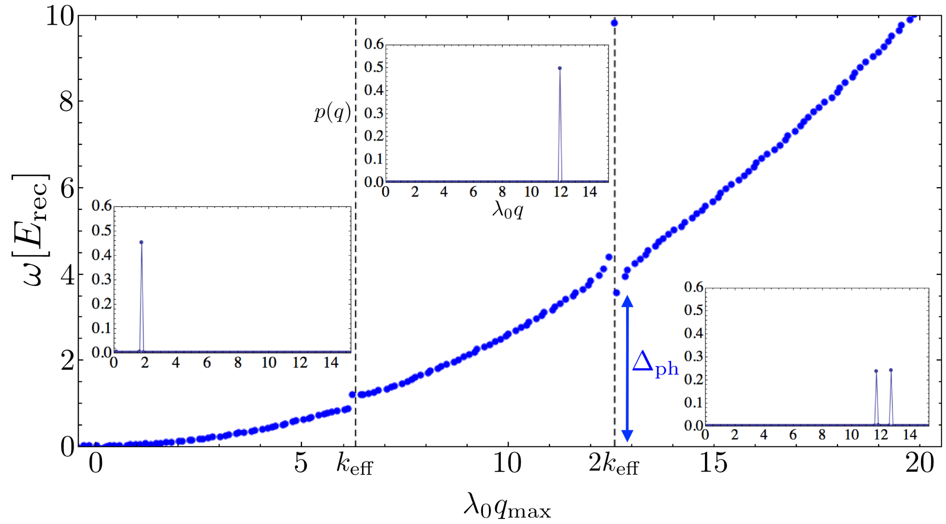

Figure 5.6: Excitation spectrum of the atom-light crystal. The blue points are the eigenvalues of the GP and Helmholtz equations linearized about the crystalline stationary state (see Appendix 5.9). The numerical diagonalization is performed with a momentum-space discretization $dq = 2\pi/L$. The parameters are the same as in Fig. 5.2 except for $L = 50$ and a fixed drive intensity $I^{L,R} = 50$ (slightly above threshold). $q_{\rm max}$ is the momentum corresponding to the largest component of the eigenvector of each eigenvalue. The insets show examples of eigenvectors (unormalized probability in momentum space) for three different eigenvalues representative of each region of the spectrum, from left to right: $\lambda_0 q_{\rm max} = 1.38 < \lambda_0 k_{\rm eff}$, $\lambda_0 k_{\rm eff} < \lambda_0 q_{\rm max} = 11.9 < 2\lambda_0 k_{\rm eff}$, and $\lambda_0 q_{\rm max} = 12.7 > 2\lambda_0 k_{\rm eff}$. The latter region corresponds to lattice phonons, characterized by a two symmetric pairs of peaks about a finite momentum. This phononic branch: $q_{\rm max} > 2k_{\rm eff}$ has a gap $\Delta_{\rm ph}$. Its analytical estimate in Eq. (5.11) yelds $\Delta_{\rm ph} \simeq 2\sqrt{2}E_{rec}$, in reasonable agreement with the numerical data.

5.5 Excitations of the Crystal: Phonons

Further insight in the properties of the atom-light crystal is provided by analyzing its excitation spectrum. As done in Section 5.3, we linearize the coupled system of Eqs. (5.1),(5.3). However, now the perturbation is performed around the symmetry-broken stationary solution. The result is presented in Fig. 5.6 for a driving intensity slightly above threshold. Details of the calculation are given in the Appendix 5.9. Since translation-invariance is broken, the matrices describing the linear system are not diagonal in momentum space requiring a discretization of the position(momentum) continuum. Moreover, while the total light intensity and atom density are periodic, the intensity of each polarization component is not, due to accumulated reflection along the density grating, introducing the decaying evelope shown in Fig. 5.5(b). This prevents the use of the quasi-momentum to label the excitation modes.

In Fig. 5.6 we labelled the eigenvalues based on their dominant momentum component $q_{\max}$, extracted from the corresponding eigenvector. This allows to split the spectrum into three regions separated by gaps at $q_{\max} = k_{\text{eff}}$ and $q_{\max} = 2k_{\text{eff}}$.

The gap at $q_{\max} = k_{\text{eff}}$ opens up for $I^{L,R} > I_c^{L,R}$ due to the appearance of an optical lattice potential for the atoms with a π/k_{eff} periodicity. It separates the two bands which, slightly above threshold, are characterized by eigenvectors with a clearly dominant momentum component (see left and middle inset in Fig. 5.6).

On the other hand, the gap at $2k_{\text{eff}}$ is the same one appearing in the homogeneous phase (see Fig. 5.2). As discussed in Section 5.3, at the critical drive intensity $I_c^{L,R}$ the gap is such that the energy of the mode with momentum $q = 2k_{\text{eff}} + 2\pi/L$ (momentum is still a good quantum number for $I^{L,R} \leq I_c^{L,R}$) vanishes. Out of this zero-energy mode at $2k_{\text{eff}}$ (not resolved with the discretization of Fig. 5.6), and beyond the critical point: $I^{L,R} > I_c^{L,R}$, the lattice phonon branch develops for $q_{\max} > 2k_{\text{eff}}$. The momentum distribution of the lattice-phonon eigenvectors is characterized by the splitting of the single peak at $2k_{\text{eff}}$ into two neighbouring peaks (see rightmost inset of Fig. 5.6). The phonon wavelength is set by the distance between the two nearby maxima appearing in the momentum distribution. This generates the slow beating in coordinate space. With a finite system size L, the longest wavelength is of the order of L.

Moreover, the lattice-phonon branch is gapped, in the sense that its lowest energy mode at $q_{\max}$ slightly above $2k_{\text{eff}}$ has a finite energy, as visible in Fig. 5.6. More importantly, this gap remains finite in the thermodynamic limit $L \to \infty$. We can estimate the size of the lattice-phonon gap close to threshold by using Eq. (5.8) and computing the energy of the mode next to the zero-energy mode. This yelds

$$\Delta_{\text{ph}}^2 \simeq 4\frac{\hbar^2 k_{\text{eff}}^2}{2m}\left(2\frac{\hbar^2 k_{\text{eff}}^2}{2m} + gn\right) , \tag{5.11}$$

which takes the value $\Delta_{\text{ph}}^2 \simeq 8E_{\text{rec}}^2$ in the thermodynamic limit $L \to \infty$ with $N = \text{const.}$. As discussed in section 5.3, in this limit $I_c^{L,R}$ remains finite while $n \to 0$ and $k_{\text{eff}} \to k_0$. Another choice of thermodynamic limit is possible: $L, N \to \infty$ with $n = \text{const.}$, where $I_c^{L,R} \to 0$ and the gap is still given by (5.11). The existence of an energy gap for lattice phonons is due to the long-range nature of the interactions, as it can be already predicted within a classical model of interacting point-like particles [5.43]. From a more general field-theoretical perspective, some of the gapless Goldstone modes expected from the continuous-symmetry breaking can indeed disappear (i.e. become gapped) due to the long range of the interactions, as it for instance happens to the longitudinal phonons of a three-dimensional Wigner crystal [5.44]. As long as retardation effects can be neglected our interactions will be infinite-ranged, the lattice-phonons gapped, and thus quantum/thermal fluctuations will not destroy crystalline order even in truly one dimension [5.45].

The existence of lattice phonons among the collective excitations is confirmed by numerical simulations of the real-time dynamics of the system, as it is described in the next section.

5.6 Crystallisation Dynamics after a Quench

In this section we investigate the real-time dynamics of the system by directly solving eqns. (5.1) and (5.3). This allows us to analyse the crystallization dynamics after a sudden turn on (quench) of the pump laser strength from zero to a value above threshold at $t = 0$. The corresponding time evolution of the BEC reflectivity, kinetic energy, as well as the evolution of the BEC density and total light intensity are shown in Figs. 5.7 and 5.9.

As apparent from the behavior of the reflectivity and kinetic energy $E_{\mathrm{kin}}(t) = \int dx \hbar^2 |\partial_x \psi|^2 / 2m$, the crystalline order is reached after a few inverse recoil frequencies, after which both quantities perform oscillations about a finite value. These residual oscillations are triggered by the energy gained by the system upon forming the density grating together with the optical lattice. The reason why this effect takes in a prominent role in the studied case is found by looking at Fig. 5.8, which shows the zoom into two peaks of the intensity distribution of the crystal. One recognizes that the maxima of the intensity distributions of the two fields coming from left and right (blue dots in Fig. 5.8) do not coincide with the maximum of the total intensity distribution (black dot in Fig. 5.8) at which the atoms are trapped. Therefore, the trapped atoms feel a strong field gradient for each single component because they do not sit at the maxima of the two counterpropagating fields, as it would be for example the case in optical lattices. This leads to a large coupling between the two counterpropagating fields and the atoms, leading to strong long-range interactions inducing collective excitations.

The corresponding dynamics of the BEC density and the total light intensity is shown in Fig. 5.9. As one can see from the solid lines marking the evolution of the intensity maxima, they start at a lattice spacing of $\lambda_0/2$ and move closer together in time reaching the emergent spacing d. In addition, we see the presence of residual oscillations about the crystalline order. In particular, the light intensity shows both compression modes, modulating the amplitude of the optical lattice in time, and phonons, modulating the spacing. The latter are clearly visible from the dynamics of the intensity maxima shown in Fig. 5.10. Since we are neglecting retardation of the fields, the energy can

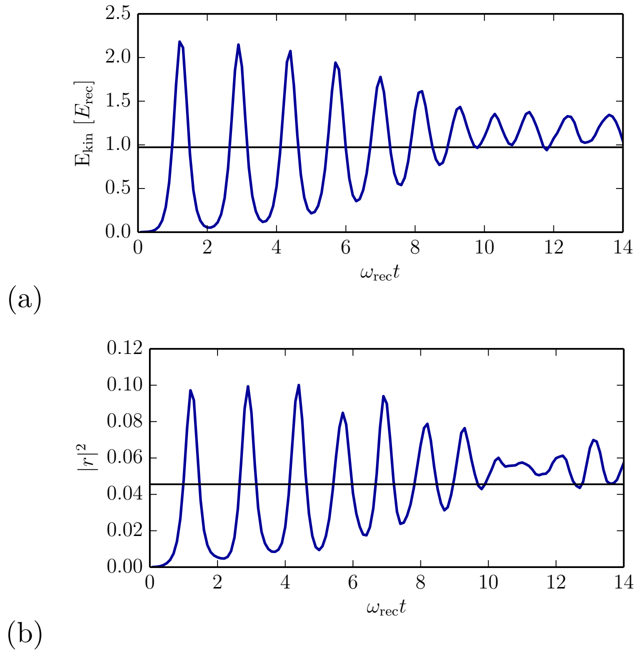

Figure 5.7: (a) Real-time evolution of the kinetic energy for $\zeta = 0.1$, $I_l = I_r = 100$, $g_c N = 1$. (b) Real-time evolution of the reflection coefficient for the same parameters as in figure (a). The solid black line shows the mean value of the corresponding functions.

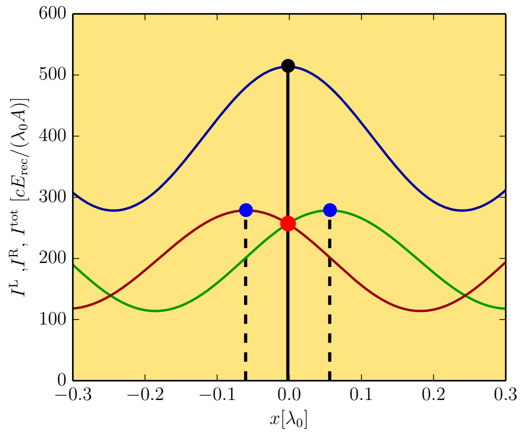

Figure 5.8: Zoom into the yellow shaded region of Fig. 5.5. The blue dots mark the maxima of the field from left (green) and right (red) whereas the black dot marks the maximum of the total field intensity (blue). The red dot shows the actual position of the particles.

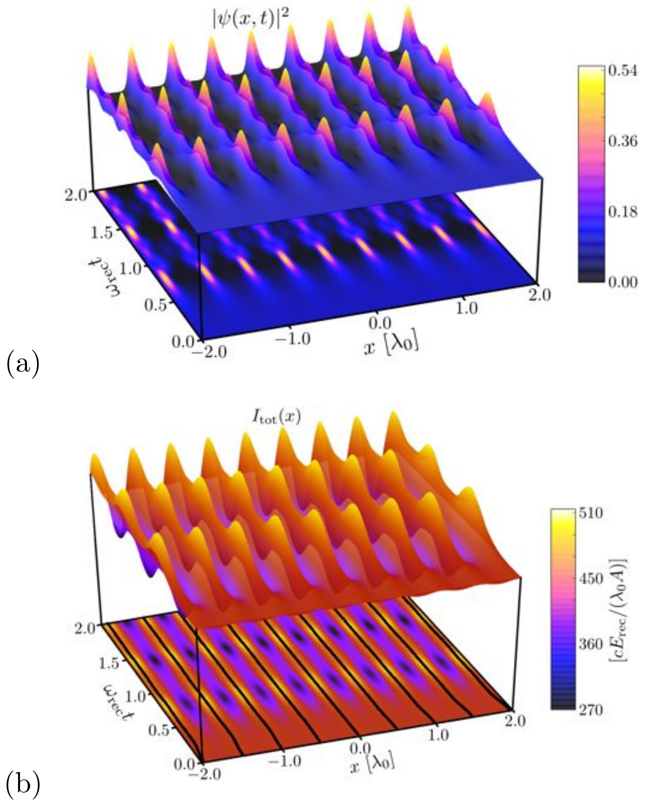

Figure 5.9: Real-time dynamics of the (a) BEC density distribution and b) the total light intensity for the same parameters as in Fig. 5.5. The solid black lines in figure (b) show the time evolution of the intensity maxima.

be redistributed among the collective degrees of freedom but not dissipated. Initially, for $\omega_{rec}t \sim 1$, mostly compression modes are excited. Subsequently part of the energy stored in compression modes is transferred to lattice phonons for $\omega_{rec}t \gtrsim 5$. In Fig. 5.10 we see a single-frequency oscillation of the intensity maxima, the latter moving almost in phase. This indeed corresponds to a low-wavelength lattice phonon, which becomes occupied for long enough times. As discussed in section 5.5, the longest wavelength is of the order of the system size L, consistently with the almost in-phase oscillations of Fig. 5.10.

As discussed in the previous section, lattice-phonons have a finite gap. They can efficently be excited in a quench experiment provided the energy available for collective excitations is large enough compared to Δ_{ph} [see Eq. (5.11]).

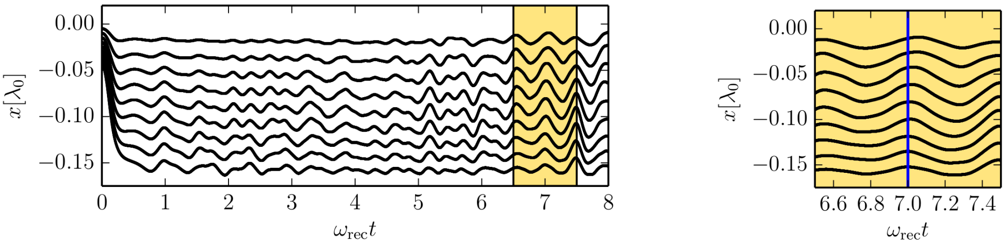

(a) (b)

Figure 5.10: Real-time evolution of the maxima of the intensity distribution as it is shown in Fig. 5.9. To simplify the comparison between the single curves the maxima positions were shifted so that they all start at $x = 0$. Fig. (a) shows the total time evolution where one can clearly recognize collective phononlike excitations of the lattice after $\omega_{rec}t \gtrsim 5$. Fig. (b) shows the zoom into the yellow marked area in fig.(a) in order to demonstrate the slight dephasing between the oscillations of the maxima. All parameters are chosen as in Fig. 5.5.

5.7 Experimental Implementation with Ultracold Bosons

BECs with high densities and a controlled shape trapped in optical dipole traps are currently available in many laboratories. In principle, the setups normally employed are already very close to the one needed to study the crystallization effects presented in this work. In the following, we will discuss the conditions needed to study our model in realistic experimental conditions, as well as the required parameter regime for observing the crystallization. Let us remark that the basic physics underlying the crystallization transition discussed here does not rely on the atoms being Bose-condensed. This phenomenon could in principle also be observed with thermal clouds or fermionic gases. Apart from the fundamentally very interesting feature of supersolidity, the practical advantage of a BEC with respect to a thermal cloud resides in its high density and low temperature, both decreasing the required laser power. On the other hand, for degenerate fermi gases, one could expect a strong dependence on the ratio between Fermi momentum and lattice constant [5.46–5.49].

We start by noting that using single beam optical traps can also lead to heating instabilities but never generate a stationary lattice [5.17]. Similarly, operating very close to an atomic resonance has been shown to generate instabilities and a short time formation of an optical lattice structures via so called end-fire modes [5.16]. As this requires significant atomic excitation, it involves fast transverse acceleration with heating and destruction of the BEC. This is prevented in our model by an improved geometry and much larger atom-field detuning.

Our model (5.1)–(5.3) is essentially 1D, which relies on the assumption that both, the atoms and the light move and propagate essentially unidirectionally along x. In practice this can be implemented by using a transverse trapping of the atoms tight enough to freeze out the dynamics along y, z. With harmonic trapping potentials this amounts to the requirement that $\omega_{y,z}^{\mathrm{ho}}$ is sufficiently larger than the BEC chemical potential μ. Here we still describe the one-dimensional BEC using the GP equation, which requires the atom density to be large enough to be in the mean-field regime [5.39]. The enforcement of unidirectional propagation of light is more demanding since an appreciable amount of diffraction out of the BEC axis would be present inducing propagation also perpendicular to x. Apart from the use of hollow-core optical fibers around the BEC [5.50], one option available in many laboratories today is using a two-dimensional array of tubes with spacing comparable with the wavelength of the light. This arrangement would generically produce destructive interference between the transverse field components diffracted from different tubes, so that if the latter are long enough only the forward propagation along the tube axis would remain. In this configuration, each tube will act equally while the field propagates inside a medium with a refractive index given by the sum of the contributions from each tube. Indeed, since all tubes share the same backreflected field there is a natural synchronization of the different tube lattices.

In any experimental realization a trap to confine the BEC along x will also be present. In addition, the two laser intensities might differ to some extend due to experimental inaccuracies. As an exemplary case we study the crystallization as in section 5.4 but add a harmonic trapping potential $V_{\mathrm{ext}}(x) = \frac{E_{\mathrm{trap}}}{2} x^2/\lambda_0^2$ and chose different pump intensities $I_l \neq I_r$. It can be seen from Fig. 5.11 that the qualitative features of the crystalline phase remain the same as in the homogeneous case. The only difference is the parabolic envelope for the density as well as for the light intensity distribution and the shift of the distribution towards the direction of the higher intensity. The threshold behaviour remains similar to the one presented in Fig. 5.4 with the only difference being an increase of the threshold intensity. A useful feature of the considered configuration is that the crystallization process can be observed in real-time by looking at the amount of reflected light, since the transmitted part of the counterpropagating beam can be separated from the reflected part having orthogonal polarization.

In order to choose the most suitable atomic transition, pump detuning and power, as well as BEC parameters like density and extension, one must consider the following constraints: we need to have i) a low enough critical driving strength (5.9), which depends on the detuning Δ_a and spontaneous emission γ through the real part of polarizability $\mathrm{Re}\alpha \sim \gamma/\Delta_a$, reading

$$I_c^{\mathrm{L,R}} \sim E_{rec} \frac{\Delta_a^2}{\gamma^2} \frac{\lambda_0}{n_A} \,, \tag{5.12}$$

and at the same time ii) a low enough BEC heating rate, which at the critical power reads

$$\Gamma_{\mathrm{heat}} \sim I_c^{\mathrm{L,R}} \frac{\gamma^2}{\Delta_a^2} \sim E_{rec} \frac{\lambda_0}{n_A} \,, \tag{5.13}$$

with $n_A = N/A$ being the surface density of the medium with respect to the light propagation. From Eqs. (5.12) and (5.13) one sees that the crystallisation is easier

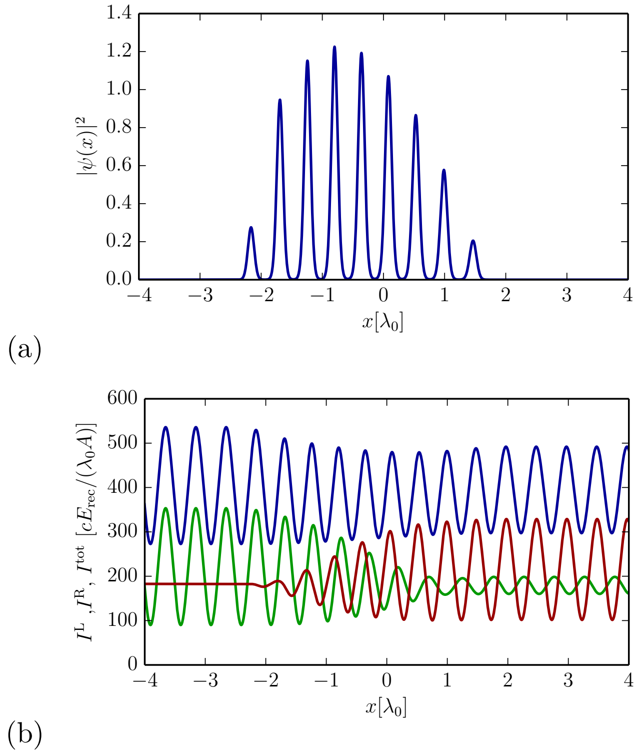

(a)

(b)

Figure 5.11: a) Crystal ground state for and b) corresponding intensity distribution for the field from left (green) and right (red) for the same parameters as in Fig. 5.5 with an additional external potential $V_{\mathrm{ext}}(x) = \frac{E_{\mathrm{trap}}}{2} x^2/\lambda_0^2$ with $E_{\mathrm{trap}} = 1.0 E_{\mathrm{rec}}$ and for different pump intensities from left and right $I_l = 200$ and $I_r = 150$. The solid blue line depicts the sum of both intensities.

achieved before the BEC is heated up if we increase the BEC surface density n_A. There is no favorable scaling neither with detuning Δ_a nor with the linewidth γ, since both heating rate (5.13) and critical power (5.12) scale with γ^2/Δ_a^2. For commonly employed transitions like the Rb or Cs D lines, the required laser power is easily achieved, but the heating rate can become a problem at too low densities due to the required laser powers and detunings. For instance, taking $N = 10^6$ atoms confined over a transverse cross section $A \sim 5 \times 5\mu\text{m}^2$ and $\lambda_0 \sim \mu$m, we estimate a required power $I_c \sim \text{W/cm}^2$ with a heating rate $\Gamma_{\text{heat}} \sim 10$ Hz for the Rubidium 780nm line with a detuning $\Delta_a = 100$GHz as well as for the Cesium $D2$ line with a detuning $\Delta_a = 20$GHz. Such a heating rate would still allow to observe the crystal fromation since, as we see in Fig. 5.9, this process takes place on the inverse recoil time scale, which is of the order of milliseconds.

5.8 Conclusions and Outlook

We predict that in suitable geometries roton instabilities originating from nonlinear free-space atom light interactions can be tailored to generate stationary crystalline states. They involve an optical lattice showing an emergent spacing and phononic excitations, trapping the atoms at the intensity maxima.

The required translation invariant, mirror symmetric geometry can be realized using two orthogonal polarization degrees of freedom or frequency shifted counterpropagating beams. We estimate that the dynamics studied in this work should be accessible in already existing experimental setups on large quasi-1D Bose-Einstein condensates. Actually, in comparison with standard crossed beam dipole traps, one simply has to adapt and control the polarizations of the trapping lasers and choose suitable detunings. The ordering process should be easily observable not only by measuring the atomic distributions but directly by looking at the reflected light from the condensate. This nondestructive measurement allows for a real-time monitoring of the dynamics.

Our results open up an intriguing new direction in quantum simulations with ultracold atoms in optical lattices, where the latter are enriched by the presence of collective phononic excitations resulting from the spontaneous crystallisation of light. In this spirit, the application of our approach to two dimensions and the inclusions of retardation effects as well as quantum fluctuations constitute the natural extension of this study.

Acknowledgements

We thank S. Krämer for support in the numerical implementation and F. Meinert and T. Donner for helpful discussions on the experimental limitations and implementability of the system. We also thank J. Lang for useful discussions. We acknowledge support by the Austrian Science Fund FWF through projects SFB FoQuS P13 and I1697-N27. FP is supported by the APART program of the Austrian Academy of Science.

5.9 Appendix: Calculation of Excitation Spectra

Here, we describe in detail how the linearization of the Helmholtz and the GP equation leads to the collective excitation spectra below [see Eq. (5.8)] and above the threshold (see Fig. 5.6).

It is convenient to slightly re-write the equations presented in section 5.2. Therefore, we define the relevant parameters of the system and useful units. We introduce the recoil energy $E_{\mathrm{rec}} := \hbar\omega_{rec} = \hbar^2 k_0^2/(2m)$ relative to the wave number $k_0 = 2\pi/\lambda_0$ of the incoming lasers in vacuum. The dimensionless time is defined through the recoil frequency: $\tilde{t} := \omega_{\mathrm{rec}} t$. The dimensionless space variable is given in units of the incoming laser wavelength $\tilde{x} := x/\lambda_0$. We also rescale the fields to have units of energy: $\tilde{E}_{\mathrm{L,R}} := \sqrt{\alpha} E_{\mathrm{L,R}}/\sqrt{A}$ and the atom-atom s-wave coupling to have units of energy times length: $\tilde{g}_{\mathrm{c}} := g_{\mathrm{c}}/A$. The GP equation [Eq. (5.1)] then reads

$$\begin{aligned} i\frac{\partial}{\partial \tilde{t}}\tilde{\psi}(\tilde{x},\tilde{t}) = &- \frac{1}{(2\pi)^2}\frac{\partial^2}{\partial \tilde{x}^2}\tilde{\psi}(\tilde{x},\tilde{t}) \\ &+ \frac{V_{\mathrm{ext}}}{E_{\mathrm{rec}}}\tilde{\psi}(\tilde{x},\tilde{t}) - \frac{1}{E_{\mathrm{rec}}}\left(|\tilde{E}_{\mathrm{L}}(\tilde{x})|^2 + |\tilde{E}_{\mathrm{R}}(\tilde{x})|^2\right)\tilde{\psi}(\tilde{x},\tilde{t}) \\ &+ \frac{\tilde{g}_c N}{E_{\mathrm{rec}}}|\tilde{\psi}(\tilde{x},\tilde{t})|^2\tilde{\psi}(\tilde{x},\tilde{t}), \end{aligned} \tag{5.14}$$

and the Helmholtz equations [Eq. (5.3)] become

$$\frac{\partial^2}{\partial \tilde{x}^2}\tilde{E}_{\mathrm{L,R}}(\tilde{x}) + (2\pi)^2\left[1 + \zeta|\tilde{\psi}(\tilde{x},t)|^2\right]\tilde{E}_{\mathrm{L,R}}(\tilde{x}) = 0\ . \tag{5.15}$$

Let us first consider the linearization of the Helmholtz equation (5.15). Inserting the ansatz already presented in section 5.3 namely $\psi = (\psi_0 + \delta\psi)e^{-i\mu t}$ and $E_{\mathrm{L,R}} = E^{(0)}_{L,R} + \delta E_{L,R}$ into (5.15) and neglecting terms of second order leads to

$$\partial_{xx}E^{(0)}_{L,R} + (2\pi)^2\left[1 + \zeta|\psi_0|^2\right]E^{(0)}_{L,R} \tag{5.16}$$

$$+\partial_{xx}\delta E_{L,R} + (2\pi)^2\left[1 + \zeta|\psi_0|^2\right]\delta E_{L,R} \tag{5.17}$$

$$+(2\pi)^2\zeta\left[\psi_0\delta\psi^* + \delta\psi\psi_0^*\right]E^{(0)}_{L,R} = 0. \tag{5.18}$$

The first line (5.16) corresponds to the Helmholtz equation for the steady state $E^{(0)}_{\mathrm{L,R}}$ an therefore it is equal to zero. The second line (5.17) is the Helmholtz equation for the field perturbation whereas the third line (5.18) describes the linear coupling between the field and the BEC.

This equation can be rewritten in the following form

$$\left(M + K^2_{\mathrm{eff}}\right)\cdot\delta\mathbf{E}_{\mathrm{L,R}} = -(2\pi)^2\zeta\mathcal{E}^{(0)}_{\mathrm{L,R}}\cdot\left(\Psi_0\cdot\delta\boldsymbol{\psi}^* + h.c.\right) \tag{5.19}$$

where we defined the matrices

$$M(x,x') := \partial_{xx}\delta(x-x') \tag{5.20}$$

$$K^2_{\text{eff}}(x,x') := (2\pi)^2\left[1+\zeta n_0(x)\right]\delta(x-x') \tag{5.21}$$

$$\mathcal{E}^{(0)}_{\text{L,R}}(x,x') := E^{(0)}_{\text{L,R}}\delta(x-x') \tag{5.22}$$

$$\Psi_0(x,x') := \psi_0\delta(x-x') \tag{5.23}$$

and the scalar product

$$M\cdot\mathbf{f} = \int dx' M(x,x')f(x'). \tag{5.24}$$

The formal solution of the linearized Helmholtz equation (5.19) is

$$\delta\mathbf{E}_{\text{L,R}} = -(2\pi)^2\zeta(M+K^2_{\text{eff}})^{-1}\cdot\mathcal{E}^{(0)}_{\text{L,R}}\cdot(\Psi_0\cdot\boldsymbol{\psi}^* + h.c.). \tag{5.25}$$

The linearization of the Gross-Pitaevski equation (5.14) follows a similar procedure as presented above. Performing the same ansatz and neglecting the second order terms leads to

$$\begin{aligned} i\partial_t\delta\psi + \mu\delta\psi = &-\frac{1}{(2\pi)^2}\partial_{xx}\delta\psi - \frac{1}{E_{rec}}[\psi_0\left(E_L^{(0)^*}\delta E_L + E_R^{(0)^*}\delta E_R + c.c.\right) \\ &+ \delta\psi\left(|E_L^{(0)}|^2 + |E_R^{(0)}|^2\right)] + \frac{g_cN}{E_{rec}}\left[|\psi_0|^2\delta\psi + \psi_0\left(\psi_0^*\delta\psi + \psi_0\delta\psi^*\right)\right] \\ &-\psi_0\mu - \frac{1}{(2\pi)^2}\partial_{xx}\psi_0 - \frac{1}{E_{rec}}\psi_0\left(|E_L^{(0)}|^2 + |E_R^{(0)}|^2\right) + \frac{g_cN}{E_{rec}}|\psi_0|^2\psi_0. \end{aligned} \tag{5.26}$$

The last line of equation (5.26) corresponds to the stationary GP equation and therefore it vanishe, as it defines how the chemical potential is related to the field amplitude and the particle particle interaction g_c, namely via

$$\mu = \frac{g_cN}{LE_{rec}} - \frac{2|E^{(0)}_{\text{L,R}}|^2}{E_{rec}}. \tag{5.27}$$

Inserting the formal solution (5.25) into the linearized GP equation (5.26) and performing a Fourier Transform via $f(x) = \frac{1}{\sqrt{L}}\sum_k e^{ikx}f(k)$ and

$$M(x,x') = \frac{1}{L}\sum_{k,k'} e^{ikx}e^{ik'x'}M(k,k')$$

gives

$$\begin{aligned} i\partial_t\mathbb{1}\boldsymbol{\psi} = &\left(-\mu\mathbb{1} + T + A_L + \tilde{A}_L + A_R + \tilde{A}_R + I_{\text{tot}} + 2\nu_0\right)\boldsymbol{\psi} \\ &+ (A_L + \tilde{A}_L + A_R + \tilde{A}_R + \nu_0)\mathcal{P}\boldsymbol{\psi}^* \end{aligned} \tag{5.28}$$

where $\mathbb{1}$ denotes the identity matrix and $\mathcal{P}$ is the parity operator, i. e. $\mathcal{P}\boldsymbol{\psi}(k) = \boldsymbol{\psi}(-k)$. We defined the following matrices:

$$T(k,k') := \frac{k^2}{(2\pi)^2}\delta(k-k') \tag{5.29}$$

$$\mathcal{I}_{\text{tot}}(k,k') := -\frac{1}{E_{\text{rec}}\sqrt{L}} I_{\text{tot}}(k-k') \tag{5.30}$$

$$\nu_0(k,k') := \frac{g_c N}{E_{\text{rec}}\sqrt{L}} n_0(k-k') \tag{5.31}$$

$$A_{\text{L,R}}(k,k') := \tag{5.32}$$

$$\frac{\zeta\pi^2}{E_{\text{rec}}L}\sum_{k_1,k_2} V^{\dagger}_{\text{L,R}}(k,k_1)Q^{-1}(k_1,k_2)V_{\text{L,R}}(k_2,k') \tag{5.33}$$

$$\tilde{A}_{\text{L,R}}(k,k') := \tag{5.34}$$

$$\frac{\zeta\pi^2}{E_{\text{rec}}L}\sum_{k_1,k_2} V_{\text{L,R}}(k,k_1)Q^{-1}(k_1,k_2)V^{\dagger}_{\text{L,R}}(k_2,k') \tag{5.35}$$

where $I_{\text{tot}}(k)$ and $n_0(k)$ are the Fourier transforms of the total intensity distribution and the BEC density. Besides we defined the additional matrices $V_{\text{L,R}}(k,k') := \sum_{k''}\psi_0^*(k'')E^{(0)}_{\text{L,R}}(k''+k-k')$ and $Q(k,k') := -k^2\delta(k-k') + 1/\sqrt{L}k^2_{\text{eff}}(k-k')$, where $k^2_{\text{eff}}(k)$ is the Fourier transform of $(2\pi)^2\left[1+\zeta n_0(x)\right]$. In the following we will call the sum of the A-matrices $\mathcal{A}(k,k') := A_L(k,k') + \tilde{A}_L(k,k') + A_R(k,k') + \tilde{A}_R(k,k')$

Let us now define the spinor $\Psi(q) := (\psi(q), \psi^*(q))^T$ where $\psi(q)$ defines a single momentum component of $\boldsymbol{\psi}$ from (5.28). This definition allows us to write the GP equation in the form $i\partial_t\Psi(q) = \sum_{q'} R(q,q')\Psi(q')$ where the matrix R is defined as follows

$$R(q,q') = \begin{pmatrix} -\mu\delta(q-q') + \frac{q^2}{(2\pi)^2}\delta(q-q')\mathcal{I}_{\text{tot}}(q-q') + \mathcal{A}(q,q') & \nu_0(q,q') + \mathcal{A}(q,q') \\ -\nu_0(q,q') - \mathcal{A}(-q,-q') & -\left[-\mu\delta(q-q') + \frac{q^2}{(2\pi)^2}\delta(q-q')\mathcal{I}_{\text{tot}}(q-q') + \mathcal{A}(q,q')\right] \end{pmatrix}. \tag{5.36}$$

This equation now enables us to calculate the excitation spectrum of the considered system for any arbitrary intensity and BEC density distribution by calculating the eigenvalues of the matrix R.

5.9.1 Collective Spectrum in the Homogeneous Phase

If we now use the ansatz already presented in section 5.3 namely $\psi_0(x,t) = 1/\sqrt{L}$ and $E^{(0)}_{\text{L,R}} = C\exp(\pm ik_{\text{eff}}x)$ we can calculate the excitation spectrum below threshold. This ansatz implies $I_{\text{tot}}(x) = |E^{(0)}_R|^2 + |E^{(0)}_L|^2 = 2|C|^2$ and $n_0(x) = 1/L$ which results in

$$\mathcal{I}_{\text{tot}}(k) = -\frac{8|C|^2}{E_{\text{rec}}}\delta(k) \tag{5.37}$$

$$\nu_0(k) = \frac{g_c N}{E_{\text{rec}}L}\delta(k). \tag{5.38}$$

In addition the matrices Q and V amount to

$$Q(k) = (k_{\text{eff}}^2 - k^2)\delta(k) \tag{5.39}$$

$$V_{\text{L}}(k) = C\sqrt{L}\delta(k + k_{\text{eff}}), \tag{5.40}$$

resulting in

$$A_{\text{L,R}}(q, q') = -\frac{\zeta}{E_{\text{rec}}} \frac{|C|^2(2\pi)^2}{L} \frac{1}{q^2 \mp 2k_{\text{eff}}q} \delta(q - q'). \tag{5.41}$$

Note that in this special case $\tilde{A}_{\text{L,R}} = A_{\text{L,R}}$. If one now calculates the matrix R via (5.36) and solves $\det\left[R(q - q') - \omega\mathbb{1}\right] = 0$ one gets

$$\omega^2 - \frac{q^2}{(2\pi)^2}\left[\frac{q^2}{2m} + 2\frac{g_c N}{E_{\text{rec}} L} - \frac{8\zeta}{E_{\text{rec}}} \frac{|C|^2(2\pi)^2}{L} \frac{1}{q^2 - 4k_{\text{eff}}^2}\right] = 0. \tag{5.42}$$

Transforming this equation back into the original units leads to the excitation spectrum (5.8) presented in section 5.3.

5.9.2 Collective Spectrum Above Threshold

Let us now move on to the calculation of the collective excitation spectrum above threshold as it is presented in section 5.5. In this case an analytical answer like the one presented in the previous section is not possible, since the translation-invariance is broken so that the matrices describing the linear system are not diagonal in momentum space. Therefore, a numerical approach is required, involving in general the discretization of the position(momentum) continuum.

The matrices defined in Eqns. (5.29)–(5.35) can be calculated by numerically finding the fourier transforms of the stationary states found via complex time evolution in section 5.4. The resulting total matrix R can then be diagonalized numerically.

A further difficulty arising in our setup is that in the stationary crystalline solution, the total light intensity and atom density are periodi, whereas the intensity of each polarization component is not. This originates from the repeated reflection from the density grating, introducing the decaying evelope shown in Fig.(5b) of the main text. This prevents the use of the quasi-momentum to label the excitation modes. Therefore we use the momentum corresponding to the largest component of the eigenvector in order to order the eigenvalues in Fig. 5.6.

5.10 Appendix: Numerical Methods

The model described in section 5.2 constitutes a scoupled system of equations[Eqs. (5.1) and (5.3)]. In this appendix we will shortly discuss the numerical methods we used to simulate the time evolution of the studied system as it is used in sections 5.4–5.7.

The algorithm consists of two parts. First we need to solve the Helmholtz equation (5.3) for a given space dependent susceptibility (5.4). This corresponds to a initial value problem with the boundary conditions

$$E(x = -L/2) = A_L + B_L, \tag{5.43}$$

$$\partial_x E(x = -L/2) = ik_0(A_L - BL). \tag{5.44}$$

Here A_L and B_L define the incoming (A_L) and outgoing (B_L) field amplitudes at the left side of the BEC. They are related to the amplitudes on the right side via

$$B_L = RA_L + TD_R \tag{5.45}$$

$$C_R = TA_L + RD_R \tag{5.46}$$

with the system's reflection and transmission coefficients R and T. Of course, these reflection and transmission coefficients depend on the system's susceptibility. They can easily be estimated by solving the HH equation for an arbitrary initial condition (5.43) and (5.44), leading to well defined fields at the boundaries allowing for an estimation of the right hand amplitudes C_R and D_R. Hence, R and T can be calculated via (5.45) and (5.46). As soon as we know the initial conditions we can find the solution of the Helmholtz equation via spatial integration performed by a fourth order Runge-Kutta solver.

The solution of the HH equation is then used to calculate the optical potential (5.5). The time evolution of the GP equation with the newly found potential is then calculated by using a split step method. Note that the HH equation has to be solved within each time step resulting in a modified potential for the next time step in the GP equation. The time evolution is finished as soon as the system is found in a stationary state.

6 Publication

New Journal of Physics **19**, 125002 (2017)

Probing and Characterizing the Growth of a Crystal of Ultracold Bosons and Light[†]

S. Ostermann[1], F. Piazza[2] and H.Ritsch[1]

[1]*Institut für Theoretische Physik, Universität Innsbruck,*
Technikerstraße 21, A-6020 Innsbruck, Austria
[2]*Max-Planck Institute for the Physics of Complex Systems, Nöthnitzer Straße 38,*
D-01187 Dresden, Germany

The non-linear coupled particle light dynamics of an ultracold gas in the field of two independent counter-propagating laser beams can lead to the dynamical formation of a self-ordered lattice structure as presented in (2016) *Phys. Rev. X* **6** 021026. Here we present new numerical studies on experimentally observable signatures to monitor the growth and properties of such a crystal in real time. While, at least theoretically, optimal non-destructive observation of the growth dynamics and the hallmarks of the crystalline phase can be performed by analyzing the scattered light, monitoring the evolution of the particle's momentum distribution via time-of-flight probing is an experimentally more accessible choice. In this work we show that both approaches allow to unambiguously distinguish the crystal from independent collective scattering as it occurs in matter wave super-radiance. As a clear crystallization signature we identify spatial locking between the two emerging standing laser waves, together creating the crystal potential. For sufficiently large systems, the system allows reversible adiabatic ramping into the crystalline phase as an alternative to a quench across the phase transition and growth from fluctuations.

doi: 10.1088/1367-2630/aa91c3

[†] The author of the present thesis performed all the calculations and numerical simulations in this publication. For all other aspects of this work F. Piazza acted as a discussion partner.

6.1 Introduction

A dilute cold atomic gas illuminated by a laser far off any optical resonance experiences an optical potential with the particles drawn to high or low intensity regions depending on the sign of their linear polarizability. The induced forces on the particles are accompanied by a forward scattering phase shift of the laser beams as well as coherent Rayleigh scattering of light. In the ultracold regime of a BEC, atoms and photons are completely delocalized and the interaction is a collective process from the photon as well as from the atom point of view [6.1–6.3]. It turns out that for a cold and large enough sample of atoms the coupled effective mean field equations for the bosonic atoms and the light are well suited to correctly capture the essence of this complex collective non-linear dynamics [6.4, 6.5]. In particular the Gross-Pitaevski (GP) equation for the atomic quantum gas and the Helmholtz equation for the photons can be used to efficiently describe the coupled nonlinear time evolution in the system. Within this approximation the atoms simply form a dynamic refractive index for the light proportional to their density, while the light creates a dynamic optical potential proportional to the local light intensity guiding the particles. Note that these mean field descriptions of atoms and fields automatically account for collective enhancement of coherent atomic scattering (Bose enhancement), which has been studied in depth in a series of experiments and theoretical models for of single laser excitation from one side. The same is true for stimulated light scattering. As has been known for quite a while now, even for single side illumination by strong enough laser light the system has an instability leading to growing density fluctuations, acceleration and heating [6.3, 6.6–6.9].

In a recent work [6.4] we studied a refined setup using a new symmetric and translation invariant geometry of an elongated large cloud of atoms in the field of two counter-propagating independent lasers. To prevent the a priori appearance of an optical lattice, we assume that the two lasers have either orthogonal polarization or sufficiently different frequency to prevent interference and coherent light scattering between the two injected fields. Interestingly, we found that despite the fact that a priori no laser intensity or atomic density modulation is present, above a certain pump intensity threshold, the system spontaneously enters an ordered crystalline phase. In this limit the particles form a periodic density grating and the two laser fields develop into two standing waves, which are coupled and synchronized by the atoms. This can be viewed as crystallization of the particles from homogeneous to periodic order together with the light field. Obviously in this phase transition the system has to choose an effective wave vector and break its continuous translational symmetry. Due to the fact that no mode selective boundaries are present, a continuum of field modes have to be taken into account allowing for the emerging wave-vector, which governs the spatial modulation of the light intensities and the properties of collective excitations in the form of phonon wave packets propagating through the crystal. This distinguishes this crystallization from related cavity based effects as collective atomic recoil lasing [6.8, 6.10–6.13] or transverse self-structuring by a reflecting mirror where the Talbot length determines the ordering length scale [6.14].

The focus of [6.4] was to present the basic physical mechanisms leading to this type of crystallization instability. However, many important questions concerning the experimental observability of the crystal phase and the connection to matter wave super-radiance were missing in [6.4]. This questions are addressed in the following. Therefore, we present new results to study the onset of crystallization and the characteristics of the buildup of the crystal. We perform detailed simulations and modify our model to contain relevant features for present experimental setups. Thereby we work out common and distinct features to conventional matter wave super-radiance [6.6]. One particular goal is of course to identify and study clearly distinguishing experimental signatures of crystal formation. Such signatures can be found from direct time dependent measurements of the scattered or transmitted light on the one hand or by analyzing the particle's momentum distribution via time of flight studies on the other hand. A extented characterization of properties of the crystalline phase is another central aim of this work. From a practical point of view it seems that many of those features are not so easy to observe as current experiments are limited in particle number. While in principle for any particle number an instability and ordering threshold exists, the necessary power to reach the ordering instability at sufficiently large detuning is very high and simultaneously leads to heating and fast particle loss. This strongly limits the observation time and accuracy of the scattered field measurements. In order get some estimates of these perturbations we phenomenologically introduce particle loss in our model equation [6.4] so that its effect on the real time dynamics can be predicted.

In particular, during the initial time evolution of the system, where only weak light back scattering occurs, the fields act rather independently and the predicted signals and atomic momentum distributions are very similar to matter wave superradiance [6.2, 6.5, 6.6]. One possible signature includes a careful analysis of the instability threshold of a homogeneous density for single side versus symmetric pumping. In this respect, we perform very detailed studies of the the short time dynamics, varying the pump geometry from symmetric pumping for ideal crystallization via asymmetric pumping towards the single side pump case as the standard configuration where matter wave super-radiance is usually observed. Such detailed predictions should be valuable to distinguish the processes even at current experimental limitations. Indeed the onset of the predicted crystal phase could be observed in a recent experiment which implements the proposed geometry [6.15].

As the atom-field crystal corresponds to an at least metastable ground state of the system one aim is certainly to prepare it as good as possible. Since a sudden quench leaves much entropy in the final crystal, an alternative approach is the controlled adiabatic ramp into the crystalline phase. Varying the switch time from a sudden quench across threshold to slow almost adiabatic ramp, we can address the created entropy via the reversibility of the ordering dynamics. Of course, a very slow ramp increases the effect of background heating which again increases the final entropy in the crystal. In fact, the best way to reach a clean crystal would be using a time dependent laser field found by optimal control algorithms [6.16, 6.17]. This is certainly interesting but goes beyond the scope of this work.

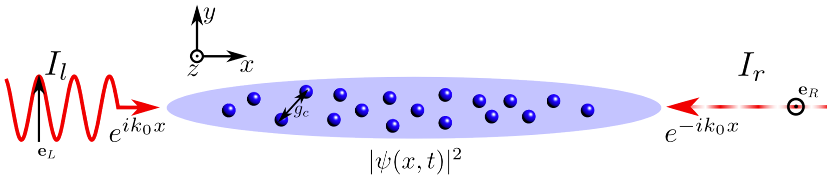

Figure 6.1: Schematic view of the setup. An elongated BEC interacts with two counterpropagating plane waves of orthogonal polarization. The beams are assumed to be far off-resonant from the atomic transition to avoid polarization mixing.

6.2 Model

As a basis of our analysis we use the effective mean field model introduced in our previous work in [6.4]. Here we will only briefly describe its main properties to give a self contained basis for our following detailed studies. For the detailed description and derivation we refer to section two in [6.4].

An extended atomic BEC interacting with two off-resonant and counter-propagating independent electromagnetic plane waves injected from two opposite sides (see figure 6.1) is studied. The two electromagnetic fields Stark shift the atomic ground state and create an optical potential for the BEC atoms, which in turn modify the field propagation as they constitute an effective density dependent index of refraction. The dynamics of this setup can be efficiently described by a coupled system of mean field equations. The BEC dynamics is well approximated by the Gross-Pitaevski (GP) meanfield regime, where the condensate wavefunction $\psi(x,t)$ satisfies the equation:

$$i\hbar\frac{\partial}{\partial t}\psi(x,t) = \left[\frac{-\hbar^2}{2m}\frac{\partial^2}{\partial x^2} + V_{\mathrm{opt}}(x)\right]\psi(x,t) + \frac{g_c N}{A}|\psi(x,t)|^2\psi(x,t). \tag{6.1}$$

Here m denotes the particle mass, g_c is the effective atom-atom interaction strength, N denotes the atom number, A is the transversal BEC cross section and $V_{\mathrm{opt}}(x)$ stands for the optical potential generated by the electromagnetic fields. The treatment of the dynamics is restricted to one dimension, i.e. we assume the dynamics in the y and z directions is frozen due to the transverse confinement of the BEC by an external trapping potential. Actually the Gaussian pump laser beams could in principle provide such a potential, but we refrain from this complication in our model and assume laser beams much broader than the BEC. Such an one dimensional treatment is only valid if the BEC's chemical potential μ is much smaller than the characteristic trap frequency $\mu << \hbar\omega_{y,z}$.

Within this limit the optical potential, which determines the BEC dynamics in the x direction can be written as

$$V_{\mathrm{opt}}(x) = -\alpha\left[|E_L(x)|^2 + |E_R(x)|^2\right] + V_{ext} \tag{6.2}$$

where α denotes the atomic polarizability. The first term corresponds to an optical dipole potential in the low-saturation regime where $E_{L,R}(x)$ are the two field envelopes of the electromagnetic fields $\mathbf{E}_{L,R}(x,t) = \left[E_{L,R}(x)e^{i\omega_L t} + c.c.\right]\mathbf{e}_{L,R}$ (with $\mathbf{e}_L \cdot \mathbf{e}_R = 0$) which satisfy the Helmholtz equations

$$\frac{\partial^2}{\partial x^2}E_{\mathrm{L,R}}(x) + k_0^2(1+\chi(x))E_{\mathrm{L,R}}(x) = 0 \tag{6.3}$$

with the wavenumber k_0 of the incoming beams and the BEC's susceptibility $\chi(x)$. The susceptibility depends again on the condensate's density via

$$\chi(x) = \frac{\alpha N}{\epsilon_0 A}|\psi(x)|^2, \tag{6.4}$$

where $\psi(x,t)$ is the solution of equation (6.1) and ε_0 denotes the free space permittivity. V_{ext} is an externally prescribed potential chosen as a square box potential for computational convenience.

Again, the constant α in equations (6.3) and (6.4) denotes the absolute value of the real part of the atomic polarizability. Hence, the absolute minus sign in equation (6.3) indicates (far off-resonant) red-detuning from any atomic transition, i. e. high field seeking atoms. In addition, this impies that the potential depth is proportional to $|\Gamma/\delta|$ where Γ is the spontaneous decay rate and δ the detuning relative to the internal atomic transition. As a result, the potential depth scales with $|\delta|^{-1}$. In the following we will use the dimensionless quantity

$$\zeta := \frac{\alpha N}{\varepsilon_0 \lambda_0 A} = \frac{\alpha}{\varepsilon_0} n \frac{L}{\lambda_0} \tag{6.5}$$

to quantify the light matter interaction where λ_0 is the wavelength of the incoming laser beams and the three-dimensional density n of the homogeneous BEC which is supposed to have length L in the x direction.

The system described by the set of equations (6.1)–(6.4) is, apart from V_{ext}, a priori translation invariant. If one simulates the dynamics described by this set of equations in a self-consistent manner, i. e. updating the electric field distribution for the corresponding BEC density within each timestep of the GPE solution, one finds the following remarkable behaviour. As long as the BEC density is homogeneous the light fields propagate through the sample without any spatial modulation. However, we have shown that when the pump light intensity exceeds a certain critical value, the light spontaneously crystallizes together with the atoms by breaking the translation invariance. For a detailed description of the numerical methods used in this context we refer to Appendix B of [6.4].

6.3 Real-Time Observation of Spontaneous Crystallization via the Back-Scattered Light Fields

When the driving intensity exceeds a certain critical value, small fluctuations will grow and break the translation invariance. Performing a linear stability analysis of equations (6.1)–(6.4) as it is presented in [6.4] leads to a critical intensity value (in the limit $L \to \infty$ and $N = \text{const.}$) which depends inversely on the particle number in the form:

$$I_c^{\mathrm{L,R}} = \frac{cE_{rec}}{\lambda_0 A} N \frac{1}{\zeta^2} = cE_{rec} \frac{\varepsilon_0^2}{\alpha^2} \frac{1}{n} \frac{\lambda_0}{L}. \tag{6.6}$$

Here we introduced the recoil energy $E_{\mathrm{rec}} := \hbar^2 k_0^2/(2m)$. In the following we will use the quantity $I_0 := cE_{rec}/(\lambda_0 A)$ as the natural unit for intensities.

We see that threshold (6.6) scales with the inverse square of the atomic polarizability $\alpha^{-2} \propto \delta^2$ and hence grows approximately with the square of the laser detuning from resonance. Qualitatively this behavior can be traced back to the non-linear nature of the interactions of the considered system. Initially, for the homogeneous system, the backscattered field amplitude is proportional to α. This coherently backscattered field interferes with the incoming laser leading to an initial potential modulation proportional to α, which then translates into an α^2 term originating from the non-linearity of the refractive index term in the Helmholtz equation. Note that also the heating via spontaneous scattering exhibits the same detuning scaling the essential route to small heating at threshold is a large particle number.

For intensities above threshold a periodic modulation of the optical potential for the atoms is formed spontaneously and the atoms crystallize into a periodic structure together with the light fields. Since we consider the full electromagnetic field in our model (see equation (6.3)) all possible modes can be addressed in general. Therefore, the lattice spacing is emergent and the the new solutions of (6.3) are plane waves of the form $E_{\mathrm{L,R}} = C \exp(\pm i k_{\mathrm{eff}} x)$ propagating with a modified wavenumber

$$k_{\mathrm{eff}} = \frac{2\pi}{\lambda_0} \sqrt{1 + \frac{\alpha}{\epsilon_0} n} \tag{6.7}$$

which is a result of the modified BEC density n. Examplary solutions for the system's ground state of the coupled set of equations (6.1)–(6.4) for the density and the fields are shown in figure 6.2. A box potential is included in the GPE equation in order to simulate the system boundaries. Obviously, the density stays homogeneous (up to small modulations which are finite size effects) for intensities below threshold and so does the intensity distribution (see figure 6.2(a) and (b)). Above threshold the continuous translational symmetry is broken and a periodic optical potential is generated for the atoms. This spontaneous crystallization relies on the fact that a counter propagating field component with the same polarization is generated from the BEC which acts as a Bragg mirror for the fields. In the limit of deep local traps the behavior resembles very closely the case of an array of mobile beam splitters which can be used as toy model to understand optical lattice dynamics as shown in fig.5 of ref. [6.18]. Hence, we expect the complete system's reflectivity to grow drastically as soon as the intensity of the incoming light fields lies above the threshold value. Indeed, both the absolute value and the phase of the reflection and transmission coefficient show this expected behavior (see figure 6.3). The change of the phase of the transmission spectrum at threshold also implies that the threshold could also be measured by phase-contrast imaging of the BEC [6.1, 6.19]. This process leads to the fact that the field amplitudes outside

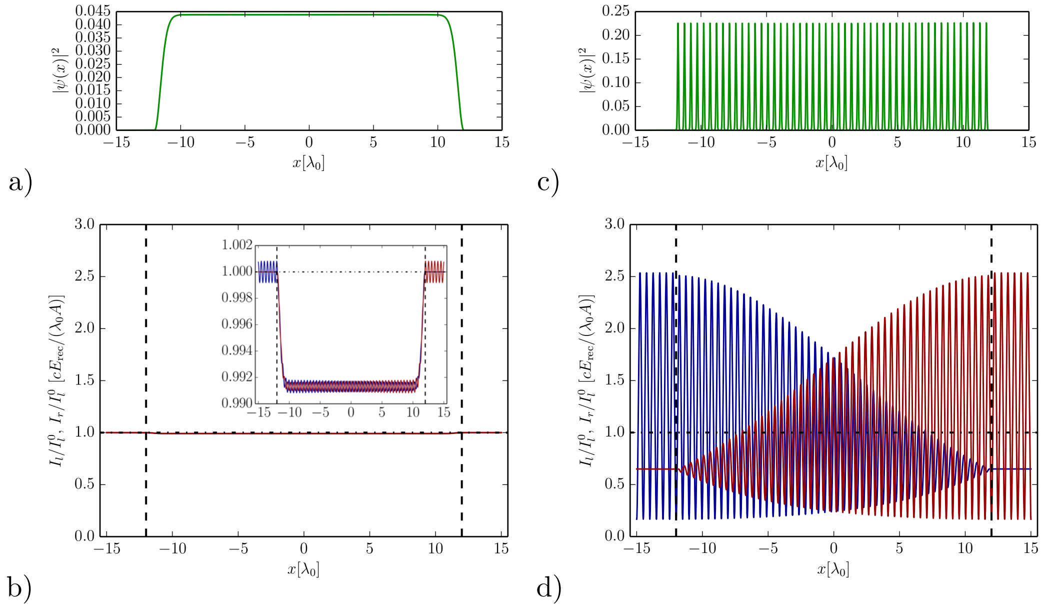

Figure 6.2: Steady state atomic density and light intensity as function of position along the axis for effective coupling strength $\zeta = 0.2$ and a calculation box length of $L = 30\lambda_0$ which is significantly larger than the external deep trapping potential wells starting at $x = -12\lambda_0$ and ending at $x = 12\lambda_0$. The intensity threshold for this regime lies at $I_c^L = I_c^R = 12.5 I_0$ (see also figure 6.3). (a) The particle density, and (b) the light intensity below threshold for an incoming light intensity $I_{l,r}^0 = 10 I_0$. The y-axis is rescaled with respect to this incoming light intensity. The inlay zooms to values close to $I_l/I_l^0 = I_r/I_r^0 = 1.0$ showing that only a small part of the light is reflected. (c) and (d) show the same densities for $I_{l,r}^0 = 200 I_0$, i. e. far above threshold where about half of the incoming intensity is back reflected by the self formed lattice.

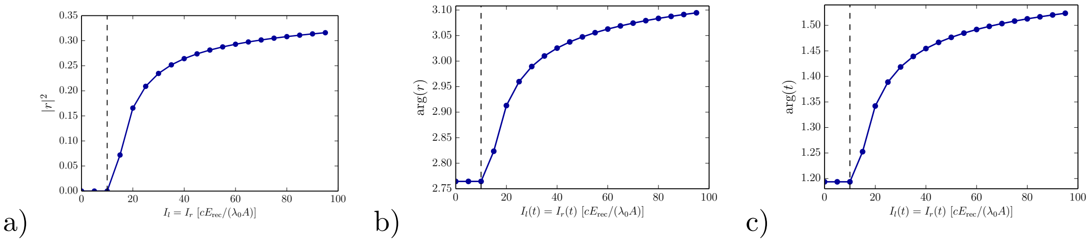

Figure 6.3: Dependence of the total reflection coefficient r on the pump intensity: (a) shows the absolute value squared, (b) the phase of the reflection coefficient (c) the phase of the transmission coefficient for $L = 100\lambda_0$ and all other parameters are chosen as in figure 6.2).

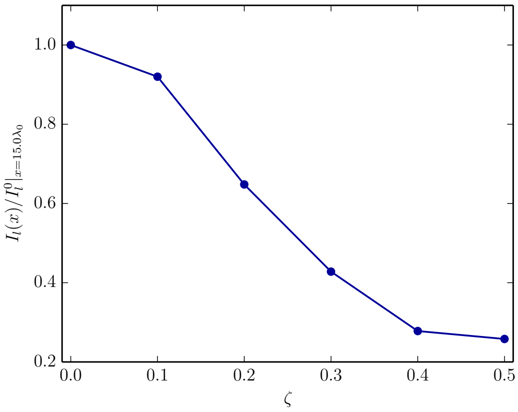

Figure 6.4: Relative fraction of the intensity transmitted through the whole atomic crystal as shown in figure 6.2(d) for different values of the effective coupling parameter ζ with all other parameters are chosen as in figure 6.2(d).

the system boundaries lie far below the initial incoming laser intensity in figure 6.2(d). In this case it is of specific interest if there is a certain upper boundary value for the index of refraction. In figure 6.4 we plot the value of the constant intensity part outside the BEC for different light interaction strengths ζ. Obviously, this value decreases drastically with increasing ζ. However, due to the interaction of the two light fields via the BEC atoms the intensity pattern always adjusts in a way that the envelope of the total intensity is not modulated at all. This "phase-locking" of the intensity patterns will be studied in more detail below.

The system's properties described above lead to the fact that the phase transition from a homogeneous BEC to a spontaneously formed crystal can be non-destructively observed by measuring the light reflected from the atomic cloud. In fact, the whole time-dynamics of the system can be mapped out by measuring these properties of the light fields.

Let us now turn to a closer analysis of the light intensity distributions. If one zooms into the region around zero in figure 6.2(d) one finds that the intensity distributions of the field coming from the right side and the field coming from left are not in phase (see figure 6.5(a)). This feature of the solution of the Helmholtz equation (6.3) is a fundamental feature of the crystal phase. The fact that the maxima of the single light fields do not coincide leads to a strong coupling of the atoms to the fields due to the large intensity gradient which is felt from each individual light field. This is a fundamental difference to for example standard optical lattices. Interestingly, the dynamics of the full system again leads to a potential which in total results in an overall homogeneous density modulation. The question one can address in this context is the intensity dependence of the dephasing $\Delta\phi$ as it is defined in figure 6.5(a). As one can see from figure 6.5(b), this dephasing is getting smaller for growing intensities until it reaches a certain constant value.

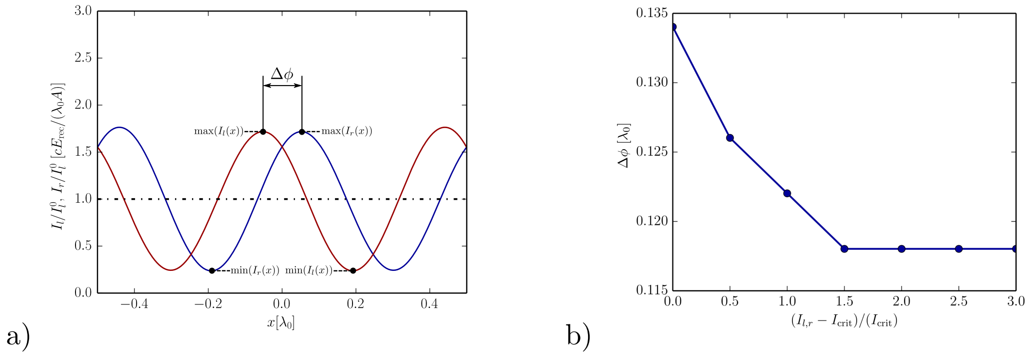

Figure 6.5: (a) Enlarged view of the central part of intensity distribution of the two fields as shown in figure 6.2(d) exhibiting a relative shift of the intensity maxima (phase shift) of the left and right injected field . (b) This phase shift for the stationary ground state for different incoming laser intensities.

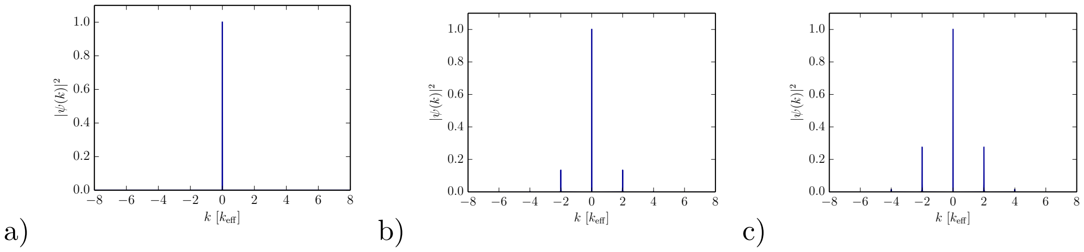

Figure 6.6: Momentum distribution (Bragg diffraction pattern) for the system ground state obtained via for imaginary time evolution for different pump intensities. (a) $I = 10I_0$, (b) $I = 100I_0$ and (c) $I = 200I_0$. The chosen system parameters are: $\zeta = 0.1$, $L = 100\lambda_0$, $g_c N = 1.0 E_{rec}$ with the height of the $k = 0$ peak normalized to 1.

6.4 Time Evolution of Atomic Momenta from Bragg Diffraction

Even though the non-destructive measurement of the properties of the coupled BEC-light crystal via the reflected light fields is a special feature of the studied system, it is of specific interest how the crystallization process and its properties can be observed with a standard experimental technique like TOF measurement. It consists in releasing the external trapping potential and letting the BEC expand ballistically. After a certain time of flight (typically a few ms) a laser pulse is imposed from the side and the absorption image generated by the BEC is then captured on a CCD camera. If the far-field regime is reached for long enough time evolution, the absorption image corresponds to the BEC momentum distribution. Therefore, the corresponding TOF measurement outcome for a specific solution of equations (6.1)–(6.3) can be easily obtained by calculating the Fourier transform of the BEC wave function. In figure 6.6 a typical example of such a

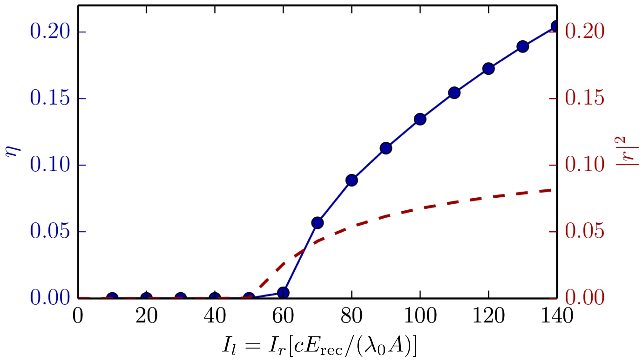

Figure 6.7: Intensity dependence of the ratio η of the height of the central peak and versus the $2k_{\mathrm{eff}}$ peak (solid blue, left axis). One recognizes good agreement of the growth point of this ratio with the threshold estimation via the reflected light (dashed red, right axis). The parameters are the same as in figure 6.6.

momentum space distribution at different intensities of the crystallization procedure is shown.

Of course, the homogeneous BEC contains only the $\hbar k = 0$ momentum component (see figure 6.6(a). However, for intensities above threshold the $\pm 2\hbar k$ and higher momentum components are getting populated (see figure 6.6(b)–(c). This is a clear indication for an emerging periodic structure. If it is possible to verify that no interference is possible between the two counterpropagating light fields this measure can be used as a clear indication for an emerging crystal. As a matter of fact, the $\pm 2\hbar k_{\mathrm{eff}}$ peak dominates among the higher momentum peaks which are present but small.This happens even at strong intensities, indicating that the emerging modulation is mostly sinusoidal.

Another important observation is that the height of the $2\hbar k_{\mathrm{eff}}$ peak relative to the central peak behaves as the system's reflectivity. This means that the value of the ratio

$$\eta = \frac{|\psi(k = 2k_{\mathrm{eff}})|^2}{|\psi(k = 0)|^2} \tag{6.8}$$

where $\psi(k) = \frac{1}{L} \int dx e^{ikx} \psi(x)$ is the Fourier transform of the BEC wavefunction can be used to measure the crystallization threshold (6.6). In this case the TOF measurement has to be performed for several different pump intensities and the ratio η has to be estimated for each measurement. The resulting threshold estimation is in good agreement with the one via the system's reflectivity $|r|^2$ (see figure 6.7). As a result, the parameter η is an easy to access quantity to measure the physical properties of the system directly via the TOF image.

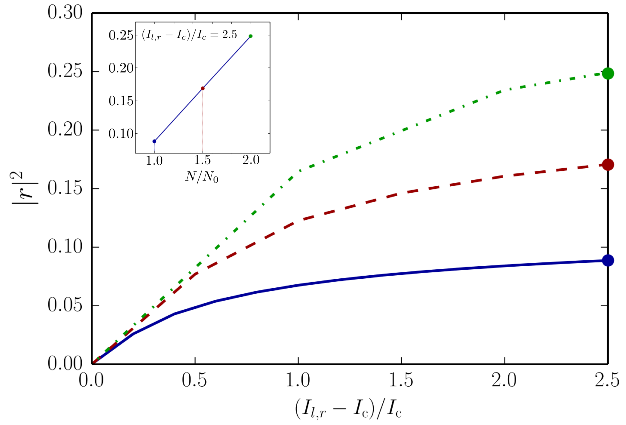

Figure 6.8: Particle number scaling of the reflection coefficient. The particle number of the dashed red curve is a factor of 1.5 larger and the one for the dash dotted green curve is a factor 2.0 bigger than the one of the solid blue curve. Note that the axes have been rescaled by the corresponding critical intensities. ($\zeta = 0.1$, $L = 100\lambda_0$, $g_c N = 1.0 E_{rec}$). The inset shows the linear dependence of the reflectivity on the particle number.

6.5 Scaling of the Collective Dynamics

One centrally important feature of the crystallization process is its collective nature. Since all atoms in the BEC interact synchronously via the scattered light field we expect a strong particle number dependence of the crystallization process. In particular the more particles the less the threshold power and saturation of the atomic transition. The collective nature of the scattering remains also in the ordered phase above threshold, which can be directly verified from the reflectivity for different particle numbers N. Indeed, the total system's reflectivity above threshold increases with the particle number (see figure 6.8) until a saturated value is reached where most of the light is reflected. It is an interesting question here, what one could expect in the thermodynamic infinite particle number limit. Is there an instability when all the light from one side is reflected and the system acts as a perfect mirror. What is the dynamics of the transition region here. For a transversely pumped case we previously found a fractioning of the system [6.20] . Unfortunately the required system sizes are too big for a straightforward analysis here.

For current realistic experimental setups the particle number is limited to well below 10^6 so that the ordering threshold occurs at rather high saturation parameters. To better understand what is going on in this case particle loss has to be included into the model. This allows how long the coherent collective growth of the reflection signal persists against the reduction of reflection due to particle particle loss. In any case only a transient signal can be expected. Since a full treatment of particle loss via the spontaneous emission heating rates would be very demanding, we simple introduce a

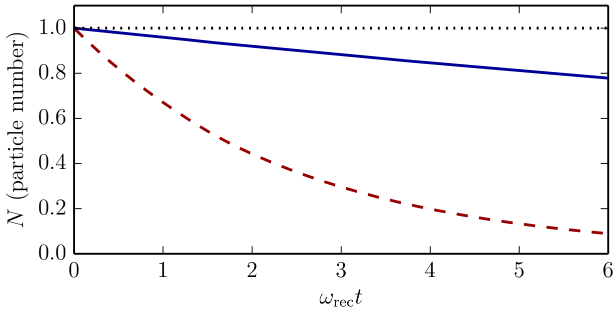

Figure 6.9: Time evolution of the particle number for different choices of the intensity dependent particle loss rate γ as defined in (6.9). $\gamma = 0.001$ (solid blue), $\gamma = 0.01$ (dashed red). The dotted black line corresponds to $\gamma = 0$. Other parameters: $I_l = I_r = 100 I_0$, $L = 10\lambda_0$, $g_c N = 1.0 E_{rec}$ and $\zeta = 0.1$.

phenomenological toy loss mechanisms to study the effect.

For this purpose, we include a loss term to the GP equation that in this case takes the form

$$i\partial_t\psi = H_0\psi + \frac{g_c N}{A}|\psi|^2\psi - i\gamma\left(|E_L(x)|^2 + |E_R(x)|^2\right)\psi \tag{6.9}$$

where γ is a phenomenological parameter corresponding to the particle loss rate. In figure 6.9 the effect of different choices of γ on the total particle number is shown. Note that the introduced type of loss term takes into account that more particles are lost at higher field intensities than at lower ones. This is due to the fact that in this regions the spontaneous decay rate leading to recoil momenta which kick the particles out of the condensate is larger.

Simulating the real time dynamics of (6.9) and looking at the dynamics of the system's reflectivity shows a clear damping of the dynamics in time. However, the crystallization still takes place as one can see on the exponential growth of $|r|^2$ at short times in figure 6.10.

Finally, the particle number dependence of the index of refraction is an interesting property as well. For this purpose we fix the loss parameter γ and calculate the time evolution of the index of refraction. From the green dash dotted line in figure 6.10 one can see that the dynamics is getting faster for higher particle numbers which is another indication for the collectivity of the effect mentioned above. In addition, it should be mentioned that the particle number dependence of the effect can already be observed in the short time regime without waiting for the crystal to fully form and stabilize. Similar curves as the ones presented in figure 6.10 have also been observed experimentally in a first implementation of the phase transition [6.15].

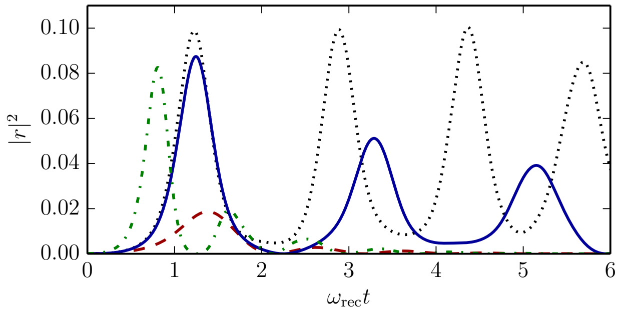

Figure 6.10: Real-time dynamics of the reflection probability for different particle loss rates and particle numbers. $\gamma = 0.0$ (dotted black), $\gamma = 0.001$ (solid blue) and $\gamma = 0.01$ (dashed red). The dash dotted green curve shows the dynamics for a BEC with a particle number which is a factor 1.5 bigger than for the other curves and $\gamma = 0.01$. All other parameters are as in figure 6.9.

6.6 Crystal Formation via a Slow Ramp Across the Phase Transition

A routine path to study quantum phase transitions in ultracold gas experiments is an adiabatic ramping of the parameters (fields) between two points in the phase diagram [6.21]. If enough time is given this process is quasi-adiabatic and reversible. As due to losses time was limited in our setup, we introduced a sudden switch of the laser and the resulting quench dynamics of the crystallization process has been studied in detail in [6.4]. In a quench a lot of interesting physics is going on at the same time, from density fluctuations to phonon excitations of the atom-light crystal. Nevertheless, the process introduces entropy and does not lead to the systems ground state.

As an alternative it is thus of specific interest, under which conditions the system's stationary ground state can be reached by performing a sufficiently slow adiabatic passage. For this, one has to ensure that no higher motional states are excited when crossing the threshold, which implies sufficiently large ramping times for the system to remain in its ground state during the whole crystallization procedure. Actually as some of our excitations are gapped due to the long range interactions this might be less critical than expected. To determine suitable ramping times the real time evolution for simple linear intensity ramps is numerically evaluated. Please note that no damping is taken into account in this case. The corresponding results are presented in figure 6.11. Most likely better ramping functions exist and one could even think of optimal control to improve the results.

The reflection coefficients again give valuable real time information on the dynamics and one sees how different ramping times affect the dynamics. We see that for ramping times more than twenty times the inverse recoil frequency only little noise is left and

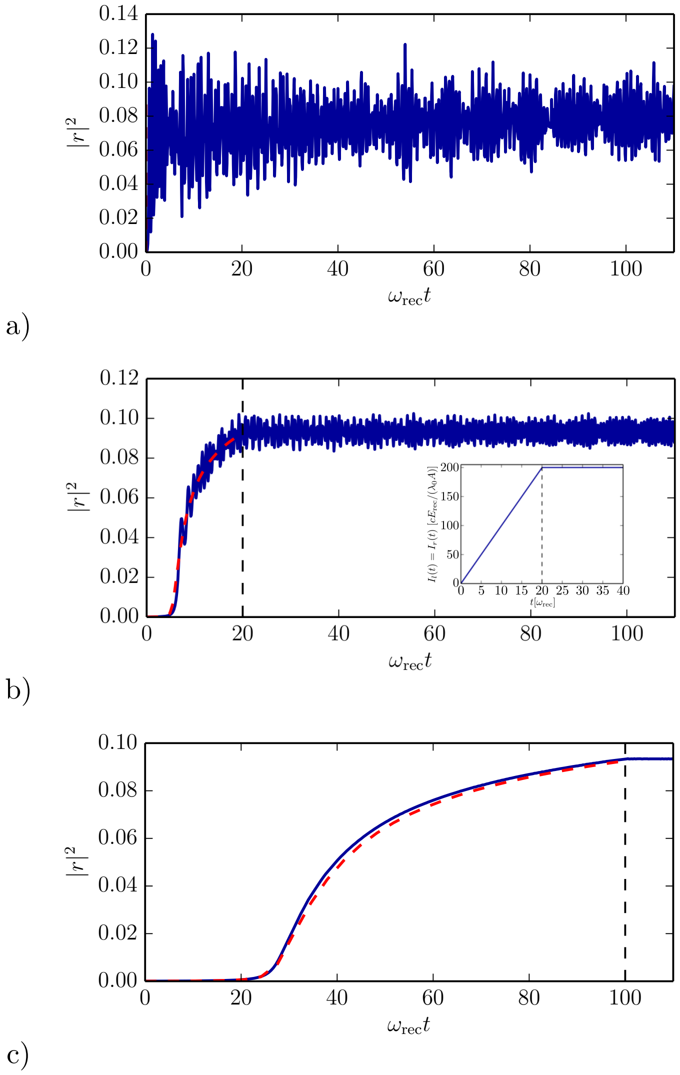

Figure 6.11: Time dependence of total reflection $|r|^2$ for different ramping times (a) $t_{\text{ramp}} = 0$, (b) $t_{\text{ramp}} = 20$ (The inset figure shows an exemplary ramping function), (c) $t_{\text{ramp}} = 100$. The blue curve shows the dynamics for real time evolution and the red dashed line the corresponding imaginary time evolution. The vertical dashed black line indicates the ramping time. $I_l = I_r = 200 I_0$, $\zeta = 0.1$, $L = 10\lambda_0$, $g_c N = 1.0 E_{rec}$.

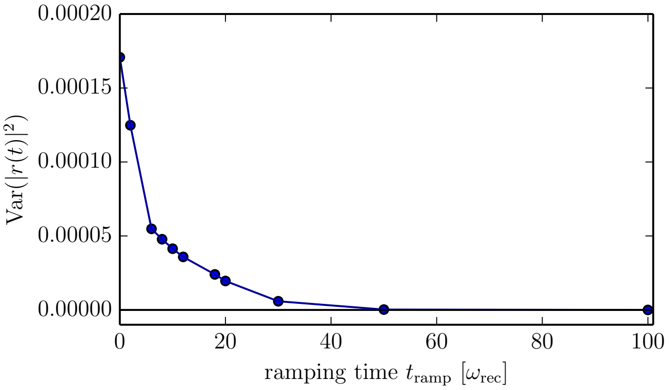

Figure 6.12: Time averaged variance of the time dependent reflection probability for a real-time evolution simulation in the stationary lattice regime during last 50 time steps for different ramping times as a quantitative measure of adiabaticity. The parameters are the same as in figure 6.11

an almost perfect adiabatic passage can be realized (see figure 6.11). To quantify the quality of the adiabaticity and the number of phonon like excitations left, we calculate the variance of the reflectivity around it's mean value for the last 50 time steps and plot it as a function of the ramping time. This variance tends to be close to zero for ramping times $t_{\text{ramp}} > 60\ \omega_{\text{rec}}$ (see figure 6.12.)

Another measure of the introduced heating and entropy through the ramp can be derived from the reversibility of the ramping process without any cooling invoked. For this purpose, one has to look at a ramp realizing a transition from homogeneous order to crystalline order and back (see figure 6.13(a)). For an ideal ramping procedure one should end back in a perfect BEC in the end. In figure 6.13(b) the space-time density plot for $|\psi(x,t)|^2$ is shown. The BEC performs the transition from homogeneous to periodic order as expected. After ramping down the laser intensity again one can recognize that the BEC is not perfectly homogeneous but some density and phase fluctuations are left. This could come as simple fluctuations or even lead to formation of vortex pairs [6.22]. Nevertheless, the periodic order is completely lost and only some higher excitations remain. It can be claimed that for increasing ramping times this higher excitations will get smaller and smaller. To quantify the energy remaining in the system we calculate at the dynamics of the kinetic energy

$$E_{\text{kin}} = \frac{1}{2m} \int dx \hbar^2 |\partial_x \psi|^2. \tag{6.10}$$

The result is shown in figure 6.14. Of course, the kinetic energy initially follows the ramping procedure. The important question is how small it is in presence of higher excitations after the ramping process. Figure 6.14 shows that for $t > 100\omega_{\text{rec}}$ the kinetic energy is very small (but not zero). This implies that the heating imposed by the ramping process is small and that despite the small excitations the BEC can be restored.

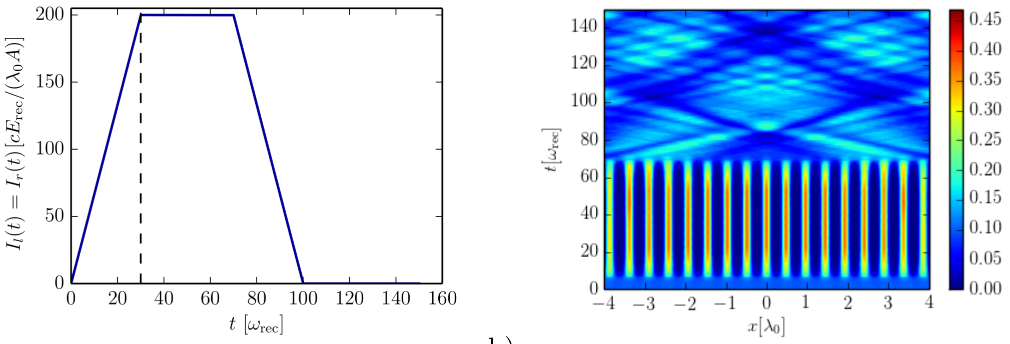

a) b)

Figure 6.13: (a) Ramping function used for quasi adiabatic transfer to the crystalline phase and back (b) Real time evolution of the particle density during a ramp with the same parameters as in figure 6.11).

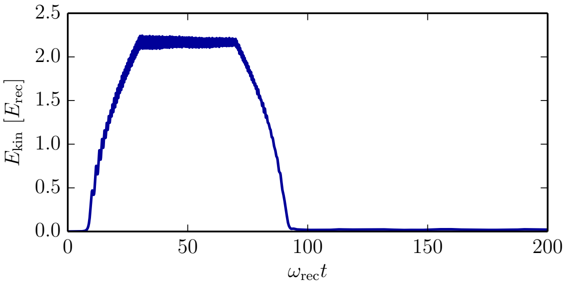

Figure 6.14: Time evolution of the system's kinetic energy during the ramping procedure shown in figure 6.13(a).

This is very similar to the physics observed in the superfluid to Mott insulator transition in a BEC. In summary, it can be posed that the spontaneous crystallization process can be reversed if the ramping times are sufficiently large.

6.7 Crystallization Versus Matter-Wave Superradiance

Laser induced instabilities of Bose-Einstein condensates have been found and studied for more than a decades now, starting with seminal experiments at MIT [6.2]. Already soon after the early experiments with BECs it became obvious that not only the Bose enhancement from the BEC but also stimulated light emission interpreted as self-stimulated Kapitza-Dirac scattering, was a key mechanism behind these observations [6.3, 6.6]. In these experiments, the BEC was driven from a single direction and above a certain pump threshold an instability towards a density modulation was found, which in turn enhanced the light scattering in analogy to collective atomic recoil lasing CARL [6.3]. This effect is known as Superradiant Rayleigh scattering (SRS). As single side pumping breaks mirror symmetry and momentum is injected only from one side, obviously no stable final state could exist. Using cavity enhancement allows better control of these scattering processes [6.13] and one can even use them for cooling [6.23]. This directly connects to cavity based selfordering phenomena for standing wave pumping [6.24].

In our configuration of symmetric counter-propagating pumping along the longitudinal BEC direction, mirror and translational symmetry is kept, but the fundamental microscopic light matter interaction parameters are rather similar. It is therefore natural to ask what is the relation between spontaneous crystallization, matterwave superradiance and collective atomic recoil lasing. In particular the initial phase of the self-ordering process, where all fields act independently should bear some similarities.

Apart from the obvious fact that a one-sided setup cannot lead to a steady-state, there seem to be deeper differences between the two phenomena. In fact, spontaneous crystallization can be understood using only optical potentials and dipole forces. Apart from creating initial fluctuations no spontaneous scattering is needed. Both, the light field and the atoms are dynamic mean fields, which exchange energy and momentum in the dispersive regime. Indeed, even though the crystallization threshold (6.6) is proportional to the Rayleigh scattering rate scaling with $1/\delta^2$ as it is the case for matter wave super-radiance, the full dynamics of crystallization actually depends on the effective dipole-potential depth proportional to $1/\delta$. The quadratic dependence of I_c on δ is only due to the non-linearity of the model, as explained in section 6.3.

Nevertheless, when applied to the case of single-side driving also the dispersive model shows a modulation instability qualitatively similar to the one observed in [6.2]. In figure 6.15 two representative examples are shown.

One clearly recognizes a certain directionality in the Bragg-diffraction pattern, but in general both positive- and negative-momentum peaks are present. In addition, a high initial peak of the reflection coefficient in time shows that at the point where the atomic bunching occurs a light flash can be observed. The effect is getting more prominent if the atom-light interaction strength (i. e. the optical density of the medium) is high. We also note that the pump threshold for the instability differs from the one for symmetric driving given in equation (6.6) only by a geometrical pre-factor of order one. The corresponding phase diagram is shown in figure 6.16 where we defined the beam asymmetry

$$\mathcal{A} := \frac{I_l - I_r}{I_l + I_r}. \tag{6.11}$$

Even though the momentum distribution of the gas and the amount of reflected light behave qualitatively similar to the SRS experiment of [6.2], there is an important quantitative difference which is an evidence for the different physical origin. The time scale over which the instability appears in our model is of the order of one inverse recoil frequency $1/\omega_{\text{rec}}$ or shorter, while in the SRS experiment of [6.2] the instability grows on time scale much longer than inverse recoil. The difference in the nature of the instability between long and short time scales was experimentally investigated in [6.6]. A more recent experiment [6.5] showing qualitatively similar results as the one presented in this work and shown in figure 6.15 has been performed in the short-pulse regime.

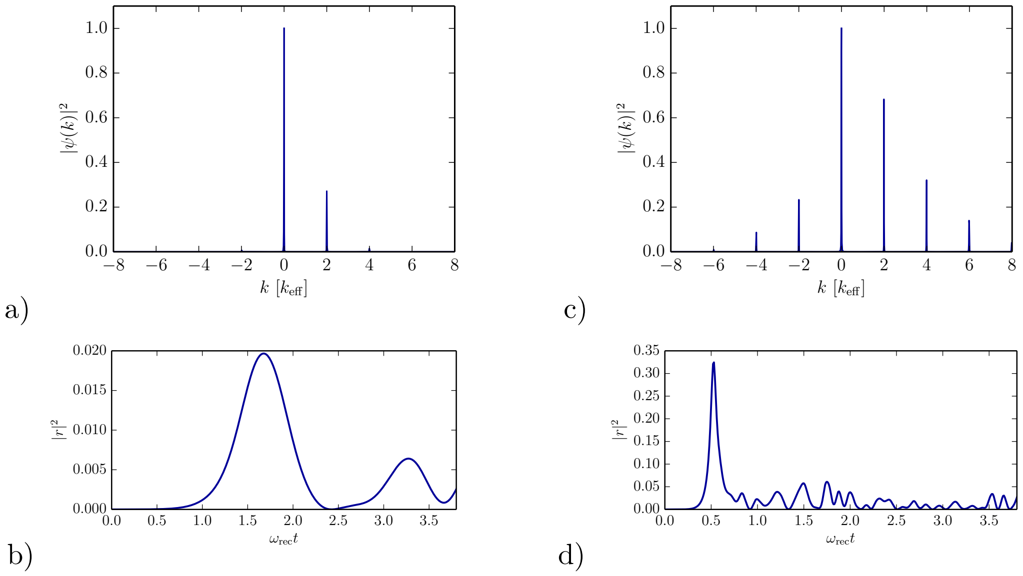

Figure 6.15: (a) BEC momentum distribution at $\omega_{\mathrm{rec}}t = 1.6$ for $\zeta = 0.1$, $g_cN = 1$, $L = 100\lambda_0$ and $I_l = 200$, $I_r = 0$ and (b) corresponding time dependent reflection coefficient. (c) Same as above at $t\omega_{\mathrm{rec}} = 0.4$ for $\zeta = 0.2$, $g_cN = 1$, $L = 100\lambda_0$ and $I_l = 300$, $I_r = 0$ with (d) the evolution of the reflection coefficient.

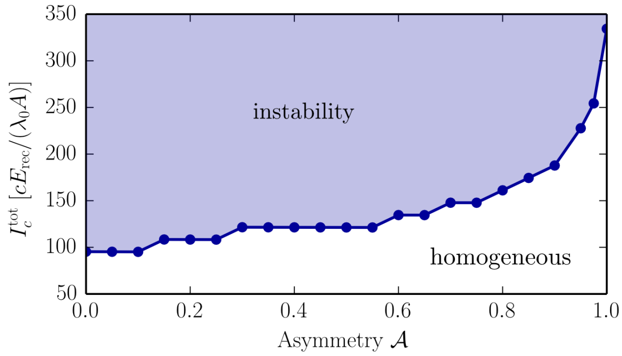

Figure 6.16: Stability region of the homogeneous phase showing the maximal threshold of the total laser power applied from both sides for different pump asymmetries as defined in (6.11). The threshold is obtained from calculating the stationary state via imaginary time evolution of the coupled field equations for different total intensities. $\zeta = 0.1$, $L = 100\lambda_0$, $g_cN = 1.0E_{rec}$.

The comparison of our prediction with the experiments of [6.6] and [6.5] suggests that the model described in 6.2 and the physics of superradiant modulational instabilities induced by dispersive forces and not by Rayleigh scattering should be relevant in the short-pulse regime.

6.8 Conclusions

Our numerical simulations illustrate that real monitoring the backscattered light as well as TOF studies of the atomic momentum distribution contain all the essential signatures to demonstrate the concept of spontaneous atom-field crystallization introduced in [6.4]. While the initial growth of the momentum distributions, apart from a threshold shift, strongly resembles single beam matter wave superradiance, the subsequent locking of the two standing waves is a unanimous sign of long range order in this translation and mirror symmetric configuration. Measuring the particle number dependent stationary reflection coefficient clearly can can be traced back to a collective effect. Additional signatures are contained in shifts and oscillations of the atomic center of mass which can be observed also via the time dependence of the atomic momentum distributions.

As our model includes atomic self-interaction, a quasi-stationary crystal will even form by a quench type sudden laser turn on, but to obtain a low entropy ordered phase a slower close to adiabatic ramping over the phase transition is required. We have seen that varying the ramping procedure presented in section 6 gives insight in the entropy generation during the crystallization process and shows that crystallization is reversible even at rather fast ramp speeds. We also see that symmetric pumping reduces the instability threshold as compared to single side super-radiance and there is strong indication for a maximum possible value of of the pump asymmetry, under which an order state is at least metastable.

Interestingly there appears no obvious size limit on the crystal and for large enough effective particle number almost a 100% of the light of both lasers will be reflected without the crystal becoming unstable as, for example, for the transverse pump case [6.20]. Outside the transition region where all the reflection happens one simple gets an ordinary atomic lattice from the atom-reflected beams.

At this point the central experimental challenge is preparation of a BEC with large enough particle numbers. In fact, the available observation time until heating sets in is short in general as an estimation in table I of [6.25] shows. However, the observation time increases at least linearly with the particle number which leads to the conclusion that for typical atomic configurations about 10^6 particles would be needed for clear signatures of stable order. When the system size is further increased by one or two orders of magnitude the formation of a stable crystal with signatures of a gapped phonon spectrum should be possible.

Acknowledgements

We would like to thank F. Meinert as well as W. Lunden, I. Dimitrova and W. Ketterle for very fruitful discussions on possible experimental implementations and observable signatures presented in the manuscript. We acknowledge support by the Austrian Science Fund FWF through projects SFB FoQuS P13 and I1697-N27.

7 Publication

Physical Review Letters **120**, 123601 (2018)

Driven-Dissipative Supersolid in a Ring Cavity†

F. Mivehvar[1], S. Ostermann[1], F. Piazza[2] and H.Ritsch[1]

[1]*Institut für Theoretische Physik, Universität Innsbruck, A-6020 Innsbruck, Austria*
[2]*Max-Planck Institut für Physik komplexer Systeme, D-01187 Dresden, Germany*

Supersolids are characterized by the counterintuitive coexistence of superfluid and crystalline order. Here we study a supersolid phase emerging in the steady state of a driven-dissipative system. We consider a transversely pumped Bose-Einstein condensate trapped along the axis of a ring cavity and coherently coupled to a pair of degenerate counterpropagating cavity modes. Above a threshold pump strength the interference of photons scattered into the two cavity modes results in an emergent superradiant lattice, which spontaneously breaks the continuous translational symmetry towards a periodic atomic pattern. The crystalline steady state inherits the superfluidity of the Bose-Einstein condensate, thus exhibiting genuine properties of a supersolid. A gapless collective Goldstone mode correspondingly appears in the superradiant phase, which can be nondestructively monitored via the relative phase of the two cavity modes on the cavity output. Despite cavity-photon losses the Goldstone mode remains undamped, indicating the robustness of the supersolid phase.

doi: 10.1103/PhysRevLett.120.123601

---

† The author of the present thesis contributed to this work primarily in an intensive advisory role, discussing the model, the numerical and analytical methods and the scientific conclusions. All the primary calculations and simulations were performed by F. Mivehvar. For many aspects of this work F. Piazza acted as a discussion partner.

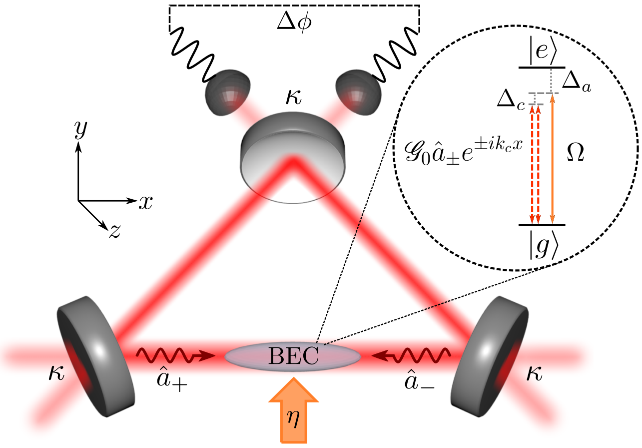

Figure 7.1: Schematic sketch of a BEC inside a ring cavity. An internal atomic transition $|g\rangle \leftrightarrow |e\rangle$ is off-resonantly driven by a transverse plane-wave laser with Rabi frequency Ω. This transition is also off-resonantly coupled to a pair of degenerate, counterpropagating cavity modes $\hat{a}_\pm$ with coupling strength $\mathscr{G}(x) = \mathscr{G}_0 e^{\pm i k_c x}$.

7.1 Introduction

A supersolid behaves as both a crystalline solid and a superfluid. It *spontaneously* breaks two continuous symmetries, namely the external spatial translation invariance and the internal superfluid gauge invariance. That is, it simultaneously possesses diagonal (i.e., density) and off-diagonal (i.e., superfluid) long-range orders [7.1]. This paradoxical state of matter has been predicted almost 50 years ago to exist in solid helium-4 [7.2–7.6]. Despite intensive experimental efforts [7.7, 7.8], supersolidity has not been conclusively observed in solid helium-4 yet [7.9–7.11].

In a different direction, very recently clear signatures of supersolidity have been observed in weakly interacting ultracold atomic systems. At MIT, synthetic spin-orbit coupling was induced in a multi-component Bose-Einstein condensate (BEC) [7.12]. The ground state of the system spontaneously breaks the continuous translational symmetry and forms a density modulated stripe pattern, while maintaining superfluidity of the BEC. At ETH, a transversally driven BEC was symmetrically coupled to two modes of two crossed linear cavities [7.13]. Interference of pump-laser photons and photons scattered into the cavity modes yields an emergent superradiant optical lattice for the BEC, which spontaneously breaks the continuous translational invariance towards a density-modulated superfluid state. In another experiment at MIT [7.14], a BEC illuminated by two noninterfering counterpropagating lasers exhibited collective Rayleigh scattering, resulting in spontaneous crystallization of both matter and light [7.15, 7.16]. However, the potential appearance of supersolidity in this system has not been thoroughly investigated yet.

Based on the state of the art in experimental quantum-gas cavity QED [7.17–7.22], we propose a novel scheme to experimentally realize and study supersolidity in a BEC trapped within a ring resonator [7.23–7.27]. The BEC, which is transversely illuminated by a standing-wave laser, is trapped along the cavity axis in a quasi one-dimensional geometry and dispersively coupled to a pair of degenerate counterpropagating field modes as depicted in Fig. 7.1. This comprises an intrinsically driven-dissipative system due to the pump laser and cavity-photon losses [7.28]. Therefore, the emergent supersolid is the steady-state of the system. The interesting questions which arise are if and how the supersolid features are modified with respect to thermal equilibrium.

Above a critical laser intensity, the collective constructive scattering of pump-laser photons into the cavity modes results in an emergent superradiant optical lattice. In contrast to the standing-wave linear cavity [7.29], the running-wave ring cavity respects the *continuous* spatial translational symmetry. Hence, the location of the emerging optical lattice is not pre-determined by the cavity mirrors and *spontaneously* breaks the continuous translational symmetry, similar to the emergent optical lattice in the crossed-cavity experiment [7.13]. Nevertheless, in the latter the continuous symmetry is merely an approximate and fine-tuned symmetry [7.30–7.32]. A similar continuous symmetry breaking can also occur for atoms trapped close to optical fibers [7.33, 7.34].

The emergent superradiant lattice drives the BEC into a density modulated state — i.e., a crystalline phase — with the spontaneously broken continuous translational symmetry [see Fig. 7.2(b)]. It, nevertheless, inherits superfluidity of the BEC with a long-range phase coherence. Therefore, the resultant steady state in the superradiant phase is a supersolid. As the cavity comprises an open system, the continuous symmetry breaking can be monitored nondestructively in real time via the cavity output, namely via the *relative phase* of the two cavity modes [7.17, 7.18]. In particular, the relative phase takes a random value between 0 and 2π in the superradiant phase, spontaneously breaking the continuous $U(1)$ symmetry [see the inset of Fig. 7.2(b)]. In fact, at the onset of superradiance a superposition of field amplitudes with different phases correlated with density fluctuations emerges, forming a highly entangled atom-field state. This state subsequently collapses to a state with a certain random relative phase via quantum jumps induced by cavity photon losses [7.35–7.37].

Analysis of collective excitations confirms the supersolidity of the superradiant steady state. At the onset of the superradiant phase transition, where the continuous $U(1)$ symmetry is spontaneously broken, a gapless Goldstone mode appears in the spectrum of collective excitations. Unlike all other collective modes, the Goldstone mode remains undamped despite cavity losses (see Fig. 7.3). This is due to the fact that photon losses do not affect the relative phase and preserve the $U(1)$ symmetry. This is in sharp contrast to the supersolid realized in the crossed-cavity setup, where the origin of the $U(1)$ symmetry is different and associated with the freedom of the photon redistribution between the two cavity modes [7.13]. Therefore, photon losses do not respect the $U(1)$ symmetry and should result in damping of the Goldstone mode [7.38].

7.2 Model

Consider bosonic two-level atoms trapped along the axis of a ring resonator by a tight confining potential along the transverse directions. The atoms are illuminated from the side by an off-resonant, standing-wave external pump laser as depicted in Fig. 7.1, which induces the transition $|g\rangle \leftrightarrow |e\rangle$ with the Rabi frequency Ω. Furthermore, the transition $|g\rangle \leftrightarrow |e\rangle$ is also off-resonantly coupled to a pair of degenerate, counterpropagating cavity modes $\hat{a}_\pm$, with coupling strength $\mathscr{G}(x) = \mathscr{G}_0 e^{\pm ik_c x}$. The cavity modes are initially in the vacuum state. The pump and cavity frequencies, respectively, ω_p and $\omega_c = ck_c$ are assumed to be near resonant with each other, but far-red detuned with respect to the atomic frequency ω_a.

In the dispersive regime $|\Delta_a| \equiv |\omega_p - \omega_a| \gg \{\Omega, \mathscr{G}_0\}$, the atomic excited state $|e\rangle$ reaches quickly to a steady state with a negligible population and its dynamics can be adiabatically eliminated [7.28]. This yields an effective Hamiltonian for the atomic ground state and the cavity modes, $H_{\text{eff}} = \int \hat{\psi}^\dagger(x)\mathcal{H}^{(1)}_{\text{eff}}\hat{\psi}(x)dx - \hbar\Delta_c(\hat{a}^\dagger_+\hat{a}_+ + \hat{a}^\dagger_-\hat{a}_-)$, with the effective single-particle atomic Hamiltonian density:

$$\begin{aligned}\mathcal{H}^{(1)}_{\text{eff}} = -\frac{\hbar^2}{2m}\frac{\partial^2}{\partial x^2} &+ \hbar U\Big(\hat{a}^\dagger_+\hat{a}_+ + \hat{a}^\dagger_-\hat{a}_- + \hat{a}^\dagger_+\hat{a}_- e^{-2ik_c x} \\ &+ \hat{a}^\dagger_-\hat{a}_+ e^{2ik_c x}\Big) + \hbar\eta\Big(\hat{a}_+ e^{ik_c x} + \hat{a}_- e^{-ik_c x} + \text{H.c.}\Big). \qquad (7.1)\end{aligned}$$

Here, $\hat{\psi}(x)$ is the bosonic annihilation field operator for the atomic ground state. We have introduced the cavity detuning with respect to the pump $\Delta_c \equiv \omega_p - \omega_c$, the maximum depth of the optical potential per photon due to two-photon scattering between cavity modes $\hbar U \equiv \hbar\mathscr{G}_0^2/\Delta_a$ and the maximum depth of the optical potential per photon due to the two-photon scattering between pump and cavity modes (or the effective cavity-pump strength) $\hbar\eta \equiv \hbar\mathscr{G}_0\Omega/\Delta_a$. Although finite atom-atom interactions are needed to ensure the superfluidity of the BEC, we have assumed them to be negligibly small with respect to the cavity-mediated interactions. This is quantitatively a good approximation for typical cavity-QED experiments, including the recent observation of the supersolid [7.13]. Finally, the cavity-photon losses with rate κ are included via Lindblad operators in the master equation for the density matrix ρ: $\mathcal{L}\rho = \kappa\sum_{\ell=+,-}\left(2\hat{a}_\ell\rho\hat{a}^\dagger_\ell - \left\{\hat{a}^\dagger_\ell\hat{a}_\ell, \rho\right\}\right)$.

The system possesses a continuous $U(1)$ symmetry, as the effective Hamiltonian H_{eff} and the Lindblad operators are invariant under the simultaneous spatial translation $x \to \mathcal{T}_X x = x + X$ and cavity-phase rotations $\hat{a}_\pm \to \mathcal{U}_X\hat{a}_\pm = \hat{a}_\pm e^{\mp ik_c X}$. This $U(1)$ symmetry is spontaneously broken in the superradiant phase, as illustrated in the inset of Fig. 7.2(b), where $\langle\hat{a}_\pm\rangle$ acquire nonzero values with arbitrary phases.

7.3 Mean-Field Approach and Continuous Symmetry Breaking

In the thermodynamic limit, where the mean-field approximation becomes accurate [7.39], the system is described by a set of three coupled mean-field (Heisenberg) equations for the cavity-field amplitudes $\langle\hat{a}_\pm(t)\rangle = \alpha_\pm(t) = |\alpha_\pm(t)|e^{i\phi_\pm(t)}$ and the atomic condensate

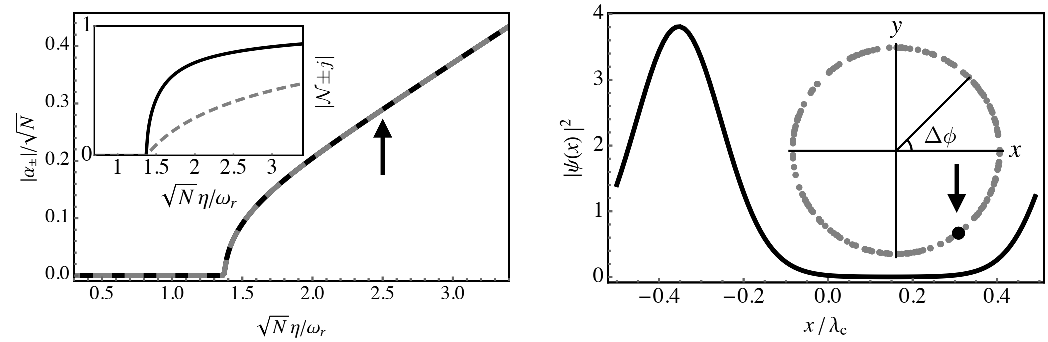

(a) (b)

Figure 7.2: Dicke superradiant phase transition and atomic self-organization. (a) The absolute values of the rescaled cavity-field amplitudes $|\alpha_\pm|/\sqrt{N}$ (black solid and grey dashed curves, respectively) are shown as a function of the rescaled effective cavity-pump strength $\sqrt{N}\eta/\omega_r$. The superradiant phase transition occurs at the critical pump strength $\sqrt{N}\eta_c \approx 1.36\omega_r$, where $|\alpha_+| = |\alpha_-| > 0$. The inset shows the absolute values of the quantities $|\mathcal{N}_{\pm 1}|$ (the solid black curve) and $|\mathcal{N}_{\pm 2}|$ (the dashed gray curve) as a function of $\sqrt{N}\eta/\omega_r$. (b) A typical self-ordered atomic density profile is shown for $\sqrt{N}\eta = 2.5\omega_r$ with $\Delta\phi \approx 1.71\pi$ and $\Phi \approx 0.09\pi$, where $\Delta\phi$ fixes the position of the density maximum $x_m \approx -0.35\lambda_c$. The inset illustrates the distribution of $\Delta\phi$ for 200 numerical runs for $\sqrt{N}\eta = 2.5\omega_r$, exhibiting the continuous $U(1)$ symmetry breaking. The parameters are set to $(\Delta_c, U, \kappa) = (-8, -1, 2)\omega_r$.

wavefunction $\langle\hat{\psi}(x,t)\rangle = \psi(x,t) = \sqrt{n(x,t)}e^{i\theta(t)}$

$$
\begin{aligned}
i\frac{\partial}{\partial t}\alpha_{\pm} &= (-\Delta_c + UN - i\kappa)\,\alpha_{\pm} + U\mathcal{N}_{\pm 2}\alpha_{\mp} + \eta\mathcal{N}_{\pm 1},\\
i\hbar\frac{\partial}{\partial t}\psi &= \mathcal{H}^{(1)}_{\text{eff}}\psi,
\end{aligned} \tag{7.2}
$$

where $N = \int n(x)dx$ is the number of the particles. See Supplemental Material in section 7.7 for the details of the derivation of the mean-field equations, the linearized equations, and the threshold pump strength. One can identify $\mathcal{N}_{\pm 1} \equiv \int n(x)e^{\mp ik_cx}dx$ as the atomic order parameters, dual to the cavity order parameters $\alpha_{\pm}$, which characterize the probability of the photon scattering between the pump and cavity modes with $\mp\hbar k_c$ momentum transfer to the atoms along the cavity axis x. Whereas, $\mathcal{N}_{\pm 2} \equiv \int n(x)e^{\mp 2ik_cx}dx$ quantifies the probability of the photon redistribution between the two cavity modes with $\mp 2\hbar k_c$ momentum transfer to the atoms in the x direction.

We self-consistently find the steady-state solutions of Eq. (7.2) by setting $\partial_t\alpha_{\pm} = 0$ and $i\hbar\partial_t\psi = \mu\psi$, with μ being the chemical potential. Figure 7.2(a) shows the absolute values of the rescaled cavity-mode amplitudes $|\alpha_{\pm}|/\sqrt{N}$ (black solid and grey dashed curves, respectively) as a function of the rescaled effective pump strength $\sqrt{N}\eta/\omega_r$, with $\omega_r \equiv \hbar k_c^2/2m$ being the recoil frequency. Below the threshold pump strength $\sqrt{N}\eta_c \approx 1.36\omega_r$, the cavity modes are empty and the BEC is uniform. By increasing the pump strength above η_c the system undergoes a superradiant phase transition, where the cavity amplitudes acquire nonzero values $|\alpha_+| = |\alpha_-| = |\alpha|$.

In the superradiant state, the relative phase $\Delta\phi \equiv (\phi_+ - \phi_-)/2$ of the two cavity modes is fixed in an arbitrary value between 0 and 2π and the continuous $U(1)$ symmetry is, therefore, spontaneously broken. This is illustrated in the inset of Fig. 7.2(b), where the distribution of $\Delta\phi$ is shown for 200 numerical runs for a pump strength $\sqrt{N}\eta = 2.5\omega_r$ [indicated by the arrow in Fig. 7.2(a)]. The emergent superradiant lattice has the form $V_{\text{SR}}(x) = 2U|\alpha|^2\cos(2k_cx + 2\Delta\phi) + 4\eta|\alpha|\cos(k_cx + \Delta\phi)\cos(\Phi)$, with $\Phi \equiv (\phi_+ + \phi_-)/2$ being the total phase. The spontaneously chosen value of $\Delta\phi$ fixes the position of the lattice minima and thus of the BEC density modulation, spontaneously breaking the continuous translational invariance and resulting in a supersolid state. A typical self-ordered, λ_c-periodic atomic density profile is shown in Fig. 7.2(b) for $\sqrt{N}\eta = 2.5\omega_r$ with $\Delta\phi \approx 1.71\pi$ [the pronounced black dot indicated by the arrow in the inset of Fig. 7.2(b)] and $\Phi \approx 0.09\pi$.

The total phase Φ solely modifies the lattice amplitude, except the special case of $\Phi = \pi/2$ where the lattice spacing is reduced from λ_c to $\lambda_c/2$. Note that Φ is not random as it is invariant under the $U(1)$ phase rotation $\alpha_{\pm} \to \alpha_{\pm}e^{\mp ik_cX}$. The total phase Φ solely depends on κ, while the relative phase $\Delta\phi$ is independent of κ. This is becuasse photon losses induce equal extra phase shifts for both cavity-field amplitudes. Therefore, the spontaneous $U(1)$-symmetry breaking and thus the supersolid order persist even in the presence of dissipation.

7.4 Collective Excitations and the Goldstone Mode

Let us now turn our attention to elementary excitations of the system, which include quantum fluctuations of both condensate wavefunction $\delta\psi(x,t) = \delta\psi^{(+)}(x)e^{-i\omega t} + [\delta\psi^{(-)}(x)]^* e^{i\omega^* t}$ and cavity-field amplitudes $\delta\alpha_\pm(t) = \delta\alpha_\pm^{(+)}e^{-i\omega t} + [\delta\alpha_\pm^{(-)}]^* e^{i\omega^* t}$ above the mean-field solutions $\psi_0(x)$ and $\alpha_{0\pm}$ (with the corresponding chemical potential μ_0). Linearizing Eq. (7.2) yields Bogoliubov-type equations for the quantum fluctuations [7.24, 7.40, 7.41],

$$\begin{aligned} i\frac{\partial}{\partial t}\delta\alpha_\pm &= (-\Delta_c + UN - i\kappa)\,\delta\alpha_\pm + U\mathcal{N}_{\pm 2}^{(0)}\delta\alpha_\mp \\ &\quad + \int A_\pm(\psi_0^*\delta\psi + \psi_0\delta\psi^*)dx, \\ i\frac{\partial}{\partial t}\delta\psi &= \frac{1}{\hbar}\left(\mathcal{H}_{\text{eff}}^{(1)} - \mu_0\right)\delta\psi \\ &\quad + \psi_0\left(A_+^*\delta\alpha_+ + A_-^*\delta\alpha_- + \text{H.c.}\right), \end{aligned} \tag{7.3}$$

where $\mathcal{N}_{\pm 2}^{(0)} = \int n_0(x)e^{\mp 2ik_c x}dx$ and we have defined $A_\pm(x) \equiv U\left(\alpha_{0\pm} + \alpha_{0\mp}e^{\mp 2ik_c x}\right) + \eta e^{\mp ik_c x}$ for shorthands. The Bogoliubov equations (7.3) can be recast in a matrix form,

$$\omega\mathbf{f} = \mathbf{M}_{\text{B}}\mathbf{f}, \tag{7.4}$$

where $\mathbf{f} = (\delta\alpha_+^{(+)}, \delta\alpha_+^{(-)}, \delta\alpha_-^{(+)}, \delta\alpha_-^{(-)}, \delta\psi^{(+)}, \delta\psi^{(-)})^\intercal$ and $\mathbf{M}_{\text{B}}$ is a Hermitian matrix; see Supplemental Material in section 7.7. The eigenvalues ω of the Bogoliubov equations (7.4) yield collective excitation spectrum of the system. We numerically solve Eq. (7.4) in one unit cell (of length λ_c) with periodic boundary conditions to obtain the collective excitations ω.

Figure 7.3 shows the real part of the six lowest-lying excitation frequencies as a function of the effective cavity-pump strength $\sqrt{N}\eta/\omega_r$. At small pump strengths, the excitation spectra are weakly dependent on η and each branch is doubly degenerate. The lowest four collective excitations at frequencies $\sim \omega_r$ (solid blue and dashed red curves) and $\sim 4\omega_r$ (dotted orange and dashed-dotted brown curves) correspond to mainly atomic fluctuations with momenta $\pm\hbar k_c$ and $\pm 2\hbar k_c$, respectively. The highest two modes (dashed-dashed-dotted black and dotted-dotted-dashed gray curves) at frequencies $\sim -\Delta_c + UN = 7\omega_r$ are mostly photon-like fluctuations.

By increasing η the collective modes are increasingly mixed with each other and begin to split up. In particular, the lowest excitation softens and the excitation gap closes at the pump strength $\sqrt{N}\eta_{\text{G}} \approx 1.37\omega_r$. By increasing pump strength beyond η_{G}, the lowest excitation splits into two branches. The lower one (solid blue curve) remains pinned at zero energy, signaling that it is a *gapless* Goldstone mode corresponding to the spontaneously broken continuous $U(1)$ symmetry. The gapped branch instead corresponds to a Higgs amplitude mode. These are reminiscent of the recently observed Goldstone and Higgs modes in the crossed-cavity experiment [7.38]. The Goldstone mode in the crossed-cavity experiment, however, should have a small gap of a few ω_r

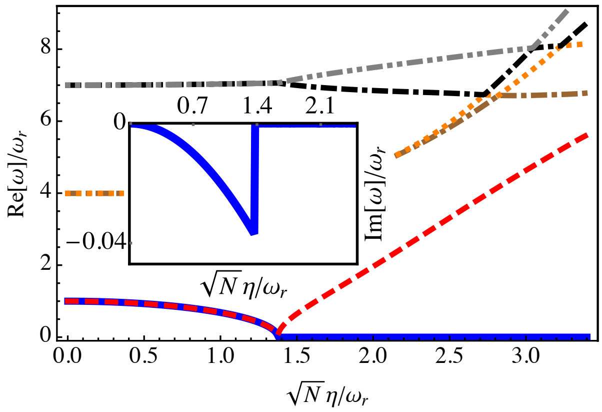

Figure 7.3: Low-lying collective excitations. The real part of the six lowest-lying excitation spectra are shown as a function of the rescaled effective cavity-pump strength $\sqrt{N}\eta/\omega_r$. By increasing $\sqrt{N}\eta/\omega_r$ from zero the lowest excitation, corresponding mainly to the atomic condensate fluctuations with momenta $\pm\hbar k_c$, softens and the excitation gap closes at $\sqrt{N}\eta_{\mathrm{G}} \approx 1.37\omega_r$. By further increasing $\sqrt{N}\eta/\omega_r$, a gap does not open in the first excitation band (the solid blue curve), indicating that this is a gapless Goldstone mode corresponding to the spontaneously broken continuous $U(1)$ symmetry. The inset shows the imaginary part of the Goldstone mode. The parameters are the same as Fig. 7.2.

due to the fact that the continuous $U(1)$ symmetry is an approximate symmetry [7.30]. Note that these are in sharp contrast to the self-organization in a linear cavity, where only a discrete $\mathbf{Z}_2$ symmetry is spontaneously broken and the first excitation gap closes at the critical pump strength but then re-opens again [7.24, 7.40, 7.42].

Due to a nonzero cavity-field decay rate $\kappa \neq 0$ the excitation frequencies can acquire imaginary parts, which would indicate the damping of the excitations [7.24, 7.40]. This would in turn result in friction forces on the atoms. Above the critical pump strength η_c, all the collective excitations except the gapless Goldstone mode acquire imaginary parts. This is illustrated in the inset of Fig. 7.3, which shows the imaginary part of the lowest mode as a function of $\sqrt{N}\eta/\omega_r$. Although it is damped for small pump strengths, it vanishes at the critical pump strength $\sqrt{N}\eta_c \approx 1.38\omega_r$ (recall that the corresponding real part vanishes at the slightly lower pump strength η_{G}, where the damping reaches its maximum value), in agreement with the mean-field results [see Fig. 7.2(a)]. This means that the center of mass of the entire modulated BEC can move freely along the cavity axis without experiencing any friction, once again illustrating the supersolidity of the system. The fact that supersolidity survives even in presence of dissipation is due to the fact that the corresponding Lindblad operators respect the $U(1)$-symmetry of the system. This is in contrast to the supersolid realized in the crossed-cavity setup, where the Goldstone mode involves photon-number redistribution between the two cavities and should therefore be damped by photon losses.

Around the critical point η_c, the atomic momentum states $\pm\hbar k_c$ are the dominant atomic fluctuations coupled to the cavity fluctuations. This can be seen from the inset of Fig. 7.2(a), where the quantities $|\mathcal{N}_{\pm j}|$ with $j = 1, 2$ are shown as a function of $\sqrt{N}\eta/\omega_r$. For $\eta \gtrsim \eta_c$, $\mathcal{N}_{\pm 1}$ (the black solid curve) are the dominant quantities. It is, therefore, a good approximation to restrict atomic fluctuations to the momentum states $\pm\hbar k_c$. Using the homogeneous solution (i.e., the solution below the Dicke transition) $\alpha_{0\pm} = 0$ and $\psi_0 = \sqrt{N/\lambda_c}$, one can diagonalize Eq. (7.4) in this restricted subspace. The zero frequency $\omega = 0$ solution yields the critical pump strength,

$$\sqrt{N}\eta_c = \sqrt{\frac{(-\Delta_c + UN)^2 + \kappa^2}{4(-\Delta_c + UN)}}\sqrt{\omega_r} \approx 1.37\omega_r, \tag{7.5}$$

which is in full agreement with the numerical results.

7.5 Experimental Detection of the Supersolid State

As discussed earlier, in our system the spontaneous breaking of the continuous translational symmetry corresponds to fixing the value of the relative phase of the two cavity modes. This can be monitored nondestructively by recombining the cavity outputs through a beam spitter. In particular, the system can be in real time repeatedly driven across the superradiant phase transition by sweeping the pump strength across the threshold to verify the uniform distribution of the relative phase in the interval $0 - 2\pi$, similar to experiments with linear cavities [7.13, 7.42]. Experimental setups coupling a BEC into fields of a ring cavity already exist for almost a decade now [7.19–7.22]. Therefore, the discussed phenomena could be observed with only minimal changes to current state-of-the-art experiments.

7.6 Outlook

Our driven-dissipative supersolid is essentially different than other proposed driven-dissipative supersolid states in Jaynes-Cummings-Hubbard lattices [7.43, 7.44], in that the latter ones are only the lattice supersolid with a broken discrete symmetry and no gapless Goldstone mode [7.45]. Crucially due to the genuine supersolidity and existence of the undamped gapless Goldstone mode, our proposal may have applications in precision measurements. By monitoring the relative phase between the cavity modes one can nondestructively follow the displacement of the BEC in real time. However, there is no back-action of the light field onto the BEC motion (apart from the one induced by the measurement of the phase) due to the existence of the undamped gapless Goldstone mode. Therefore, it could be used as a free-falling zero temperature mass for gravitational acceleration measurements, as an alternative to the atomic fountains [7.46–7.49]. We defer the investigation of the performance of such a device to a future work.

Acknowledgements

FM is grateful to Tobias Donner and Manuele Landini for fruitful discussions. We acknowledge support by the Austrian Science Fund FWF through the projects SFB FoQuS P13 and I1697-N27.

7.7 Supplemental Material

Here we present the details of the derivation of the mean-field equations [Eq. (2) in the main text], the linearized equations [Eqs. (3) and (4) in the main text], and the threshold pump strength [Eq. (5) in the main text].

7.7.1 Mean-Field Equations

The Heisenberg equations of motion of the photonic and atomic field operators can be obtained using the many-body effective Hamiltonian H_{eff}, given in the manuscript, as

$$\begin{aligned} i\hbar\frac{\partial}{\partial t}\hat{a}_\pm &= [\hat{a}_\pm, H_{\text{eff}}] = \hbar\left(-\Delta_c + U\hat{N} - i\kappa\right)\hat{a}_\pm + \hbar U\hat{\mathcal{N}}_{\pm 2}\hat{a}_\mp + \hbar\eta\hat{\mathcal{N}}_{\pm 1}, \\ i\hbar\frac{\partial}{\partial t}\hat{\psi} &= [\hat{\psi}, H_{\text{eff}}] = \mathcal{H}_{\text{eff}}^{(1)}\hat{\psi}, \end{aligned} \tag{7.6}$$

where $\hat{N} = \int \hat{\psi}^\dagger(x)\hat{\psi}(x)dx$, $\hat{\mathcal{N}}_{\pm 1} \equiv \int \hat{\psi}^\dagger(x)e^{\mp ik_cx}\hat{\psi}(x)dx$, and

$$\hat{\mathcal{N}}_{\pm 2} \equiv \int \hat{\psi}^\dagger(x)e^{\mp 2ik_cx}\hat{\psi}(x)dx.$$

Here we have added field damping terms proportional to the cavity decay rate κ. By replace the photonic and atomic field operators with their corresponding quantum averages, $\hat{a}_\pm(t) \to \langle\hat{a}_\pm(t)\rangle = \alpha_\pm(t) = |\alpha_\pm(t)|e^{i\phi_\pm(t)}$ and $\hat{\psi}(x,t) \to \langle\hat{\psi}(x,t)\rangle = \psi(x,t) = \sqrt{n(x,t)}e^{i\theta(t)}$, respectively, one obtains the three mean-field coupled equations (2) in the manuscript.

7.7.2 Linearized Equations

Assuming $\psi(x,t) = e^{-i\mu_0t/\hbar}[\psi_0(x) + \delta\psi(x,t)]$ and $\alpha_\pm(t) = \alpha_{0\pm} + \delta\alpha_\pm(t)$, where $\psi_0(x)$ and $\alpha_{0\pm}$ are the mean-field stationary-state solutions of Eq. (2) in the main text with the chemical potential μ_0, linearizing Eq. (2) yields

$$\begin{aligned} i\frac{\partial}{\partial t}\delta\alpha_\pm &= (-\Delta_c + UN - i\kappa)\,\delta\alpha_\pm + U\mathcal{N}_{\pm 2}^{(0)}\delta\alpha_\mp + \int A_\pm(\psi_0^*\delta\psi + \psi_0\delta\psi^*)dx, \\ i\frac{\partial}{\partial t}\delta\psi &= \frac{1}{\hbar}\left(\mathcal{H}_{\text{eff}}^{(1)} - \mu_0\right)\delta\psi + \psi_0\left(A_+^*\delta\alpha_+ + A_+\delta\alpha_+^* + A_-^*\delta\alpha_- + A_-\delta\alpha_-^*\right), \end{aligned} \tag{7.7}$$

where $\mathcal{N}_{\pm 2}^{(0)} = \int n_0(x)e^{\mp 2ik_cx}dx$ and we have defined $A_\pm(x) \equiv U\left(\alpha_{0\pm} + \alpha_{0\mp}e^{\mp 2ik_cx}\right) + \eta e^{\mp ik_cx}$ for shorthands. Since the linearized equations (7.7) couple $\delta\psi$ and $\delta\alpha_\pm$ to their complex conjugates, we make the ansätze $\delta\psi(x,t) = \delta\psi^{(+)}(x)e^{-i\omega t} + [\delta\psi^{(-)}(x)]^* e^{i\omega^* t}$ and $\delta\alpha_\pm(t) = \delta\alpha_\pm^{(+)} e^{-i\omega t} + [\delta\alpha_\pm^{(-)}]^* e^{i\omega^* t}$ for the quantum fluctuations. Substituting these ansätze in Eq. (7.7) and setting the coefficients of $e^{-i\omega t}$ and $e^{i\omega^* t}$ separately to zero yields a set of six coupled Bogoliubov-type equations for the positive- and negative-frequency components of the quantum fluctuations,

$$\begin{aligned}
\omega\delta\alpha_\pm^{(+)} &= (-\Delta_c + UN - i\kappa)\,\delta\alpha_\pm^{(+)} + U\mathcal{N}_{\pm 2}^{(0)}\delta\alpha_\mp^{(+)} + \int A_\pm \left[\psi_0^*\delta\psi^{(+)} + \psi_0\delta\psi^{(-)}\right] dx,\\
\omega\delta\alpha_\pm^{(-)} &= -\left(-\Delta_c + UN - i\kappa\right)^* \delta\alpha_\pm^{(-)} - U\mathcal{N}_{\pm 2}^{(0)*}\delta\alpha_\mp^{(-)} - \int A_\pm^* \left[\psi_0^*\delta\psi^{(+)} + \psi_0\delta\psi^{(-)}\right] dx,\\
\omega\delta\psi^{(+)} &= \frac{1}{\hbar}\left[\mathcal{H}_{\text{eff}}^{(1)} - \mu_0\right]\delta\psi^{(+)} + \psi_0\left[A_+^*\delta\alpha_+^{(+)} + A_+\delta\alpha_+^{(-)} + A_-^*\delta\alpha_-^{(+)} + A_-\delta\alpha_-^{(-)}\right],\\
\omega\delta\psi^{(-)} &= -\frac{1}{\hbar}\left[\mathcal{H}_{\text{eff}}^{(1)} - \mu_0\right]\delta\psi^{(-)} - \psi_0^*\left[A_+^*\delta\alpha_+^{(+)} + A_+\delta\alpha_+^{(-)} + A_-^*\delta\alpha_-^{(+)} + A_-\delta\alpha_-^{(-)}\right].
\end{aligned} \tag{7.8}$$

We recast these equations in a matrix form

$$\omega\mathbf{f} = \mathbf{M}_{\text{B}}\mathbf{f}, \tag{7.9}$$

where $\mathbf{f} = (\delta\alpha_+^{(+)}, \delta\alpha_+^{(-)}, \delta\alpha_-^{(+)}, \delta\alpha_-^{(-)}, \delta\psi^{(+)}, \delta\psi^{(-)})^\mathsf{T}$ and

$$\mathbf{M}_{\text{B}} = \begin{pmatrix}
\delta_c & 0 & U\mathcal{N}_{+2}^{(0)} & 0 & \mathcal{I}_{+*} & \mathcal{I}_+\\
0 & -\delta_c^* & 0 & -U\mathcal{N}_{+2}^{(0)*} & -\mathcal{I}_+^* & -\mathcal{I}_{+*}^*\\
U\mathcal{N}_{-2}^{(0)} & 0 & \delta_c & 0 & \mathcal{I}_{-*} & \mathcal{I}_-\\
0 & -U\mathcal{N}_{-2}^{(0)*} & 0 & -\delta_c^* & -\mathcal{I}_-^* & -\mathcal{I}_{-*}^*\\
\psi_0 A_+^* & \psi_0 A_+ & \psi_0 A_-^* & \psi_0 A_- & (\mathcal{H}_{\text{eff}}^{(1)} - \mu_0)/\hbar & 0\\
-\psi_0^* A_+^* & -\psi_0^* A_+ & -\psi_0^* A_-^* & -\psi_0^* A_- & 0 & -(\mathcal{H}_{\text{eff}}^{(1)} - \mu_0)/\hbar
\end{pmatrix}, \tag{7.10}$$

with $\delta_c \equiv -\Delta_c + UN - i\kappa$. Here we have introduced the integral operators,

$$\begin{aligned}
\mathcal{I}_\pm\xi &= \int A_\pm(x)\psi_0(x)\xi dx,\\
\mathcal{I}_{\pm *}\xi &= \int A_\pm(x)\psi_0^*(x)\xi dx.
\end{aligned} \tag{7.11}$$

We find eigenvalues ω of Eq. (7.9) by numerically diagonalizing the Bogoliubov matrix (7.10) on one unit cell (of length λ_c) with a periodic boundary condition. We discretize the space and replace the kinetic energy term $-(\hbar^2/2m)\partial_x^2$ and the integral operators $\{\mathcal{I}_\pm, \mathcal{I}_{\pm *}\}$ with the corresponding finite-difference terms.

7.7.3 The Threshold Pump Strength

In order to find an analytical equation for the critical threshold, we analyze the stability of the the trivial solution (i.e., the solution below the Dicke transition) $\alpha_{0\pm} = 0$ and

$\psi_0 = \sqrt{N/\lambda_c}$ with $\mu_0 = 0$, by restricting the atomic fluctuations to the momentum states $\pm\hbar k_c$. Using this trivial solution and the ansatz $\delta\psi^{(\pm)}(x) = \delta\psi_+^{(\pm)} e^{ik_c x} + \delta\psi_-^{(\pm)} e^{-ik_c x}$ for the positive- and negative-frequency condensate fluctuations with momenta $\pm\hbar k_c$, the Bogoliubov matrix (7.10) takes the following form,

$$\tilde{\mathbf{M}}_{\mathrm{B}} = \begin{pmatrix} \delta_c & 0 & 0 & 0 & \sqrt{N\lambda_c}\eta & \sqrt{N\lambda_c}\eta & 0 & 0 \\ 0 & -\delta_c^* & 0 & 0 & 0 & 0 & -\sqrt{N\lambda_c}\eta & -\sqrt{N\lambda_c}\eta \\ 0 & 0 & \delta_c & 0 & 0 & 0 & \sqrt{N\lambda_c}\eta & \sqrt{N\lambda_c}\eta \\ 0 & 0 & 0 & -\delta_c^* & -\sqrt{N\lambda_c}\eta & -\sqrt{N\lambda_c}\eta & 0 & 0 \\ \sqrt{N/\lambda_c}\eta & 0 & 0 & \sqrt{N/\lambda_c}\eta & \omega_r & 0 & 0 & 0 \\ -\sqrt{N/\lambda_c}\eta & 0 & 0 & -\sqrt{N/\lambda_c}\eta & 0 & -\omega_r & 0 & 0 \\ 0 & \sqrt{N/\lambda_c}\eta & \sqrt{N/\lambda_c}\eta & 0 & 0 & 0 & \omega_r & 0 \\ 0 & -\sqrt{N/\lambda_c}\eta & -\sqrt{N/\lambda_c}\eta & 0 & 0 & 0 & 0 & -\omega_r \end{pmatrix}. \tag{7.12}$$

The eigenvalues ω of $\tilde{\mathbf{M}}_{\mathrm{B}}$ is obtained via the eighth-order characteristic equation $\mathrm{Det}(\tilde{\mathbf{M}}_{\mathrm{B}} - \omega I_{8\times 8}) = 0$:

$$[(\omega^2 - \omega_r^2)(\omega - \delta_c)(\omega + \delta_c^*) + 4N\eta^2\omega_r(\Delta_c - UN)]^2 = 0. \tag{7.13}$$

The solution of the characteristic equation (7.13) yields the spectra ω of the atomic and photonic excitations, which below the threshold η_c are in excellent agreement with the first and last excitation bands of Fig. 3 in the manuscript obtained from the full numerical calculations. Above η_c the solutions of Eq. (7.13) develop positive imaginary parts, signaling that the trivial solution $\alpha_{0\pm} = 0$ and $\psi_0 = \sqrt{N/\lambda_c}$ is unstable towards the superradiant phase. The zero-frequency solution $\omega = 0$ of the characteristic equation (7.13) yields the self-ordering threshold,

$$\sqrt{N}\eta_c = \sqrt{\frac{(-\Delta_c + UN)^2 + \kappa^2}{4(-\Delta_c + UN)}}\sqrt{\omega_r}. \tag{7.14}$$

8 Preprint

arXiv 1807.03316 (2018)

Cavity-Induced Emergent Topological Spin-Textures in a Bose-Einstein Condensate†

S. Ostermann[1], H.-W. Lau[2,3], H.Ritsch[1] and F. Mivehvar[1]

[1]*Institut für Theoretische Physik, Universität Innsbruck, A-6020 Innsbruck, Austria*
[2]*Max-Planck-Institut für Physik komplexer Systems, D-01187 Dresden, Germany*
[3]*Institute for Quantum Science and Technology and Department of Physics and Astronomy, University of Calgary, Calgary T2N 1N4, Alberta, Canada*

The coupled nonlinear dynamics of ultracold quantum matter and electromagnetic field modes in an optical resonator exhibits a wealth of intriguing collective phenomena. Here we study a Λ-type, three-component Bose-Einstein condensate coupled to four dynamical running-wave modes of a ring cavity, where only two of the modes are externally pumped. However, the unpumped modes play a crucial role in the dynamics of the system due to coherent back-scattering of photons. On a mean- field level we identify three fundamentally different steady-state phases with distinct characteristics in the density and spatial spin textures: a combined density and spin wave, a continuous spin spiral with a homogeneous density, and a spin spiral with a modulated density. The spin-spiral states, which are topological, are intimately related to cavity-induced spin-orbit coupling emerging beyond a critical pump power. The topologically trivial density-wave–spin-wave state has the characteristics of a supersolid with two broken continuous symmetries. The transitions between different phases are either simultaneously topological and first order, or second order. The proposed setup allows the simulation of intriguing many-body quantum phenomena by solely tuning the pump amplitudes and frequencies, with the cavity output fields serving as a built-in nondestructive observation tool.

arXiv:1807.03316

---

† The author of the present thesis performed all the calculations and numerical simulations in this publication except the simulations for the occupation of the momentum components for the whole parameter space, which were obtained by H.-W. Lau. F. Mivehvar contributed in an intensive advisory role.

8.1 Introduction

The experimental progresses in reaching the quantum degeneracy limit in atomic gases paved the way for the realization of quantum many-body phenomena in these highly tunable systems [8.1, 8.2]. Some of the most remarkable examples include the realization of the superfluid to Mott-insulator quantum phase transition [8.3], quantum magnetism and magnetic orderings [8.4–8.8], synthetic magnetic fields (i.e., Abelian gauge potentials) [8.9–8.11], and spin-orbit coupling (i.e., non-Abelian gauge potentails) [8.12–8.14] in ultracold quantum gases. While the first generation of experiments was limited to static lattices and local contact interactions, the study of highly nonlinear optical systems, where the back-action of the matter on the radiation fields is not negligible, has opened up new frontiers towards dynamical optical potentials, long-range atom-atom interactions, and exotic collective phenomena [8.15–8.18]. The most prominent examples include the coupling of ultracold atoms to dynamic quantized radiation fields of high-quality cavities [8.19–8.21], leading to the realization of the Dicke superradiance phase transition [8.22, 8.23], atomic recoil lasing [8.24–8.26], and the quantum phase transition between superfluid, supersolid, Mott-insulator, and density-wave phases [8.27, 8.28].

Almost all experimental works and most theoretical studies of coupled atom-cavity systems in the past were limited to systems where either the atomic internal states [8.29–8.32] or the atomic external degrees of freedom [8.33–8.44] are taken into account. Only recently theoretical investigations towards including both atomic internal and external degrees of freedom in cavity QED have been conducted. These systems exhibit many

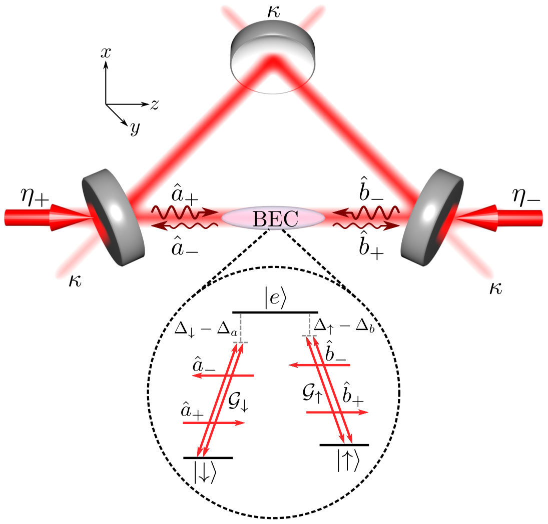

Figure 8.1: Sketch of the system. A spin-1 BEC is tightly confined along one leg of a longitudinally pumped ring cavity with four nearly resonant modes $\{\hat{a}_\pm e^{\pm ikz}, \hat{b}_\pm e^{\pm ikz}\}$. The modes $\hat{a}_\pm$ ($\hat{b}_\pm$) induce the transitions $|\downarrow\rangle \leftrightarrow |e\rangle$ ($|\uparrow\rangle \leftrightarrow |e\rangle$) with a coupling strength $\mathcal{G}_\downarrow$ ($\mathcal{G}_\uparrow$). The modes $\hat{a}_+$ and $\hat{b}_-$ are pumped by external lasers with strengths η_+ and η_-, respectively.

more interesting phenomena, including the emergence of synthetic strong magnetic fields and spin-orbit coupling [8.45–8.48], disorder-driven density and spin self-ordering [8.49], topological states [8.50, 8.51], and a variety of magnetic orders [8.52, 8.53]. Very recently, the first experimental implementation with a spin-1 BEC inside a linear cavity revealed spontaneous self-ordering of the atoms into a crystalline structure with an antiferromagnetic order [8.54].

In this work we study a novel type of hybrid atom-cavity system, where Λ-type spin-1 ultracold bosons are confined into quasi one dimension along one leg of a ring cavity with two "pairs" of nearly resonant modes [8.55, 8.56]. Each pair consists of two counterpropagating modes with the same polarization which is orthogonal to the polarization of the other pair. In contrast to Ref. [8.57], each pair of modes only couples to one of the transitions in the Λ scheme, where the atoms are assumed to posses two ground states (e.g., two different Zeeman sublevels) and an electronic excited state; see Fig. 8.1. The adiabatic elimination of the upper atomic electronic state as well as of other Zeeman sublevels results in an effective two-component pseudospin model. We consider a case where two counterpropagating modes of orthogonal polarizations are externally pumped by lasers through the cavity mirrors as depicted in Fig. 8.1. These two modes do not interfere with one another and the system is, therefore, initially homogeneous. This is reminiscent of the scheme for generating equal Rashba-Dresselhaus synthetic spin-orbit coupled for neutral atoms in free space [8.12].

That said, in the present case the cavity modes are dynamic and affected by the atomic dynamics as well as by photon losses through the cavity mirrors. Crucially, the unpumped modes are "dynamically" populated by coherently scattered photons and, therefore, couple to the pumped modes and the atomic internal and external degrees of freedom. As an important consequence, the cavity-induced spin-orbit coupling for the atoms only emerges above a critical pump power, which in turn gives rise to novel nonequilibrium quantum phases and quantum phase transitions of various natures in our system. It is this dynamical population of the unpumped cavity modes and its nontrivial interplay with the other degrees of freedom which marks a sharp contrast to the free-space spin-orbit coupling [8.12–8.14, 8.58, 8.59] as well as all other previous cavity-based spin-orbit coupling schemes [8.45–8.47, 8.50].

As the frequency and the strength of the pump lasers are varied, in the mean-field regime the system displays three fundamentally different phases with distinct characteristics in density and spatial spin texture as shown in Fig. 8.2. The first phase is the *density-wave–spin-wave* (DW-SW) state, where the density has a crystalline structure and the pseudospin exhibits a spatial spin-wave texture along the cavity axis; see Fig. 8.4(a). The second phase is the *plane-wave–spin-spiral* (PW-SS) state, where the density is homogeneous while the pseudospin exhibits a spin-spiral texture as illustrated in Fig. 8.4(b). The third phase is the *density-wave–spin-spiral* (DW-SS) state, where a crystalline-ordered density is accompanied with a spin-spiral pseudospin texture; see Fig. 8.4(c). The latter two states with the spin-spiral texture have a Skyrmionic nature with a nontrivial topology [8.60, 8.61], and are intimately related to the emergence of cavity-induced spin-orbit coupling. The topologically trivial DW-SW state, on the other hand, breaks the continuous screw-like symmetry of the system, resulting in the

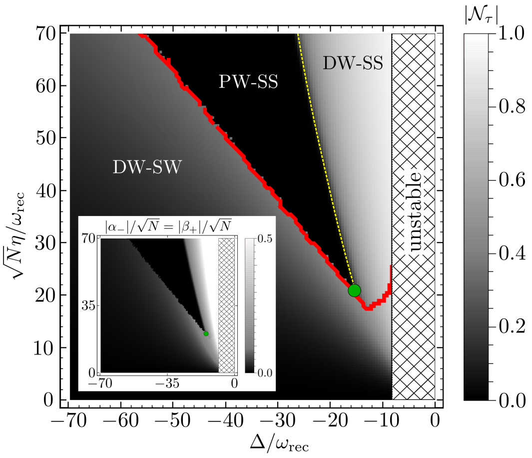

Figure 8.2: The mean-field atomic phase diagram in the rescaled parameter space $\{\sqrt{N}\eta/\omega_{\rm rec}, \Delta/\omega_{\rm rec}\}$. It displays three distinct phases: density-wave–spin-wave (DW-SW), plane-wave–spin-spiral (PW-SS), and density-wave–spin-spiral (DW-SS) states. The color coding shows the absolute values of the density-wave order parameters, $|\mathcal{N}_\downarrow| = |\mathcal{N}_\uparrow|$. The solid red curve marks the onset of the topological phase transition. The dashed yellow curve indicates the boundary of the second-order phase transition and the green dot indicates the tricritical point. The unstable parameter regions are marked by the hased pattern. The inset illustrates the cavity-field phase diagram in the same parameter space, where the color coding shows the absolute values of the cavity-field order parameters, $|\alpha_-|\sqrt{N} = |\beta_+|/\sqrt{N}$. It coincides precisely with the atomic phase diagram. The other parameters are set to $(U_0, \Omega_{0\rm R}, \kappa) = (-1, -1, 1)\omega_{\rm rec}$.

appearance of a gapless Goldstone mode in addition to the phonon sound mode, a characteristic of a supersolid with two broken continuous symmetries [8.14, 8.28, 8.44]. The topological phase transitions between the DW-SW and the spin-spiral states, which is a direct consequence of the emergence of cavity-induced spin-orbit coupling, exhibit first-order characteristics, while the quantum phase transition between the two spin-spiral states are second order. Remarkably, all the quantum phase transitions can be monitored *in situ* through the cavity output, as can be seen from the inset of Fig. 8.2.

The paper is organized as follows. We introduce the model in Sec. 8.2 and then derive the effective Hamiltonian and the Heisenberg equations of motion. We then find the steady-state solutions of the equations of motion in the mean-field limit in Sec. 8.3. In this section we discuss the atomic phase diagram (Sec. 8.3.1), the cavity-field phase diagram (Sec. 8.3.2), and the effect of cavity-induced emergent spin-orbit coupling (Sec. 8.3.3). Section 8.4 is devoted to the elementary excitations and the (broken) symmetries of the system. We present the concluding remarks in Sec. 8.5. Appendices 8.6 and 8.7 show the details of the adiabatic elimination of the atomic excited state and linearization of the Heisenberg equations of motion, respectively.

8.2 Model

Consider a Λ-type spin-1 BEC tightly confined into quasi-one dimension along one leg of a ring cavity in z direction as depicted in Fig. 8.1. The internal atomic states of interest consist of two pseudospin ground states, designated by $|\downarrow\rangle$ and $|\uparrow\rangle$, and an electronic excited state $|e\rangle$ with energies $\{\hbar\omega_\downarrow, \hbar\omega_\uparrow, \hbar\omega_e\}$. The transition $|\downarrow\rangle \leftrightarrow |e\rangle$ ($|\uparrow\rangle \leftrightarrow |e\rangle$) couples to a pair of degenerate, counterpropagating electromagnetic modes $\hat{a}_\pm e^{\pm ik_a z}$ ($\hat{b}_\pm e^{\pm ik_b z}$) of the ring cavity as shown in Fig. 8.1. The operator $\hat{a}_{+/-}$ ($\hat{b}_{+/-}$) annihilates a forward/backward moving photon in the first (second) pair of ring-cavity modes with a wave vector $k_a = \omega_a/c = 2\pi/\lambda_a$ ($k_b = \omega_b/c = 2\pi/\lambda_b$). For our desired system, the condition $|\omega_a - \omega_b|/\omega_{a(b)} \ll 1$ holds in general. Therefore, the assumptions $k := k_a \approx k_b$ and $\lambda := \lambda_a \approx \lambda_b$ are legitimate and will be used throughout this work. Each pair of modes (i.e., $\hat{a}_\pm$ or $\hat{b}_\pm$) has the same polarization, which is orthogonal to the polarization of the other pair; e.g., $\{\epsilon_+, \epsilon_-\}$. The mode $\hat{a}_+$ ($\hat{b}_-$) is driven by an external pump laser through the cavity mirror with a frequency $\tilde{\omega}_a$ ($\tilde{\omega}_b$) and an amplitude η_+ (η_-).

The single-particle Hamiltonian density of the system in the dipole and rotating-wave approximation reads

$$\mathcal{H} = \mathcal{H}_{0,\text{at}} + H_{0,\text{cav}} + \mathcal{H}_{\text{ac}} + H_{\text{pump}}, \tag{8.1}$$

with

$$\begin{aligned}
\mathcal{H}_{0,\text{at}} &= \frac{\hat{p}^2}{2m} + \hbar \sum_{\tau=\downarrow,\uparrow,e} \omega_\tau \hat{\sigma}_{\tau\tau}, \\
H_{0,\text{cav}} &= \hbar \sum_{j=+,-} \left(\omega_a \hat{a}_j^\dagger \hat{a}_j + \omega_b \hat{b}_j^\dagger \hat{b}_j\right), \\
\mathcal{H}_{\text{ac}} &= \hbar \Big\{ \Big[\mathcal{G}_\downarrow \left(e^{ikz}\hat{a}_+ + e^{-ikz}\hat{a}_-\right) \hat{\sigma}_{e\downarrow} \\
&\qquad + \mathcal{G}_\uparrow \left(e^{ikz}\hat{b}_+ + e^{-ikz}\hat{b}_-\right) \hat{\sigma}_{e\uparrow} \Big] + \text{H.c.} \Big\}, \\
H_{\text{pump}} &= i\hbar \left(\eta_+ \hat{a}_+^\dagger e^{-i\tilde{\omega}_a t} + \eta_- \hat{b}_-^\dagger e^{-i\tilde{\omega}_b t} - \text{H.c.}\right).
\end{aligned} \tag{8.2}$$

Here m is the atomic mass, $\hat{p} = i\hbar\partial_z$ is the atomic momentum operator and $\hat{\sigma}_{\tau\tau'} = |\tau\rangle\langle\tau'|$ are the atomic transition operators. The atom-photon coupling for the transition $|\downarrow\rangle \leftrightarrow |e\rangle$ ($|\uparrow\rangle \leftrightarrow |e\rangle$) is denoted as $\mathcal{G}_\downarrow$ ($\mathcal{G}_\uparrow$) and H.c. stands for the Hermitian conjugate. $\mathcal{H}_{0,\text{at}}$ and $H_{0,\text{cav}}$ are the bare atomic Hamiltonian density and the cavity-field Hamiltonian, respectively. $\mathcal{H}_{\text{ac}}$ represents the coupling between the atom and the cavity fields, and H_{pump} accounts for the pumping of the cavity fields.

The corresponding many-body Hamiltonian is obtained as

$$\begin{aligned}
H = &\int \hat{\Psi}^\dagger(z)(\mathcal{H}_{0,\text{at}} + \mathcal{H}_{\text{ac}})\hat{\Psi}(z) dz \\
&+ H_{0,\text{cav}} + H_{\text{pump}} + H_{\text{int}},
\end{aligned} \tag{8.3}$$

where $\hat{\Psi} = (\hat{\psi}_e, \hat{\psi}_\uparrow, \hat{\psi}_\downarrow)^\top$ is the three-component atomic field operator which satisfies the bosonic commutation relation $[\hat{\psi}_\tau(z), \hat{\psi}^\dagger_{\tau'}(z')] = \delta(z - z')\delta_{\tau,\tau'}$. The Hamiltonian

H_{int} accounts for two-body contact interactions between the atoms, and ensures the thermalization and relaxation of the BEC. However, we assume that the two-body contact interactions are negligibly small compared to cavity-mediated long-range interactions, which is a good approximation for typical cavity-QED experiments [8.28, 8.62]. Therefore, we will not explicitly include two-body contact interactions in our model.

The dynamics of the system is governed by the Heisenberg equations of motion of the atomic field operators $i\hbar\partial_t\hat{\psi}_\tau = [\hat{\psi}_\tau, H]$, and the photonic field operators $i\hbar\partial_t\hat{a}_\pm = [\hat{a}_\pm, H] - i\hbar\kappa\hat{a}_\pm$ and $i\hbar\partial_t\hat{b}_\pm = [\hat{b}_\pm, H] - i\hbar\kappa\hat{b}_\pm$. The decay (i.e., leakage) of cavity photons is included phenomenologically by adding the terms proportional to κ in the latter equations for the photonic-field operators. If the relative atomic detunings with respect to the pump lasers $\Delta_{\downarrow(\uparrow)} := \tilde{\omega}_{a(b)} - [\omega_e - \omega_{\downarrow(\uparrow)}]$ are large compared to the two-photon detuning $\delta := \Delta_\uparrow - \Delta_\downarrow$ and the atom-photon couplings $\{\mathcal{G}_\downarrow, \mathcal{G}_\uparrow\}$, the atomic excited state reaches a steady-state on a short time scale and its dynamics can be adiabatically eliminated. This results in a set of six coupled effective Heisenberg equations for the atomic pseudospin and photonic field operators

$$i\hbar\frac{\partial}{\partial t}\begin{pmatrix}\hat{\psi}_\downarrow\\ \hat{\psi}_\uparrow\end{pmatrix} = \mathcal{H}_{\mathrm{at}}\begin{pmatrix}\hat{\psi}_\downarrow\\ \hat{\psi}_\uparrow\end{pmatrix}, \tag{8.4a}$$

$$i\hbar\frac{\partial}{\partial t}\begin{pmatrix}\hat{a}_+\\ \hat{a}_-\\ \hat{b}_+\\ \hat{b}_-\end{pmatrix} = \mathcal{H}_{\mathrm{cav}}\begin{pmatrix}\hat{a}_+\\ \hat{a}_-\\ \hat{b}_+\\ \hat{b}_-\end{pmatrix} + i\hbar\begin{pmatrix}\eta_+\\ 0\\ 0\\ \eta_-\end{pmatrix}. \tag{8.4b}$$

The details are presented in Appendix 8.6.

Now $\mathcal{H}_{\mathrm{at}}$ and $\mathcal{H}_{\mathrm{cav}}$ are the “effective” atomic and cavity-field Hamiltonian densities, respectively, which contain the couplings between all atomic and photonic degrees of freedom. The effective atomic Hamiltonian density has the matrix form

$$\mathcal{H}_{\mathrm{at}} = \begin{pmatrix}\frac{\hat{p}^2}{2m} + \hbar\hat{U}_\downarrow(z) - \frac{\hbar\delta}{2} & \hbar\hat{\Omega}_{\mathrm{R}}(z)\\ \hbar\hat{\Omega}^\dagger_{\mathrm{R}}(z) & \frac{\hat{p}^2}{2m} + \hbar\hat{U}_\uparrow(z) + \frac{\hbar\delta}{2}\end{pmatrix}, \tag{8.5}$$

with the potential operators

$$\begin{aligned}\hat{U}_\downarrow(z) &= U_{0\downarrow}(\hat{a}^\dagger_+\hat{a}_+ + \hat{a}^\dagger_-\hat{a}_- + e^{-2ikz}\hat{a}^\dagger_+\hat{a}_- + e^{2ikz}\hat{a}^\dagger_-\hat{a}_+),\\ \hat{U}_\uparrow(z) &= U_{0\uparrow}(\hat{b}^\dagger_+\hat{b}_+ + \hat{b}^\dagger_-\hat{b}_- + e^{-2ikz}\hat{b}^\dagger_+\hat{b}_- + e^{2ikz}\hat{b}^\dagger_-\hat{b}_+),\end{aligned} \tag{8.6}$$

and the two-photon Raman coupling operator

$$\hat{\Omega}_{\mathrm{R}}(z) = \Omega_{0\mathrm{R}}(\hat{a}^\dagger_+\hat{b}_+ + \hat{a}^\dagger_-\hat{b}_- + e^{-2ikz}\hat{a}^\dagger_+\hat{b}_- + e^{2ikz}\hat{a}^\dagger_-\hat{b}_+). \tag{8.7}$$

Here we have introduced the maximum depth of the optical potential per photon $U_{0\tau} := 2|\mathcal{G}_\tau|^2/(\Delta_\downarrow + \Delta_\uparrow)$ and the maximum two-photon Raman transition frequency $\Omega_{0\mathrm{R}} := 2\mathcal{G}^*_\downarrow\mathcal{G}_\uparrow/(\Delta_\downarrow + \Delta_\uparrow)$. The former potential depth results from two-photon scatterings between cavity modes with the same polarization without changing the atomic internal state, whereas the latter frequency $\Omega_{0\mathrm{R}}$ is due to two-photon scatterings between

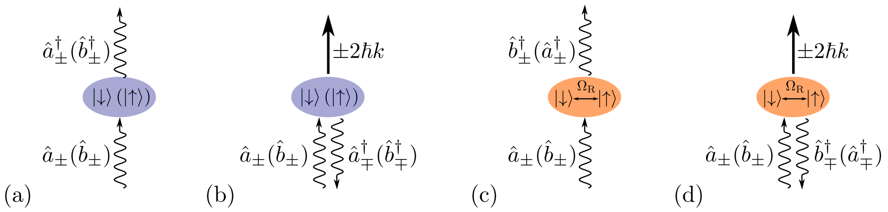

Figure 8.3: Schematic visualization of the two-photon Raman processes. The coherent scattering of a photon from a mode into itself (a) and into the corresponding degenerate counterpropagating mode with the same polarization (b) without changing the atomic internal state result in position-independent and position-dependent potential terms in $\hat{U}_\tau(z)$. The coherent scattering of a photon from a mode into another mode with an orthogonal polarization propagating in the same (c) and opposite (d) direction, accompanied with the atomic pseudospin flip $|\downarrow\rangle \leftrightarrow |\uparrow\rangle$, gives rise to position-independent and position-dependent Raman coupling terms in $\hat{\Omega}_\mathrm{R}(z)$, respectively.

cavity modes with orthogonal polarizations accompanied by an atomic pseudospin flip $|\downarrow\rangle \leftrightarrow |\uparrow\rangle$.

The coherent scattering of photons from a mode back into itself results in the position-independent energy shifts (i. e. , the terms $\hat{a}^\dagger_\pm \hat{a}_\pm$ and $\hat{b}^\dagger_\pm \hat{b}_\pm$) in the potential operators $\hat{U}_\tau(z)$, while the scattering of photons from a mode (say, $\hat{a}_+$) into its degenerate counterpropagating mode (i.e., $\hat{a}_-$) results in the position-dependent terms proportional to $e^{\pm 2ikz}$ in the potential operators. The former photon scatterings do not transfer any momentum to the atom, while the latter scatterings lead to $\pm 2\hbar k$ momentum kicks to the atom. These particular processes are schematically shown in Fig. 8.3(a) and Fig. 8.3(b), respectively.

The photon scattering between modes with orthogonal polarizations and the same propagation direction (that is, between $\hat{a}_\pm$ and $\hat{b}_\pm$) gives rise to the position-independent Raman coupling terms (i.e., the terms $\hat{a}^\dagger_+ \hat{b}_+$ and $\hat{a}^\dagger_- \hat{b}_-$) in $\hat{\Omega}_\mathrm{R}(z)$, while scattering between modes with orthogonal polarizations and opposite propagation directions (that is, between $\hat{a}_\pm$ and $\hat{b}_\mp$) results in the position-dependent Raman coupling terms proportional to $e^{\pm 2ikz}$ in the two-photon Raman coupling operator. These two-photon Raman processes are illustrated in Fig. 8.3(c) and Fig. 8.3(d). While the atomic pseudospin is flipped in both Raman processes, there is no net momentum transfer to the atom in the former processes, whereas the latter processes impart a $\pm 2\hbar k$ momentum to the atom. These latter Raman transition processes with $\pm 2\hbar k$ momentum kicks can induce a synthetic spin-orbit coupling for the atom.

The effective cavity-field Hamiltonian “density” in matrix form is given by

$$\mathcal{H}_{\mathrm{cav}} = \hbar \begin{pmatrix} -\tilde{\Delta}_a & U_{0\downarrow}\hat{\mathcal{N}}_{\downarrow} & \Omega_{0\mathrm{R}}\hat{S}_{-} & \Omega_{0\mathrm{R}}\hat{\mathcal{S}}_{-}^{(-)} \\ U_{0\downarrow}\hat{\mathcal{N}}_{\downarrow}^{\dagger} & -\tilde{\Delta}_a & \Omega_{0\mathrm{R}}\hat{\mathcal{S}}_{-}^{(+)} & \Omega_{0\mathrm{R}}\hat{S}_{-} \\ \Omega_{0\mathrm{R}}^{*}\hat{S}_{+} & \Omega_{0\mathrm{R}}^{*}\hat{\mathcal{S}}_{+}^{(-)} & -\tilde{\Delta}_b & U_{0\uparrow}\hat{\mathcal{N}}_{\uparrow} \\ \Omega_{0\mathrm{R}}^{*}\hat{\mathcal{S}}_{+}^{(+)} & \Omega_{0\mathrm{R}}^{*}\hat{S}_{+} & U_{0\uparrow}\hat{\mathcal{N}}_{\uparrow}^{\dagger} & -\tilde{\Delta}_b \end{pmatrix}, \tag{8.8}$$

where we have introduced the effective cavity detunings $\tilde{\Delta}_{a(b)} := (\Delta_{a(b)} + i\kappa) - U_{0\downarrow(\uparrow)}\hat{N}_{\downarrow(\uparrow)}$ with the relative cavity detunings with respect to the pump frequencies $\Delta_{a(b)} := \tilde{\omega}_{a(b)} - \omega_{a(b)}$ and the particle number operators

$$\hat{N}_{\tau} = \int \hat{\psi}_{\tau}^{\dagger}(z)\hat{\psi}_{\tau}(z)dz. \tag{8.9}$$

The off-diagonal coupling operators are given by

$$\hat{\mathcal{N}}_{\tau} = \int e^{-2ikz}\hat{\psi}_{\tau}^{\dagger}(z)\hat{\psi}_{\tau}(z)dz, \tag{8.10a}$$

$$\hat{S}_{-} = \hat{S}_{+}^{\dagger} = \int \hat{\psi}_{\downarrow}^{\dagger}(z)\hat{\psi}_{\uparrow}(z)dz, \tag{8.10b}$$

$$\hat{\mathcal{S}}_{-}^{(\pm)} = (\hat{\mathcal{S}}_{+}^{(\mp)})^{\dagger} = \int e^{\pm 2ikz}\hat{\psi}_{\downarrow}^{\dagger}(z)\hat{\psi}_{\uparrow}(z)dz, \tag{8.10c}$$

where $\hat{S}_{+}$ ($\hat{S}_{-}$) is the collective atomic spin raising (lowering) operator. The operators $\hat{\mathcal{N}}_{\tau}$ and $\hat{\mathcal{S}}_{\pm}^{(\pm)}$ are the density- (for pseudospin τ) and spin-wave operators, respectively.

The matrix elements of the effective cavity-field Hamiltonian density $\mathcal{H}_{\mathrm{cav}}$ give the strengths of the two-photon processes depicted in Fig. 8.3. The diagonal terms proportional to $\hat{N}_{\tau}$ correspond to the processes illustrated in Fig. 8.3(a) and result in the dispersive shifts $U_{0\tau}\hat{N}_{\tau}$ of the cavity frequencies. Terms proportional to $\hat{\mathcal{N}}_{\tau}$ (and their Hermitian conjugates) correspond to the processes shown in Fig. 8.3(b) and provide the couplings between degenerate counterpropagating modes with the same polarization. Finally, the matrix elements proportional to $\hat{S}_{\pm}$ and $\hat{\mathcal{S}}_{\pm}^{(\pm)}$ correspond to the pseudospin flipping processes depicted in Fig. 8.3(c) and Fig. 8.3(d), respectively, and yield the nontrivial couplings between modes with orthogonal polarizations.

The system possesses a screw-like continuous symmetry. It is manifested in the invariance of the total effective Hamiltonian corresponding to Eqs. (8.4) under a simultaneous spatial translation $z \to z + \Delta z$, phase rotations of the unpumped photonic field operators $\hat{a}_{-} \to \hat{a}_{-}e^{2ik\Delta z}$ and $\hat{b}_{+} \to \hat{b}_{+}e^{-2ik\Delta z}$, and phase rotations of the atomic field operators $\hat{\psi}_{\downarrow} \to \hat{\psi}_{\downarrow}e^{-ik\Delta z}$ and $\hat{\psi}_{\uparrow} \to \hat{\psi}_{\uparrow}e^{+ik\Delta z}$. Note that the phases of the pumped cavity modes $\hat{a}_{+}$ and $\hat{b}_{-}$ are fixed by the cavity pumps $\eta_{\pm}$. The phase rotation of $\hat{a}_{-}$ and $\hat{b}_{+}$ results in a shift of the potential minima in Eq. (8.6), defining the position of the atomic-density maxima. On the other hand, the phase shift of the atomic field operators leads to rotations of the spin operators: $\hat{S}_{+} \to \hat{S}_{+}e^{-2ik\Delta z}$ and $\hat{\mathcal{S}}_{+}^{(\pm)} \to \hat{\mathcal{S}}_{+}^{(\pm)}e^{-2ik\Delta z}$. Hence, a translation in space is tied to a corresponding rotation of the atomic spin, where the

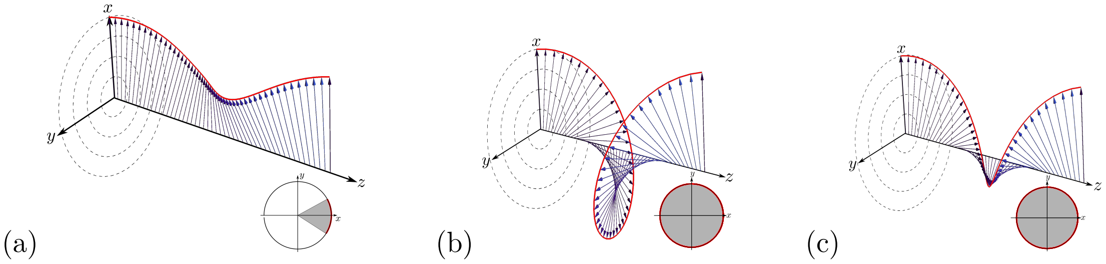

Figure 8.4: Spin textures along the cavity axis z in one unit cell of length $\lambda/2$ in different phases. The local atomic pseudospin vector $\mathbf{s}(z)$ is shown in the DW-SW phase for the parameters $(\Delta, \sqrt{N}\eta) = (-20, 20)\omega_{\mathrm{rec}}$ (a), the PW-SS phase for $(\Delta, \sqrt{N}\eta) = (-20, 30)\omega_{\mathrm{rec}}$ (b), and the DW-SS phase for $(\Delta, \sqrt{N}\eta) = (-20, 50)\omega_{\mathrm{rec}}$ (c). The small circles in the lower right corners display the projection of the spin textures in the x-y plane, where the grey regions indicate the angles swept by the pseudospin vector over a $\lambda/2$ distance. The other parameters are the same as Fig. 8.2.

rotation angle directly depends on the length of the spatial translation Δz. This leads to a screw-like continuous symmetry.

The system is highly nonlinear. The effective atomic Hamiltonian density depends on the cavity fields through the potential $\hat{U}_\tau(z)$ and the Raman operators $\hat{\Omega}_{\mathrm{R}}(z)$, while the effective cavity-field Hamiltonian density depends on the atomic fields via the atomic number $\hat{N}_\tau$, the density-wave $\hat{\mathcal{N}}_\tau$, the collective atomic spin $\hat{S}_\pm$, and the spin-wave $\hat{\mathcal{S}}_\pm^{(\pm)}$ operators. It is this nonlinear dynamics and the nontrivial interplay between various degrees of freedom which give rise to intriguing phenomena in our system, as it will be discussed in the subsequent sections. These nonlinear dynamics and the nontrivial interplay between the cavity modes survive even in the strong pumping limit $\eta_\pm \gg \omega_{\mathrm{rec}}$, with $\omega_{\mathrm{rec}} := \hbar k^2/2m$ being the recoil frequency. Although in the strong pumping limit the pumped cavity fields $\{\hat{a}_+, \hat{b}_-\}$ behave as classical fields, the unpumped modes $\{\hat{a}_-, \hat{b}_+\}$ still retain their quantum nature and behave as dynamical fields.

8.3 Mean-Field Results

In the following, we restrict our analysis to red-detuned pump lasers with respect to both bare atomic and cavity frequencies, i.e., $\{\Delta_{\downarrow,\uparrow}, \Delta_{a,b}\} < 0$. The atoms are therefore attracted to the intensity maxima of the light fields, while experiencing cavity cooling. In order to reduce the number of free parameters and capture the fundamental physics, we further focus on the special case of a completely symmetric configuration: $\Delta := \Delta_a = \Delta_b$, $\eta := \eta_+ = \eta_-$, $\delta = 0$, and $\mathcal{G}_\downarrow = \mathcal{G}_\uparrow$ which results in $U_0 := U_{0\downarrow} = U_{0\uparrow} = \Omega_{0\mathrm{R}}$. Despite these simplifying assumptions, the system is still very complex and gives rise to intriguing phenomena.

We find the stationary states of the system by self-consistently solving Eqs. (8.4)–(8.10) in the mean-field regime in the parameter space $\{\eta, \Delta\}$. This amounts to omitting quantum fluctuations and replacing the atomic and cavity field operators by their corresponding quantum averages: $\hat{\psi}_\tau \to \psi_\tau := \langle\hat{\psi}_\tau\rangle$, $\hat{a}_j \to \alpha_j := \langle\hat{a}_j\rangle$, and $\hat{b}_j \to \beta_j := \langle\hat{b}_j\rangle$. The parameters η and Δ are related, respectively, to the intensity and the frequency of the external pump lasers and can be readily tuned in experiment.

The effective atomic Hamiltonian density (8.5) is $\lambda/2$ periodic. Nonetheless, solving the equations for different numbers of unit cells (of length $\lambda/2$) reveals that the atomic condensate wave functions $\psi_\tau(z)$ are λ periodic in parameter regimes possessing cavity-induced spin-orbit coupling. Therefore, we always solve the mean-field equations corresponding to Eqs. (8.4)–(8.10) in two unit cells of total length λ with periodic boundary conditions. The relation between cavity-induced spin-orbit coupling and the doubling of the periodicity of the condensate wave functions will be discussed in more details in Sec. 8.3.3.

8.3.1 Atomic Phase Diagram

The mean-field density-wave order parameters $\mathcal{N}_\tau = \langle\hat{\mathcal{N}}_\tau\rangle$, cf. Eq. (8.10a), can be used to characterize the density structure of each BEC component. They quantify the magnitude of the density modulations of each BEC component, where a zero density-wave order parameter corresponds to a homogenous density distribution. Because of the symmetric choice of the parameters as described above, we always find that the absolute values of the two density-wave order parameters are equal to one another, $|\mathcal{N}_\downarrow| = |\mathcal{N}_\uparrow|$.

On the other hand, the mean-field local pseudospin vector

$$\mathbf{s}(z) = (s_x(z), s_y(z), s_z(z)) = \langle\psi_{\text{eff}}(z)|\,\boldsymbol{\sigma}\,|\psi_{\text{eff}}(z)\rangle\,,$$

where $|\psi_{\text{eff}}(z)\rangle := (\psi_\uparrow(z), \psi_\downarrow(z))^\top$ and $\boldsymbol{\sigma} = (\sigma_x, \sigma_y, \sigma_z)$ is the vector of the Pauli matrices, can be used to illustrate the spatial spin texture of the steady-states. The z component of the local pseudospin $s_z(z) = [|\psi_\uparrow(z)|^2 - |\psi_\downarrow(z)|^2]/2$ is zero everywhere in all parameter regimes due to the symmetric choice of the parameters. Therefore, the local pseudospin vector always lies in the x-y plane. We find that the transverse local pseudospin vector varies in space in all parameter regimes. In some regimes $\mathbf{s}(z)$ exhibits a $\lambda/2$-periodic "spin wave" of ferromagnetic-magnon nature, meaning that the spin angle $\phi(z) := \arctan(s_y(z)/s_x(z))$ only sweeps a small sector within the interval $[0, \pi/2]$ over a $\lambda/2$ distance. While for other parameter regimes, $\phi(z)$ sweeps a full 2π angle in the x-y plane over a $\lambda/2$ distance, leading to a $\lambda/2$-periodic "spin spiral" of topological Skyrmionic nature [8.60, 8.61]. As a result, the mean-field collective atomic pseudospins $S_\pm = \langle\hat{S}_\pm\rangle = \int[s_x(z) \pm is_y(z)]dz$ and the spin-wave order parameters $\mathcal{S}_\pm^{(\pm)} = \langle\hat{\mathcal{S}}_\pm^{(\pm)}\rangle = \int e^{\pm 2ikz}[s_x(z) \pm is_y(z)]dz$, cf. Eqs. (8.10b) and (8.10c), exhibit different behaviors in the spin-wave and the spin-spiral states.

The spin-wave and spin-spiral states can be quantitatively distinguished by their distinct topological structures via an appropriate topological invariant. The relevant topological invariant to characterize the spin texture of the system is the winding

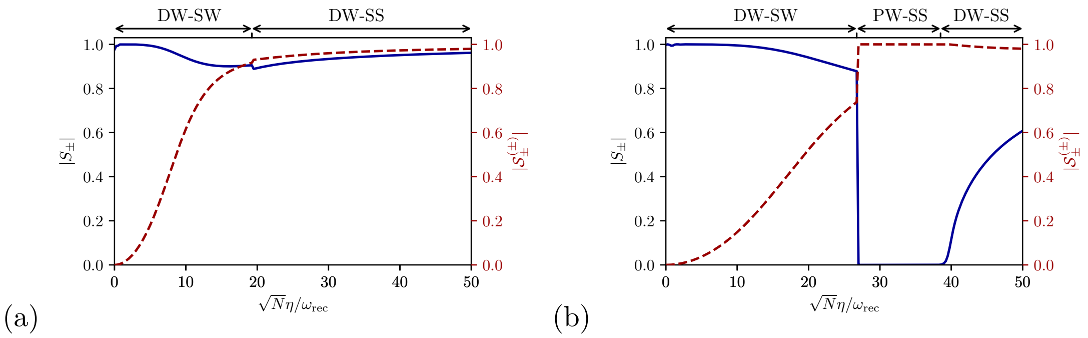

Figure 8.5: The absolute values of the collective atomic spins $|S_\pm|$ (blue solid curve) and the spin-wave order parameters $|\mathcal{S}_\pm^{(\pm)}|$ (red dashed curve) as a function of the rescaled pump strength $\sqrt{N}\eta/\omega_{\mathrm{rec}}$ for $\Delta = -10\omega_{\mathrm{rec}}$ (a) and $\Delta = -20\omega_{\mathrm{rec}}$ (b). The collective atomic spins $S_\pm$ are the dominant parameters in the DW-SW phase, while the spin-wave order parameters $\mathcal{S}_\pm^{(\pm)}$ are dominant in the PW-SS and DW-SS phases. Both parameters $\{S_\pm, \mathcal{S}_\pm^{(\pm)}\}$ exhibit first-order (second-order) characteristics across the phase transitions between the DW-SW and the DW-SS/PW-SS (between the PW-SS and the DW-SS). The other parameters are the same as Fig. 8.2.

number [8.63, 8.64]

$$\mathcal{W} := \frac{1}{2\pi}\int_0^{\lambda/2} [\partial_z \phi(z)] dz = \frac{\phi(\lambda/2) - \phi(0)}{2\pi}, \tag{8.11}$$

where $\phi(z)$ defines the direction of the local pseudospin vector $\mathbf{s}(z)$ in the x-y plane. Note that the angle $\phi(z)$ is tied to the relative phase between the two condensate wave functions $\psi_\downarrow(z)$ and $\psi_\uparrow(z)$. The winding number essentially counts the number of full rotations of the local pseudospin vector $\mathbf{s}(z)$ around the origin in one unit cell. Zero winding number corresponds to the topologically trivial spin-wave state, while a nonzero winding number (i.e., $\mathcal{W} = +1$) indicates the topological spin-spiral state.

The atomic phase diagram of the system in the rescaled parameter space $\{\sqrt{N}\eta/\omega_{\mathrm{rec}}, \Delta/\omega_{\mathrm{rec}}\}$ is shown in Fig. 8.2 and displays three fundamentally different phases. In the first phase, which corresponds to the region below the solid red curve in the phase diagram, the density order parameters are nonzero, $|\mathcal{N}_\tau| \neq 0$, while the winding number is zero, $\mathcal{W} = 0$. This implies that the atomic density distribution $n_\tau(z) = |\psi_\tau(z)|^2$ has a ($\lambda/2$-periodic) crystalline order and the local pseudospin $\mathbf{s}(z)$ exhibits a (also $\lambda/2$-periodic) spin-wave texture. Hence, we refer to this phase as the density-wave–spin-wave (DW-SW) state. Recall that $|\mathcal{N}_\downarrow| = |\mathcal{N}_\uparrow|$ due to the symmetric choice of parameters. The amplitude of the density modulations increases with increasing η, indicated by the increasing density-wave order parameters $|\mathcal{N}_\tau|$. Because of the direct pumping of two of the cavity modes and the presence of two-photon Raman processes which scatter photons into the unpumped modes without transfering momentum to the atoms as shown in Fig. 8.3(c), there is no threshold behavior for the onset of the density waves. This is in contrast to transversally pumped ring cavities [8.35, 8.44] and to the case where both pairs of modes $\{\hat{a}_\pm, \hat{b}_\pm\}$ couple to the same atomic transition [8.57]. The angle in the x-y plane which is sweeped by the local pseudospin vector $\mathbf{s}(z)$ over a distance of $\lambda/2$, is always restricted to the interval $[0, \pi/2]$ for the entire parameter regime of the DW-SW phase. Hence, the spin-wave oscillations remain small in this phase. A typical spin-wave texture in the DW-SW phase is illustrated in Fig. 8.4(a), where the local pseudospin vector $\mathbf{s}(z)$ exhibits small oscillations in the x-y plane. The change in the length of the local pseudospin vector is due to the density modulations of the condensates. Note that the local pseudospin vector $\mathbf{s}(z)$ always lies in the x-y plane, as $s_z(z) = 0$ owing to the symmetric choice of the parameters.

The second phase, corresponding to the uniform black region in the phase diagram of Fig. 8.2, is the plane-wave–spin-spiral (PW-SS) state. In this regime the density-wave order parameters are identically zero, $|\mathcal{N}_\tau| = 0$, while the winding number is nonzero, $\mathcal{W} = 1$. Therefore, the condensate densities are homogeneous in this phase, while the local pseudospin exhibits a spin-spiral texture. Figure 8.4(b) depicts a representative spin-spiral state in this phase. As indicated by the winding number $\mathcal{W} = 1$, the local pseudospin vector $\mathbf{s}(z)$ sweeps a full 2π angle over a $\lambda/2$ distance. The length of the local pseudospin vector is constant in space due to the uniform condensate densities in this phase. Note that again the local pseudospin vector has no z component, $s_z(z) = 0$.

In the third phase, both the density order parameters and the winding number are nonzero, $\{|\mathcal{N}_\tau| \neq 0, \mathcal{W} = 1\}$. This implies that the density wave and the spin-spiral coexist in this phase, hence the name density-wave–spin-spiral (DW-SS) state. The BEC densities exhibit strong modulations in this phase. The local pseudospin vector $\mathbf{s}(z)$, therefore, inherits this and its length changes drastically in space, while again sweeping a full 2π angle over a $\lambda/2$ distance as shown in Fig. 8.4(c). As for the other two phases, the local pseudospin vector lies in the x-y plane in the DW-SS phase.

For small cavity detuning, $\Delta \lesssim -9\omega_{\mathrm{rec}}$, the system becomes unstable (hashed region in Fig. 8.2). This is due to the fact that the effective relative cavity detuning, i.e., the dispersively shifted bare relative cavity detuning due to the presence of the atoms, becomes positive (i.e., blue detuned) resulting in cavity heating. In contrast to a single component BEC in a cavity where the dispersive shift is solely given by the factor $U_0 N$, an analytical expression for the dispersive shift of the cavity detuning in our model is nontrivial due to the various dispersive terms and coupling terms in the effective cavity-field Hamiltonian density (8.8).

The collective atomic spins $S_\pm$ and the spin-wave order parameters $\mathcal{S}_\pm^{(\pm)}$ exhibit distinct behaviors in these three phases. Figures 8.5(a) and 8.5(b) show the absolute values of $S_\pm$ (solid blue curves) and $\mathcal{S}_\pm^{(\pm)}$ (dashed red curves) as a function of the rescaled pump strength $\sqrt{N}\eta/\omega_{\mathrm{rec}}$ for constant cavity detunings $\Delta/\omega_{\mathrm{rec}} = -10$ and -20, respectively. By increasing the pump strength η from zero, for $\Delta = -10\omega_{\mathrm{rec}}$ in Fig. 8.5(a) the system undergoes a phase transition from the DW-SW state to the DW-SS state, while for $\Delta = -20\omega_{\mathrm{rec}}$ in Fig. 8.5(b) the phase transition from the DW-SW to the DW-SS occurs indirectly via the intermediate PW-SS state (cf. Fig. 8.2). While the collective atomic spins $S_\pm$ are nonzero in both DW-SW and DW-SS phases, it vanishes in the PW-SS phase. The latter can be understood by the fact that the local pseudospin vector $\mathbf{s}(z)$ has a constant length over space in the PW-SS phase and it does a full 2π rotation uniformly over one unit cell, resulting in $S_\pm = \int s_x(z)dz \pm \int is_y(z)dz = 0$. On the other hand the spin-wave order parameters $\mathcal{S}_\pm^{(\pm)}$ are nonzero in all three phases, indicating spin modulations in all regimes.

The winding number $\mathcal{W}$ jumps from zero to one across the phase transitions from the DW-SW to the PW-SS/DW-SS, signaling that these are topological phase transitions (the red solid curve in the phase diagram in Fig. 8.2, which is somewhat ragged due to the extremely slow convergence of numerics around these phase boundaries). In addition, the density-wave order parameters $\mathcal{N}_\tau$, the collective atomic spins $S_\pm$, and the spin-wave order parameters $\mathcal{S}_\pm^{(\pm)}$ exhibit discontinuous behaviors on the onset of these phase transitions (see Figs. 8.2 and 8.5). This indicates that the topological phase transitions from the DW-SW state to the PW-SS/DW-SS states also have first-order characteristics.

Although the atomic parameters $\{\mathcal{N}_\tau, S_\pm, \mathcal{S}_\pm^{(\pm)}\}$ change continuously across the PW-SS to DW-SS phase transition [see Figs. 8.2 and 8.5(b)], they exhibit nonanalytical behavior, a characteristic of a second-order phase transition. Therefore, the phase transition from the PW-SS to the DW-SS is second order (yellow dashed curve in the phase diagram in Fig. 8.2). Note that the winding number $\mathcal{W}$ is one in both phases, and therefore it does not change across this phase transition.

The phase boundary between the DW-SW and PW-SS phases is linear, whereas the other phase boundaries show more complex behaviors. All phase boundaries with different natures (i.e., topological first-order, and topologically trivial second-order phase transitions) meet at a single tricritical point, denoted by a green dot in the phase diagram in Fig. 8.2.

8.3.2 Cavity-Field Phase Diagram

The mean-field amplitudes of the unpumped cavity modes α_- and β_+ can be exploited as the cavity-field order parameters to further characterize the system. The inset of Fig. 8.2 shows the absolute values of the rescaled unpumped modes $|\alpha_-|/\sqrt{N} = |\beta_+|/\sqrt{N}$ in the rescaled parameter space $\{\sqrt{N}\eta/\omega_{\text{rec}}, \Delta/\omega_{\text{rec}}\}$. The absolute values of the unpumped modes are equal to each other once again due to the symmetric choice of the parameters. The cavity-field phase diagram has a similar form as the atomic phase diagram. In particular, the field phase boundaries coincide precisely with the atomic phase boundaries. The field order parameters $\{\alpha_-, \beta_+\}$ are nonzero in the DW-SW and DW-SS phases and increase monotonically by increasing pump strength. However, they are identically zero in the entire PW-SS phase. This can be understood by noting that the density-order parameters $\mathcal{N}_\tau$ and the collective spins $S_\pm$ are zero in this regime as discussed above. The dynamics of the two umpumped modes $\{\alpha_-, \beta_+\}$ then decouple completely from the pumped ones $\{\alpha_+, \beta_-\}$ [see Eq. (8.8)], and, therefore, no photons are scattered into these unpumped modes in this phase. This leads to uniform potentials and Raman coupling [see Eqs. (8.6) and (8.7)], which in turn results in homogeneous condensate densities in a self-consistent manner. This signifies the nonlinear dynamical nature of

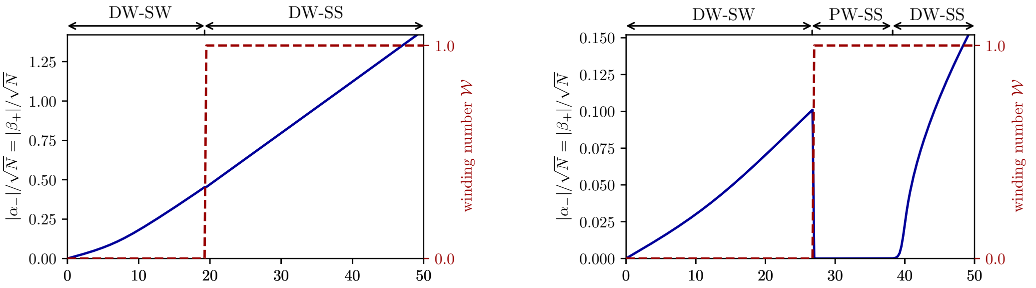

(a) (b)

Figure 8.6: The absolute values of the cavity-field order parameters $|\alpha_-|/\sqrt{N} = |\beta_-|/\sqrt{N}$ (blue solid curve) an the winding number $\mathcal{W}$ (red dashed curve) as a function of the rescaled pump strength $\sqrt{N}\eta/\omega_{\rm rec}$ for $\Delta = -10\omega_{\rm rec}$ (a) and $\Delta = -20\omega_{\rm rec}$ (b). The cavity-field order parameters display first-order (second-order) characteristics across the phase transitions from the DW-SW to the PW-SS/DW-SS (from the PW-SS to the DW-SS). The first-order phase transition coincides with the topological phase transition, where the winding number $\mathcal{W}$ jumps from zero to one. The other parameters are the same as Fig. 8.2.

the system.

Figures 8.6(a) and 8.6(b) show cuts through the field phase diagram along the rescaled pump strength $\sqrt{N}\eta/\omega_{\rm rec}$ at constant cavity detunings $\Delta/\omega_{\rm rec} = -10$ and -20, together with the corresponding winding numbers $\mathcal{W}$. The field-order parameters $\{\alpha_-, \beta_+\}$ exhibit similar behavior as the atomic parameters $\{\mathcal{N}_\tau, S_\pm, \mathcal{S}_\pm^{(\pm)}\}$. They display first-order (second-order) characteristics across the phase transitions from the DW-SW state to the PW-SS/DW-SS states (from the PW-SS state to the DW-SS phase), in accordance with the atomic phase transitions. Likewise, the first-oder phase transition coincides with the topological phase transition, where the winding $\mathcal{W}$ jumps from zero to one. Therefore, there is a one to one correspondence between the atomic parameters $\{\mathcal{N}_\tau, S_\pm, \mathcal{S}_\pm^{(\pm)}\}$ on the one hand and the cavity-field order parameters $\{\alpha_-, \beta_+\}$ on the other hand. As a consequence, all the quantum phase transitions (and their natures) can be mapped out nondestructively through the cavity outputs. This is an important and distinct feature of the system.

8.3.3 Atomic Momentum Distributions and Cavity-Induced Spin-Orbit Coupling

The discrete momentum exchange between the atoms and the light fields allows the decomposition of the condensate wave functions into plane waves $\psi_\tau(z) = \sum_{j=-\infty}^{\infty} c_{\tau,j} e^{ijkz}$. The absolute values of the probability amplitudes $c_{\tau,j}$ of the lowest six momentum states $j \in \{0, \pm1, \pm2, +3\}$ in the rescaled parameter space $\{\sqrt{N}\eta/\omega_{\rm rec}, \Delta/\omega_{\rm rec}\}$ for each condensate component τ are shown in Fig. 8.7. Note that the even and odd momentum

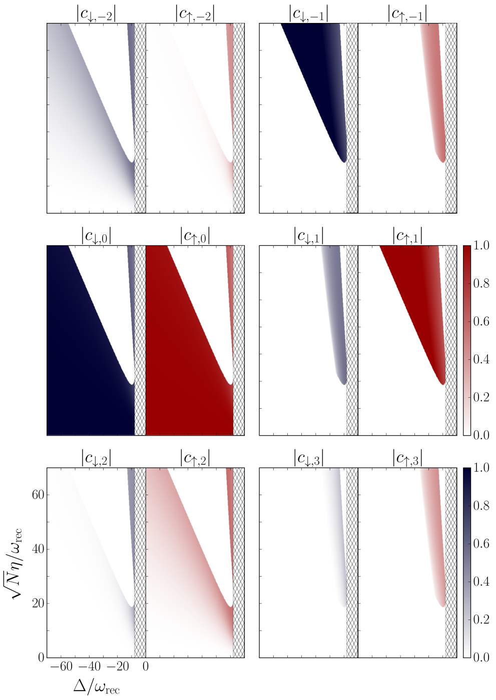

Figure 8.7: The absolute values of the probability amplitudes $c_{\tau,j}$ of the lowest six momentum states $j \in \{0, \pm1, \pm2, +3\}$ for each condensate component τ in the parameter space $\{\sqrt{N}\eta/\omega_{\rm rec}, \Delta/\omega_{\rm rec}\}$. For the the sake of clarity, vertical cuts of these diagrams for fixed $\Delta = -20\omega_{\rm rec}$ are presented in Fig. 8.8. The other parameters are the same as Fig. 8.2.

states do not coexist together. The boundary separating even and odd momenta coincides precisely with the topological phase boundary between the DW-SW state and the PW-SS/DW-SS states, illustrated in Fig. 8.2. The region where even (odd) momenta are occupied corresponds to the DW-SW (PW-SS or DW-SS) phase. In the DW-SW phase the zero momentum $c_{\tau,0}$ is the dominant state for both condensates and the nonzero higher momenta result in density modulations. In the PW-SS phase, the condensate wave functions are solely composed of one momentum component $|c_{\downarrow,1}| = |c_{\uparrow,-1}| = 1/\sqrt{2}$, as expected for a homogeneous condensate. While in the DW-SS phase, higher odd momenta are also populated, leading to density modulations. For the sake of clarity, vertical cuts along the rescaled pump strength $\sqrt{N}\eta/\omega_{\rm rec}$ for constant cavity detuning $\Delta = -20\omega_{\rm rec}$ of these momentum phase diagrams are also shown in Fig. 8.8.

The phase boundaries where the even momenta completely deplete and the odd momenta are populated coincide exactly with the first-order topological phase transitions from the DW-SW state to the PW-SS/DW-SS state. That is, the onset of the occupation of the odd momenta marks the appearance of spin spirals and the discrete jump of the winding number $\mathcal{W}$ from zero to one; cf. Figs. 8.5(b), 8.6(b) and 8.8. This is intimately connected to the emergence of cavity-induced spin-orbit coupling for the atoms. The transition from the even to the odd momenta can be triggered and relaxed by (even very weak) two-body contact interactions, which are not included explicitly in our model.

The emergence of cavity-induced spin-orbit coupling can be most easily seen in the PW-SS phase, where the umpumped cavity modes $\{\alpha_-, \beta_+\}$ are zero. The effective atomic Hamiltonian density (8.5) in the mean-field approximation then simplifies to

$$\begin{aligned}\mathcal{H}_{\mathrm{SOC}} = \frac{1}{2m}(pI_{2\times 2} - \hbar k\sigma_z)^2 + \frac{\hbar U_0}{2}(|\alpha_+|^2 - |\beta_-|^2)\sigma_z \\ + \hbar\Omega_{0\mathrm{R}}\left(\alpha_+^*\beta_-\sigma_{\downarrow\uparrow} + \alpha_+\beta_-^*\sigma_{\uparrow\downarrow}\right),\end{aligned} \tag{8.12}$$

after applying a unitary transformation [8.45]. Here $I_{2\times 2}$ is the identity matrix in the pseudospin space, σ_z is the third Pauli matrix and $\sigma_{\downarrow\uparrow}$ and $\sigma_{\uparrow\downarrow}$ are the transition matrices in the pseudospin basis. The Hamiltonian (8.12) has exactly the form of an equal Rashba-Dresselhaus spin-orbit coupled Hamiltonian, saving that the the Raman coupling now depends on the cavity fields $\{\alpha_+, \beta_-\}$ and is determined self-consistently. This Hamiltonian has been studied before in Refs. [8.45, 8.46, 8.48] and indeed exhibits characteristics of spin-orbit coupled quantum gases, with extra features resulting from the dynamical nature of the synthetic spin-orbit coupling.

The effect of the spin-orbit coupling can be seen in the momentum distributions of the condensate wavefuctions in the PW-SS phase, where different pseudospin states are coupled to different momentum states. That is, the pseudospin down is solely coupled to the $+\hbar k$ momentum (recall that in the PW-SS phase $|c_{\downarrow,1}| = 1/\sqrt{2}$), while the the pseudospin up is only coupled to the $-\hbar k$ momentum ($|c_{\uparrow,-1}| = 1/\sqrt{2}$). Since the PW-SS phase sets in at large pump strengths η, the effective Raman transition rate $\Omega_{0\mathrm{R}}\alpha_+^*\beta_-$ is, therefore, always large. Hence, the single-particle energy dispersion of the spin-orbit coupled Hamiltonian (8.12) possesses a single minimum at $p = 0$, as expected for large Raman transition rates [8.12]. This is also the reason that both condensates have equal particle numbers, $|c_{\downarrow,1}| = |c_{\uparrow,-1}| = 1/\sqrt{2}$, as the state at $p = 0$ has an equal contribution from the up and down components due to the symmetric choice of the parameters.

Despite of the fact that in the DW-SS phase the effective atomic Hamiltonian density (8.5) cannot be recast in the usual form of the equal Rashba-Dresselhaus spin-orbit-coupled Hamiltonian (8.12), the cavity-induced synthetic spin-orbit coupling still manifests itself in the momentum distributions of the condensate wave functions. Although higher odd momenta are also populated, the $\pm\hbar k$ momenta are still the dominant states, and different pseudospin states are strongly coupled to solely one of them, $|c_{\downarrow,1}| = |c_{\uparrow,-1}| \lesssim 1/\sqrt{2}$. This is in sharp contrast to the DW-SW phase, where both pseudospin states couple to the same zero momentum state, $|c_{\downarrow,0}| = |c_{\uparrow,0}| \lesssim 1/\sqrt{2}$, resulting in no cavity-induced spin-orbit coupling.

The period doubling of the condensate wave functions in the spin-orbit coupled PW-SS and DW-SS regimes, as it was mentioned at the beginning of Sec. 8.3, can be understood through the momentum decomposition of the wave functions in these phases. In these spin-orbit coupled states, the condensate wave functions $\psi_\tau(z) = \sum_{j=-\infty}^{\infty} c_{\tau,2j+1}e^{i(2j+1)kz}$ are composed of solely odd momenta and are, therefore, λ

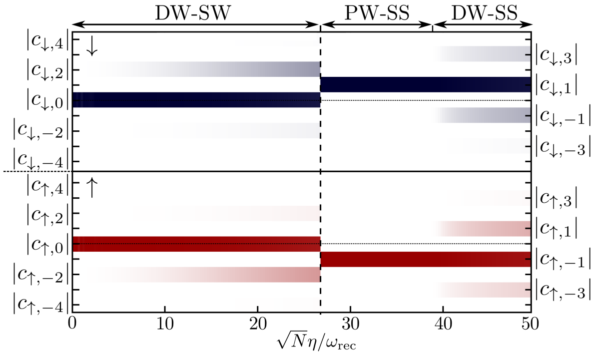

Figure 8.8: The absolute values of the probability amplitudes $c_{\tau,j}$ of the lowest six momentum states $j \in \{0, \pm 1, \pm 2, +3\}$ for each condensate component τ as a function of $\sqrt{N}\eta/\omega_{\mathrm{rec}}$ for a constant $\Delta = -20\omega_{\mathrm{rec}}$. The even and odd momenta do not coexist. In the onset of the first-order topological phase transition from the DW-SW state to the PW-SS phase, the even momenta completely deplete and give way to the odd momenta. The other parameters are the same as Fig. 8.2.

periodic. This is in contrast to the $\lambda/2$ periodicity of the condensate wave functions $\psi_\tau(z) = \sum_{j=-\infty}^{\infty} c_{\tau,2j} e^{2ijkz}$ in the DW-SW state (which are comprised of only even momenta) and the Hamiltonian density (8.5).

The unpumped cavity modes $\{\hat{a}_-, \hat{b}_+\}$ play an important role in the emergence of cavity-induced spin-orbit coupling beyond a threshold for the pump-strength. This can be understood by re-examining the possible spin flipping processes in the system (see Fig. 8.3). The essential photon-scattering processes for the spin-orbit coupling are the ones depicted in Fig. 8.3(d), where photons are scattered between the modes $\hat{a}_\pm \leftrightarrow \hat{b}_\mp$ (via the atomic pseudospin flipping $|\downarrow\rangle \leftrightarrow |\uparrow\rangle$) and a $\pm 2\hbar k$ momentum is transferred to the atom. Whereas the scattering processes shown in Fig. 8.3(c), where photons are scattered between the modes $\hat{a}_\pm \leftrightarrow \hat{b}_\pm$ (again via the atomic pseudospin flipping $|\downarrow\rangle \leftrightarrow |\uparrow\rangle$) without any momentum kick to the atom, are not vital for the spin-orbit coupling. However, triggering the former processes costs more energy than the latter ones due to the atomic kinetic energy gain. Therefore, for lower pump strengths (i.e., in the DW-SW phase) the spin flipping processes with no momentum kick to the atoms are energetically favored and are the dominant processes. The essential spin-orbit coupling processes become energetically favored and dominant beyond the pump-strength threshold on the onset of the PW-SS and DW-SS states, where the sum of the kinetic energies of the odd momenta becomes less than the corresponding even ones.

The interplay between spin flipping processes with and without momentum transfer to the atom can be seen by comparing the collective atomic spins $S_\pm$ and the spin-wave order parameters $\mathcal{S}_\pm^{(\pm)}$. Recall that $S_\pm$ ($\mathcal{S}_\pm^{(\pm)}$) quantifies the spin flipping processes without (with $\pm 2\hbar k$) momentum kick to the atom. As can be seen from Fig. 8.5,

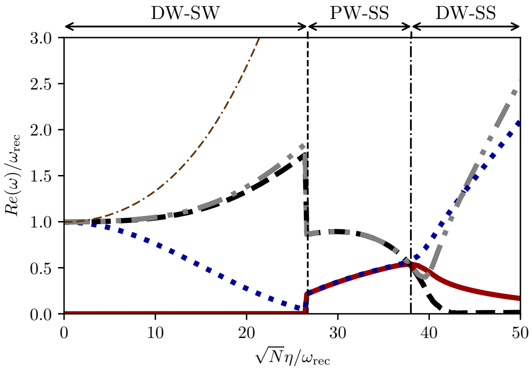

Figure 8.9: Real part of the five lowest-lying collective excitations of the system for $\Delta = -20\omega_{\rm rec}$ as a function of the rescaled pump strength $\sqrt{N}\eta/\omega_{\rm rec}$. The other parameters are the same as Fig. 8.2.

the collective spins $S_\pm$ are the dominant quantities in the DW-SW phase, while the spin-wave order parameters $\mathcal{S}_\pm^{(\pm)}$ become dominant only in the PW-SS and DW-SS phases. Consequently, cavity-induced spin-orbit coupling emerges only in the PW-SS and DW-SS regimes. This is in sharp contrast to the free space spin-orbit-coupled BEC, where spin-orbit coupling emerges at an infinitesimal Raman frequency [8.12].

8.4 Collective Excitations

In order to check the stability of our mean-field results and to obtain a deeper understanding of the system, we calculate the collective excitations of the system above the mean-field steady-states. To this end, we linearize the Heisenberg equations of motion (8.4) for quantum fluctuations of both atomic condensate wave functions $\delta\psi_\tau(x,t) = \delta\psi_\tau^{(+)}(x)e^{-i\omega t} + [\delta\psi_\tau^{(-)}(x)]^* e^{i\omega^* t}$, and field mode fluctuations $\delta\alpha_\pm(t) = \delta\alpha_\pm^{(+)}e^{-i\omega t} + [\delta\alpha_\pm^{(-)}]^* e^{i\omega^* t}$ and $\delta\beta_\pm(t) = \delta\beta_\pm^{(+)}e^{-i\omega t} + [\delta\beta_\pm^{(-)}]^* e^{i\omega^* t}$ around the mean-field stationary solutions $\{\psi_{0\tau}(x), \alpha_{0\pm}, \beta_{0\pm}\}$. The linearized equations can be recast in matrix form,

$$\omega\mathbf{f} = \mathbf{M}_{\rm B}\mathbf{f} \tag{8.13}$$

where $\mathbf{f}$ is a vector composed of the atomic condensate and the field-mode fluctuations $\{\delta\psi_\tau^{(\pm)}, \delta\alpha_\pm^{(\pm)}, \delta\beta_\pm^{(\pm)}\}$ and $\mathbf{M}_{\rm B}$ is a (nonhermitian) Bogoliubov matrix. We relegate the details to Appendix 8.7.

We numerically diagonalize the Bogoliubov matrix $\mathbf{M}_{\rm B}$ as a function of the pump strength to obtain the collective excitation spectrum $\omega(\eta)$. Figure 8.9 shows the real part of the five lowest lying positive-frequency excitations of the system as a function of the rescaled pump strength $\sqrt{N}\eta/\omega_{\rm rec}$ at a fixed cavity detuning $\Delta = -20\omega_{\rm rec}$.

In the DW-SW regime corresponding to $\sqrt{N}\eta \lesssim 27\omega_{\rm rec}$, there exists a gapless Goldstone mode, i. e. $\mathrm{Re}(\omega) = 0$. This is associated with the spontaneously broken continuous screw-like symmetry of the system in this regime. This symmetry breaking is a consequence of the occupation of the even (in particular, the zero) momentum states in this phase, which leads to wave functions of the form $\psi_\tau(z) = (c_{\tau,0} + c_{\tau,\pm 2}e^{\pm 2ikz} + \dots)$. A spatial translation of the wave functions $\psi_\tau(z) \rightarrow \psi_\tau(z + \Delta z)$ cannot be compensated by the phase rotation of the condensate wave functions $\psi_\downarrow \rightarrow \psi_\downarrow e^{-ik\Delta z}$ and $\psi_\uparrow \rightarrow \psi_\uparrow e^{ik\Delta z}$, because of the occupation of the zero momentum state $c_{\tau,0} \neq 0$. Hence, the condensate wave functions in the DW-SW regime are not invariant under the continuous symmetry group of the Hamiltonian and, therefore, they spontaneously break the continuous symmetry of the system. The appearance of this extra gapless Goldstone mode, in addition to the gapless phonon mode resulting from the spontaneous breaking of the internal gauge symmetry which is not shown here, indicates that the DW-SW state is a supersolid, i. e. a state with two spontaneously broken continuous symmetries [8.14, 8.28, 8.44]. A supersolid has the characteristics of both a crystal and a superfluid, that is, it is a state with a long-range periodic density order which can flow without experiencing any friction force.

For infinitely small values of η, the collective excitations at frequencies $\sim \omega_{\mathrm{rec}}$ are fourfold degenerate. These excitations correspond to condensate fluctuations of both BEC components at momenta $\pm\hbar k$. With increasing η, one of these branches approaches the zero energy. The point where this excitation branch touches zero coincides exactly with the mean-field critical pump strength for the phase transition from the DW-SW state to the PW-SS phase (dashed line in Fig. 8.9). As soon as the gap of the lowest $\pm\hbar k$ branch closes, the odd momenta become the lower energy states and the synthetic spin-orbit coupling emerges. Hence, it is the interplay between the two lowest even and odd excitation branches (solid red and dotted blue in Fig. 8.9) that leads to emergent spin-orbit coupling in this system.

In the PW-SS regime all excitation branches are doubly degenerate and gapped, indicating that the continuous symmetry of the system is not broken. This is intuitively obvious since the spin spiral with no density modulation perfectly respects the screw-like symmetry of the system. This can be seen most readily by the fact that the condensate wave functions $\psi_\downarrow(z) = c_{\downarrow,1}e^{ikz}$ and $\psi_\uparrow(z) = c_{\uparrow,-1}e^{-ikz}$ are invariant under the screw-like symmetry transformation: $\psi_\downarrow(z) \rightarrow \psi_\downarrow(z + \Delta z)e^{-ik\Delta z} = \psi_\downarrow(z)$ and $\psi_\uparrow(z) \rightarrow \psi_\uparrow(z + \Delta z)e^{ik\Delta z} = \psi_\uparrow(z)$.

With further increasing pump strength η the degenerate branches start to split up at the value of η which perfectly coincides with the mean-field critical pump strength for the phase transition from the PW-SS state to the DW-SS regime (horizontal dash dotted line). One of the excitation branches (dashed black curve) exhibits an exotic "quasi" gapless-mode behavior in large pump strengths. This can be understood by examining the condensate wave functions in this regime. For the sake of simplicity we restrict our argument to one pseudospin, say, $\psi_\downarrow(z) = (c_{\downarrow,1}e^{ikz} + c_{\downarrow,-1}e^{-ikz} + c_{\downarrow,3}e^{3ikz} + \dots)$. In general, this state is not invariant under the screw-like symmetry transformation $\psi_\downarrow(z) \rightarrow \psi_\downarrow(z + \Delta z)e^{-ik\Delta z} \neq \psi_\downarrow(z)$. That said, at the onset of the DW-SS state $c_{\downarrow,1}$ is the dominant probability amplitude in this expansion as can be seen from Fig. 8.7, i.e., $|c_{\downarrow,1}| \gg \{|c_{\downarrow,-1}|, |c_{\downarrow,3}|, \cdots\}$. Therefore, this wave function can be approximated as $\psi_\downarrow(z) \simeq c_{\downarrow,1}e^{ikz}$, which approximately preserves the screw-like symmetry of the system. For larger pump strengths, however, the higher momentum-state coefficients are not negligible anymore, resulting in a state which breaks the screw-like symmetry of the system. This leads to the appearance of a quasi gapless mode $\sim 0\omega_{\text{rec}}$ at large η, which never reaches the zero energy exactly because $c_{\downarrow,1}$ remains dominant throughout the entire regime. This is in stark contrast to the DW-SW state, where even in the onset of this phase at very small pump strengths the screw-like symmetry is broken completely. This is due to the dominant population of the zero momentum state $|c_{\tau,0}| \gg \{|c_{\tau,\pm2}|, |c_{\tau,\pm4}|, \cdots\}$ in this entire regime (recall that the zero momentum state is the one that breaks the screw-like symmetry of the system in the DW-SW state).

It should be mentioned that imaginary parts of the collective excitations remain remarkably small for a dissipative system, i. e. $\kappa \neq 0$. This is a hint for the dynamical stability of the phases which is also confirmed by performing a real time evolution of the stationary state solutions.

8.5 Conclusion and Outlook

We theoretically studied an effective two-component BEC inside a ring cavity, which possesses two pairs of nearly resonant running-wave modes with orthogonal polarizations. Our proposed model takes into account both atomic internal and external degrees of freedom, as well as the field amplitude and polarizations degrees of freedom. We predict that even in the simplest symmetric choice of parameters, the interplay between various degrees of freedom already results in novel phases and exotic quantum phase transitions of different natures. All the phases and the quantum phase transitions between them can be readily realized by solely tuning the frequencies and powers of the pump lasers, relevant parameters in cavity-QED experiments [8.26, 8.27, 8.62]. Remarkably, all the quantum phase transitions, including the topological one, can be monitored directly through the cavity outputs. Our proposal can be implemented with minor modifications to state-of-the-art experiments in cavity QED [8.19, 8.20, 8.25, 8.26, 8.62, 8.65–8.67] and it may open a new direction for studying topological effects in ultracold atoms via *in situ* monitoring. Additional physics may arise for asymmetric choices of the parameters as well as the inclusion of large two-body contact interactions. However, we leave the investigation of these interesting issues for future works.

Acknowledgements

We thank C. Simon, F. Piazza, and C. Zimmermann for fruitful discussions. We acknowledge support by the Austrian Science Fund FWF through the Projects SFB FoQuS P13 and No. I1697-N27.

8.6 Appendix: Adiabatic Elimination of the Excited State

Here we demonstrate how the model given in Eq. (8.4) can be obtained from the single-particle Hamiltonian density (8.1). The single-particle Hamiltonian density (8.1) can be transferred into the rotating frame of the pump lasers through $\tilde{\mathcal{H}} = \mathcal{U}\mathcal{H}\mathcal{U}^\dagger + i\hbar(\partial_t\mathcal{U})\mathcal{U}^\dagger$ and exploiting the unitary transformation

$$
\begin{aligned}
\mathcal{U} = \exp\Big\{ i\Big[&(\hat{a}_+^\dagger \hat{a}_+ + \hat{a}_-^\dagger \hat{a}_- - \hat{\sigma}_{\downarrow\downarrow})\tilde{\omega}_a \\
&+(\hat{b}_+^\dagger \hat{b}_+ + \hat{b}_-^\dagger \hat{b}_- - \hat{\sigma}_{\uparrow\uparrow})\tilde{\omega}_b\Big] t\Big\}.
\end{aligned}
$$

The corresponding many-body Hamiltonian expressed in the formalism of second quantization then reads,

$$
\begin{aligned}
H = &\int dz \hat{\mathbf{\Psi}}^\dagger \mathcal{M} \hat{\mathbf{\Psi}} - \hbar \sum_{j=+,-} \left(\Delta_a \hat{a}_j^\dagger \hat{a}_j + \Delta_b \hat{b}_j^\dagger \hat{b}_j\right) \\
&+ i\hbar \left[\eta_+ \hat{a}_+^\dagger + \eta_- \hat{b}_-^\dagger - \text{H.c.}\right],
\end{aligned}
\tag{8.14}
$$

where $\hat{\mathbf{\Psi}}(z) = (\hat{\psi}_\downarrow(z), \hat{\psi}_\uparrow(z), \hat{\psi}_e(z))^\mathsf{T}$, and

$$
\mathcal{M} = \begin{pmatrix}
\frac{\hat{p}^2}{2m} - \frac{\hbar\delta}{2} & 0 & \mathcal{M}_{13} \\
0 & \frac{\hat{p}^2}{2m} + \frac{\hbar\delta}{2} & \mathcal{M}_{23} \\
\mathcal{M}_{31} & \mathcal{M}_{32} & \frac{\hat{p}^2}{2m} - \frac{\hbar}{2}(\Delta_\downarrow + \Delta_\uparrow)
\end{pmatrix},
\tag{8.15}
$$

with the elements

$$
\begin{aligned}
\mathcal{M}_{31} = \mathcal{M}_{13}^\dagger = \hbar\mathcal{G}_\downarrow \left(e^{ikz}\hat{a}_+ + e^{-ikz}\hat{a}_-\right), \\
\mathcal{M}_{32} = \mathcal{M}_{23}^\dagger = \hbar\mathcal{G}_\uparrow \left(e^{ikz}\hat{b}_+ + e^{-ikz}\hat{b}_-\right).
\end{aligned}
\tag{8.16}
$$

The constant term $[(\omega_\downarrow + \tilde{\omega}_a)/2 + (\omega_\uparrow + \tilde{\omega}_b)/2] I_{3\times3}$ is omitted. The dynamics of the atomic and cavity field operators can be determined by simultaneously solving the following Heisenberg equations of motion $i\hbar\partial_t\hat{\psi}_\tau = [\psi_\tau, H]$ and $i\hbar\partial_t\hat{a}_j/\hat{b}_j = [\hat{a}_j/\hat{b}_j, H] - i\hbar\kappa\hat{a}_j/\hat{b}_j$. Substituting the Hamiltonian (8.14) leads to the following set of coupled differential equations

$$
\begin{aligned}
i\hbar\frac{\partial}{\partial t}\hat{\psi}_\downarrow &= \left(\frac{\hat{p}^2}{2m}-\frac{\hbar}{2}\delta\right)\hat{\psi}_\downarrow+\hbar\mathcal{G}_\downarrow^*\left(e^{-ikz}\hat{a}_+^\dagger+e^{ikz}\hat{a}_-^\dagger\right)\hat{\psi}_e,\\
i\hbar\frac{\partial}{\partial t}\hat{\psi}_\uparrow &= \left(\frac{\hat{p}^2}{2m}+\frac{\hbar}{2}\delta\right)\hat{\psi}_\uparrow+\hbar\mathcal{G}_\uparrow^*\left(e^{-ikz}\hat{b}_+^\dagger+e^{ikz}\hat{b}_-^\dagger\right)\hat{\psi}_e,\\
i\hbar\frac{\partial}{\partial t}\hat{a}_+ &= -\hbar(\Delta_a+i\kappa)\hat{a}_++\hbar\mathcal{G}_\downarrow^*\int dze^{-ikz}\hat{\psi}_\downarrow^\dagger\hat{\psi}_e+i\hbar\eta_+,\\
i\hbar\frac{\partial}{\partial t}\hat{a}_- &= -\hbar(\Delta_a+i\kappa)\hat{a}_-+\hbar\mathcal{G}_\downarrow^*\int dze^{ikz}\hat{\psi}_\downarrow^\dagger\hat{\psi}_e,\\
i\hbar\frac{\partial}{\partial t}\hat{b}_+ &= -\hbar(\Delta_b+i\kappa)\hat{b}_++\hbar\mathcal{G}_\uparrow^*\int dze^{-ikz}\hat{\psi}_\uparrow^\dagger\hat{\psi}_e,\\
i\hbar\frac{\partial}{\partial t}\hat{b}_- &= -\hbar(\Delta_b+i\kappa)\hat{b}_-+\hbar\mathcal{G}_\uparrow^*\int dze^{ikz}\hat{\psi}_\uparrow^\dagger\hat{\psi}_e+i\hbar\eta_-.
\end{aligned}
\tag{8.17}
$$

If the relative atomic detunings $\Delta_\uparrow$ and $\Delta_\downarrow$ are large compared to the two-photon detuning δ and the atom-photon couplings $\mathcal{G}_\uparrow$ and $\mathcal{G}_\downarrow$, the atomic excited state reaches a steady-state on a short time scale and its dynamics can be eliminated adiabatically. By setting $\partial_t\hat{\psi}_e=0$ in the Heisenberg equation of motion for $\hat{\psi}_e$ and omitting the kinetic energy compared to the term proportional to $\hbar(\Delta_\uparrow+\Delta_\downarrow)$, we obtain the steady-state field operator of the atomic excited state

$$
\begin{aligned}
\hat{\psi}_e^{\mathrm{ss}} \simeq \frac{2}{(\Delta_\downarrow+\Delta_\uparrow)}\Big[&\mathcal{G}_\downarrow\left(e^{ikz}\hat{a}_++e^{-ikz}\hat{a}_-\right)\hat{\psi}_\downarrow\\
&+\mathcal{G}_\uparrow\left(e^{ikz}\hat{b}_++e^{-ikz}\hat{b}_-\right)\hat{\psi}_\uparrow\Big].
\end{aligned}
\tag{8.18}
$$

This steady-state field operator can be substituted into the Heisenberg equations of motion (8.17) resulting in a set of six coupled nonlinear equations for $\{\hat{\psi}_\downarrow,\hat{\psi}_\uparrow,\hat{a}_\pm,\hat{b}_\pm\}$ given in Eq. (8.4).

8.7 Appendix: Linearized Equations

In this appendix we describe the calculations leading to the collective excitation spectrum presented in section 8.4 in more detail. Plugging the ansatz $\psi_\tau(x,t) = \psi_{0\tau}(x) + \delta\psi(x,t)$, $\alpha_\pm(t) = \alpha_{\pm 0} + \delta\alpha_\pm(t)$ and $\beta_\pm(t) = \beta_{\pm 0} + \delta\beta_\pm(t)$ into the mean field version of Eq. (8.4) and performing the Bogoliubov transformation as it is already discussed in section 8.4 leads to the following linearized equations for the modes

$$
\begin{aligned}
\omega\delta\alpha_+^{(+)} &= -\tilde{\Delta}_a\delta\alpha_+^{(+)} + U_{0\downarrow}\mathcal{N}_\downarrow\delta\alpha_+^{(+)} + \Omega_{0\mathrm{R}}S_-\delta\beta_+^{(+)} + \Omega_{0\mathrm{R}}\mathcal{S}_-^{(1/2)}\delta\beta_-^{(+)} \\
&\quad + U_{0\downarrow}\mathcal{A}_{+*}^{\downarrow}\delta\psi_\downarrow^{(+)} + U_{0\downarrow}\mathcal{A}_+^{\downarrow}\delta\psi_\downarrow^{(-)} + \Omega_{0\mathrm{R}}\mathcal{B}_{+*}^{\downarrow}\delta\psi_\uparrow^{(+)} + \Omega_{0\mathrm{R}}\mathcal{B}_+^{\uparrow}\delta\psi_\downarrow^{(-)}, \\
\omega\delta\alpha_+^{(-)} &= \tilde{\Delta}_a^*\delta\alpha_+^{(-)} - U_{0\downarrow}\mathcal{N}_\downarrow^*\delta\alpha_-^{(-)} - \Omega_{0\mathrm{R}}^*S_-^*\delta\beta_+^{(-)} - \Omega_{0\mathrm{R}}^*\mathcal{S}_-^{(1)*}\delta\beta_-^{(-)} \\
&\quad - U_{0\downarrow}\mathcal{A}_{+*}^{\downarrow*}\delta\psi_\downarrow^{(-)} - U_{0\downarrow}\mathcal{A}_+^{\downarrow*}\delta\psi_\downarrow^{(+)} - \Omega_{0\mathrm{R}}^*\mathcal{B}_{+*}^{\downarrow*}\delta\psi_\uparrow^{(-)} - \Omega_{0\mathrm{R}}^*\mathcal{B}_+^{\uparrow*}\delta\psi_\downarrow^{(+)}, \\
\omega\delta\alpha_-^{(+)} &= -\tilde{\Delta}_a\delta\alpha_-^{(+)} + U_{0\downarrow}\mathcal{N}_\downarrow^*\delta\alpha_+^{(+)} + \Omega_{0\mathrm{R}}S_-\delta\beta_-^{(+)} + \Omega_{0\mathrm{R}}\mathcal{S}_-^{(2)}\delta\beta_+^{(+)} \\
&\quad + U_{0\downarrow}\mathcal{A}_{-*}^{\downarrow}\delta\psi_\downarrow^{(+)} + U_{0\downarrow}\mathcal{A}_-^{\downarrow}\delta\psi_\downarrow^{(-)} + \Omega_{0\mathrm{R}}\mathcal{B}_{-*}^{\downarrow}\delta\psi_\uparrow^{(+)} + \Omega_{0\mathrm{R}}\mathcal{B}_-^{\uparrow}\delta\psi_\downarrow^{(-)}, \\
\omega\delta\alpha_-^{(-)} &= \tilde{\Delta}_a^*\delta\alpha_-^{(-)} - U_{0\downarrow}\mathcal{N}_\downarrow\delta\alpha_+^{(-)} - \Omega_{0\mathrm{R}}^*S_-^*\delta\beta_-^{(-)} - \Omega_{0\mathrm{R}}^*\mathcal{S}_-^{(2)*}\delta\beta_+^{(-)} \\
&\quad - U_{0\downarrow}\mathcal{A}_{-*}^{\downarrow*}\delta\psi_\downarrow^{(-)} - U_{0\downarrow}\mathcal{A}_-^{\downarrow*}\delta\psi_\downarrow^{(+)} - \Omega_{0\mathrm{R}}^*\mathcal{B}_{-*}^{\downarrow*}\delta\psi_\uparrow^{(-)} - \Omega_{0\mathrm{R}}^*\mathcal{B}_-^{\uparrow*}\delta\psi_\downarrow^{(+)}, \\
\omega\delta\beta_+^{(+)} &= -\tilde{\Delta}_a\delta\beta_+^{(+)} + U_{0\uparrow}\mathcal{N}_\uparrow\delta\beta_-^{(+)} + \Omega_{0\mathrm{R}}^*S_-^*\delta\alpha_+^{(+)} + \Omega_{0\mathrm{R}}\mathcal{S}_-^{(2)*}\delta\alpha_-^{(+)} \\
&\quad + U_{0\uparrow}\mathcal{B}_{+*}^{\uparrow}\delta\psi_\uparrow^{(+)} + U_{0\uparrow}\mathcal{B}_+^{\uparrow}\delta\psi_\uparrow^{(-)} + \Omega_{0\mathrm{R}}^*\mathcal{A}_{+*}^{\uparrow}\delta\psi_\downarrow^{(+)} + \Omega_{0\mathrm{R}}^*\mathcal{A}_+^{\downarrow}\delta\psi_\uparrow^{(-)}, \\
\omega\delta\beta_+^{(-)} &= \tilde{\Delta}_a^*\delta\beta_+^{(-)} - U_{0\uparrow}\mathcal{N}_\uparrow^*\delta\beta_-^{(-)} - \Omega_{0\mathrm{R}}S_-\delta\alpha_+^{(-)} - \Omega_{0\mathrm{R}}\mathcal{S}_-^{(2)}\delta\alpha_-^{(-)} \\
&\quad - U_{0\uparrow}\mathcal{B}_{+*}^{\uparrow*}\delta\psi_\uparrow^{(-)} - U_{0\uparrow}\mathcal{B}_+^{\uparrow*}\delta\psi_\uparrow^{(+)} - \Omega_{0\mathrm{R}}\mathcal{A}_{+*}^{\uparrow*}\delta\psi_\downarrow^{(-)} - \Omega_{0\mathrm{R}}\mathcal{A}_+^{\downarrow*}\delta\psi_\uparrow^{(+)}, \\
\omega\delta\beta_-^{(+)} &= -\tilde{\Delta}_a\delta\beta_-^{(+)} + U_{0\uparrow}\mathcal{N}_\uparrow^*\delta\beta_+^{(+)} + \Omega_{0\mathrm{R}}^*S_-^*\delta\alpha_-^{(+)} + \Omega_{0\mathrm{R}}^*\mathcal{S}_-^{(1)*}\delta\alpha_+^{(+)} \\
&\quad + U_{0\uparrow}\mathcal{B}_{-*}^{\uparrow}\delta\psi_\uparrow^{(+)} + U_{0\uparrow}\mathcal{B}_-^{\uparrow}\delta\psi_\uparrow^{(-)} + \Omega_{0\mathrm{R}}^*\mathcal{A}_{-*}^{\uparrow}\delta\psi_\downarrow^{(+)} + \Omega_{0\mathrm{R}}^*\mathcal{A}_-^{\downarrow}\delta\psi_\uparrow^{(-)}, \\
\omega\delta\beta_-^{(-)} &= \tilde{\Delta}_a^*\delta\beta_-^{(-)} - U_{0\uparrow}\mathcal{N}_\uparrow\delta\beta_+^{(-)} - \Omega_{0\mathrm{R}}S_-\delta\alpha_-^{(-)} - \Omega_{0\mathrm{R}}\mathcal{S}_-^{(1)}\delta\alpha_+^{(-)} \\
&\quad - U_{0\uparrow}\mathcal{B}_{-*}^{\uparrow*}\delta\psi_\uparrow^{(-)} - U_{0\uparrow}\mathcal{B}_-^{\uparrow*}\delta\psi_\uparrow^{(+)} - \Omega_{0\mathrm{R}}\mathcal{A}_{-*}^{\uparrow*}\delta\psi_\downarrow^{(-)} - \Omega_{0\mathrm{R}}\mathcal{A}_-^{\downarrow*}\delta\psi_\uparrow^{(+)},
\end{aligned}
\tag{8.19}
$$

where we introduced the following shorthand notations

$$
\begin{aligned}
\mathcal{A}_\pm^{\downarrow\uparrow}\xi &:= \int A_\pm^{\downarrow\uparrow}\xi dz, \\
\mathcal{A}_{\pm*}^{\downarrow\uparrow}\xi &:= \int A_{\pm*}^{\downarrow\uparrow}\xi dz, \\
\mathcal{B}_\pm^{\downarrow\uparrow}\xi &:= \int B_\pm^{\downarrow\uparrow}\xi dz, \\
\mathcal{B}_{\pm*}^{\downarrow\uparrow}\xi &:= \int B_{\pm*}^{\downarrow\uparrow}\xi dz,
\end{aligned}
\tag{8.20}
$$

with

$$\begin{aligned}
A_{\pm}^{\downarrow\uparrow} &= \psi_0^{\downarrow\uparrow}\left(\alpha_{0\pm} + e^{\mp 2ikz}\alpha_{0\mp}\right),\\
A_{\pm *}^{\downarrow\uparrow} &= \psi_0^{\downarrow\uparrow *}\left(\alpha_{0\pm} + e^{\mp 2ikz}\alpha_{0\mp}\right),\\
B_{\pm}^{\downarrow\uparrow} &= \psi_0^{\downarrow\uparrow}\left(\beta_{0\pm} + e^{\mp 2ikz}\beta_{0\mp}\right),\\
B_{\pm *}^{\downarrow\uparrow} &= \psi_0^{\downarrow\uparrow *}\left(\beta_{0\pm} + e^{\mp 2ikz}\beta_{0\mp}\right).
\end{aligned} \tag{8.21}$$

The linearized equations for the atomic degrees of freedom read in

$$\begin{aligned}
\omega\delta\psi_{\downarrow}^{(+)} &= \frac{1}{\hbar}\left[D_{\downarrow,1} - \mu\right]\delta\psi_{\downarrow}^{(+)} + \hbar\Omega_{\mathrm{R}}(z)\delta\psi_{\uparrow}^{(+)}\\
&\quad + U_{0\downarrow}\left(A_{+*}^{\downarrow *}\delta\alpha_{+}^{(+)} + A_{-*}^{\downarrow *}\delta\alpha_{-}^{(+)} + A_{+}^{\downarrow}\delta\alpha_{+}^{(-)} + A_{-}^{\downarrow}\delta\alpha_{-}^{(-)}\right)\\
&\quad + \Omega_{0\mathrm{R}}\left(B_{+}^{\uparrow}\delta\alpha_{+}^{(-)} + B_{-}^{\uparrow}\delta\alpha_{-}^{(-)} + A_{+*}^{\uparrow *}\delta\beta_{+}^{(+)} + A_{-*}^{\uparrow *}\delta\beta_{-}^{(+)}\right),\\
\omega\delta\psi_{\downarrow}^{(-)} &= -\frac{1}{\hbar}\left[D_{\downarrow,1} - \mu\right]^{*}\delta\psi_{\downarrow}^{(-)} - \hbar\Omega_{\mathrm{R}}^{*}(z)\delta\psi_{\uparrow}^{(-)}\\
&\quad - U_{0\downarrow}\left(A_{+*}^{\downarrow}\delta\alpha_{+}^{(-)} + A_{-*}^{\downarrow}\delta\alpha_{-}^{(-)} + A_{+}^{\downarrow *}\delta\alpha_{+}^{(+)} + A_{-}^{\downarrow *}\delta\alpha_{-}^{(+)}\right)\\
&\quad - \Omega_{0\mathrm{R}}^{*}\left(B_{+}^{\uparrow *}\delta\alpha_{+}^{(+)} + B_{-}^{\uparrow *}\delta\alpha_{-}^{(+)} + A_{+*}^{\uparrow}\delta\beta_{+}^{(-)} + A_{-*}^{\uparrow}\delta\beta_{-}^{(-)}\right),\\
\omega\delta\psi_{\uparrow}^{(+)} &= \frac{1}{\hbar}\left[D_{\uparrow,2} - \mu\right]\delta\psi_{\uparrow}^{(+)} + \hbar\Omega_{\mathrm{R}}^{*}(z)\delta\psi_{\downarrow}^{(+)}\\
&\quad + U_{0\uparrow}\left(B_{+*}^{\uparrow *}\delta\beta_{+}^{(+)} + B_{-*}^{\uparrow *}\delta\beta_{-}^{(+)} + B_{+}^{\uparrow}\delta\beta_{+}^{(-)} + B_{-}^{\uparrow}\delta\beta_{-}^{(-)}\right)\\
&\quad + \Omega_{0\mathrm{R}}^{*}\left(B_{+*}^{\downarrow *}\delta\alpha_{+}^{(+)} + B_{-*}^{\downarrow *}\delta\alpha_{-}^{(+)} + A_{+}^{\downarrow}\delta\beta_{+}^{(-)} + A_{-}^{\downarrow}\delta\beta_{-}^{(-)}\right),\\
\omega\delta\psi_{\uparrow}^{(-)} &= -\frac{1}{\hbar}\left[D_{\uparrow,2} - \mu\right]^{*}\delta\psi_{\uparrow}^{(-)} - \hbar\Omega_{\mathrm{R}}(z)\delta\psi_{\downarrow}^{(-)}\\
&\quad - U_{0\uparrow}\left(B_{+*}^{\uparrow}\delta\beta_{+}^{(-)} + B_{-*}^{\uparrow}\delta\beta_{-}^{(-)} + B_{+}^{\uparrow *}\delta\beta_{+}^{(+)} + B_{-}^{\uparrow *}\delta\beta_{-}^{(+)}\right)\\
&\quad - \Omega_{0\mathrm{R}}\left(B_{+*}^{\downarrow}\delta\alpha_{+}^{(-)} + B_{-*}^{\downarrow}\delta\alpha_{-}^{(-)} + A_{+}^{\downarrow *}\delta\beta_{+}^{(+)} + A_{-}^{\downarrow *}\delta\beta_{-}^{(+)}\right),
\end{aligned} \tag{8.22}$$

where we introduce the shorthand notation $D_{\downarrow\uparrow,i} := -\frac{p^2}{2m} + \hbar U_{\downarrow\uparrow}(z) + (-1)^i\frac{\hbar\delta}{2}$ and μ denotes the chemical potential.

The set of equations (8.19) and (8.22) can be written in matrix form which results in Eq. (8.13). Since we do not have an analytical steady-state solution for the condensate wave functions and the cavity modes, we numerically diagonalize the Bogoliubov matrix for a numerically determined steady-state solution to obtain the collective excitation spectrum presented in Fig. 8.9.

9 Conclusions and Outlook

The publications presented above advance the growing field of research aiming for novel many-body cavity QED setups to simulate new types of emergent quantum phenomena.

To present the research articles in a consistent manner, the necessary theoretical background, which is needed to understand the studied systems and models, was provided. The different methods and concepts covering the interaction of classical or quantized matter with light fields in free space or inside resonators were then applied to specific problems. Since the focus of the present thesis was to study systems with continuous symmetries and light induced long-range interactions, we studied systems where ultracold atom clouds are coupled to the plane wave modes of a ring resonator or to two non-interfering light fields in free space.

The initially posed question whether the self-ordering phase transition in systems with continuous symmetries leads to phases with new intruiging properties was answered in several steps. To get a basic understanding of the underlying physics, we first studied a classical model of a ring cavity with non-interfering pump fields. It revealed that the system's continuous symmetry can be broken for sufficiently large light intensities. Tuning the relative intensity ratio between the two pump lasers allows the realization of either a collective atomic recoil laser (CARL) or a self-ordered state with a constant center-of-mass velocity.

This collective instability leading to a self-ordered state in a longitudinally pumped ring cavity raised the question whether a similar effect could be obtained in free space. In this case, the whole continuum of electromagnetic modes can be accessed, which resulted in the prediction of the effect of spontaneous crystallization of ultracold atoms in an optical lattice with emergent lattice spacing. This system allows the efficient simulation of crystal-like structures with dynamic long-range interactions.

In a later work we again focused on ring cavities and showed that the self-ordered state of a BEC in a transversally pumped ring cavity realizes a supersolid, which is a direct result of the continuous translational symmetry of the system.

A particularly interesting direction in quantum gas cavity QED is the inclusion of spin degrees of freedom. Thus, in a final step, we calculated the phase diagram for a Spinor-Bose gas coupled to the counterpropagating modes of a ring cavity. This reveals different non-trivial spin phases ranging from spin-waves with supersolid features to topologically non-trivial states. In particular, the possibility to trigger a topological phase transition by tuning the cavity pump parameters is a prominent feature of this setup.

In conclusion, the present thesis shows, that light-induced collective instabilities in systems with continuous symmetries allow the simulation of new non-trivial phases of quantum matter. The light mediated long-range interactions result in emergent optical lattices for the atoms which exhibit different properties compared to the externally prescribed lattices in conventional quantum simulation setups. This makes these systems an ideal tool to simulate new types of synthetic solid-state systems with ultracold atoms.

The findings of this thesis motivate the future study of related systems in a more generalized context. Possible objectives and extensions would, for example, be generalizations to higher dimensions and the analysis of the influence of quantum fluctuations on the predicted quantum phase transitions. The extension of the spontaneous crystallization effect in free space to spin degrees of freedom is expected to result in the emergence of non-trivial spin-states. Furthermore, the study of similar setups for fermions are a promising research direction. Another idea would be including atomic dipole-dipole interactions to these models. In this case, long-range interactions with competing length scales can lead to effects like frustration or the appearance of superlattices. In addition, the supersolid features of the self-ordered phases imply that they could be used as free-falling zero temperature masses for gravitational acceleration sensors.

Finally, it should be remarked that first experimental evidences of spontaneous crystallization for a Bose-Einstein condensate in free space and the growing number of experiments, which are closely related to the setups studied in this thesis, promise the experimental realization of the proposed effects in the near future.

10 Publication

Journal of Optics **19**, 065401 (2017)

Generating a Stationary Infinite Range Tractor Force via a Multimode Optical Fibre[†]

C. A. Ebongue[1], D. Holzmann[1], S. Ostermann[1] and H Ritsch[1]

[1]*Institut für Theoretische Physik, Universität Innsbruck,*
Technikerstraße 21, A-6020 Innsbruck, Austria

Optical fibres confine and guide light almost unattenuated and thus convey light forces to polarizable nano-particles over very long distances. Radiation pressure forces arise from scattering of guided photons into free space while gradient forces are based on coherent scattering between different fibre modes or propagation directions. Interestingly, even scattering between co-propagating modes induces longitudinal forces as the transverse confinement of the light modes creates mode dependent longitudinal wave-vectors and photon momenta. We generalize a proven scattering matrix based approach to calculate single as well as inter-particle forces to include several forward and backward propagating modes. We show that an injection of the higher order mode only in a two mode fibre will induce a stationary tractor force against the injection direction, when the mode coupling to the lower order mode dominates against backscattering and free space losses. Generically this arises for non-absorbing particles at the centre of a waveguide. The model also gives improved predictions for inter-particle forces in evanescent nanofibre fields as experimentally observed recently. Surprisingly strong tractor forces can also act on whole optically bound arrays.

doi: 10.1088/2040-8986/aa69f2

[†] The author of the present thesis, together with D. Holzmann, contributed to this work primarily in an intensive advisory role, discussing the model, the numerical and analytical methods and the scientific conclusions. All the primary calculations and simulations were performed by C. A. Ebongue.

10.1 Introduction

In an optical fibre, light is transversely confined and transmitted over very long distances without attenuation. The field can be well decomposed in transverse modes, each of them associated with a specific transverse field pattern and a corresponding longitudinal propagation wave vector. For specially designed fibres as optical nano-fibres or hollow core fibres a significant fraction of the light intensity is propagating in free space outside the actual fibre material and can interact with particles in this region [10.1, 10.2]. Such a geometry can either be realized by placing the particles inside a multi-mode hollow core fibre [10.3, 10.4] or trap them close to the surface of a tapered nanofibre with strong evanescent field components [10.5].

If one places a nanoscopic particle or even a single atom into the fibre fields, it will significantly perturb the light propagation and redistribute the field among different modes and propagation directions. As the light carries momentum, the corresponding photon redistribution leads to a net optical force [10.5]. The magnitude and direction of this force strongly depends on the fibre and particle geometry and the properties of the injected field. For several particles coupled to the same fibre, collective scattering enhances these forces and creates strong inter-particle forces depending on their relative distance. This leads to optical binding, selfordering and non-linear motional dynamics [10.6–10.8].

In some recent work we exhibited that important properties of these forces can be well understood from a generalized beam splitter approach involving only two fibre modes and an additional free space loss mode [10.5]. Surprisingly this model also allows to identify a parameter regime, where the total force on a particle points against the wave-vector of the impinging light, i.e. we get a tractor beam force [10.9]. This feature even persists for arrays of several bound particles.

Physically the tractor beam phenomenon is tight to the fact, that scattering from a higher order to a lower order mode requires a momentum contribution from the particle along the field propagation. Thus due to momentum conservation the particle is thus pushed in the opposite direction. The momentum exchange is, however, smaller than for backscattering a photon into the opposite direction. Hence for a more realistic calculation one needs to include the backscattered fields and absorption as competing processes.

Note that injecting phase coherent superpositions of light simultaneously into two transverse modes can create 3D optical trapping positions along the fibre [10.10]. Particles in these traps can be moved along the fibre in any direction by moving the traps via a relative phase control of the two modes in time [10.11]. This is different from our tractor beam mechanism, which is independent of position along the fibre and does not require external phase control.

Here we will investigate the properties and limitations of implementing such a generic tractor beam mechanism for small beads trapped in the field of an optical two-mode nanofibre. While a full numerical calculation using 3D finite element software is possible [10.12], it does not allow to scan large parameter and size ranges. Hence it is difficult to get good qualitative understanding and the whole range of possibilities

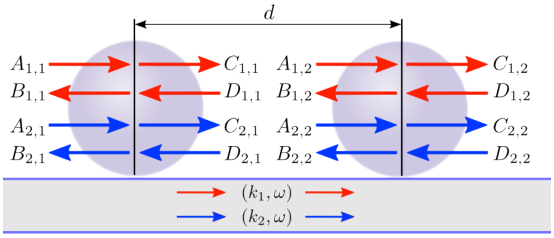

Figure 10.1: Schematic picture of two micro-spheres trapped close to an optical two mode fibre. In the presented model the spheres are approximated as beam splitters and the fields are determined by the incoming and outgoing amplitudes. The red arrows denote the amplitudes for the first (fundamental) mode and blue arrows characterize the second (higher order) mode. The first index for the amplitudes defines the mode number whereas the second index stands for the particle number. An analogous picture holds for a particle in the field of a hollow waveguide [10.13, 10.14].

offered by such a system.

Hence to better get the central idea, we will first study a rather idealized two mode model including only for forward scattering and some general absorption losses to identify the key parameter region for the appearance of tractor forces. In a second step we will generalize to a more realistic description including the backscattered fields and loss to free space. While it seems difficult to find realistic favourable parameters for a tractor forces in multi mode nanofibres, hollow core fibres seem much more promising. Finally we go beyond the case of single particles and study how ordering and optical binding can be combined with tractor forces.

10.2 Model

We consider N polarizable spherical particles within the field of a multimode optical waveguide [10.13–10.15]. The beads in the field are modelled as effective beam-splitters as shown in Fig. 10.1, which couple the local field mode amplitudes left and right of the beam splitter. These mode amplitudes are connected via an effective scattering matrix representing the underlying microscopic scattering processes integrated over the bead volume. As the bead only interacts with a spatial fraction of the mode, this matrix on the one hand includes forward and backward scattering of photons into the same transverse fibre mode as well as on the other hand it allows cross-coupling between the fundamental and the higher order transverse modes.

As depicted in Fig. 10.2 the amplitudes $0 \leq t_{ij} \leq 1$ describe forward scattering processes (into the same mode for $i = j$ and into any other mode for $i \neq j$) the reflection coefficients $0 \leq r_{ij} \leq 1$ describe reflections into the same mode as well as mode mixing reflections into the other transverse mode (cf. Fig. 10.2). In principle all these coefficients have to be derived from solving the corresponding Helmholtz equations for

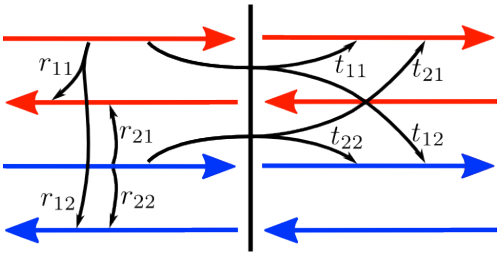

Figure 10.2: The fundamental processes which are described by the presented model. All reflection processes are shown on the left side of the beam-splitter and all transmission processes are shown towards the right side of the beam-splitter. Of course, all processes are mirror symmetric and can also occur into the opposite direction.

any specific implementation and boundary conditions. This has to be done numerically or by fitting experimental results [10.5]. We will stay with a general approach for the moment and only give some estimates for specific examples in Appendix A.

At this point we thus end up with four independent mode amplitudes connected via a four-port beam splitter matrix. The most general matrix, which describes the occurring processes as they are depicted in Fig. 10.2 takes the form

$$\mathbf{M}_{4p} = \begin{pmatrix} t_{11}e^{i\phi_{11}} & t_{21}e^{i\phi_{21}} & r_{11}e^{i\psi_{11}} & r_{21}e^{i\psi_{21}} \\ t_{12}e^{i\phi_{12}} & t_{22}e^{i\phi_{22}} & r_{12}e^{i\psi_{12}} & r_{22}e^{i\psi_{22}} \\ r_{11}e^{i\psi_{11}} & r_{21}e^{i\psi_{21}} & t_{11}e^{i\phi_{11}} & t_{21}e^{i\phi_{21}} \\ r_{12}e^{i\psi_{12}} & r_{22}e^{i\psi_{22}} & t_{12}e^{i\phi_{12}} & t_{22}e^{i\phi_{22}} \end{pmatrix}. \tag{10.1}$$

It connects the four input and output fields of the jth particle via

$$\begin{pmatrix} C_{1,j} \\ C_{2,j} \\ B_{1,j} \\ B_{1,j} \end{pmatrix} = \mathbf{M}_{4p} \begin{pmatrix} A_{1,j} \\ A_{2,j} \\ D_{1,j} \\ D_{2,j} \end{pmatrix}. \tag{10.2}$$

Due to the fact that photon losses are neglected within our treatment the matrix (10.1) has to fulfil the unitary condition $\mathbf{M}_{4p}^{\dagger}\mathbf{M}_{4p} = \mathbb{I}$. This ensures that the number of photons is conserved. A generalization to include some internal loss or scattering to other modes is straightforward and certainly helps to quantitatively model a specific experiment, but will not give qualitatively new insights.

In order to make statements about a tractor beam behaviour of the injected light fields, we need to calculate the light induced force onto the particles. This can be done by following proven recipes [10.5, 10.6]. We calculate the forces acting on the particle via a Maxwell stress tensor based approach. In the effective 1D geometry of a fibre, it suffices to consider the Minkwoski's photon momenta P inside a medium with refractive index n

$$P = n\hbar k. \tag{10.3}$$

The total momentum of the light propagating in the ith ($i \in \{1,2\}$) mode at the left and right side of the jth bead can be expressed in terms of the propagating photon numbers

$$N^{\mathrm{L}}_{i,j} = \frac{cn\epsilon_0}{2}\left(|A_{i,j}|^2 + |B_{i,j}|^2\right), \tag{10.4}$$

$$N^{\mathrm{R}}_{i,j} = \frac{cn\epsilon_0}{2}\left(|C_{i,j}|^2 + |D_{i,j}|^2\right) \tag{10.5}$$

at each side of the bead. The momentum left and right of the beads then reads

$$P^{\mathrm{L}}_{tot} = N^{\mathrm{L}}_{1,j}\hbar k_1 + N^{L}_{2,j}\hbar k_2, \tag{10.6}$$

$$P^{\mathrm{R}}_{tot} = N^{\mathrm{R}}_{1,j}\hbar k_1 + N^{\mathrm{R}}_{2,j}\hbar k_2. \tag{10.7}$$

The force on the jth bead thus can be simply found from the missing momentum which results in

$$F_j = \hbar k_1 (N^{L}_{1,j} - N^{R}_{1,j}) + \hbar k_2 (N^{\mathrm{L}}_{2,j} - N^{\mathrm{R}}_{2,j}). \tag{10.8}$$

Hence, the force onto the jth beam-splitter in terms of the amplitudes is given as

$$\begin{aligned} F_j = \frac{cn\epsilon_0\hbar}{2}&(k_1(|A_{1,j}|^2 + |B_{1,j}|^2 - |C_{1,j}|^2 - |D_{1,j}|^2) \\ &+k_2(|A_{2,j}|^2 + |B_{2,j}|^2 - |C_{2,j}|^2 - |D_{2,j}|^2)). \end{aligned} \tag{10.9}$$

For the remainder of this work we will always set $|D_{i,j}|^2 \equiv 0$ because only co-propagating beams imposed from the left side are studied.

The presented model allows us to efficiently calculate the force onto N beads for several different parameters. However, a full analytic treatment is rather tedious and we will focus on some special cases of reduced complexity before including all possible processes in the following. A concrete generic example can be found in Appendix A.

10.3 Forces for Two Forward Propagating Modes

While for very small point like scatterers there is a symmetry between forward and backward scattered light [10.6], for larger or thicker objects forward scattering is usually dominant with respect to reflection [10.5, 10.16] and the coupling between modes of the same propagation direction dominates (see e.g. Appendix A). Therefore we first consider larger particles of lower contrast and restrict our treatment to two different transverse forward propagating modes and injection from a single side. This already will show the essential physics without requiring a too complex analytic form.

10.3.1 Single Particle

To study the fundamental effects of transverse forward mode coupling, we first investigate only a single particle in the fibre field, which will introduce coherent coupling between the two propagating modes. In this special case the non-trivial part of the four port matrix (10.1) reduces to a two port matrix and the amplitudes left and right of the beam splitter are connected via the following matrix

$$\begin{pmatrix} C_1 \\ C_2 \end{pmatrix} = \mathbf{M}_{2p} \begin{pmatrix} A_1 \\ A_2 \end{pmatrix} = \begin{pmatrix} t_{11}e^{i\phi_{11}} & t_{21}e^{i\phi_{21}} \\ t_{12}e^{i\phi_{12}} & t_{22}e^{i\phi_{22}} \end{pmatrix} \begin{pmatrix} A_1 \\ A_2 \end{pmatrix}, \tag{10.10}$$

where we chose $A_1 \equiv A_{1,1}$, $A_2 \equiv A_{2,1}$, $C_1 \equiv C_{1,1}$ and $C_2 \equiv C_{2,1}$. The scattering process changes the relative mode amplitudes and adds a light phase via $e^{i\phi_{ij}}$. Here we can choose $\phi_{11} = 0$ without any restriction and for a single particle also ϕ_{22} will not change the force expression.

The unitarity condition $\mathbf{M}_{2p}^{\dagger} \cdot \mathbf{M}_{2p} = \mathbb{I}$ then reduces the number of physically relevant parameters to

$$t_{11} = t_{22} = t, \tag{10.11}$$

$$t_{12} = t_{21} = \sqrt{1-t^2}, \tag{10.12}$$

$$\phi_{12} = -\phi_{21} + (2n+1)\pi = \phi, \ n \in \mathbb{N}, \tag{10.13}$$

which finally leads to a much simpler form of the scattering matrix

$$\mathbf{M}'_{2p} = \begin{pmatrix} t & -e^{-i\phi}\sqrt{1-t^2} \\ e^{i\phi}\sqrt{1-t^2} & t \end{pmatrix}. \tag{10.14}$$

As a result the output amplitudes are connected with the input amplitudes via

$$C_1 = tA_1 + e^{i\phi}\sqrt{1-t^2}A_2, \tag{10.15}$$

$$C_2 = -e^{-i\phi}\sqrt{1-t^2}A_1 + tA_2. \tag{10.16}$$

To calculate the force we insert this result into (10.9) which leads to the force onto a single particle in two forward propagating modes

$$F_{\mathrm{SP}}^{2p} = \frac{cn\epsilon_0\hbar}{2}(k_2 - k_1)\left(\left(t^2 - 1\right)\left(|A_1|^2 - |A_2|^2\right) + t\sqrt{1-t^2}\left(e^{i\phi}A_1^*A_2 + e^{-i\phi}A_1A_2^*\right)\right). \tag{10.17}$$

The two wavenumbers (k_1 for the fundamental and k_2 for the higher order mode) differ in general and fulfil the condition $k_1 > k_2$.

Let us now look at the special translation invariant case, where only one of the two modes is pumped and the other mode is only populated by scattered photons. There are two possible cases to consider. On the one hand only the fundamental mode can be pumped ($A_1 \neq 0$, $A_2 = 0$) and on the other hand only the higher order mode can be injected ($A_1 = 0$, $A_2 \neq 0$). The corresponding forces are shown in Fig. 10.3. One finds that the force on the particle is always negative, if the higher order mode is chosen as the input field. The negative force implies that for this configuration the particle is pulled in the direction against the incoming beam. It is fundamental to state that due

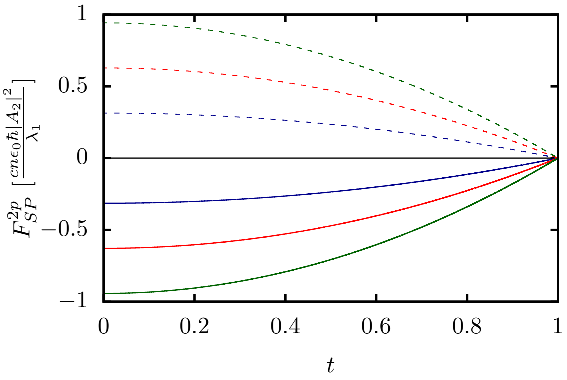

Figure 10.3: Force on a single particle in only forward propagating modes considering only the fundamental (dashed line) or the higher order mode field (solid line) as input. The blue line corresponds to $k_2 = 0.9\ k_1$, the red line to $k_2 = 0.8\ k_1$ and the green line to $k_2 = 0.7\ k_1$.

to translation symmetry of the system, this force is the same anywhere along the fibre and the particle will be continuously pulled towards the source over very long distances.

Mathematically this behavior gets obvious, if one looks at the analytic expression for the force (10.18). Assuming only a higher order mode input field ($A_1 = 0$, $A_2 \neq 0$) the force simplifies to

$$F_{\mathrm{SP}}^{2p}|_{A_1=0} = \frac{cn\epsilon_0\hbar}{2}(k_1 - k_2)\left(t^2 - 1\right)|A_2|^2. \tag{10.18}$$

As mentioned above the conditions $0 \leq t \leq 1$ and $k_2 < k_1$ have to hold. Consequently, the force is always negative in this case. Following the same procedure but using the fundamental mode field as the input beam, leads to a positive force as depicted in Fig. 10.3 following the conventional expectation.

Lets now discuss the essential physics leading to this somewhat counter intuitive result. Due to the fact that the higher order mode contains a higher amount of transverse momentum and thus less longitudinal momentum than the fundamental mode, the scattering process between those modes (with amplitude t_{12}) is generally suppressed. Only some additional momentum provided by the bead closes this momentum gap and allows for scattering between the two modes. This is quite analogous to the case of Bessel tractor beams [10.17], but due to the presence of a light confining geometry the range of the effect is infinite in the studied case.

10.3.2 Two Particles

As it has been seen and experimentally demonstrated in previous work [10.5] the two mode forward scattering model also well describes the long range inter-particle forces in this system. In the simplified case with no backscattering, however, the fields and the force on the first particle cannot be affected by a second one downstream the mode.

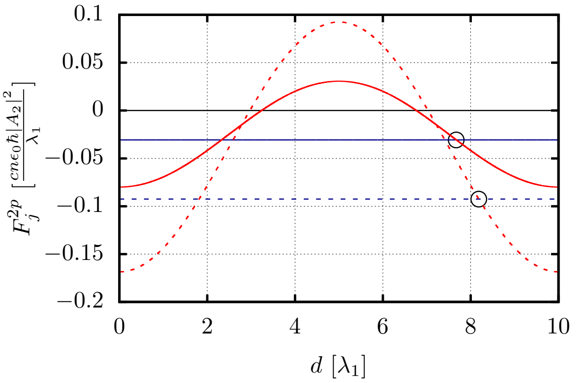

Figure 10.4: Force on the first (blue) and second particle (red) as a function of the inter-particle distance d in only forward propagating modes. Only the higher order mode field is considered as input field and $k_2 = 0.9\ k_1$. The solid line corresponds to $t = 0.95$, thus Eq. (10.12) implies $t_{12} = 0.31$. The dashed line shows the results for $t = 0.84$ and $t_{12} = 0.54$. The black circles indicate stable distances.

Nevertheless, the field impinging on the second particle is the result of the mode mixing by the first and thus significantly depends on the relative distance allowing for stable configurations. Using the scattering matrix approach the outgoing amplitudes after the second particle can be calculated in the following manner:

$$\begin{pmatrix} C_{1,2} \\ C_{2,2} \end{pmatrix} = \mathbf{M}'_{2p} \cdot \mathbf{P}(d) \cdot \mathbf{M}'_{2p} \begin{pmatrix} A_{1,1} \\ A_{2,1} \end{pmatrix}, \tag{10.19}$$

with $A_{i,j}$ and $C_{i,j}$ being the input and output fields with mode i at the jth particle. In addition, the free field propagation over a distance d (i. e. the propagation face shift) is included via a transfer matrix which connects the amplitudes on the right hand side of the first and the left side of the second beam-splitter

$$\mathbf{P}(d) = \begin{pmatrix} e^{ik_1 d} & 0 \\ 0 & e^{ik_2 d} \end{pmatrix}. \tag{10.20}$$

Here we assume identical particles for simplicity so that the scattering process is the same for both particles. Of course, the presented scheme can be generalized to more particles in a straightforward manner. The force on the jth particle is then again defined by Eq. (10.9).

To keep the discussion compact, we will restrict our treatment here to the two particle case. Due to the fact that the analytical expression of the forces is rather lengthy, it will be omitted here but the spatial dependence of the forces is presented in Fig. 10.4. Interestingly, one finds that for certain distances between the two particles, both particles can experience a negative or tractor force. Obviously as a next step one can ask for

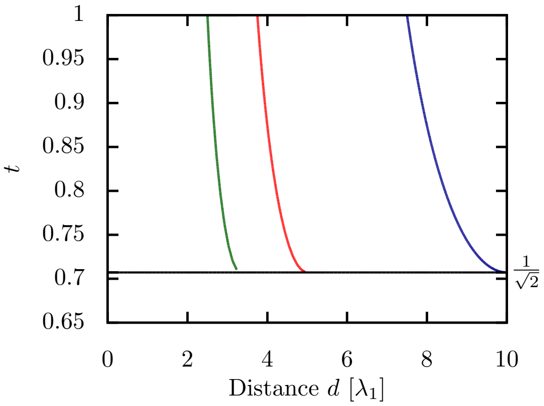

Figure 10.5: Optical binding distances d as a function of the transmission coefficient t for two particles in forward propagating modes considering only the higher order mode field as input. The blue line corresponds to $k_2 = 0.9\ k_1$, the red line to $k_2 = 0.8\ k_1$ and the green line to $k_2 = 0.7\ k_1$.

stable configurations of the two particles, i. e. configurations in which the particle's distance d remains constant and locked against small perturbations. Similar effects have already been observed experimentally in free-space geometries [10.9]. This requires both forces to have the same value ($F_1 - F_2 = 0$) and at the same time the conditions $\frac{\partial F_1}{\partial d} > 0$ and $\frac{\partial F_2}{\partial d} < 0$ have to be fulfilled. These conditions imply that a restoring force is acting if the particles deviate from their equilibrium position.

As an example we again choose the higher order mode as the input field ($A_1 = 0$, $A_2 \neq 0$). Interestingly, here stable distance configurations with a negative force on both particles can be found for the chosen parameters. Therefore, the particles are commonly attracted towards the beam source while they stay at a constant distance. This corresponds to a stable collective tractor beam configuration for the particles. Another interesting fact, which can be seen in Fig. 10.4 is that for certain distances beyond the stable point, the tractor force on the second particle can even be stronger than the one on a single particle. Hence the mode phase lock introduced by the first particle creates an even stronger trap than on itself.

Note the lower cutoff of the distances in Fig. 10.5, which reflects the fact that stable tractor beam configurations cannot be found for values of t below certain values. In particular the transmission t by the first particle has to exceed a certain threshold value in order to find a stationary two particle configuration. This is due to the fact that if too much light is scattered to the fundamental mode by the first particle, the relative mode amplitude ratio in the fibre between the two particles will be rather small and the tractor force on the second particle will always be too small to follow the first one against the beam propagation direction at a constant distance. Note that the particle force can also be seen as the simplest possible form of optical binding as the scattering of the first particle creates a series of dipole traps for the second one.

10.4 Four Mode Model Including Backscattering

Lets now turn to a more realistic model. While the relative magnitude of backward versus forward scattering can be small for large particles at low index contrast, it will of course never be exactly zero [10.5]. As the momentum transfer per photon in reflection is much larger than for forward mode mixing even a small amplitude could induce some changes. In this section we will thus treat the whole 4-mode model as already described above and investigate, how much even small backscattering at the particles position can induce substantial force contributions. The scattering processes in this case are described by the general 4-port matrix (10.1). Losses to other modes or absorption also can be included by modifying the diagonal of this matrix.

Obviously the set of available parameters is rather large in this case and hardly can be exhaustively treated. Nevertheless, at least in principle for any concrete bead size, position, shape and mode geometry, they could be at least numerically calculated from a generalized Helmholtz equation. Here we will use a different approach and look at physically interesting parameter ranges. Once interesting parameters are found, one could look for geometries, where one could implement such scattering properties. In order to reduce the complexity we will first assume that both modes experience the same forward scattering amplitudes and phase shifts with negligible backscattering into the very same mode. This allows us to concentrate on the effects of mode cross-scattering processes which are at the origin of interesting multi-mode physics. A concrete example is presented in the appendix.

Based on the above arguments we first set:

$$t_{11} = t_{22} = t, \tag{10.21}$$

$$r_{11} = r_{22} = 0. \tag{10.22}$$

We again also set the reference phases to zero ($\phi_{11} = \phi_{22} = 0$). The unitary condition for the full coupling matrix then again gives the following set of necessary conditions

$$t_{12} = t_{21}, \tag{10.23}$$

$$r_{12} = r_{21}, \tag{10.24}$$

$$t_{12} = \sqrt{1 - t^2 - r_{12}^2}, \tag{10.25}$$

$$\phi_{21} = -\phi + (2m-1)\pi, \tag{10.26}$$

$$\psi_{21} = -\phi - (n + 1/2)\pi, \tag{10.27}$$

$$\psi_{12} = \phi + (n - 1/2)\pi, \quad m, n \in \mathbb{N}, \tag{10.28}$$

where we defined $\phi = \phi_{12}$. In this case the scattering matrix simplifies to

$$\mathbf{M}'_{4p} = \begin{pmatrix} t & -e^{-i\phi}t_{12} & 0 & ie^{-i\phi}r_{12} \\ e^{i\phi}t_{12} & t & ie^{i\phi}r_{12} & 0 \\ 0 & ie^{-i\phi}r_{12} & t & -e^{-i\phi}t_{12} \\ ie^{i\phi}r_{12} & 0 & e^{i\phi}t_{12} & t \end{pmatrix}. \tag{10.29}$$

Of course the two-port system as it has been investigated in the previous section can be reproduced by setting $r_{12} = 0$.

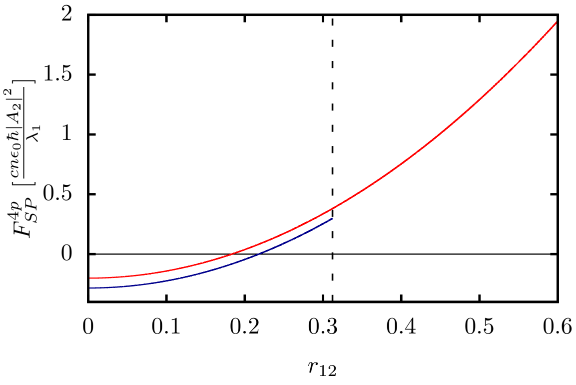

Figure 10.6: Force on a single particle including back-reflection and considering only the higher order mode field as input field and $k_2 = 0.9\ k_1$. The blue line corresponds to $t_{12} = 0.95$ and the red line to $t_{12} = 0.8$. The dashed line illustrates the threshold on the reflection r_{12} defined by Eq. (10.25).

10.4.1 Single Particle

We again start with investigating the forces acting on a single particle along the fibre. We follow the same procedure as presented above but with more amplitudes coupled by a larger matrix. Using (10.9) in order to calculate the force leads to

$$\begin{aligned} F_{\mathrm{SP}}^{4p} =& \frac{cn\epsilon_0\hbar}{2}\left(|A_1|^2\left(k_1\left(r_{12}^2+t_{12}^2\right)+k_2\left(r_{12}^2-t_{12}^2\right)\right)\right. \\ &+|A_2|^2\left(k_1\left(r_{12}^2-t_{12}^2\right)+k_2\left(r_{12}^2+t_{12}^2\right)\right) \\ &\left.+t_{12}t\left(k_1-k_2\right)\left(A_1A_2^*e^{i\phi}+A_1^*A_2e^{-i\phi}\right)\right). \end{aligned} \tag{10.30}$$

For injection of only a higher order mode field ($A_1 = 0$) this reduces to

$$F_{\mathrm{SP}}^{4p} = \frac{cn\epsilon_0\hbar}{2}\left[t_{12}^2\left(k_2-k_1\right)+r_{12}^2\left(k_1+k_2\right)\right]|A_2|^2, \tag{10.31}$$

which can be negative as long as the parameters fulfil the following condition:

$$\frac{r_{12}^2}{t_{12}^2} \leq \frac{k_1-k_2}{k_1+k_2}. \tag{10.32}$$

Fig. 10.6 shows an example how the backscattering process gives a negative force on the particle as long as r_{12} is not too large. Note that as the two momenta are usually not too different the condition on the smallness of back-reflection can be rather stringent.

10.4.2 Two Particles

As the scattering matrix (10.29) expresses the outgoing fields in terms of the incoming fields the expression for the fields generated by two beads formally looks similar to the

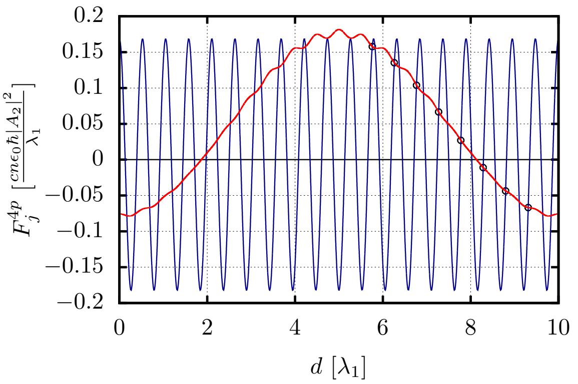

Figure 10.7: Force on two particles including back-reflection and considering only the higher order mode field as input field and $k_2 = 0.9\ k_1$. The blue line corresponds to the force on the first and the red line to the force on the second particle. Here, we chose $t_{12} = 0.54$ and $r_{12} = 0.12$. Black circles indicate stable points.

case above. However, to find the amplitudes on two beads, the total transfer matrix M_{TM} has to be found in accordance with the prescribed boundary conditions. Here one immediately gets an infinite series of reflections and back reflections. As shown in previous work [10.18] this can be efficiently calculated by rearranging the terms of the matrix in a form which connects the amplitudes to the left and to the right of a particle in the form

$$\mathbf{M}_{TF} = \begin{pmatrix} \frac{t}{1-r_{12}^2} & \frac{ir_{12}t_{12}}{1-r_{12}^2} & -\frac{t_{12}e^{-i\phi}}{1-r_{12}^2} & -\frac{ir_{12}te^{-i\phi}}{1-r_{12}^2} \\ \frac{ir_{12}t_{12}}{1-r_{12}^2} & \frac{t}{1-r_{12}^2} & \frac{ir_{12}te^{-i\phi}}{1-r_{12}^2} & \frac{t_{12}e^{-i\phi}}{1-r_{12}^2} \\ \frac{t_{12}e^{i\phi}}{1-r_{12}^2} & -\frac{ie^{i\phi}r_{12}t}{1-r_{12}^2} & \frac{t}{1-r_{12}^2} & -\frac{ir_{12}t_{12}}{1-r_{12}^2} \\ \frac{ir_{12}te^{i\phi}}{1-r_{12}^2} & -\frac{t_{12}e^{i\phi}}{1-r_{12}^2} & -\frac{ir_{12}t_{12}}{1-r_{12}^2} & \frac{t}{1-r_{12}^2} \end{pmatrix}, \tag{10.33}$$

so that

$$\begin{pmatrix} C_{1,2} \\ D_{1,2} \\ C_{2,2} \\ D_{2,2} \end{pmatrix} = \mathbf{M}_{TF} \cdot \mathbf{P}_4(d) \cdot \mathbf{M}_{TF} \begin{pmatrix} A_{1,1} \\ B_{1,1} \\ A_{2,1} \\ B_{2,1} \end{pmatrix}, \tag{10.34}$$

where $\mathbf{P}_4(d)$ is the 4 mode generalized propagation matrix for the fields:

$$\mathbf{P}_4(d) = \begin{pmatrix} e^{ik_1 d} & 0 & 0 & 0 \\ 0 & e^{-ik_1 d} & 0 & 0 \\ 0 & 0 & e^{ik_2 d} & 0 \\ 0 & 0 & 0 & e^{-ik_2 d} \end{pmatrix}. \tag{10.35}$$

In this rearranged form, the amplitudes on the particles can be found by solving these four equations for the required input and output fields. As the analytical expression even

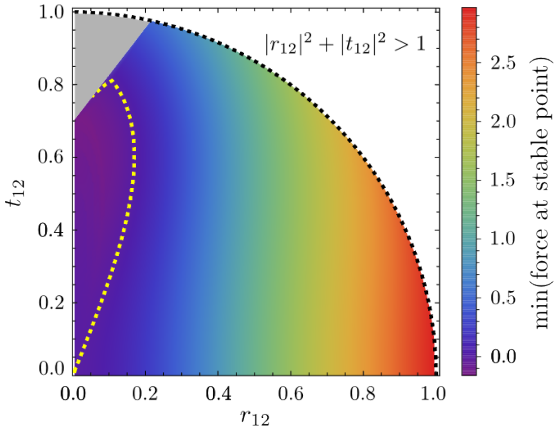

Figure 10.8: The minimal possible force at a stable point plotted for different values of r_{12} and t_{12}. The yellow dashed line marks the zero line. In the grey region no stable solution exists at all and the black dashed line shows the threshold for reflection and transmission imposed by Eq. (10.25).

for the single particle force is rather complex, we will not give it here and simply show some numerical examples. We see that the presence of the second particle changes the interaction between the particles and the fields in a much more complex way as above. Indeed, both particles now are influenced by the presence and position of the other one. This mechanism can lead to multi-stable optical binding effects as it has already been shown in [10.19, 10.20]. Indeed, as demonstrated in Fig. 10.7 the force on the second particle now exhibits small but spatially fast fluctuations due to the interference of the reflected fields in addition to the larger oscillations from mode beating. Also the force on the first particle is oscillating now. These oscillations are a consequence of the interference between the incoming and backscattered fields. Here we see that the effective total backscattered field can be less than for a single bead as the field amplitudes from the two particles interfere like in a Fabry-Perot resonator driven with a resonant wavelength. Hence we can find parameter ranges with an even bigger tractor force than for a single particle. This can be enhanced by a collective mode coupling of the two particles.

In general the distance of maximal tractor force on the first particle does not correspond to a stable distance, but we find a large number of potentially stable distances. A fair fraction of these correspond to a net negative force on both particles. Hence, we see that also the full model allows for a many particle tractor beam configurations.

If we analyze this fact in more detail, we find that there exists a certain region of parameters in which a stable two particle tractor beam comparable to the one which has already been implemented in free-space geometries [10.9], can be realized . This region corresponds to the one on the left side of the yellow dashed line in Fig. 10.8. Obviously, in order to establish a negative tractor beam force the reflection as well as the transmission coefficients between the two modes must not exceed a certain critical value. On the one hand if the transmission is above a certain critical value no more stable point (i. e. points which fulfil the condition $F_1 - F_2 = 0$) can be found.) On the other hand, if the reflection coefficient exceeds a certain value the force can no longer be negative and the particles will always be pushed in the direction of the incoming laser beam. This effect is related to the result for two particles in forward propagating fields (cf. Eq. (10.32)). Nevertheless, due to the fact that the back-reflection for extended objects is in general rather small, the necessary parameter regime can be reached in some specific geometries like for example for beads trapped inside a two-mode hollow core fibre (see Appendix A).

10.5 Conclusions and Outlook

We demonstrated that optical fibres supporting at least two transverse modes can be the basis of translation invariant tractor beam implementations dragging particles and even pairs of optically bound particles against the injected beam direction without the need of any external control or feedback. The results are easily generalizable to several particles. In practical implementations the remaining backscattering seems to be one of the central obstacles to overcome here. For the implementation, only the higher order mode has to be pumped via the one end of the fibre, where the particles should be transported with hardly any restrictions on the bandwidth or coherence length. Apart from being a neat physical mechanism, the tractor effect could be helpful in setups where one plans to extract particles from a trap source and load them into a dipole trap at the other end of the fibre [10.21].

In this work we have primarily shown that such tractor beams are theoretically possible and given the necessary boundary conditions on the parameters to be achieved. The main challenge in practice actually is to design the fibre in a way to maximize cross coupling between two modes and minimizing loss to others. In a multi-mode fibre the tractor force will be the bigger the higher the order of the injected mode and the larger the amplitude of the fundamental mode at the particle position. For a hollow core fibre coupling should be good using modes of the same symmetry as the TEM_{00} and TEM_{20} mode with a particle of about wavelength size at its centre as it is shown in the Appendix A.

Acknowledgements

We thank C. Genes for helpful discussions and acknowledge support by the Austrian Science Fund FWF through projects SFB FoQuS P13 and I1697-N27. We also acknowledge fruitful discussions from S. Nic Chormaic, V. G. Truong and A. Maimaiti from the Okinawa Institute of Science and Technology Japan.

10.6 Appendix

A small particle placed inside the mode field of an optical waveguide or optical fiber will locally perturb the field and change its propagation. If one considers positions

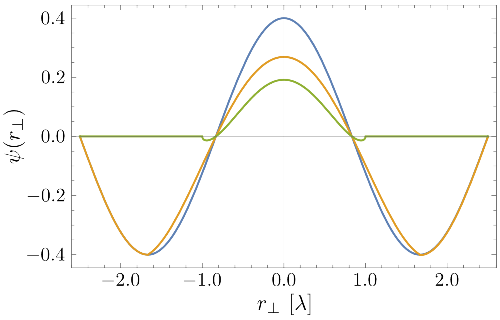

Figure 10.9: Shape of the original (blue) and distorted mode function (real part orange, imaginary part green) for a spherical bead of refractive index $n = 1.25$ and diameter 2λ in the center of a rectangular waveguide for a waveguide diameter $a = 5\lambda$.

significantly left and right of the bead, where near field effects can be neglected, the propagation field can still be expanded in terms of the transverse eigenmodes of the waveguide. For a bead made of linear optical material the corresponding expansion coefficients on both sides are linearly connected by an effective transfer matrix.

The effect of the particle will be phase and amplitude changes of the modes induced by light scattering between various forward and backward propagation modes. In addition, some of the field could be absorbed or, equivalently, scattered to free space modes not guided by the fiber so that the transfer matrix is not necessarily unitary. As the latter effect cannot positively contribute to the tractor effect or inter-particle forces we will neglect it for this calculation of the mode coupling coefficients.

To obtain the coefficients one needs to solve the corresponding Helmholtz equation including proper boundary conditions, which for a detailed modelling requires rather extensive numerical calculations as e.g. presented in [10.5, 10.12]. Here we are mainly interested in the basic physics of the tractor force effect, which is contained in the relative magnitude of the effective coupling between different transverse modes. As shown above a strong tractor force requires stronger coupling of a mode to lower order modes than to higher order modes as well as very low reflection. For only two modes the coupling between the modes needs to be stronger than free space losses.

In order to keep the complexity low we thus refrain to a paraxial approximation for the propagation of the fields. In this case the field evolution along a non-absorbing bead can be approximated by the effective optical Schrödinger equation, where the bead creates an effective potential for the transverse light field amplitude $\psi(r_\perp)$ propagating along the fiber direction z [10.22]:

$$\frac{i}{n_0 k_0}\partial_z \psi(r_\perp) = \left[\frac{-\Delta_\perp}{2n_0 k_0^2} + V_{opt}(r_\perp)\right]\psi(r_\perp). \tag{10.36}$$

In this case the optical potential of the bead

$$V_{opt}(r_\perp) = \frac{n_0^2 - n(r_\perp^2)}{2n_0^2} \tag{10.37}$$

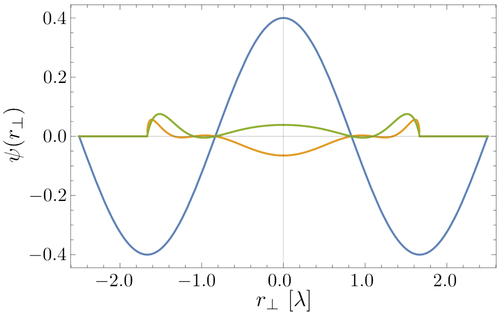

Figure 10.10: Shape of the original (blue) and the reflected mode function for a spherical bead of refractive index $n = 1.25$ and diameter 2λ in the center of a rectangular waveguide for a waveguide diameter $a = 5\lambda$.

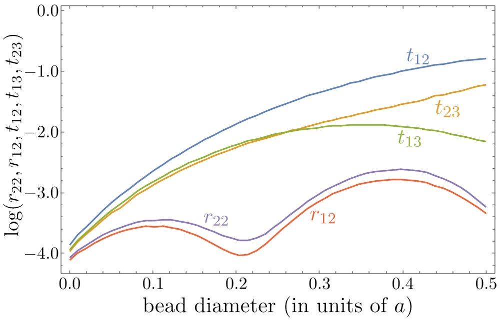

Figure 10.11: Mode coupling coefficients for the three lowest order symmetric modes for a spherical bead of index $n = 1.5$ in the center of a rectangular waveguide as function of bead diameter in units of the waveguide diameter $a = 9\lambda$.

creates an effective local attractive potential which couples the various transverse modes. Here $n(r_\perp))$ is the bead refractive index distribution and n_0 the background refractive index.

Below we will try to identify a favorable case for generating a tractor force in a simple configuration. To show the qualitative behaviour we simply assume a perfect square waveguide with with a certain diamater a [10.15] or a hollow guide with sharp (metallic) boundaries [10.14] where the mode functions are simply given by harmonic functions vanishing at the boundaries.

For a small refractive index of the bead and a not too large size, the effect of a bead of diameter d on the field can then be simply estimated by the spatially accumulated phase shift

$$e^{i\phi(r_\perp)} \approx e^{i\int_0^d V_{opt}(r_\perp)dz} \tag{10.38}$$

by field while traversing the bead and a small reflected component [10.13]. This is shown in the example in Fig. 10.9 below, where we plot the original third order mode function and its distorted form (real and imaginary part) after the bead on a cut along the x-axis. Similarly we can estimate the reflected contribution as shown in Fig. 10.10.

In this limit the mode coupling coefficients can then be simply obtained by projecting the distorted and reflected fields onto the original modes. This will strongly depend on position, size and refractive index of the bead. If we want strong overlap between a higher order and a lower order mode it is thus favourable to put the bead at a position, where the target mode has a high amplitude but the unwanted modes are low or strongly varying. As an example here in Fig. 10.11 we show the case of a bead of varying size exactly at the center of the waveguide where the first and third order mode amplitudes are large, while others are small. We see that indeed the desired coupling between mode one and two is about one order of magnitude bigger than the other couplings and reflections. Hence, this configuration should lead to a sizeable tractor force for a suitable particle size range.

Bibliography

References for Chapter 1

[1.1] M. Planck, "Zur Theorie des Gesetzes der Energieverteilung im Normalspektrum," *Verhandl. Dtsc. Phys. Ges.*, vol. 2, p. 237, 1900.

[1.2] M. Plank, "Über das Gesetz der Energieverteilung im Normalspektrum," *Annalen der Physik*, vol. 4, no. 553, p. 43, 1901.

[1.3] A. Einstein, "Über einen die Erzeugung und Verwandlung des Lichtes betreffenden heuristischen Gesichtspunkt," *Annalen der Physik*, vol. 322, no. 6, pp. 132–148, 1905.

[1.4] L. De Broglie, "Waves and quanta," *Nature*, vol. 112, no. 2815, p. 540, 1923.

[1.5] E. Schrödinger, "An undulatory theory of the mechanics of atoms and molecules," *Phys. Rev.*, vol. 28, no. 6, p. 1049, 1926.

[1.6] P. A. M. Dirac, "The quantum theory of the emission and absorption of radiation," *Proc. R. Soc. Lond. A*, vol. 114, no. 767, pp. 243–265, 1927.

[1.7] E. Fermi, "Quantum theory of radiation," *Rev. Mod. Phys.*, vol. 4, no. 1, p. 87, 1932.

[1.8] R. P. Feynman, "Mathematical formulation of the quantum theory of electromagnetic interaction," *Phys. Rev.*, vol. 80, no. 3, p. 440, 1950.

[1.9] R. Frisch, "Experimenteller Nachweis des Einsteinschen Strahlungsrückstoßes," *Zeitschrift für Physik A, Hadrons and Nuclei*, vol. 86, no. 1, pp. 42–48, 1933.

[1.10] T. Maiman, "Stimulated optical radiation in ruby," *Nature*, vol. 187, p. 493, 1960.

[1.11] A. L. Schawlow and C. H. Townes, "Infrared and optical masers," *Phys. Rev.*, vol. 112, no. 6, p. 1940, 1958.

[1.12] C. Cohen-Tannoudji, "Atomic motion in laser light," *Fundamental systems in quantum optics*, no. 53, pp. 1–164, 1990.

[1.13] T. W. Hänsch and A. L. Schawlow, "Cooling of gases by laser radiation," *Opt. Commun.*, vol. 13, no. 1, pp. 68–69, 1975.

[1.14] I. W. M. Wineland, D J, "Laser cooling of atoms," *Phys. Rev. A*, vol. 20, p. 1521, 1979.

[1.15] J. Dalibard and C. Cohen-Tannoudji, “Laser cooling below the doppler limit by polarization gradients: simple theoretical models,” *JOSA B*, vol. 6, no. 11, pp. 2023–2045, 1989.

[1.16] K. B. Davis, M.-O. Mewes, M. R. Andrews, N. Van Druten, D. Durfee, D. Kurn, and W. Ketterle, “Bose-einstein condensation in a gas of sodium atoms,” *Phys. Rev. Lett.*, vol. 75, no. 22, p. 3969, 1995.

[1.17] M. H. Anderson, J. R. Ensher, M. R. Matthews, C. E. Wieman, and E. A. Cornell, “Observation of bose-einstein condensation in a dilute atomic vapor,” *science*, vol. 269, no. 5221, pp. 198–201, 1995.

[1.18] R. Grimm, M. Weidemüller, and Y. B. Ovchinnikov, “Optical dipole traps for neutral atoms,” in *Adv. Atom. Mol. Opt. Phy.*, vol. 42, pp. 95–170, Elsevier, 2000.

[1.19] A. Ashkin, J. M. Dziedzic, J. Bjorkholm, and S. Chu, “Observation of a single-beam gradient force optical trap for dielectric particles,” *Optics letters*, vol. 11, no. 5, pp. 288–290, 1986.

[1.20] J. I. Cirac and P. Zoller, “Quantum computations with cold trapped ions,” *Phys. Rev. Lett.*, vol. 74, no. 20, p. 4091, 1995.

[1.21] C. A. Muschik, I. de Vega, D. Porras, and J. I. Cirac, “Quantum processing photonic states in optical lattices,” *Phys. Rev. Lett.*, vol. 100, no. 6, p. 063601, 2008.

[1.22] M. Takamoto, F.-L. Hong, R. Higashi, and H. Katori, “An optical lattice clock,” *Nature*, vol. 435, no. 7040, p. 321, 2005.

[1.23] R. P. Feynman, “Simulating physics with computers,” *International journal of theoretical physics*, vol. 21, no. 6-7, pp. 467–488, 1982.

[1.24] D. Jaksch, C. Bruder, J. I. Cirac, C. W. Gardiner, and P. Zoller, “Cold bosonic atoms in optical lattices,” *Phys. Rev. Lett.*, vol. 81, no. 15, p. 3108, 1998.

[1.25] H. Gersch and G. Knollman, “Quantum cell model for bosons,” *Phys. Rev.*, vol. 129, no. 2, p. 959, 1963.

[1.26] M. P. Fisher, P. B. Weichman, G. Grinstein, and D. S. Fisher, “Boson localization and the superfluid-insulator transition,” *Phys. Rev. B*, vol. 40, no. 1, p. 546, 1989.

[1.27] M. Greiner, O. Mandel, T. Esslinger, T. W. Hänsch, and I. Bloch, “Quantum phase transition from a superfluid to a mott insulator in a gas of ultracold atoms,” *Nature*, vol. 415, no. 6867, p. 39, 2002.

[1.28] I. Bloch, J. Dalibard, and W. Zwerger, “Many-body physics with ultracold gases,” *Rev. Mod. Phys.*, vol. 80, no. 3, p. 885, 2008.

[1.29] M. F. Parsons, A. Mazurenko, C. S. Chiu, G. Ji, D. Greif, and M. Greiner, “Site-resolved measurement of the spin-correlation function in the fermi-hubbard model,” *Science*, vol. 353, no. 6305, pp. 1253–1256, 2016.

[1.30] Y.-C. He, F. Grusdt, A. Kaufman, M. Greiner, and A. Vishwanath, “Realizing and adiabatically preparing bosonic integer and fractional quantum hall states in optical lattices,” *Phys. Rev. B*, vol. 96, no. 20, p. 201103, 2017.

[1.31] J. Zeiher, J.-y. Choi, A. Rubio-Abadal, T. Pohl, R. van Bijnen, I. Bloch, and C. Gross, “Coherent many-body spin dynamics in a long-range interacting ising chain,” *Phys. Rev. X*, vol. 7, no. 4, p. 041063, 2017.

[1.32] H. P. Lüschen, S. Scherg, T. Kohlert, M. Schreiber, P. Bordia, X. Li, S. D. Sarma, and I. Bloch, “Single-particle mobility edge in a one-dimensional quasiperiodic optical lattice,” *Phys. Rev. Lett.*, vol. 120, no. 16, p. 160404, 2018.

[1.33] M. Saffman, T. G. Walker, and K. Mølmer, “Quantum information with rydberg atoms,” *Rev. Mod. Phys.*, vol. 82, no. 3, p. 2313, 2010.

[1.34] S. Baier, M. J. Mark, D. Petter, K. Aikawa, L. Chomaz, Z. Cai, M. Baranov, P. Zoller, and F. Ferlaino, “Extended bose-hubbard models with ultracold magnetic atoms,” *Science*, vol. 352, no. 6282, pp. 201–205, 2016.

[1.35] S. Haroche, “Nobel lecture: Controlling photons in a box and exploring the quantum to classical boundary,” *Rev. Mod. Phys.*, vol. 85, no. 3, p. 1083, 2013.

[1.36] H. Ritsch, P. Domokos, F. Brennecke, and T. Esslinger, “Cold atoms in cavity-generated dynamical optical potentials,” *Rev. Mod. Phys.*, vol. 85, no. 2, p. 553, 2013.

[1.37] C. Maschler and H. Ritsch, “Cold atom dynamics in a quantum optical lattice potential,” *Phys. Rev. Lett.*, vol. 95, no. 26, p. 260401, 2005.

[1.38] J. Larson, B. Damski, G. Morigi, and M. Lewenstein, “Mott-insulator states of ultracold atoms in optical resonators,” *Phys. Rev. Lett.*, vol. 100, no. 5, p. 050401, 2008.

[1.39] C. Maschler, H. Ritsch, A. Vukics, and P. Domokos, “Entanglement assisted fast reordering of atoms in an optical lattice within a cavity at t= 0,” *Opt. Commun.*, vol. 273, no. 2, pp. 446–450, 2007.

[1.40] J. Larson, S. Fernández-Vidal, G. Morigi, and M. Lewenstein, “Quantum stability of mott-insulator states of ultracold atoms in optical resonators,” *New J. Phys.*, vol. 10, no. 4, p. 045002, 2008.

[1.41] P. Domokos and H. Ritsch, “Collective cooling and self-organization of atoms in a cavity,” *Phys. Rev. Lett.*, vol. 89, no. 25, p. 253003, 2002.

[1.42] A. T. Black, H. W. Chan, and V. Vuletić, “Observation of collective friction forces due to spatial self-organization of atoms: from rayleigh to bragg scattering,” *Phys. Rev. Lett.*, vol. 91, no. 20, p. 203001, 2003.

[1.43] K. Baumann, C. Guerlin, F. Brennecke, and T. Esslinger, “Dicke quantum phase transition with a superfluid gas in an optical cavity,” *Nature*, vol. 464, no. 7293, p. 1301, 2010.

[1.44] R. H. Dicke, “Coherence in spontaneous radiation processes,” *Phys. Rev.*, vol. 93, no. 1, p. 99, 1954.

[1.45] S. Gopalakrishnan, B. L. Lev, and P. M. Goldbart, “Emergent crystallinity and frustration with bose–einstein condensates in multimode cavities,” *Nat. Phys.*, vol. 5, no. 11, p. 845, 2009.

[1.46] D. Chang, V. Gritsev, G. Morigi, V. Vuletić, M. Lukin, and E. Demler, “Crystallization of strongly interacting photons in a nonlinear optical fibre,” *Nat. Phys.*, vol. 4, no. 11, p. 884, 2008.

[1.47] T. Grießer and H. Ritsch, “Light-induced crystallization of cold atoms in a 1d optical trap,” *Phys. Rev. Lett.*, vol. 111, no. 5, p. 055702, 2013.

[1.48] D. E. Chang, J. I. Cirac, and H. J. Kimble, “Self-organization of atoms along a nanophotonic waveguide,” *Phys. Rev. Lett.*, vol. 110, no. 11, p. 113606, 2013.

[1.49] A. Goban, C.-L. Hung, S.-P. Yu, J. Hood, J. Muniz, J. Lee, M. Martin, A. McClung, K. Choi, D. E. Chang, *et al.*, “Atom–light interactions in photonic crystals,” *Nat. Commun.*, vol. 5, p. 3808, 2014.

[1.50] J. Léonard, A. Morales, P. Zupancic, T. Esslinger, and T. Donner, “Supersolid formation in a quantum gas breaking a continuous translational symmetry,” *Nature*, vol. 543, no. 7643, p. 87, 2017.

[1.51] S. Ostermann, T. Grießer, and H. Ritsch, “Atomic self-ordering in a ring cavity with counterpropagating pump fields,” *EPL (Europhys. Lett.)*, vol. 109, no. 4, p. 43001, 2015.

[1.52] S. Ostermann, F. Piazza, and H. Ritsch, “Spontaneous crystallization of light and ultracold atoms,” *Phys. Rev. X*, vol. 6, no. 2, p. 021026, 2016.

[1.53] S. Ostermann, F. Piazza, and H. Ritsch, “Probing and characterizing the growth of a crystal of ultracold bosons and light,” *New J. Phys.*, vol. 19, no. 12, p. 125002, 2017.

[1.54] I. Dimitrova, W. Lunden, J. Amato-Grill, N. Jepsen, Y. Yu, M. Messer, T. Rigaldo, G. Puentes, D. Weld, and W. Ketterle, “Observation of two-beam collective scattering phenomena in a bose-einstein condensate,” *Phys. Rev. A*, vol. 96, no. 5, p. 051603, 2017.

[1.55] F. Mivehvar, S. Ostermann, F. Piazza, and H. Ritsch, “Driven-dissipative supersolid in a ring cavity,” *Phys. Rev. Lett.*, vol. 120, no. 12, p. 123601, 2018.

[1.56] S. Ostermann, H.-W. Lau, H. Ritsch, and F. Mivehvar, “Cavity-induced emergent topological spin textures in a bose einstein condensate,” *arXiv preprint arXiv:1807.03316*, 2018.

[1.57] C. A. Ebongue, D. Holzmann, S. Ostermann, and H. Ritsch, “Generating a stationary infinite range tractor force via a multimode optical fibre,” *J.Opt.*, vol. 19, no. 6, p. 065401, 2017.

References for Chapter 2

[2.1] S. Haroche, “Nobel lecture: Controlling photons in a box and exploring the quantum to classical boundary,” *Rev. Mod. Phys.*, vol. 85, no. 3, p. 1083, 2013.

[2.2] J. D. Jackson, *Classical electrodynamics*. John Wiley & Sons, 2012.

[2.3] E. Hecht, *Optik*. Walter de Gruyter GmbH & Co KG, 2018.

[2.4] B. E. Saleh, M. C. Teich, and B. E. Saleh, *Fundamentals of photonics*, vol. 22. Wiley New York, 1991.

[2.5] M. O. Scully and M. S. Zubairy, *Quantum optics*. Cambridge University Press, 1997.

[2.6] C. Cohen-Tannoudji, “Atomic motion in laser light,” *Fundamental systems in quantum optics*, no. 53, pp. 1–164, 1990.

[2.7] R. Grimm, M. Weidemüller, and Y. B. Ovchinnikov, “Optical dipole traps for neutral atoms,” in *Adv. Atom. Mol. Opt. Phy.*, vol. 42, pp. 95–170, Elsevier, 2000.

[2.8] E. T. Jaynes and F. W. Cummings, “Comparison of quantum and semiclassical radiation theories with application to the beam maser,” *Proceedings of the IEEE*, vol. 51, no. 1, pp. 89–109, 1963.

[2.9] T. Grießer, H. Ritsch, M. Hemmerling, and G. Robb, “A vlasov approach to bunching and selfordering of particles in optical resonators,” *Eur. Phys. J. D*, vol. 58, no. 3, pp. 349–368, 2010.

[2.10] E. Tesio, G. Robb, T. Ackemann, W. Firth, and G.-L. Oppo, “Kinetic theory for transverse optomechanical instabilities,” *Phys. Rev. Lett.*, vol. 112, no. 4, p. 043901, 2014.

[2.11] K. B. Davis, M.-O. Mewes, M. R. Andrews, N. Van Druten, D. Durfee, D. Kurn, and W. Ketterle, “Bose-einstein condensation in a gas of sodium atoms,” *Phys. Rev. Lett.*, vol. 75, no. 22, p. 3969, 1995.

[2.12] M. H. Anderson, J. R. Ensher, M. R. Matthews, C. E. Wieman, and E. A. Cornell, “Observation of bose-einstein condensation in a dilute atomic vapor,” *science*, vol. 269, no. 5221, pp. 198–201, 1995.

[2.13] S. N. Bose, “Plancks Gesetz und Lichtquantenhypothese,” *Zeitschrift für Physik*, 1924.

[2.14] A. Einstein, “Quantentheorie des einatomigen idealen Gases,” *Akademie der Wissenshaften, in Kommission bei W. de Gruyter*, vol. 20, 1924.

[2.15] L. Pitaevskii and S. Stringari, *Bose-Einstein condensation and superfluidity*, vol. 164. Oxford University Press, 2016.

[2.16] C. J. Pethick and H. Smith, *Bose-Einstein condensation in dilute gases.* Cambridge university press, 2002.

References for Chapter 3

[3.1] H. Ritsch, P. Domokos, F. Brennecke, and T. Esslinger, “Cold atoms in cavity-generated dynamical optical potentials,” *Rev. Mod. Phys.*, vol. 85, no. 2, p. 553, 2013.

[3.2] R. Bonifacio, L. De Salvo, L. Narducci, and E. D’Angelo, “Exponential gain and self-bunching in a collective atomic recoil laser,” *Phys. Rev. A*, vol. 50, no. 2, p. 1716, 1994.

[3.3] R. Bonifacio and L. De Salvo, “Collective atomic recoil laser (carl) optical gain without inversion by collective atomic recoil and self-bunching of two-level atoms,” *Nuclear Instruments and Methods in Physics Research Section A: Accelerators, Spectrometers, Detectors and Associated Equipment*, vol. 341, no. 1-3, pp. 360–362, 1994.

[3.4] R. Bonifacio, C. Pellegrini, and L. M. Narducci, “Collective instabilities and high-gain regime free electron laser,” *Opt. Commun.*, vol. 50, p. 373, 1984.

[3.5] S. Inouye, A. Chikkatur, D. Stamper-Kurn, J. Stenger, D. Pritchard, and W. Ketterle, “Superradiant rayleigh scattering from a bose-einstein condensate,” *Science*, vol. 285, no. 5427, pp. 571–574, 1999.

[3.6] D. Kruse, C. von Cube, C. Zimmermann, and P. W. Courteille, “Observation of lasing mediated by collective atomic recoil,” *Phys. Rev. Lett.*, vol. 91, no. 18, p. 183601, 2003.

[3.7] S. Slama, G. Krenz, S. Bux, C. Zimmermann, and P. W. Courteille, “Cavity-enhanced superradiant rayleigh scattering with ultracold and bose-einstein condensed atoms,” *Phys. Rev. A*, vol. 75, no. 6, p. 063620, 2007.

[3.8] T. Grießer, H. Ritsch, M. Hemmerling, and G. Robb, “A vlasov approach to bunching and selfordering of particles in optical resonators,” *Eur. Phys. J. D*, vol. 58, no. 3, pp. 349–368, 2010.

[3.9] P. Domokos and H. Ritsch, “Collective cooling and self-organization of atoms in a cavity,” *Phys. Rev. Lett.*, vol. 89, no. 25, p. 253003, 2002.

[3.10] A. T. Black, H. W. Chan, and V. Vuletić, “Observation of collective friction forces due to spatial self-organization of atoms: from rayleigh to bragg scattering,” *Phys. Rev. Lett.*, vol. 91, no. 20, p. 203001, 2003.

[3.11] D. Nagy, G. Szirmai, and P. Domokos, “Self-organization of a bose-einstein condensate in an optical cavity,” *Eur. Phys. J. D*, vol. 48, no. 1, pp. 127–137, 2008.

[3.12] K. Baumann, C. Guerlin, F. Brennecke, and T. Esslinger, “Dicke quantum phase transition with a superfluid gas in an optical cavity,” *Nature*, vol. 464, no. 7293, p. 1301, 2010.

[3.13] R. H. Dicke, “Coherence in spontaneous radiation processes,” *Phys. Rev.*, vol. 93, no. 1, p. 99, 1954.

[3.14] M. Tavis and F. W. Cummings, “Exact solution for an n-molecule—radiation-field hamiltonian,” *Phys. Rev.*, vol. 170, no. 2, p. 379, 1968.

[3.15] D. Nagy, G. Kónya, G. Szirmai, and P. Domokos, “Dicke-model phase transition in the quantum motion of a bose-einstein condensate in an optical cavity,” *Phys. Rev. Lett.*, vol. 104, no. 13, p. 130401, 2010.

[3.16] J. Léonard, A. Morales, P. Zupancic, T. Esslinger, and T. Donner, “Supersolid formation in a quantum gas breaking a continuous translational symmetry,” *Nature*, vol. 543, no. 7643, p. 87, 2017.

[3.17] T. Grießer and H. Ritsch, “Light-induced crystallization of cold atoms in a 1d optical trap,” *Phys. Rev. Lett.*, vol. 111, no. 5, p. 055702, 2013.

[3.18] D. E. Chang, J. I. Cirac, and H. J. Kimble, “Self-organization of atoms along a nanophotonic waveguide,” *Phys. Rev. Lett.*, vol. 110, no. 11, p. 113606, 2013.

[3.19] V. Torggler, S. Krämer, and H. Ritsch, “Quantum annealing with ultracold atoms in a multimode optical resonator,” *Phys. Rev. A*, vol. 95, no. 3, p. 032310, 2017.

[3.20] S. Gopalakrishnan, B. L. Lev, and P. M. Goldbart, “Emergent crystallinity and frustration with bose–einstein condensates in multimode cavities,” *Nat. Phys.*, vol. 5, no. 11, p. 845, 2009.

References for Chapter 4

[4.1] R. Bonifacio, L. De Salvo, L. Narducci, and E. D'Angelo, "Exponential gain and self-bunching in a collective atomic recoil laser," *Phys. Rev. A*, vol. 50, no. 2, p. 1716, 1994.

[4.2] H. Ritsch, P. Domokos, F. Brennecke, and T. Esslinger, "Cold atoms in cavity-generated dynamical optical potentials," *Rev. Mod. Phys.*, vol. 85, no. 2, p. 553, 2013.

[4.3] K. Baumann, C. Guerlin, F. Brennecke, and T. Esslinger, "Dicke quantum phase transition with a superfluid gas in an optical cavity," *Nature*, vol. 464, no. 7293, pp. 1301–1306, 2010.

[4.4] S. Gopalakrishnan, B. L. Lev, and P. M. Goldbart, "Viewpoint: Liquid-crystalline phases of ultracold atoms," *Phys. Rev. A*, vol. 82, p. 043612, 2010.

[4.5] F. A. Hopf, P. Meystre, M. O. Scully, and W. H. Louisell, "Classical theory of a free-electron laser," *Opt. Commun.*, vol. 18, no. 4, pp. 413–416, 1976.

[4.6] D. Schmidt, H. Tomczyk, S. Slama, and C. Zimmermann, "Dynamical instability of a bose-einstein condensate in an optical ring resonator," *Phys. Rev. Lett.*, vol. 112, no. 11, p. 115302, 2014.

[4.7] S. Bux, H. Tomczyk, D. Schmidt, P. W. Courteille, N. Piovella, and C. Zimmermann, "Control of matter-wave superradiance with a high-finesse ring cavity," *Phys. Rev. A*, vol. 87, no. 2, p. 023607, 2013.

[4.8] P. Domokos and H. Ritsch, "Collective cooling and self-organization of atoms in a cavity," *Phys. Rev. Lett.*, vol. 89, no. 25, p. 253003, 2002.

[4.9] A. T. Black, H. W. Chan, and V. Vuletić, "Observation of collective friction forces due to spatial self-organization of atoms: from rayleigh to bragg scattering," *Phys. Rev. Lett.*, vol. 91, no. 20, p. 203001, 2003.

[4.10] K. J. Arnold, M. P. Baden, and M. D. Barrett, "Self-organization threshold scaling for thermal atoms coupled to a cavity," *Phys. Rev. Lett.*, vol. 109, no. 15, p. 153002, 2012.

[4.11] D. Nagy, G. Kónya, G. Szirmai, and P. Domokos, "Dicke-model phase transition in the quantum motion of a bose-einstein condensate in an optical cavity," *Phys. Rev. Lett.*, vol. 104, no. 13, p. 130401, 2010.

[4.12] S. Ostermann, M. Sonnleitner, and H. Ritsch, "Scattering approach to two-colour light forces and self-ordering of polarizable particles," *New J. Phys.*, vol. 16, no. 4, p. 043017, 2014.

[4.13] M. Gangl and H. Ritsch, "Cavity-mediated dark-state cooling without spontaneous emission," *Phys. Rev. A*, vol. 64, no. 6, p. 063414, 2001.

[4.14] T. Salzburger and H. Ritsch, "Collective transverse cavity cooling of a dense molecular beam," *New J. Phys.*, vol. 11, no. 5, p. 055025, 2009.

[4.15] M. Gangl and H. Ritsch, "Cold atoms in a high-q ring cavity," *Phys. Rev. A*, vol. 61, no. 4, p. 043405, 2000.

[4.16] C. Maes, J. K. Asboth, and H. Ritsch, "Self ordering threshold and superradiant backscattering to slow a fast gas beam in a ring cavity with counter propagating pump," *Opt. Express*, vol. 15, no. 10, pp. 6019–6035, 2007.

[4.17] J. Klinner, M. Lindholdt, B. Nagorny, and A. Hemmerich, "Normal mode splitting and mechanical effects of an optical lattice in a ring cavity," *Phys. Rev. Lett.*, vol. 96, no. 2, p. 023002, 2006.

[4.18] T. Grießer, H. Ritsch, M. Hemmerling, and G. R. M. Robb, "A vlasov approach to bunching and selfordering of particles in optical resonators," *Eur. Phys. J. D*, vol. 58, no. 3, pp. 349–368, 2010.

[4.19] E. Tesio, G. R. M. Robb, T. Ackemann, W. Firth, and G.-L. Oppo, "Kinetic theory for transverse optomechanical instabilities," *Phys. Rev. Lett.*, vol. 112, no. 4, p. 043901, 2014.

[4.20] W. Niedenzu, T. Grießer, and H. Ritsch, "Kinetic theory of cavity cooling and self-organisation of a cold gas," *EPL*, vol. 96, no. 4, p. 43001, 2011.

[4.21] L. Landau, "On the thermodynamics of photoluminescence," *J. Phys.*, vol. 10, pp. 503–506, 1946.

[4.22] I. B. Bernstein, J. M. Greene, and M. D. Kruskal, "Exact nonlinear plasma oscillations," *Phys. Rev.*, vol. 108, no. 3, p. 546, 1957.

[4.23] H. Keßler, J. Klinder, M. Wolke, and A. Hemmerich, "Steering matter wave superradiance with an ultranarrow-band optical cavity," *Phys. Rev. Lett.*, vol. 113, p. 070404, Aug 2014.

References for Chapter 5

[5.1] A. V. Andreev, V. I. Emel'yanov, and Y. A. Il'inski, "Collective spontaneous emission (dicke superradiance)," *Phys. Usp.*, vol. 23, no. 8, pp. 493–514, 1980.

[5.2] I. B. Mekhov, C. Maschler, and H. Ritsch, "Light scattering from ultracold atoms in optical lattices as an optical probe of quantum statistics," *Phys. Rev. A*, vol. 76, no. 5, p. 053618, 2007.

[5.3] H. Zoubi and H. Ritsch, "Metastability and directional emission characteristics of excitons in 1d optical lattices," *EPL (Europhys. Lett.)*, vol. 90, no. 2, p. 23001, 2010.

[5.4] A. Braun, G. Korn, X. Liu, D. Du, J. Squier, and G. Mourou, “Self-channeling of high-peak-power femtosecond laser pulses in air,” *Opt. Lett.*, vol. 20, no. 1, pp. 73–75, 1995.

[5.5] D. Kartashov, S. Ališauskas, A. Pugžlys, A. Voronin, A. Zheltikov, M. Petrarca, P. Béjot, J. Kasparian, J.-P. Wolf, and A. Baltuška, “Mid-infrared laser filamentation in molecular gases,” *Opt. Lett.*, vol. 38, no. 16, pp. 3194–3197, 2013.

[5.6] A. Zheltikov, A. LHuillier, and F. Krausz, “Nonlinear optics,” in *Springer Handbook of Lasers and Optics*, pp. 161–251, Springer, 2012.

[5.7] W. Singer, M. Frick, S. Bernet, and M. Ritsch-Marte, “Self-organized array of regularly spaced microbeads in a fiber-optical trap,” *J. Opt. Soc. Am. B*, vol. 20, no. 7, pp. 1568–1574, 2003.

[5.8] M. M. Burns, J.-M. Fournier, and J. A. Golovchenko, “Optical matter: crystallization and binding in intense optical fields,” *Science*, vol. 249, no. 4970, p. 749, 1990.

[5.9] S. Tatarkova, A. Carruthers, and K. Dholakia, “One-dimensional optically bound arrays of microscopic particles,” *Phys. Rev. Lett.*, vol. 89, no. 28, p. 283901, 2002.

[5.10] V. Demergis and E.-L. Florin, “Ultrastrong optical binding of metallic nanoparticles,” *Nano Lett.*, vol. 12, no. 11, pp. 5756–5760, 2012.

[5.11] V. Karásek, T. Čižmár, O. Brzobohatỳ, P. Zemánek, V. Garcés-Chávez, and K. Dholakia, “Long-range one-dimensional longitudinal optical binding,” *Phys. Rev. Lett.*, vol. 101, no. 14, p. 143601, 2008.

[5.12] V. Karásek, O. Brzobohatỳ, and P. Zemánek, “Longitudinal optical binding of several spherical particles studied by the coupled dipole method,” *J. Opt. A*, vol. 11, no. 3, p. 034009, 2009.

[5.13] K. Dholakia and P. Zemánek, “Colloquium: Gripped by light: Optical binding,” *Rev. Mod. Phys.*, vol. 82, no. 2, p. 1767, 2010.

[5.14] R. Bonifacio and L. De Salvo, “Collective atomic recoil laser (carl) optical gain without inversion by collective atomic recoil and self-bunching of two-level atoms,” *Nuclear Instruments and Methods in Physics Research Section A: Accelerators, Spectrometers, Detectors and Associated Equipment*, vol. 341, no. 1, pp. 360–362, 1994.

[5.15] M. Saffman, “Self-induced dipole force and filamentation instability of a matter wave,” *Phys. Rev. Lett.*, vol. 81, no. 1, p. 65, 1998.

[5.16] S. Inouye, A. Chikkatur, D. Stamper-Kurn, J. Stenger, D. Pritchard, and W. Ketterle, “Superradiant rayleigh scattering from a bose-einstein condensate,” *Science*, vol. 285, no. 5427, pp. 571–574, 1999.

[5.17] N. Piovella, R. Bonifacio, B. McNeil, and G. Robb, “Superradiant light scattering and grating formation in cold atomic vapours,” *Opt. Commun.*, vol. 187, no. 1, pp. 165–170, 2001.

[5.18] D. O’dell, S. Giovanazzi, and G. Kurizki, “Rotons in gaseous bose-einstein condensates irradiated by a laser,” *Phys. Rev. Lett.*, vol. 90, no. 11, p. 110402, 2003.

[5.19] Y. Yoshikawa, Y. Torii, and T. Kuga, “Superradiant light scattering from thermal atomic vapors,” *Phys. Rev. Lett.*, vol. 94, p. 083602, Mar 2005.

[5.20] G. A. Muradyan, Y. Wang, W. Williams, and M. Saffman, “Absolute instability and pattern formation in cold atomic vapors,” in *Nonlinear Guided Waves and Their Applications*, Optical Society of America, 2005.

[5.21] S. Slama, S. Bux, G. Krenz, C. Zimmermann, and P. W. Courteille, “Superradiant rayleigh scattering and collective atomic recoil lasing in a ring cavity,” *Phys. Rev. Lett.*, vol. 98, p. 053603, Feb 2007.

[5.22] J. A. Greenberg, B. L. Schmittberger, and D. J. Gauthier, “Bunching-induced optical nonlinearity and instability in cold atoms [invited],” *Opt. Express*, vol. 19, no. 23, pp. 22535–22549, 2011.

[5.23] B. L. Schmittberger and D. J. Gauthier, “Spontaneous emergence of free-space optical and atomic patterns,” *arXiv preprint arXiv:1603.06294*, 2016.

[5.24] G. Labeyrie, E. Tesio, P. M. Gomes, G.-L. Oppo, W. J. Firth, G. R. Robb, A. S. Arnold, R. Kaiser, and T. Ackemann, “Optomechanical self-structuring in a cold atomic gas,” *Nature Photon.*, vol. 8, no. 4, pp. 321–325, 2014.

[5.25] G. R. M. Robb, E. Tesio, G.-L. Oppo, W. J. Firth, T. Ackemann, and R. Bonifacio, “Quantum threshold for optomechanical self-structuring in a bose-einstein condensate,” *Phys. Rev. Lett.*, vol. 114, p. 173903, May 2015.

[5.26] P. Domokos and H. Ritsch, “Collective cooling and self-organization of atoms in a cavity,” *Phys. Rev. Lett.*, vol. 89, no. 25, p. 253003, 2002.

[5.27] A. T. Black, H. W. Chan, and V. Vuletić, “Observation of collective friction forces due to spatial self-organization of atoms: From rayleigh to bragg scattering,” *Phys. Rev. Lett.*, vol. 91, p. 203001, Nov 2003.

[5.28] K. J. Arnold, M. P. Baden, and M. D. Barrett, “Self-organization threshold scaling for thermal atoms coupled to a cavity,” *Phys. Rev. Lett.*, vol. 109, p. 153002, Oct 2012.

[5.29] H. Ritsch, P. Domokos, F. Brennecke, and T. Esslinger, “Cold atoms in cavity-generated dynamical optical potentials,” *Rev. Mod. Phys.*, vol. 85, no. 2, p. 553, 2013.

[5.30] K. Baumann, C. Guerlin, F. Brennecke, and T. Esslinger, “Dicke quantum phase transition with a superfluid gas in an optical cavity,” *Nature*, vol. 464, no. 7293, pp. 1301–1306, 2010.

[5.31] H. Keßler, J. Klinder, M. Wolke, and A. Hemmerich, “Steering matter wave superradiance with an ultranarrow-band optical cavity,” *Phys. Rev. Lett.*, vol. 113, no. 7, p. 070404, 2014.

[5.32] S. Ostermann, T. Grießer, and H. Ritsch, “Atomic self-ordering in a ring cavity with counterpropagating pump fields,” *EPL (Europhys. Lett.)*, vol. 109, no. 4, p. 43001, 2015.

[5.33] R. Mottl, F. Brennecke, K. Baumann, R. Landig, T. Donner, and T. Esslinger, “Roton-type mode softening in a quantum gas with cavity-mediated long-range interactions,” *Science*, vol. 336, no. 6088, pp. 1570–1573, 2012.

[5.34] T. Grießer and H. Ritsch, “Light-induced crystallization of cold atoms in a 1d optical trap,” *Phys. Rev. Lett.*, vol. 111, no. 5, p. 055702, 2013.

[5.35] D. Chang, J. I. Cirac, and H. Kimble, “Self-organization of atoms along a nanophotonic waveguide,” *Phys. Rev. Lett.*, vol. 110, no. 11, p. 113606, 2013.

[5.36] S. Gopalakrishnan, B. L. Lev, and P. M. Goldbart, “Emergent crystallinity and frustration with bose–einstein condensates in multimode cavities,” *Nat. Phys.*, vol. 5, no. 11, pp. 845–850, 2009.

[5.37] D. Chang, V. Gritsev, G. Morigi, V. Vuletić, M. Lukin, and E. Demler, “Crystallization of strongly interacting photons in a nonlinear optical fibre,” *Nat. Phys.*, vol. 4, no. 11, pp. 884–889, 2008.

[5.38] J. Otterbach, M. Moos, D. Muth, and M. Fleischhauer, “Wigner crystallization of single photons in cold rydberg ensembles,” *Phys. Rev. Lett.*, vol. 111, p. 113001, Sep 2013.

[5.39] S. Stringari and L. Pitaevskii, *Bose-Einstein Condensation.* Oxford University Press, 2003.

[5.40] P. Chaikin and T. Lubensky, *Principles of Condensed Matter Physics.* Cambridge University Press, 2000.

[5.41] S. Ostermann, M. Sonnleitner, and H. Ritsch, “Scattering approach to two-colour light forces and self-ordering of polarizable particles,” *New J. Phys.*, vol. 16, no. 4, p. 043017, 2014.

[5.42] I. Deutsch, R. Spreeuw, S. Rolston, and W. Phillips, “Photonic band gaps in optical lattices,” *Phys. Rev. A*, vol. 52, no. 2, p. 1394, 1995.

[5.43] N. W. Ashcroft and N. D. Mermin, “Solid state phys,” *Saunders, Philadelphia*, vol. 293, 1976.

[5.44] E. Wigner, “Effects of the electron interaction on the energy levels of electrons in metals,” *Transactions of the Faraday Society*, vol. 34, pp. 678–685, 1938.

[5.45] V. I. Yukalov and K. Ziegler, “Instability of insulating states in optical lattices due to collective phonon excitations,” *Phys. Rev. A*, vol. 91, p. 023628, Feb 2015.

[5.46] J. Keeling, M. J. Bhaseen, and B. D. Simons, “Fermionic superradiance in a transversely pumped optical cavity,” *Phys. Rev. Lett.*, vol. 112, p. 143002, Apr 2014.

[5.47] F. Piazza and P. Strack, “Umklapp superradiance with a collisionless quantum degenerate fermi gas,” *Phys. Rev. Lett.*, vol. 112, p. 143003, Apr 2014.

[5.48] Y. Chen, Z. Yu, and H. Zhai, “Superradiance of degenerate fermi gases in a cavity,” *Phys. Rev. Lett.*, vol. 112, p. 143004, Apr 2014.

[5.49] R. M. Sandner, W. Niedenzu, F. Piazza, and H. Ritsch, “Self-ordered stationary states of driven quantum degenerate gases in optical resonators,” *EPL (Europhys. Lett.)*, vol. 111, no. 5, p. 53001, 2015.

[5.50] C. A. Christensen, S. Will, M. Saba, G.-B. Jo, Y.-I. Shin, W. Ketterle, and D. Pritchard, “Trapping of ultracold atoms in a hollow-core photonic crystal fiber,” *Phys. Rev. A*, vol. 78, no. 3, p. 033429, 2008.

References for Chapter 6

[6.1] M. R. Andrews, M. O. Mewes, N. J. Van Druten, D. S. Durfee, *et al.*, “Direct, nondestructive observation of a bose condensate,” *Science*, vol. 273, no. 5271, p. 84, 1996.

[6.2] S. Inouye, A. Chikkatur, D. M. Stamper-Kurn, J. Stenger, D. Pritchard, and W. Ketterle, “Superradiant rayleigh scattering from a bose-einstein condensate,” *Science*, vol. 285, no. 5427, pp. 571–574, 1999.

[6.3] N. Piovella, M. Gatelli, and R. Bonifacio, “Quantum effects in the collective light scattering by coherent atomic recoil in a bose–einstein condensate,” *Opt. Commun.*, vol. 194, no. 1, pp. 167–173, 2001.

[6.4] S. Ostermann, F. Piazza, and H. Ritsch, “Spontaneous crystallization of light and ultracold atoms,” *Phys. Rev. X*, vol. 6, no. 2, p. 021026, 2016.

[6.5] J. H. Müller, D. Witthaut, R. le Targat, J. J. Arlt, E. S. Polzik, and A. J. Hilliard, “Semi-classical dynamics of superradiant rayleigh scattering in a bose–einstein condensate,” *J. Mod. Opt.*, vol. 63, no. 18, pp. 1886–1897, 2016.

[6.6] D. Schneble, Y. Torii, M. Boyd, E. W. Streed, D. E. Pritchard, and W. Ketterle, “The onset of matter-wave amplification in a superradiant bose-einstein condensate,” *Science*, vol. 300, no. 5618, pp. 475–478, 2003.

[6.7] N. Piovella, R. Bonifacio, B. W. J. McNeil, and G. R. M. Robb, “Superradiant light scattering and grating formation in cold atomic vapours,” *Opt. Commun.*, vol. 187, no. 1, pp. 165–170, 2001.

[6.8] S. Slama, S. Bux, G. Krenz, C. Zimmermann, and P. W. Courteille, “Superradiant rayleigh scattering and collective atomic recoil lasing in a ring cavity,” *Phys. Rev. Lett.*, vol. 98, no. 5, p. 053603, 2007.

[6.9] J. H. Müller, D. Witthaut, R. le Targat, J. J. Arlt, E. S. Polzik, and A. J. Hilliard, “Semi-classical dynamics of superradiant rayleigh scattering in a bose–einstein condensate,” *J. Mod. Opt.*, vol. 63, no. 18, pp. 1886–1897, 2016.

[6.10] J.-Y. Courtois, G. Grynberg, B. Lounis, and P. Verkerk, “Recoil-induced resonances in cesium: An atomic analog to the free-electron laser,” *Phys. Rev. Lett.*, vol. 72, no. 19, p. 3017, 1994.

[6.11] P. Horak, K. Gheri, and H. Ritsch, “Recoil-induced lasing of cold atoms,” *Phys. Rev. A*, vol. 52, no. 1, p. 554, 1995.

[6.12] C. Von Cube, S. Slama, D. Kruse, C. Zimmermann, P. W. Courteille, G. R. M. Robb, N. Piovella, and R. Bonifacio, “Self-synchronization and dissipation-induced threshold in collective atomic recoil lasing,” *Phys. Rev. Lett.*, vol. 93, no. 8, p. 083601, 2004.

[6.13] H. Keßler, J. Klinder, M. Wolke, and A. Hemmerich, “Steering matter wave superradiance with an ultranarrow-band optical cavity,” *Phys. Rev. Lett.*, vol. 113, no. 7, p. 070404, 2014.

[6.14] G. R. M. Robb, E. Tesio, G.-L. Oppo, W. J. Firth, T. Ackemann, and R. Bonifacio, “Quantum threshold for optomechanical self-structuring in a bose-einstein condensate,” *Phys. Rev. Lett.*, vol. 114, no. 17, p. 173903, 2015.

[6.15] I. Dimitrova, W. Lunden, J. Amato-Grill, N. Jepsen, Y. Yu, M. Messer, T. Rigaldo, G. Puentes, D. Weld, and W. Ketterle, “Observation of new superradiant regimes in a bose-einstein condensate,” *arXiv preprint arXiv:1709.02028*, 2017.

[6.16] P. Doria, T. Calarco, and S. Montangero, “Optimal control technique for many-body quantum dynamics,” *Phys. Rev. Lett.*, vol. 106, no. 19, p. 190501, 2011.

[6.17] R. Bücker, T. Berrada, S. Van Frank, J.-F. Schaff, T. Schumm, J. Schmiedmayer, G. Jäger, J. Grond, and U. Hohenester, “Vibrational state inversion of a bose–einstein condensate: optimal control and state tomography,” *J. Phys. B: At. Mol. Opt. Phys.*, vol. 46, no. 10, p. 104012, 2013.

[6.18] S. Ostermann, M. Sonnleitner, and H. Ritsch, “Scattering approach to two-colour light forces and self-ordering of polarizable particles,” *New J. Phys.*, vol. 16, no. 4, p. 043017, 2014.

[6.19] S. Szigeti, M. R. Hush, A. R. R. Carvalho, and J. J. Hope, “Continuous measurement feedback control of a bose-einstein condensate using phase-contrast imaging,” *Phys. Rev. A*, vol. 80, no. 1, p. 013614, 2009.

[6.20] T. Grießer and H. Ritsch, “Light-induced crystallization of cold atoms in a 1d optical trap,” *Phys. Rev. Lett.*, vol. 111, no. 5, p. 055702, 2013.

[6.21] I. Bloch, J. Dalibard, and W. Zwerger, “Many-body physics with ultracold gases,” *Rev. Mod. Phys*, vol. 80, no. 3, p. 885, 2008.

[6.22] F. Piazza and H. Ritsch, “Self-ordered limit cycles, chaos, and phase slippage with a superfluid inside an optical resonator,” *Phys. Rev. Lett.*, vol. 115, no. 16, p. 163601, 2015.

[6.23] R. M. Sandner, W. Niedenzu, F. Piazza, and H. Ritsch, “Self-ordered stationary states of driven quantum degenerate gases in optical resonators,” *EPL (Europhys. Lett.)*, vol. 111, no. 5, p. 53001, 2015.

[6.24] H. Ritsch, P. Domokos, F. Brennecke, and T. Esslinger, “Cold atoms in cavity-generated dynamical optical potentials,” *Rev. Mod. Phys.*, vol. 85, no. 2, p. 553, 2013.

[6.25] J. K. Asbóth, H. Ritsch, and P. Domokos, “Optomechanical coupling in a one-dimensional optical lattice,” *Phys. Rev. A*, vol. 77, no. 6, p. 063424, 2008.

References for Chapter 7

[7.1] M. Boninsegni and N. V. Prokof’ev, “Colloquium: Supersolids: What and where are they?,” *Rev. Mod. Phys.*, vol. 84, pp. 759–776, 2012.

[7.2] E. P. Gross, “Unified theory of interacting bosons,” *Phys. Rev.*, vol. 106, pp. 161–162, 1957.

[7.3] D. Thouless, “The flow of a dense superfluid,” *Ann. Phys. (N. Y.)*, vol. 52, no. 3, pp. 403–427, 1969.

[7.4] A. F. Andreev and I. M. Lifshitz, “Quantum theory of defects in crystals,” *Sov. Phys. JETP*, vol. 29, p. 1107, 1969.

[7.5] G. V. Chester, “Speculations on bose-einstein condensation and quantum crystals,” *Phys. Rev. A*, vol. 2, pp. 256–258, 1970.

[7.6] A. J. Leggett, “Can a solid be "superfluid"?,” *Phys. Rev. Lett.*, vol. 25, pp. 1543–1546, 1970.

[7.7] E. Kim and M. H. W. Chan, “Probable observation of a supersolid helium phase,” *Nature*, vol. 427, no. 6971, pp. 225–227, 2004.

[7.8] E. Kim and M. H. W. Chan, “Observation of superflow in solid helium,” *Science*, vol. 305, no. 5692, pp. 1941–1944, 2004.

[7.9] J. Day and J. Beamish, “Low-temperature shear modulus changes in solid 4he and connection to supersolidity,” *Nature*, vol. 450, no. 7171, pp. 853–856, 2007.

[7.10] D. Y. Kim and M. H. W. Chan, “Absence of supersolidity in solid helium in porous vycor glass,” *Phys. Rev. Lett.*, vol. 109, p. 155301, 2012.

[7.11] H. J. Maris, “Effect of elasticity on torsional oscillator experiments probing the possible supersolidity of helium,” *Phys. Rev. B*, vol. 86, p. 020502, 2012.

[7.12] J.-R. Li, J. Lee, W. Huang, S. Burchesky, B. Shteynas, F. Ç. Top, A. O. Jamison, and W. Ketterle, “A stripe phase with supersolid properties in spin–orbit-coupled bose–einstein condensates,” *Nature*, vol. 543, no. 7643, pp. 91–94, 2017.

[7.13] J. Léonard, A. Morales, P. Zupancic, T. Esslinger, and T. Donner, “Supersolid formation in a quantum gas breaking a continuous translational symmetry,” *Nature*, vol. 543, no. 7643, pp. 87–90, 2017.

[7.14] I. Dimitrova, W. Lunden, J. Amato-Grill, N. Jepsen, Y. Yu, M. Messer, T. Rigaldo, G. Puentes, D. Weld, and W. Ketterle, “Observation of two-beam collective scattering phenomena in a bose-einstein condensate,” *Phys. Rev. A*, vol. 96, p. 051603, 2017.

[7.15] S. Ostermann, F. Piazza, and H. Ritsch, “Spontaneous crystallization of light and ultracold atoms,” *Phys. Rev. X*, vol. 6, p. 021026, 2016.

[7.16] S. Ostermann, F. Piazza, and H. Ritsch, “Probing and characterizing the growth of a crystal of ultracold bosons and light,” *New J. Phys.*, vol. 19, no. 12, p. 125002, 2017.

[7.17] D. Kruse, M. Ruder, J. Benhelm, C. von Cube, C. Zimmermann, P. W. Courteille, T. Elsässer, B. Nagorny, and A. Hemmerich, “Cold atoms in a high-q ring cavity,” *Phys. Rev. A*, vol. 67, p. 051802, 2003.

[7.18] B. Nagorny, T. Elsässer, H. Richter, A. Hemmerich, D. Kruse, C. Zimmermann, and P. Courteille, “Optical lattice in a high-finesse ring resonator,” *Phys. Rev. A*, vol. 67, p. 031401, 2003.

[7.19] S. Slama, G. Krenz, S. Bux, C. Zimmermann, and P. W. Courteille, “Cavity-enhanced superradiant rayleigh scattering with ultracold and bose-einstein condensed atoms,” *Phys. Rev. A*, vol. 75, p. 063620, 2007.

[7.20] S. Bux, H. Tomczyk, D. Schmidt, P. W. Courteille, N. Piovella, and C. Zimmermann, “Control of matter-wave superradiance with a high-finesse ring cavity,” *Phys. Rev. A*, vol. 87, p. 023607, 2013.

[7.21] D. Schmidt, H. Tomczyk, S. Slama, and C. Zimmermann, “Dynamical instability of a bose-einstein condensate in an optical ring resonator,” *Phys. Rev. Lett.*, vol. 112, p. 115302, 2014.

[7.22] D. S. Naik, G. Kuyumjyan, D. Pandey, P. Bouyer, and A. Bertoldi, “Bec network in a malleable optical trap formed in a traveling wave cavity,” *pre-print: arXiv:1712.06491*, 2017.

[7.23] M. G. Moore, O. Zobay, and P. Meystre, “Quantum optics of a bose-einstein condensate coupled to a quantized light field,” *Phys. Rev. A*, vol. 60, pp. 1491–1506, 1999.

[7.24] P. Horak and H. Ritsch, “Dissipative dynamics of bose condensates in optical cavities,” *Phys. Rev. A*, vol. 63, p. 023603, 2001.

[7.25] D. Nagy, J. K. Asbóth, P. Domokos, and H. Ritsch, “Self-organization of a laser-driven cold gas in a ring cavity,” *EPL (Europhys. Lett.)*, vol. 74, no. 2, pp. 254–260, 2006.

[7.26] W. Chen, D. S. Goldbaum, M. Bhattacharya, and P. Meystre, “Classical dynamics of the optomechanical modes of a bose-einstein condensate in a ring cavity,” *Phys. Rev. A*, vol. 81, p. 053833, 2010.

[7.27] S. Ostermann, T. Grießer, and H. Ritsch, “Atomic self-ordering in a ring cavity with counterpropagating pump fields,” *EPL (Europhys. Lett.)*, vol. 109, no. 4, p. 43001, 2015.

[7.28] H. Ritsch, P. Domokos, F. Brennecke, and T. Esslinger, “Cold atoms in cavity-generated dynamical optical potentials,” *Rev. Mod. Phys.*, vol. 85, pp. 553–601, 2013.

[7.29] K. Baumann, C. Guerlin, F. Brennecke, and T. Esslinger, “Dicke quantum phase transition with a superfluid gas in an optical cavity,” *Nature*, vol. 464, p. 1301, 2010.

[7.30] J. Lang, F. Piazza, and W. Zwerger, “Collective excitations and supersolid behavior of bosonic atoms inside two crossed optical cavities,” *New J. Phys.*, vol. 19, no. 12, p. 123027, 2017.

[7.31] R. I. Moodie, K. E. Ballantine, and J. Keeling, “Generalized classes of continuous symmetries in two-mode dicke models,” *pre-print: arXiv:1711.03915*, 2017.

[7.32] A. Morales, P. Zupancic, J. Léonard, T. Esslinger, and T. Donner, “Coupling two order parameters in a quantum gas,” *pre-print: arXiv:1711.07988*, 2017.

[7.33] T. Grießer and H. Ritsch, “Light-induced crystallization of cold atoms in a 1d optical trap,” *Phys. Rev. Lett.*, vol. 111, p. 055702, 2013.

[7.34] D. E. Chang, J. I. Cirac, and H. J. Kimble, “Self-organization of atoms along a nanophotonic waveguide,” *Phys. Rev. Lett.*, vol. 110, p. 113606, 2013.

[7.35] C. Maschler, H. Ritsch, A. Vukics, and P. Domokos, “Entanglement assisted fast reordering of atoms in an optical lattice within a cavity at t=0,” *Optics Communications*, vol. 273, no. 2, pp. 446–450, 2007.

[7.36] A. Vukics, C. Maschler, and H. Ritsch, “Microscopic physics of quantum self-organization of optical lattices in cavities,” *New J. Phys.*, vol. 9, no. 8, pp. 255–255, 2007.

[7.37] S. Krämer and H. Ritsch, “Self-ordering dynamics of ultracold atoms in multicolored cavity fields,” *Phys. Rev. A*, vol. 90, p. 033833, 2014.

[7.38] J. Léonard, A. Morales, P. Zupancic, T. Donner, and T. Esslinger, “Monitoring and manipulating higgs and goldstone modes in a supersolid quantum gas,” *Science*, vol. 358, no. 6369, pp. 1415–1418, 2017.

[7.39] F. Piazza, P. Strack, and W. Zwerger, “Bose–einstein condensation versus dicke–hepp–lieb transition in an optical cavity,” *Annals of Physics*, vol. 339, pp. 135–159, 2013.

[7.40] D. Nagy, G. Szirmai, and P. Domokos, “Self-organization of a bose-einstein condensate in an optical cavity,” *Eur. Phys. J. D*, vol. 48, no. 1, pp. 127–137, 2008.

[7.41] F. Mivehvar, F. Piazza, and H. Ritsch, “Disorder-driven density and spin self-ordering of a bose-einstein condensate in a cavity,” *Phys. Rev. Lett.*, vol. 119, p. 063602, 2017.

[7.42] K. Baumann, R. Mottl, F. Brennecke, and T. Esslinger, “Exploring symmetry breaking at the dicke quantum phase transition,” *Phys. Rev. Lett.*, vol. 107, p. 140402, 2011.

[7.43] J. Jin, D. Rossini, R. Fazio, M. Leib, and M. J. Hartmann, “Photon solid phases in driven arrays of nonlinearly coupled cavities,” *Phys. Rev. Lett.*, vol. 110, p. 163605, 2013.

[7.44] B. Bujnowski, J. K. Corso, A. L. C. Hayward, J. H. Cole, and A. M. Martin, “Supersolid phases of light in extended jaynes-cummings-hubbard systems,” *Phys. Rev. A*, vol. 90, p. 043801, 2014.

[7.45] R. Landig, L. Hruby, N. Dogra, M. Landini, R. Mottl, T. Donner, and T. Esslinger, “Quantum phases from competing short- and long-range interactions in an optical lattice,” *Nature*, vol. 532, no. 7600, pp. 476–479, 2016.

[7.46] P. R. Berman, *Atom interferometry.* Academic press, 1997.

[7.47] A. D. Cronin, J. Schmiedmayer, and D. E. Pritchard, “Optics and interferometry with atoms and molecules,” *Rev. Mod. Phys.*, vol. 81, pp. 1051–1129, 2009.

[7.48] F. Sorrentino, K. Bongs, P. Bouyer, L. Cacciapuoti, M. de Angelis, H. Dittus, W. Ertmer, A. Giorgini, J. Hartwig, M. Hauth, S. Herrmann, M. Inguscio, E. Kajari, T. Könemann, C. Lämmerzahl, A. Landragin, G. Modugno, F. Pereira dos Santos, A. Peters, M. Prevedelli, E. Rasel, W. Schleich, M. Schmidt, A. Senger, K. Sengstock, G. Stern, G. Tino, and R. Walser, "A compact atom interferometer for future space missions," *Microgravity Science and Technology*, vol. 22, no. 4, pp. 551–561, 2010.

[7.49] P. Hamilton, M. Jaffe, J. M. Brown, L. Maisenbacher, B. Estey, and H. Müller, "Atom interferometry in an optical cavity," *Phys. Rev. Lett.*, vol. 114, p. 100405, 2015.

References for Chapter 8

[8.1] M. Lewenstein, A. Sanpera, V. Ahufinger, B. Damskic, A. Sen(De), and U. Sen, "Ultracold atomic gases in optical lattices: mimicking condensed matter physics and beyond," *Adv. Phys.*, vol. 56, p. 243, 2007.

[8.2] I. Bloch, J. Dalibard, and W. Zwerger, "Many-body physics with ultracold gases," *Rev. Mod. Phys.*, vol. 80, p. 885, 2008.

[8.3] M. Greiner, O. Mandel, T. Esslinger, T. W. Hänsch, and I. Bloch, "Quantum phase transition from a superfluid to a mott insulator in a gas of ultracold atoms," *Nature*, vol. 415, p. 39, 2002.

[8.4] J. Struck, M. Weinberg, C. Ölschläger, P. Windpassinger, J. Simonet, K. Sengstock, R. Höppner, P. Hauke, A. Eckardt, M. Lewenstein, and L. Mathey, "Engineering ising-XY spin-models in a triangular lattice using tunable artificial gauge fields," *Nature Physics*, vol. 9, no. 11, pp. 738–743, 2013.

[8.5] D. Greif, T. Uehlinger, G. Jotzu, L. Tarruell, and T. Esslinger, "Short-range quantum magnetism of ultracold fermions in an optical lattice," *Science*, vol. 340, no. 6138, pp. 1307–1310, 2013.

[8.6] D. Greif, G. Jotzu, M. Messer, R. Desbuquois, and T. Esslinger, "Formation and dynamics of antiferromagnetic correlations in tunable optical lattices," *Phys. Rev. Lett.*, vol. 115, p. 260401, 2015.

[8.7] R. A. Hart, P. M. Duarte, T.-L. Yang, X. Liu, T. Paiva, E. Khatami, R. T. Scalettar, N. Trivedi, D. A. Huse, and R. G. Hulet, "Observation of antiferromagnetic correlations in the hubbard model with ultracold atoms," *Nature*, vol. 519, no. 7542, pp. 211–214, 2015.

[8.8] A. Mazurenko, C. S. Chiu, G. Ji, M. F. Parsons, M. Kanász-Nagy, R. Schmidt, F. Grusdt, E. Demler, D. Greif, and M. Greiner, "A cold-atom fermi–hubbard antiferromagnet," *Nature*, vol. 545, no. 7655, pp. 462–466, 2017.

[8.9] Y.-J. Lin, R. L. Compton, K. Jiménez-García, J. V. Porto, and I. B. Spielman, "Synthetic magnetic fields for ultracold neutral atoms," *Nature*, vol. 462, no. 7273, pp. 628–632, 2009.

[8.10] M. Aidelsburger, M. Atala, M. Lohse, J. T. Barreiro, B. Paredes, and I. Bloch, "Realization of the hofstadter hamiltonian with ultracold atoms in optical lattices," *Phys. Rev. Lett.*, vol. 111, no. 18, 2013.

[8.11] H. Miyake, G. A. Siviloglou, C. J. Kennedy, W. C. Burton, and W. Ketterle, "Realizing the harper hamiltonian with laser-assisted tunneling in optical lattices," *Phys. Rev. Lett.*, vol. 111, p. 185302, 2013.

[8.12] Y.-J. Lin, K. Jiménez-García, and I. B. Spielman, "Spin–orbit-coupled bose–einstein condensates," *Nature*, vol. 471, no. 7336, p. 83, 2011.

[8.13] Z. Wu, L. Zhang, W. Sun, X.-T. Xu, B.-Z. Wang, S.-C. Ji, Y. Deng, S. Chen, X.-J. Liu, and J.-W. Pan, "Realization of two-dimensional spin-orbit coupling for bose-einstein condensates," *Science*, vol. 354, no. 6308, pp. 83–88, 2016.

[8.14] J.-R. Li, J. Lee, W. Huang, S. Burchesky, B. Shteynas, F. Ç. Top, A. O. Jamison, and W. Ketterle, "A stripe phase with supersolid properties in spin–orbit-coupled bose–einstein condensates," *Nature*, vol. 543, no. 7643, p. 91, 2017.

[8.15] H. Ritsch, P. Domokos, F. Brennecke, and T. Esslinger, "Cold atoms in cavity-generated dynamical optical potentials," *Rev. Mod. Phys.*, vol. 85, p. 553, 2013.

[8.16] S. Ostermann, F. Piazza, and H. Ritsch, "Spontaneous crystallization of light and ultracold atoms," *Phys. Rev. X*, vol. 6, p. 021026, 2016.

[8.17] I. Dimitrova, W. Lunden, J. Amato-Grill, N. Jepsen, Y. Yu, M. Messer, T. Rigaldo, G. Puentes, D. Weld, and W. Ketterle, "Observation of two-beam collective scattering phenomena in a bose-einstein condensate," *Phys. Rev. A*, vol. 96, p. 051603, 2017.

[8.18] A. Vochezer, T. Kampschulte, K. Hammerer, and P. Treutlein, "Light-mediated collective atomic motion in an optical lattice coupled to a membrane," *Phys. Rev. Lett.*, vol. 120, p. 073602, 2018.

[8.19] D. Kruse, M. Ruder, J. Benhelm, C. von Cube, C. Zimmermann, P. W. Courteille, T. Elsässer, B. Nagorny, and A. Hemmerich, "Cold atoms in a high-q ring cavity," *Phys. Rev. A*, vol. 67, p. 051802, 2003.

[8.20] B. Nagorny, T. Elsässer, H. Richter, A. Hemmerich, D. Kruse, C. Zimmermann, and P. Courteille, "Optical lattice in a high-finesse ring resonator," *Phys. Rev. A*, vol. 67, p. 031401, 2003.

[8.21] F. Brennecke, T. Donner, S. Ritter, T. Bourdel, M. Köhl, and T. Esslinger, "Cavity qed with a bose-einstein condensate," *Nature*, vol. 450, p. 268, 2007.

[8.22] K. Baumann, C. Guerlin, F. Brennecke, and T. Esslinger, “Dicke quantum phase transition with a superfluid gas in an optical cavity,” *Nature*, vol. 464, p. 1301, 2010.

[8.23] J. Klinder, H. Keßler, M. R. Bakhtiari, M. Thorwart, and A. Hemmerich, “Observation of a superradiant mott insulator in the dicke-hubbard model,” *Phys. Rev. Lett.*, vol. 115, no. 23, 2015.

[8.24] D. Kruse, C. von Cube, C. Zimmermann, and P. W. Courteille, “Observation of lasing mediated by collective atomic recoil,” *Phys. Rev. Lett.*, vol. 91, p. 183601, 2003.

[8.25] S. Slama, S. Bux, G. Krenz, C. Zimmermann, and P. W. Courteille, “Superradiant rayleigh scattering and collective atomic recoil lasing in a ring cavity,” *Phys. Rev. Lett.*, vol. 98, p. 053603, 2007.

[8.26] D. Schmidt, H. Tomczyk, S. Slama, and C. Zimmermann, “Dynamical instability of a bose-einstein condensate in an optical ring resonator,” *Phys. Rev. Lett.*, vol. 112, p. 115302, 2014.

[8.27] R. Landig, L. Hruby, N. Dogra, M. Landini, R. Mottl, T. Donner, and T. Esslinger, “Quantum phases from competing short- and long-range interactions in an optical lattices,” *Nature*, vol. 532, p. 476, 2016.

[8.28] J. Léonard, A. Morales, P. Zupancic, T. Esslinger, and T. Donner, “Supersolid formation in a quantum gas breaking a continuous translational symmetry,” *Nature*, vol. 543, no. 7643, p. 87, 2017.

[8.29] F. Dimer, B. Estienne, A. S. Parkins, and H. J. Carmichael, “Proposed realization of the dicke-model quantum phase transition in an optical cavity qed system,” *Phys. Rev. A*, vol. 75, p. 013804, 2007.

[8.30] J. Larson and M. Lewenstein, “Dilute gas of ultracold two-level atoms inside a cavity: generalized dicke model,” *New J. Phys.*, vol. 11, no. 6, p. 063027, 2009.

[8.31] S. Gopalakrishnan, B. L. Lev, and P. M. Goldbart, “Frustration and glassiness in spin models with cavity-mediated interactions,” *Phys. Rev. Lett.*, vol. 107, p. 277201, 2011.

[8.32] Z. Zhiqiang, C. H. Lee, R. Kumar, K. J. Arnold, S. J. Masson, A. S. Parkins, and M. D. Barrett, “Nonequilibrium phase transition in a spin-1 dicke model,” *Optica*, vol. 4, no. 4, p. 424, 2017.

[8.33] M. G. Moore, O. Zobay, and P. Meystre, “Quantum optics of a bose-einstein condensate coupled to a quantized light field,” *Phys. Rev. A*, vol. 60, pp. 1491–1506, 1999.

[8.34] P. Domokos and H. Ritsch, “Collective cooling and self-organization of atoms in a cavity,” *Phys. Rev. Lett.*, vol. 89, p. 253003, 2002.

[8.35] D. Nagy, J. K. Asbóth, P. Domokos, and H. Ritsch, “Self-organization of a laser-driven cold gas in a ring cavity,” *EPL (Europhys. Lett.)*, vol. 74, no. 2, p. 254, 2006.

[8.36] C. Maschler, I. B. Mekhov, and H. Ritsch, “Ultracold atoms in optical lattices generated by quantized light fields,” *Eur. Phys. J. D*, vol. 46, no. 3, pp. 545–560, 2008.

[8.37] D. Nagy, G. Szirmai, and P. Domokos, “Self-organization of a bose-einstein condensate in an optical cavity,” *Eur. Phys. J. D*, vol. 48, no. 1, pp. 127–137, 2008.

[8.38] D. Nagy, G. Kónya, G. Szirmai, and P. Domokos, “Dicke-model phase transition in the quantum motion of a bose-einstein condensate in an optical cavity,” *Phys. Rev. Lett.*, vol. 104, no. 13, p. 130401, 2010.

[8.39] F. Piazza, P. Strack, and W. Zwerger, “Bose-einstein condensation versus dicke-hepp-lieb transition in an optical cavity,” *Annals of Physics*, vol. 339, no. 0, pp. 135 – 159, 2013.

[8.40] F. Piazza and P. Strack, “Umklapp superradiance with a collisionless quantum degenerate fermi gas,” *Phys. Rev. Lett.*, vol. 112, p. 143003, 2014.

[8.41] J. Keeling, J. Bhaseen, and B. Simons, “Fermionic superradiance in a transversely pumped optical cavity,” *Phys. Rev. Lett.*, vol. 112, p. 143002, 2014.

[8.42] F. Piazza and H. Ritsch, “Self-ordered limit cycles, chaos, and phase slippage with a superfluid inside an optical resonator,” *Phys. Rev. Lett.*, vol. 115, p. 163601, 2015.

[8.43] F. Mivehvar, H. Ritsch, and F. Piazza, “Superradiant topological peierls insulator inside an optical cavity,” *Phys. Rev. Lett.*, vol. 118, p. 073602, 2017.

[8.44] F. Mivehvar, S. Ostermann, F. Piazza, and H. Ritsch, “Driven-dissipative supersolid in a ring cavity,” *Phys. Rev. Lett.*, vol. 120, p. 123601, 2018.

[8.45] F. Mivehvar and D. L. Feder, “Synthetic spin-orbit interactions and magnetic fields in ring-cavity qed,” *Phys. Rev. A*, vol. 89, p. 013803, 2014.

[8.46] L. Dong, L. Zhou, B. Wu, B. Ramachandhran, and H. Pu, “Cavity-assisted dynamical spin-orbit coupling in cold atoms,” *Phys. Rev. A*, vol. 89, p. 011602(R), 2014.

[8.47] Y. Deng, J. Cheng, H. Jing, , and S. Yi, “Bose-einstein condensates with cavity-mediated spin-orbit coupling,” *Phys. Rev. Lett.*, vol. 112, p. 143007, 2014.

[8.48] F. Mivehvar and D. L. Feder, “Enhanced stripe phases in spin-orbit-coupled bose-einstein condensates in ring cavities,” *Phys. Rev. A*, vol. 92, p. 023611, 2015.

[8.49] F. Mivehvar, F. Piazza, and H. Ritsch, "Disorder-driven density and spin self-ordering of a bose-einstein condensate in a cavity," *Phys. Rev. Lett.*, vol. 119, p. 063602, 2017.

[8.50] J.-S. Pan, X.-J. Liu, W. Zhang, W. Yi, and G.-C. Guo, "Topological superradiant states in a degenerate fermi gas," *Phys. Rev. Lett.*, vol. 115, p. 045303, 2015.

[8.51] D. Yu, J.-S. Pan, X.-J. Liu, W. Zhang, and W. Yi, "Topological superradiant state in fermi gases with cavity induced spin–orbit coupling," *Frontiers of Physics*, vol. 13, no. 1, 2017.

[8.52] J. Fan, X. Zhou, W. Zheng, W. Yi, G. Chen, and S. Jia, "Magnetic orders in a fermi gas induced by cavity-field fluctuations," *pre-print: arXiv:1801.08254*, 2017.

[8.53] E. Colella, R. Citro, M. Barsanti, D. Rossini, and M.-L. Chiofalo, "Quantum phases of spinful fermi gases in optical cavities," *Phys. Rev. B*, vol. 97, no. 13, p. 134502, 2018.

[8.54] M. Landini, N. Dogra, K. Kröger, L. Hruby, T. Donner, and T. Esslinger, "Formation of a spin texture in a quantum gas coupled to a cavity," *arXiv preprint arXiv:1803.01803*, 2018.

[8.55] M. Gangl and H. Ritsch, "Cavity-mediated dark-state cooling without spontaneous emission," *Phys. Rev. A*, vol. 64, no. 6, p. 063414, 2001.

[8.56] M. Gangl and H. Ritsch, "Cavity-enhanced polarization gradient cooling," *Journal of Physics B: Atomic, Molecular and Optical Physics*, vol. 35, no. 22, p. 4565, 2002.

[8.57] S. Ostermann, T. Grießer, and H. Ritsch, "Atomic self-ordering in a ring cavity with counterpropagating pump fields," *EPL (Europhys. Lett.)*, vol. 109, no. 4, p. 43001, 2015.

[8.58] Y. Li, L. P. Pitaevskii, and S. Stringari, "Quantum tricriticality and phase transitions in spin-orbit coupled bose-einstein condensates," *Phys. Rev. Lett.*, vol. 108, no. 22, 2012.

[8.59] Y. Li, G. I. Martone, L. P. Pitaevskii, and S. Stringari, "Superstripes and the excitation spectrum of a spin-orbit-coupled bose-einstein condensate," *Phys. Rev. Lett.*, vol. 110, no. 23, 2013.

[8.60] N. Nagaosa and Y. Tokura, "Topological properties and dynamics of magnetic skyrmions," *Nat. nanotechnol.*, vol. 8, no. 12, p. 899, 2013.

[8.61] A. Fert, V. Cros, and J. Sampaio, "Skyrmions on the track," *Nat. nanotechnol.*, vol. 8, no. 3, p. 152, 2013.

[8.62] S. Schuster, P. Wolf, D. Schmidt, S. Slama, and C. Zimmermann, "Pinning transition of bose-einstein condensates in optical ring resonators," *arXiv preprint arXiv:1803.02293*, 2018.

[8.63] J. K. Asbóth, L. Oroszlány, and A. Pályi, “A short course on topological insulators,” *Lecture Notes in Physics*, vol. 919, 2016.

[8.64] H.-B. Braun, “Topological effects in nanomagnetism: from superparamagnetism to chiral quantum solitons,” *Advances in Physics*, vol. 61, no. 1, pp. 1–116, 2012.

[8.65] S. Slama, G. Krenz, S. Bux, C. Zimmermann, and P. W. Courteille, “Cavity-enhanced superradiant rayleigh scattering with ultracold and bose-einstein condensed atoms,” *Phys. Rev. A*, vol. 75, p. 063620, 2007.

[8.66] S. Bux, H. Tomczyk, D. Schmidt, P. W. Courteille, N. Piovella, and C. Zimmermann, “Control of matter-wave superradiance with a high-finesse ring cavity,” *Phys. Rev. A*, vol. 87, p. 023607, 2013.

[8.67] D. Naik, G. Kuyumjyan, D. Pandey, P. Bouyer, and A. Bertoldi, “Bec network in a malleable optical trap formed in a traveling wave cavity,” *arXiv preprint arXiv:1712.06491*, 2017.

References for Chapter 10

[10.1] E. Vetsch, D. Reitz, G. Sagué, R. Schmidt, S. Dawkins, and A. Rauschenbeutel, “Optical interface created by laser-cooled atoms trapped in the evanescent field surrounding an optical nanofiber,” *Phys. Rev. Lett.*, vol. 104, no. 20, p. 203603, 2010.

[10.2] S. Marksteiner, C. Savage, P. Zoller, and S. Rolston, “Coherent atomic waveguides from hollow optical fibers: quantized atomic motion,” *Phys. Rev. A*, vol. 50, no. 3, p. 2680, 1994.

[10.3] P. Russell, “Photonic crystal fibers,” *Science*, vol. 299, no. 5605, pp. 358–362, 2003.

[10.4] M. J. Renn, D. Montgomery, O. Vdovin, D. Anderson, C. Wieman, and E. Cornell, “Laser-guided atoms in hollow-core optical fibers,” *Phys. Rev. Lett.*, vol. 75, no. 18, p. 3253, 1995.

[10.5] A. Maimaiti, D. Holzmann, V. G. Truong, H. Ritsch, and S. N. Chormaic, “Nonlinear force dependence on optically bound arrays of micro-particles trapped in the evanescent fields of fundamental and higher order microfibre modes,” *arXiv preprint arXiv:1604.06208*, 2016.

[10.6] J. Asbóth, H. Ritsch, and P. Domokos, “Optomechanical coupling in a one-dimensional optical lattice,” *Phys. Rev. A*, vol. 77, no. 6, p. 063424, 2008.

[10.7] D. E. Chang, J. I. Cirac, and H. J. Kimble, “Self-organization of atoms along a nanophotonic waveguide,” *Phys. Rev. Lett.*, vol. 110, p. 113606, 2013.

[10.8] T. Grießer and H. Ritsch, "Light induced crystallization of cold atoms in a thin 1D optical tube," *arXiv preprint arXiv:1303.7359*, 2013.

[10.9] O. Brzobohatỳ, V. Karásek, M. Šiler, L. Chvátal, T. Čižmár, and P. Zemánek, "Experimental demonstration of optical transport, sorting and self-arrangement using a/tractor beam/'," *Nat. Photon.*, vol. 7, no. 2, pp. 123–127, 2013.

[10.10] F. Le Kien, V. Balykin, and K. Hakuta, "Atom trap and waveguide using a two-color evanescent light field around a subwavelength-diameter optical fiber," *Phys. Rev. A*, vol. 70, no. 6, p. 063403, 2004.

[10.11] M. Sadgrove, S. Wimberger, and S. N. Chormaic, "Quantum coherent tractor beam effect for atoms trapped near a nanowaveguide," *Scientific Reports*, vol. 6, 2016.

[10.12] A. Maimaiti, V. G. Truong, M. Sergides, I. Gusachenko, and S. N. Chormaic, "Higher order microfibre modes for dielectric particle trapping and propulsion," *Scientific Reports*, vol. 5, p. 9077, 2015.

[10.13] P. Domokos, P. Horak, and H. Ritsch, "Quantum description of light-pulse scattering on a single atom in waveguides," *Phys. Rev. A*, vol. 65, no. 3, p. 033832, 2002.

[10.14] R. Gómez-Medina, P. San José, A. García-Martín, M. Lester, M. Nieto-Vesperinas, and J. Sáenz, "Resonant radiation pressure on neutral particles in a waveguide," *Phys. Rev. Lett.*, vol. 86, no. 19, p. 4275, 2001.

[10.15] P. Horak, P. Domokos, and H. Ritsch, "Giant lamb shift of atoms near lossy multimode optical micro-waveguides," *EPL (Europhys. Lett.)*, vol. 61, no. 4, p. 459, 2003.

[10.16] M. Sonnleitner, M. Ritsch-Marte, and H. Ritsch, "Optical forces, trapping and strain on extended dielectric objects," *EPL (Europhys. Lett.)*, vol. 94, no. 3, p. 34005, 2011.

[10.17] D. B. Ruffner and D. G. Grier, "Optical conveyors: a class of active tractor beams," *Phys. Rev. Lett.*, vol. 109, no. 16, p. 163903, 2012.

[10.18] S. Ostermann, M. Sonnleitner, and H. Ritsch, "Scattering approach to two-colour light forces and self-ordering of polarizable particles," *New J. Phys.*, vol. 16, no. 4, p. 043017, 2014.

[10.19] K. Dholakia and P. Zemánek, "Colloquium: Gripped by light: Optical binding," *Rev. Mod. Phys.*, vol. 82, no. 2, p. 1767, 2010.

[10.20] W. Singer, M. Frick, S. Bernet, and M. Ritsch-Marte, "Self-organized array of regularly spaced microbeads in a fiber-optical trap," *JOSA B*, vol. 20, no. 7, pp. 1568–1574, 2003.

[10.21] S. Vorrath, S. Möller, P. Windpassinger, K. Bongs, and K. Sengstock, "Efficient guiding of cold atoms through a photonic band gap fiber," *New J. Phys.*, vol. 12, no. 12, p. 123015, 2010.

[10.22] C. Lamprecht and M. A. Marte, "Comparing paraxial atom and light optics," *Quantum and Semiclassical Optics: Journal of the European Optical Society Part B*, vol. 10, no. 3, p. 501, 1998.

List of Publications

Publications During the PhD

Preprint

- S. Ostermann, H.-W. Lau, H. Ritsch, F. Mivehvar, *Cavity-induced emergent topological spin-textures in a Bose-Einstein condensate*, arXiv:1807.03316 (2018)

Articles

- F. Mivehvar, S. Ostermann, F. Piazza, H. Ritsch, *Driven-Dissipative Supersolid in a Ring Cavity*, Phys. Rev. Lett. **120**, 123601 (2018)
- S. Ostermann, F. Piazza, H. Ritsch, *Probing and characterizing the growth of a crystal of ultracold bosons and light*, New J. Phys. **19**, 125002 (2017)
- C. A. Ebongue, D. Holzmann, S. Ostermann, H. Ritsch, *Generating a stationary infinite range tractor force via a multimode optical fibre*, J. Opt. **19**, 065401 (2017)
- S. Ostermann, F. Piazza, H. Ritsch, *Spontaneous crystallization of light and ultracold atoms*, Phys. Rev. X **6**, 0210026 (2016)
- S. Ostermann, T. Grießer, H. Ritsch, *Atomic self-ordering in a ring cavity with counterpropagating pump fields*, EPL (Europhys. Lett.) **109**, 43001 (2015)

Publications Before Starting the PhD

- S. Ostermann, M. Sonnleitner, H. Ritsch, *Scattering approach to two-colour light forces and self-ordering of polarizable particles*, New J. Phys. **16**, 043017 (2014)

Talks

- *Emergent Skyrmions in a two-component Bose-Einstein condensate in a ring cavity*, International Conference on Quantum Optics 2018, (Obergurgl, Austria, February, 28, 2018)

- *Emergent Skyrmions in a two-component Bose-Einstein condensate in a ring cavity*, 39th SFB Meeting (Vienna, Austria, , December 14, 2017)

- *Multiple scattering approach to collective light forces and interactions of polarizable particles in the field of optical fibers*, Highland Spring School on Mesoscopic Phyics: Towards quantum technologies, (Trest, Czech Republik, April, 4, 2017)

- *Spontaneous Crystallization of Light and Ultracold Atoms*, TU Munich - Group Seminar of the research group of Prof. Wilhelm Zwerger (Munich, Germany, July, 19, 2017)

- *Spontaneous Crystallization of Light and Ultracold Atoms*, Optics and Atomic Physics Seminar – Weizmann Institute of Science, (Rehovot, Israel, September, 27, 2016)

- *Atomic self-ordering in a ring cavity with counterpropagating pump fields*, Young Atom Opticians Conference (YAO 2015) (Zurich, Switzerland, April, 21, 2015)

- *Scattering approach to two-colour light forces and self-ordering of polarizable particles*, 25th SFB-Meeting (Vienna, Austria, April, 11, 2014)

Poster Presentations

- *Emergent Skyrmions in a two component Bose-Einstein condensate in a ring cavity*, C3QS: Coherent Control of Complex Quantum Systems (Okinawa, Japan, April, 17-20, 2018)

- *Growing, probing and characterizing a crystal of ultracold bosons and light*, 4th Granada Summer School on Quantum Matter Out of Equilibrium (Granada, Spain, August, 30, 2017)

- *Growing, probing and characterizing a crystal of ultracold bosons and light*, 36th SFB FoQuS Meeting (Innsbruck, Austria, March, 30 - 31, 2017)

- *Spontaneous Crystallization of Light and Ultracold Atoms*, International Conference on Quantum Optics 2016, (Obergurgl, Austria, February, 21 - 27, 2016)

- *Dynamical crystallization of light and matter*, 31st SFB FoQuS Meeting, (Wien, Austria, December, 17 - 18, 2015)

- *Atomic self-ordering in a ring cavity with counterpropagating pump fields*, Joint 2015 Annual Meeting of the Austrian Physical Society and the Swiss Physical Society, (Wien, Austria, September, 26 - 29, 2015)
- *Atomic self-ordering in a ring cavity with counterpropagating pump fields*, Winterschool on Non-Equilibrium Quantum Systems: Theory and Experimental Implementation (Obergurgl, Austria, April, 07 - 10, 2015)
- *Atomic self-ordering in a ring cavity with counterpropagating pump fields*, 29th SFB Meeting (Innsbruck, Austria, March 12 - 13, 2015)
- *Scattering approach to multicolour light forces and self-ordering of polarizable particles*, International Conference on Quantum Optics 2014 (Obergurgl, Austria, February 23 - March 1, 2014)
- *Scattering approach to multicolour light forces and self-ordering of polarizable particles*, Workshop, Cavity Optomechanics – from the micro- to the macro scale (Innsbruck, Austria, November, 4-6, 2013)
- *Scattering approach to multicolour light forces and self-ordering of polarizable particles*, 22nd SFB FoQuS Meeting (Innsbruck, Austria, October, 24-25, 2013)